University of Strathclyde

Department of Physics

A W-BAND GYROTRON BACKWARD WAVE OSCILLATOR WITH HELICALLY CORRUGATED WAVEGUIDE

Craig Ross Donaldson

(B.Sc. (Hons.), M.Sc., University of Strathclyde)

A thesis presented in fulfilment of the requirements for

the degree of Doctor of Philosophy

September 2009

Copyright

This thesis is the result of the author's original research. It has been composed by the author and has not been previously submitted for examination which has led to the award of a degree.

The copyright of this thesis belongs to the author under the terms of the United Kingdom Copyright Acts as qualified by University of Strathclyde Regulation 3.50. Due acknowledgement must always be made of the use of any material contained in, or derived from, this thesis.

Dedication

I would like to dedicate this thesis to my wife Karen, my mother, Mary, and my father, Jim, for being the three people who always believed I could do more than I thought possible.

Table of Contents

Acknowledgments

I would primarily like to acknowledge the work of my supervisor Dr. W. He who was the driving force behind this work. Dr. He provided much needed guidance, encouragement and support through the course of this PhD. Also, my other supervisors Prof. A.D.R. Phelps and Dr. A.W. Cross provided much needed help and advice throughout the course of this PhD. I would also like to thank them for providing me the opportunity of studying under the tutelage of such talented people.

Also, I would like to acknowledge the hard work of my fellow colleagues Mr. F. Li and Mr. L. Zhang who have both directly been involved with the experimental side of the work contained within this thesis.

Furthermore, I would like to acknowledge the contributions of my colleagues Dr. K. Ronald, Dr. C.G. Whyte and Dr. C.W. Robertson who helped with the experimental construction of both the gyro-BWO experiment and Vector Network Analyzer measurements.

I would like to offer my sincerest thanks to both Mrs. K. Donaldson and Mr. D. Constable for their many contributions to the thesis. Mrs. Donaldson has provided much assistance in all areas throughout the course of this PhD. Mr. Constable has provided invaluable help to both the preparation and content of this piece of work.

Mr. D. Barclay must be acknowledged for his technical skill and advice in constructing the many varied and challenging parts of the gyro-BWO experiment.

Finally, I would like to thank my friends and family for the support I have received throughout my university career. It would have been difficult to complete without the full backing of those people closest to me.

Abstract

This thesis presents the results of a successful W-band gyrotron backward wave oscillator experiment. Three major achievements presented in this thesis are: 1) The design, simulation, construction and operation of a cusp electron gun; 2) The design, simulation, optimisation, construction and experimental measurement of a W-band helically corrugated waveguide and 3) the operation of the world's first W-band gyro-BWO using both a helically corrugated waveguide and a cusp electron gun. Gyro-BWO interaction with a 2nd cyclotron harmonic axis-encircling annular electron beam was observed.

The interaction region was constructed through an accurate electroplating method while the designed dispersion characteristics agreed well to the experimental measurements. The loss through the optimised construction method was low, recorded around 1dB through the frequency range of interest.

The following work presents the analytical, numerical and experimental investigation of a proof of principle gyro-BWO experiment. The design, simulation and optimisation of a thermionic cusp electron gun that can generate a 1.5A, 40kV axis-encircling electron beam are discussed. Simulations showed a high quality electron beam with ~8% velocity spread and ~10% alpha spread. Experiments were conducted using this electron gun and the accelerating voltage pulse, diode current, transported beam current are presented. The electron beam profile was recorded showing a clear axis-encircling beam image from which the electron beam diameter and alpha values can be measured.

Microwave radiation was measured over a frequency range of ~91-100GHz with a approximate maximum power of ~0.37kW. Operating over the magnetic field range 1.79T to 1.9T and measured over a range of alpha values this result was very impressive and proved the successful operation of the gyro-BWO.

Abbreviation List

BWO	Backward Wave Oscillator
TWT	Travelling Wave Tube
Gyro-BWO	Gyrotron Backward Wave Oscillator
Gyro-TWT	Gyrotron Travelling Wave Tube
Gyro-TWA	Gyrotron Travelling Wave Amplifier
CW	Continuous Wave
ECM	Electron Cyclotron Maser
TE	Transverse Electric
TM	Transverse Magnetic
TEM	Transverse Electric and Magnetic
UHF	Ultra High Frequency
SNA	Scalar Network Analyzer
VNA	Vector Network Analyzer
ESR	Electron Spin Resonance
EPR	Electron Paramagnetic Resonance
CC-TWT	Coupled-Cavity Travelling Wave Tube
CFA	Crossed-Field Amplifier
FEL	Free Electron Laser
PPM	Periodic Permanent Magnets
PFL	Pulse Forming Line
DUT	Device Under Test
EIK	Extended Interaction Region

Nomenclature

A	Vector potential.
A	Cross-sectional area of a conductor.
A_c	Area of cathode.
A_{CF}	Area correction factor.
A_e	Area of emitter.
A_{k_z}	Constant multiplier that differs depending on electromagnetic mode.
A_θ	Magnetic vector potential in the θ direction.
a_+	Amplitude of the co-rotating mode A inside the helical waveguide.
a_-	Amplitude of the counter-rotating mode A inside the helical waveguide.
a_w, a_n	Radius of waveguide w and n respectively.
B	Magnetic field flux density.
b_+	Amplitude of the co-rotating mode B inside the helical waveguide.
B_0	Cavity magnetic field.
B_1	The magnetic field of the electromagnetic wave.
B_c	Magnetic field at cathode side of the electron gun.
B_x, B_y, B_z	Magnetic field flux density in the x, y and z direction respectively.
B_{z_0}	Cavity magnetic field.
B_θ	Magnetic field flux density in the θ direction.
c	Speed of EM wave in free-space, $c = 3 \times 10^8 \text{ ms}^{-1}$.
C	Pierce parameter.
C_d	Diode capacitance.

D	Electric displacement field.
D_{ant}	Diameter of antenna.
d_{ac}	Distance between anode and cathode.
E	Electric field.
E_c	Electric field in a conductor.
$E_{k_{max}}$	Kinetic energy of electrons ejected by absorption of photon.
E_x, E_y, E_z	Electric field component in the x, y and z direction respectively.
E_0	Amplitude of the electromagnetic wave.
E_{0x}, E_{0y}, E_{0z}	The amplitude of the electromagnetic wave in the x, y and z direction respectively.
E_t	Transverse electric field.
E_{0t}	Initial transverse electric field.
E_T	Electric field at the thermionic cathode surface.
E_r	Radial electric field.
e	Charge on the electron, e = 1.602 x 10^{-19} C.
e_x, e_y	The x and y direction unit vector respectively.
f	Frequency.
F	Any function that satisfies $\nabla \cdot \mathbf{D} = 0$.
F	Force.
F_r	Radial force.
G	Transverse spatial function.
G	Antenna gain.
H	Magnetic field.
H_t	Transverse magnetic field.

H_{0t}	Initial transverse magnetic field.
H_z	Magnetic field in z direction.
$\bar{h}$	Axial index of Bragg periodicity.
h_A	Axial wavenumber of mode A.
h_B	Axial wavenumber of mode B.
H	Hamiltonian.
H_s	Coupling coefficient.
I	Current.
I_d	Displacement current.
I_o	Incident energy of light.
j	Volume current density.
J	Current density.
J_e	Emission current density.
J_m	Bessel function of order m.
J_s	Bessel function of order s.
k	Wavenumber.
k_c	Cut-off wavenumber.
$\hat{k}$	Unit vector.
k_n	n[th] nonzero root of $J_1(x) = 0$.
k_0	Cut-off wavenumber for the A mode.
k_{0_B}	Cut-off wavenumber for the B mode.
k_{z_1}	Axial wavenumber at lowest measurement frequency.
k_{z_2}	Axial wavenumber at highest measurement frequency.
k_t	Transverse wavenumber.

k_x, k_y, k_z	Wavenumber in the x, y and z direction respectively.
l	Amplitude of the corrugation in a helically corrugated waveguide.
l_{cab}	Length of cable.
L	Length.
L	Lagrangian.
n_0	Electron beam density.
n	Mode number in the x direction.
m	Mode number in the y direction.
m	Particle mass.
m_e	Mass of an electron.
m_A	Azimuthal wavenumber of mode A.
m_B	Aximuthal wavenumber of mode B.
$\overline{m}$	Azimuthal index of the helical waveguide.
N	Turn density.
P	Power.
P	Perviance.
$P_{canonical}$	Canonical angular momentum.
P_i	Transmitting antenna power
P_r	Receiving antenna power
P_r, P_z, P_θ	Canonical moment in the r, z and θ directions respectively.
q	Charge of a particle.
r	Radius.
r_a	Anode aperture radius.
r_0	Mean radius of corrugation in a helically corrugated waveguide.
r_{0L}	Initial Larmor radius.

r_L	Larmor radius.
r_{inj}	Injected electron radius.
r_{cath}	Average radius of the cathode.
r_W	Waveguide radius.
r_c	Average radius of cathode.
r_g	Guiding centre of electrons.
r_{cy}	Cyclotron radius.
R	Resistance.
R_{ant}	Separation distance between transmitter and receiver antenna.
R_m	A function that satisfies the Bessel equation.
R_{SWS}	Radius of the helical slow-wave structure.
R_1, R_2	Resistance.
R_{e1}, R_{e2}	Inner and outer radii of the emitting strip respectively.
s	Harmonic number.
t	Time.
T	Temperature.
T	Kinetic energy.
T_c	Temperature of cathode surface.
u	Heaviside unit step function.
v_p	Phase velocity.
v_g	Group velocity.
$v_\parallel$	Axial velocity of electrons.
$v_\perp$	Perpendicular velocity of electrons.
$v_{0\perp}$	Initial perpendicular velocity of electrons.

v_c	Charging voltage.
v_t	Transverse velocity.
v_x, v_y, v_z	Velocity in the x, y and z direction respectively.
V	Voltage.
V	Scalar potential.
V_{out}	Output voltage from a cable Blumlein or PFL.
V	Potential Energy.
V_{ac}	Accelerating voltage.
V_o	Electron velocity.
v_c	Speed of an electromagnetic wave through a cable.
$v_{z,av}$	Average axial velocity.
v_{crit}	Minimum velocity of particle that passes the cusped magnetic field.
v_{z1}	Velocity upstream of the cusp transition.
v_{z2}	Velocity downstream of the cusp transition.
v_{zth}	Threshold velocity for electrons passing a cusped magnetic field.
x	x coordinate in a Cartesian coordinate system.
y	y coordinate in a Cartesian coordinate system.
z	z coordinate in a Cartesian coordinate system.
Z_L	Load impedance.
Z_0, Z_1, Z_2	Impedance of a cable.
z_{opt}	Optical path length.

Greek:

α	Attenuation constant.

α	Velocity ratio, alpha.
α_c	Absorption coefficient.
β	Relativistic velocity factor.
$\beta_{\perp_0}$	Relative transverse velocity.
β_{z_0}	Relative longitudinal velocity.
γ, γ_0	Lorentz relativistic factor.
$\gamma_{0\perp}$	Initial transverse Lorentz relativistic factor.
Δ_g	Geometrical mismatch.
Δ_H	Relative frequency mismatch.
δ	Frequency mismatch.
δ_s	Skin depth.
$\delta(z)$	Dirac delta function.
ε	Permittivity of a medium.
ε_0	Permittivity of a free space, $\varepsilon_0 = 8.854 \times 10^{-12}$ Fm^{-1}.
ε_r	Relative permittivity of a medium.
$\tilde{\varepsilon}$	Corrugation in permittivity of a medium.
ξ_{mn}	The nth zero of the mth Bessel function.
ξ'_{mn}	The nth zero of the differential of the mth Bessel function.
ζ'_A, ζ'_B	The nth zero of the differential of the mth Bessel function corresponding to the A and B waveguide mode respectively.
ζ_{scale}	Scaling factor.
η	Electron charge-to-mass ratio.
θ_2, θ_1	Phase with and without the device under test respectively.
λ	Wavelength.

λ_c	Cut-off wavelength.
λ_g	Guide waveguide.
λ_{g1}, λ_{g2}	Wavelength in waveguide of waves 1 and 2 respectively.
λ_0	Free space wavelength.
μ	Permeability of a medium.
μ_r	Relative permeability of a medium.
μ_0	Permeability of free space, $\mu_0 = 4\pi \times 10^{-7}$ Hm^{-1}.
ν	Frequency of a photon.
ρ	Charge density.
ρ	Electrical resistivity of a conductor.
ρ_P	Power density.
σ	Coupling coefficient.
σ_c	Conductivity of the conductor.
σ_m	Conductivity of the medium.
τ	Time of voltage pulse.
Φ	Magnetic flux.
ϕ	Polar coordinate, angle.
ϕ_w	Material work function.
ψ	Effective potential.
ψ_{min}	Minimum electron energy to pass through the cusped magnetic field.
ψ	Phase shift.
ψ_w, ψ_n, ψ_e	Phase shift of wave E_1 and E_2 through the ellipse respectively.
Ω	Cyclotron frequency.
Ω_0	Non-relativistic cyclotron frequency.

ω	Angular frequency.
ω_c	Cut-off angular frequency.
ω_r	Real solution of the angular frequency.
ω_i	Imaginary solution of the angular frequency.
ω_g	Cyclotron frequency.
ω_{ca}	Cyclotron frequency in the cathode region.
ω_o	Cyclotron frequency in the cavity region.

List of Figures

List of Tables

Chapter 1.

Vacuum Electronic Devices

1.1 Introduction

For more than a century microwave radiation has been the focus of much research, first through the low power proof-of-concept experiments of Hertz,[1,2,3,4,5] to the modern day when microwaves are prevalent in many areas of life. In the mid-1900's, the research focus was on creating low frequency microwave sources to be used in many important applications such as radar and food preparation; however recent studies have focused on pushing the limits of microwaves to higher frequencies at higher powers, due to the many emerging applications in the medical and biological areas, as well as high resolution radars and communications. Microwaves are defined as radiation with frequency between 1GHz and 300GHz. This wide range of frequencies is sectioned into bands with each denoted by a letter as defined by the IEEE and given in Table 1.1. In the last few decades the frequencies and powers being obtained has greatly increased, due to progress in "relativistic high frequency electronics" and the invention of the gyrotron class of devices. Reaching W-band frequencies through these methods is critical, since the older, conventional, devices such as the travelling wave tube (TWT) operated at W-band in micro-fabricated form[6,7,8] at very low power, typically less than watts, which limits the application utility.

Microwave band	Frequency range (GHz)	Wavelength (cm)
X	8 – 12	3.75 – 2.50
Ku	12 – 18	2.50 – 1.67
K	18 – 27	1.67 – 1.11
Ka	27 – 40	1.11 – 0.75
V	40 – 75	0.75 – 0.40
W	75 – 110	0.40 – 0.27
mm	110 – 300	0.27 – 0.10

Table 1.1. Microwave frequency bands based on the IEEE standard 521-2002.

Microwaves can be obtained through many different types of devices; however one class stands out above the rest - the vacuum tubes. Previous studies[9] have shown that vacuum tubes can produce very high powers at higher frequencies, within the microwave region. As the name suggests, such devices generate microwaves in an

evacuated environment through the extraction of energy from an electron beam. The vacuum is required to allow the beam to propagate without collisions with ions, atoms or molecules. Another type of source that is important for many different applications, even though their output powers are not very high, are solid-state sources. These are used for local oscillator purposes, seed signals for amplifiers and cases where high reliability at low powers are important. Solid-state sources demonstrate properties unobtainable through any other means, such as high stability of the signal and low noise. The method of operation differs between the vacuum electronic devices and the solid-state sources. The former requires a vacuum to extract energy from a bunched electron beam while the later operates inside a solid material bunching the electron stream with a bias voltage source.

The history of microwaves spans over one hundred years, dating back to the mid 19th century with the pioneering research of: Faraday, Maxwell, Rayleigh and Hertz. These were the forefathers of microwaves and much of their work is taught to physics students today. The main achievements of each can be summarised as follows: Michael Faraday discovered electromagnetic induction in 1831[1]; James Clerk Maxwell theorised the famous "Maxwell equations" in 1864[1]; Lord Rayleigh theorised sound propagation in 1877[10]; and Hertz ingenious experiments proved electromagnetic-wave propagation. Publishing 14 papers[11] on the subject through 1886-1889 Hertz was the most instrumental person in generating electromagnetic radiation. Initially working at only 50MHz, ~6m wavelength and 430MHz, ~70cm wavelength, Hertz was able to confirm Maxwell equations.

1.1.1 History of vacuum tubes

The first vacuum tubes originated with the magnetron in 1921, klystron in 1930 and the travelling wave tube in 1942. There are sources that existed before the magnetron however these came in the form of spark gap generators[11,12] and triodes[13] (a part of the gridded tube family that includes the tetrode). In a historical perspective the invention of the magnetron was a great milestone and the first commercially viable vacuum tube. The TWT has different varieties, with the most popular of these being the coupled-cavity TWT (CC-TWT) and the helix TWT. The names refer to the type

of slow-wave structure used, explained in-depth in Section 1.2. Originally the klystron and TWT were used for important radar operation during World War II. As the war progressed it became necessary to increase the frequency range from X-band to K-band. Another vacuum tube in the same family as the magnetron, is the crossed-field amplifier (CFA). This device is capable of producing higher powers at higher efficiencies than the klystron and TWT; however, this is at the sacrifice of bandwidth and gain. This source was invented in 1950 by Warnecke, Kleen, Lerbs, Doehler and Huber[14]. Until this point the emphasis was on producing microwaves with a relatively low frequency.

The first millimetre wave source was made by Beringer[15] using a crystal harmonic generator driven by a centimetre-wave klystron to produce a second-harmonic signal at 5mm wavelength. In 1954 the magnetron was pushed up to 115GHz at 3.3kW by Columbia University Radiation Laboratory.[16] The higher frequency meant that the magnetron suffered from poor lifetime and duty cycle. A klystron generated up to 120GHz and 40mW CW in 1958.[17] After this time millimetre and sub-millimetre wave sources were reported by many groups with articles regularly appearing in journals.

A free electron laser (FEL), also called Ubitron, is a microwave source that uses an electron beam travelling through a magnetic arrangement, known as an undulator or "wiggler", comprising of alternating poles to make the beam travel in a sinusoidal path. This causes the beam to rapidly accelerate and decelerate emitting the light through Bremsstrahlung radiation. There are instabilities in this electron beam which cause the beam to bunch so that the light emitted is coherent and therefore more useful for applications. The history of the FEL started in the 1960's with the thermionic experiments of Philips.[18] These were later expanded upon by Friedman[19] trying to produce higher peak power levels using more powerful electron beams. Since that time very high powers have been achieved even at millimetre wavelengths. The first breakthrough experiment was at NRL[20] producing 35MW at 70GHz although relatively low efficiency 2.5%.

A new breed of devices came about which vastly increased the achievable powers at millimetre wave frequencies. The gyrotron class of devices, based on the electron cyclotron maser (ECM) instability, was invented in 1967 by A.V. Gaponov-Grekhov, A.L. Goldenberg, V.A. Flyagin, B.K. Yulpatov[21]. Gyro-devices have many different varieties now[22,23]. The behaviour of the ECM instability was explained by Schneider[24] and Gaponov[25] using classical and quantum mechanical theory. The detailed historical development has been previously documented[26]. The linear and nonlinear theory of the electron cyclotron maser instability was presented by Sprangle, Granatstein and Drobot[27,28].

As time has increased the output power of microwave sources has rapidly increased as shown in Figure 1.1. The large difference in powers between vacuum tubes and solid-state sources is clear to see. This graph uses a scaled factor of the average power, P_{ave}, and microwave frequency, f, squared in order to give a simpler understanding of the advances each device has made over time. In each device the achievable power varies approximately as the inverse square of the frequency.
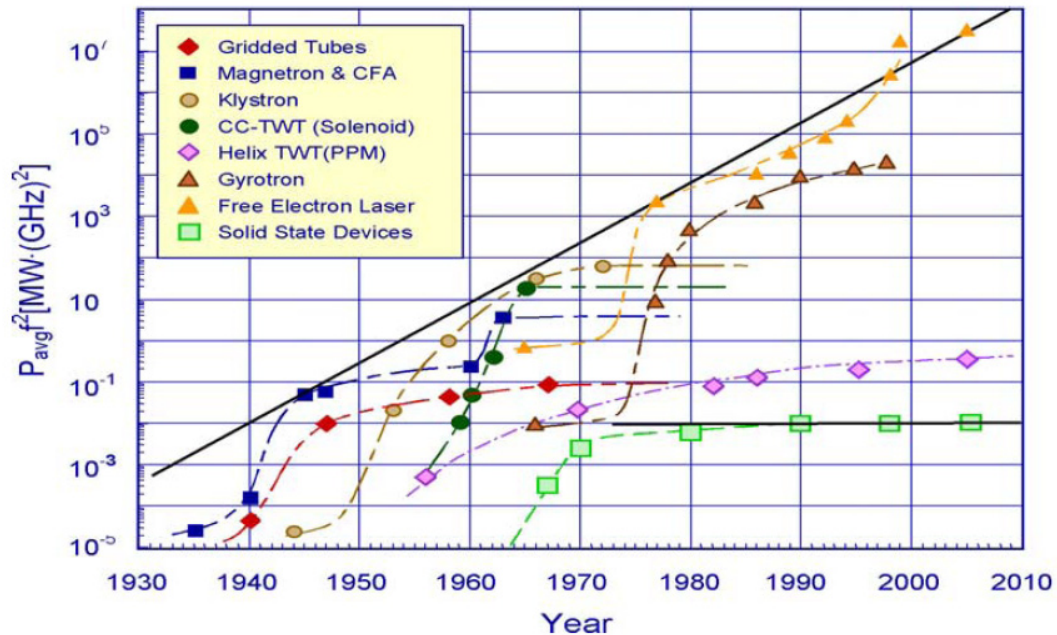
Figure 1.1. Variation in performance of vacuum tubes and solid-state microwave sources since the 1930's. Graph taken from the Department of Defence compiled in 2008[29].

Omitted from the above table is one of the highest power, yet unstable microwave sources, the vircator[30,31]. Known as the virtual cathode oscillator, the vircator is part of the space-charge device family unlike the other sources. This source is able to produce ultra-high powers into the gigawatt-level[32]. Work on space-charge devices did not start experimentally until the 1970's when electron beams of current 10^4-10^6A and energy 0.1-10MeV were readily available. The first applications proposed for these devices were in ultra-short-pulse generation with a virtual cathode discharge[33] and collective ion acceleration in natural gas[34]. However, it was not until 1977 that Mahaffey et al.[35] were able to produce microwaves through the oscillation of a virtual cathode by using a reflect triode.

1.1.2 Classification of microwave sources

Despite many types of microwave sources and different names associated with them any microwave tube can be classified by the following aspects:

1. The growth characteristic - oscillator/amplifier/self amplified spontaneous emission (SASE).
2. Mode of operation – pulsed/continuous.
3. The direction of the electron beam relative to magnetic field – O-type/P-type/ M-type.
4. Wave speed relative to the speed of light in the medium – fast-wave/slow-wave.
5. Direction of the wave in the tube – forward/backward wave.

These areas will be expanded briefly and it is through these five definitions that each microwave source can be described.

The first definition listed is one of the most fundamental: does the tube generate microwaves itself, i.e. an oscillator, or amplify a source of microwaves - an amplifier. The former is able to produce microwaves from noise inherent in every system while the latter is able to couple an electron beam to the oscillation frequency of the source of microwaves in order to amplify the power of the wave. Oscillators include some of the previously mentioned devices such as the magnetron, gyrotron, gyro-BWO and vircator while amplifiers encompass the TWT, crossed-field

amplifiers, gyroklystron, gyro-TWT etc. Self amplified spontaneous emission[36,37] refers to the emission model used in some free-electron lasers.

The output power of the tube can either be continuous wave (CW), producing high average powers, or pulsed power, which produces extremely high peak, but low average, powers. If a tube is able to produce long pulses of over microseconds then this can be classified as CW. Most devices discussed so far are able to operate at CW if they are able to be cooled effectively and if the input power source (for an amplifier) can be operated at CW.

The effect of the magnetic field direction to the direction of the electron beam can produce different types of microwave tubes. These are normally split into three different categories: O-type (linear-beam); M-type (crossed-field); and P-type (fast-wave). The first of these, the O-type, couples an electron beam that travels confined to an axial magnetic field. The most well known of this type of device are the klystron, travelling-wave tube and backward wave oscillator. When the electrons move under the force of $E \times B$ (so called $E \times B$ drift) due to the existence of crossed electric and magnetic fields they are referred to as M-type. The most well known, and historically important, of the M-type devices is the magnetron. Finally, P-type sources are more commonly known as the fast-wave sources. Synchronism of the beam and wave interaction in conventional tubes is achieved by slowing the phase velocity of the electromagnetic wave. However in P-type devices there is no requirement to slow the electromagnetic wave.

The difference between a slow-wave and a fast-wave source is a slow-wave source reduces the speed of the electromagnetic wave inside the interaction region through some means, generally through a slow-wave structure. This allows the electron beam and the wave to travel at the same speed to allow coupling. Fast-wave sources use smooth-bore waveguides as an interaction circuit to convert electron beam energy to electromagnetic wave energy.

With device classification one can use the electron beam movement to categorise the

microwave device i.e. M-type, O-type or P-type, or one can use the interaction with the electromagnetic wave i.e. slow-wave or fast-wave. Whatever choice is used there can be overlapping of the categories for some devices for example a FEL can be considered both a fast-wave and an O-type (linear beam) device.
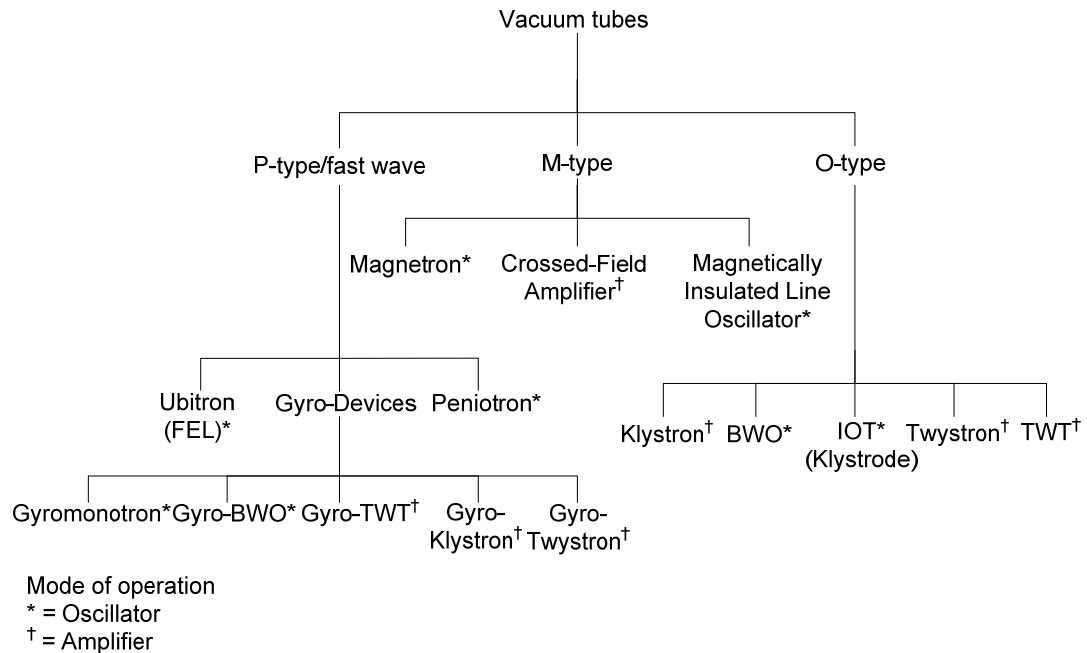
Figure 1.2. Family tree of vacuum electronic tubes. The different classifications of sources are clear to see here with P-type, M-type and O-type devices separated.

1.1.3 Applications

The use of microwave technology spans many different industries and provides an essential service. Since their conception, lower frequency conventional microwave sources have been used in communications, more specifically television/radio broadcasting and more recently mobile phone communication[38]. Other uses for these sources are in airport radars[39] and food processing[40,41,42] and cooking. With these applications the use of low frequency is useful because of the cost and, time-wise, only low frequency devices had been developed when the applications were needed. More recently, THz microwave sources have received a lot of publicity due to their desirable applications in imaging[43,44,45], spectroscopy with potential medical[46,47,48] and biological[49,50,51] uses, security[52,53,54] and Electron Spin Resonance (ESR)[55].

The atmosphere surrounding the earth contains water vapour which absorbs

8

microwaves, with such applications as radars experiencing a great loss in the signal. However, there are certain frequencies where the water absorption is lowest and these are known as "atmospheric windows". In the W-band frequency range, such a window exists at ~94GHz. The loss at this frequency is, for humid conditions, 1dB/km an acceptable loss when working at high powers and only that high at relatively low distances from the earths' surface at 3km or less. Such microwave windows open up a lot of applications for W-band sources and is part-reason why the gyro-BWO was designed to centre at this frequency. This window opens up applications such as: millimetre wave cloud radars, atmospheric probes and space debris radar. There are windows for radar communication at ~94GHz and ~35GHz. The advantage of W-band radar lies with improved resolution, which comes from the small wavelength of the radiation, improving the resolution of the objects, making this ideal for airport surface movement detection. Both the Italian Space Agency (ASI) and the National Aeronautics and Space Administration (NASA) in America have been investigating W-Band radars. The ASI have launched two major projects called DAVID[56,57] (DAta and Video Interactive Distribution) and WAVE[58,59] (W-band Analysis and VErification". Both these projects investigate the feasibility of using W-band for telecommunications. NASA launched a mission called CloudSat[60,61] in 2006 which is the first space mission to carry a space-ready high-power W-band amplifier operating at 94GHz. The satellite launched will be one of six Earth Observing Satellites used for the "A-Train"[61] constellation used for continuous observation of weather, climate and air quality.

Terrestrial radars applications are employed at airports. A mini-radar, called such due to the small dimensions of W-band technology, called SMART[62] is in operation in airport surveillance applications. These are installed at Frankfurt Airport in 2001 and at the Venezia "Marco Polo" airport. These two are used for the control of air traffic on the airport surface (surface movement radar). These operate at 95GHz and have shown improved target detection compared to other similar radars.

Electron Spin Resonance[63,64] (ESR), sometimes called Electron Paramagnetic Resonance[65] (EPR), is an area where the use of W-band microwave sources has

enabled many breakthroughs. The concept of ESR is that in a sample with one or more unpaired electrons, such as free radicals having unpaired electrons, a transition between spin state can be induced by the application of a magnetic field and electromagnetic energy in the form of microwaves. This allows one to measure the absorption spectra and from this classify the sample. The use of W-band allows superior sensitivity and resolution in the measurement of samples. Many different journal papers now have been published[66,67,68] using W-band microwaves to investigate many different samples.

1.2 Slow-wave devices

As mentioned in Section 1.1.2 microwave tubes can be either a slow-wave or fast-wave device. One is through Cherenkov radiation, which occurs when electrons travel through a medium with refractive index, $n > 1$, in which case the electrons velocity, v, is greater than the phase velocity, v_p, of electromagnetic waves, given by $v_p = c / n$ where c is the speed of an electromagnetic wave in a vacuum. In order to reduce the phase velocity of the electromagnetic waves a slow-wave structure can be used. The slow-wave structure (SWS) makes it possible to support electromagnetic waves which have a phase velocity less than the speed of light. These come in many different forms and the first of these was a helix, as shown in Figure 1.3, invented by Kompfner[69,70].
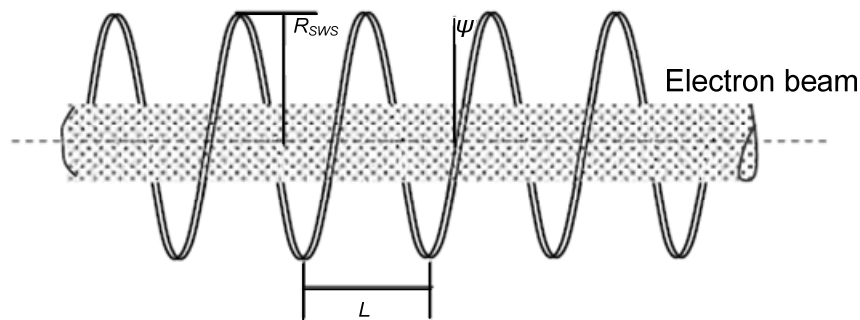
Figure 1.3. Helical slow-wave structure used in devices based upon Cherenkov/Smith-Purcell radiation. Here R_{SWS} is the radius of the helical tape, L is the period length and ψ is the pitch angle of the helix.

The slow-wave structure is used to make the microwave slower than the speed of

light and thus slower than the electron beam. The phase velocity can be given as equation (1.1) showing the effect of the slow-wave structure to reduce the phase velocity of this wave.

$$\mathrm{v}_p = c \sin \psi \qquad \textbf{(1.1)}$$

Radiation emission through a periodic slow-wave structure is known as Smith-Purcell radiation. Microwave sources that use the Cherenkov/Smith-Purcell radiation are for instance the travelling wave tube and backward wave oscillator. The M-type interaction also known as the crossed-field devices, such as magnetron described in the subsequent section. The reason for the name is because electrons drift across a magnetic field in crossed electric and magnetic fields which is called an $\boldsymbol{E} \times \boldsymbol{B}$ drift.

1.2.1 The magnetron

The magnetron was invented in 1921 by A.W. Hall[71]. The magnetron is synonymous with microwaves since there are over 500 million magnetrons in the world today. The co-axial geometry is detailed schematically in Figure 1.4, taken from Ref. 72, which shows the inner conductor, acting as the cathode, and the outer conductor, acting as the anode. On the outer walls is a periodic R.F. (radio frequency) structure that creates an azimuthally alternating electric field. Electrons travel in an azimuthal path through the magnetron due to the effect of an applied axial magnetic field and radial dc electric field. Electron bunching and velocity modulation is obtained through the effect of the magnetron cavities and as a result, microwaves are produced. Introducing cavity resonators to the anode was an important improvement in magnetrons. Through this adjustment to the magnetron design J.T. Randall and A.H. Boot[73] were able to produce 10kW pulses at 3GHz in 1939-40 which was then used for the radars during World War II. This was also independently invented by Soviet[74] scientists in 1940. Other alternative magnetron structures such as the rod configuration and rising-sun were also designed to operate using different cavity modes such as the π-mode.

1.2.2 The klystron

The klystron was one of the earliest microwave sources to be developed after the
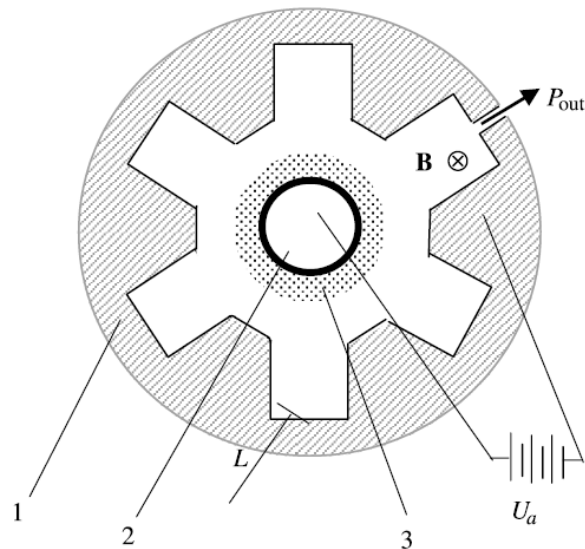
Figure 1.4. Schematic of the six-resonator magnetron highlighting: 1. Anode with resonators; 2. Cathode; 3. Electron beam.

triode in 1906 and the magnetron in 1921. The development came from a requirement to produce high frequency microwaves. The invention is attributed to Russell and Sigurd Varian at Stanford in 1939[75]. The klystron is a microwave amplifier which uses two cavities separated by a drift section to amplify microwaves.

Used in both rectangular and cylindrical waveguides, amplification of a seed signal occurs through interaction with a bunched electron beam. The geometry of a klystron can be seen in Figure 1.5 taken from Ref. 76. In the first cavity a R.F. signal is injected causing an electric field to exist across the opening of the cavity. The electric field cause some electrons to decelerate and some accelerate, producing a "velocity modulation" on the electron beam. Therefore electron bunches are formed with the same frequency as the input R.F. signal. These electrons travel along the tube with a large negative charge. This charge draws a positive charge along the wall of the tube to satisfy the boundary conditions of Maxwell's equations, causing the positive charge to travel along with the electron beam. When this beam travels past the final cavity the positive charge excites the cavity, producing electric and magnetic fields inside it, which have the same frequency as the electron beam. The electric field causes the electrons to decelerate and hence this electromagnetic energy can be extracted through a co-axial transmission line or waveguide as an amplified

microwave signal.

The efficiency of the system can be increased through the addition of intermediate cavities that are located between the input and output cavity. These are used to further increase the density of bunching of the electrons and to trap more electrons to each bunch. The extra cavities are unloaded with a high quality factor, known as Q-factor[77] and describes the rate at which a cavity loses energy. The klystron is the most efficient of the linear beam devices able to operate at 65% efficiency[78] and can produce extremely high gains of up to 60dB. The power of klystrons is only limited by electric breakdown with 75MW being reported at X-band and 150MW at S-band. With CW operation, the limitation is with cooling of the klystron body.
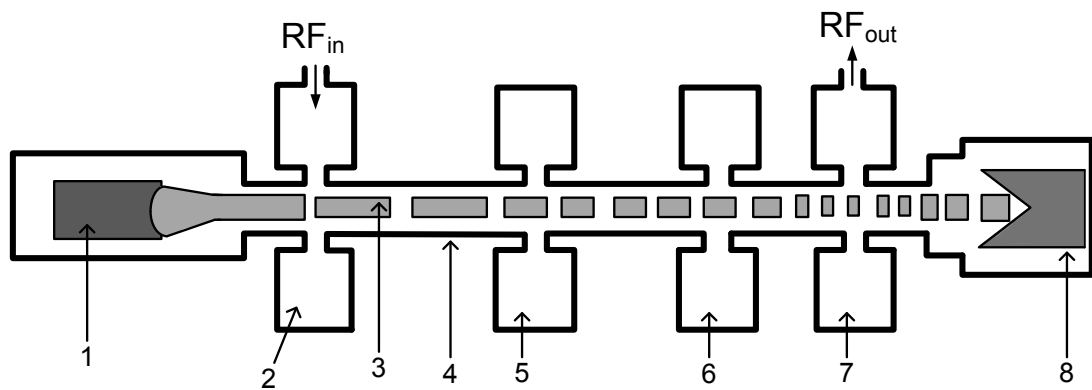
Figure 1.5. Schematic of a four-cavity klystron highlighting: 1. Electron gun; 2. Input cavity; 3. Bunched electron beam; 4. Drift tube; 5. Intermediate cavity; 6. Penultimate cavity; 7. Output cavity; 8. Collector.

1.2.3 The inductive output tube

An inductive output tube (IOT), also known as a klystrode, is a one-cavity oscillator with a similar method of operation to the klystron. The bunching mechanism occurs at the cathode side of the tube through a control grid only 0.1mm thick, similar to a triode. This mesh has an R.F. signal applied to it which is used to allow electrons to pass when the charge is positive and when negative the electrons are repelled where they "wait" until the charge switches positive again. When "waiting" the electrons are forced to bunch together as they are being emitted from the cathode yet cannot pass the grid until the electric field is in the positive regime. Thus only bunches of

electrons pass the grid with a set frequency controlled by the R.F. signal applied to the grid. This bunched beam then travels, confined by a magnetic field, through a small drift region, and then through a resonant cavity. The IOT appears to be a simpler concept than the klystron due to the one-cavity configuration; however the bunching of electrons at the cavity is very complex to achieve. The IOT was invented in 1939 by A. V. Haeff[79] around the same time as the klystron and was the first transmitter of the television signal during the 1939 New York World's Fair.

1.2.4 The travelling wave tube

A relativistic Čerenkov amplifier known as the travelling wave tube is an early microwave source and one of the most important due to wide bandwidth output at high gain. In 1942, Rudolf Kompfner[80] proposed that by the continuous deceleration of an electron beam, travelling synchronously with a guided travelling electromagnetic wave, the wave could be amplified. This synchronism occurs through the slowing down of the electromagnetic wave through a slow-wave structure. The SWS is used to increase the path-length the electromagnetic wave has to travel while the electron beam travels straight along the tube, confined longitudinally by an external magnetic field. There are many different types of slow-wave structures that have been used to meet this requirement, including helix transmission lines, coupled-cavity, folded waveguide and ladder circuits. The wave is launched into the input end of the SWS causing an electric field to radiate from the SWS. When electrons pass through the SWS, the fringing electric field of this structure induces velocity modulation on the electron beam, either decelerating or accelerating the electrons depending on what phase of electric field they travel through. This results in electron bunching an effect similar to the klystrons mode of operation. The electron beams current induces a modified wave on the SWS which has the same frequency as the original wave. As this wave travels along the tube the electron bunches are in the decelerating phase of the wave constantly lose energy and result in the induced wave to grow exponentially.

A conventional TWT will produce microwaves in the frequency range 1GHz and 80GHz and at powers of 10kW-100W respectively. The use of the conventional

TWT at W-band is highly limited by the SWS and power handling of this. Although few W-band TWT's, with use in communications, exist the power is relatively low. At the Beijing Vacuum Electronics Research Institute a 10W folded waveguide TWT has been designed[81]. Another source reports initial testing of a W-band TWT with a goal of 250W peak power with 125W average power at ~94GHz. L.M. Earley et al.[82] created a vane loaded R.F. structure for a 94GHz TWT driven with a mW solid-state source. The result from their testing was a gain of 20dB and power out in the lower mW's. For communications at low frequencies TWT's provide a reliable and cost effective source and are in production by many companies. For high frequencies in the W-band and above, the power out of the TWT is very low and the similar gyro-TWT microwave device far surpasses their performance.

1.2.5 The backward wave oscillator

A backward wave oscillator (BWO) can generate extremely high power microwaves due to insensitivity to velocity spread and an internal feedback mechanism which builds up the microwaves over time. Invented in 1953 by Kumpfner and Williams[83] the BWO was the first microwave source, in the 1970's, to be driven by a relativistic electron beam creating efficient coherent microwaves. Microwaves are generated through an interaction between the slow-space-charge wave and the negative slope of the dispersion curve thus the microwaves created has a negative phase velocity. The theory of operation is the same principle as a TWT except it uses a Bragg structure with rippled waveguides. BWO's have been used to create millimetre waves, however efficiencies reported have been low. For instance, for wavelengths of 8.8-0.9mm the efficiencies are 6% to 0.1% however powers are high at 50MW-0.5MW[84]. Power levels as high as gigawatts have been reported for BWOs[85].

1.2.6 The twystron

There have been many devices before using a combination of the klystron and TWT to try and improve performance[86,87,88]. However, the most successful widely used one is called the twystron amplifier[89]. The twystron is a hybrid device of the klystron and TWT, which combines the advantages of both to produce a device with wide

bandwidth and high gain. This device uses the input stage of a klystron, the cavities, and the output section of the TWT. This tube has wider bandwidth, higher efficiency and flatter gain than the klystron even at the megawatt power level. In a klystron, a method of increasing bandwidth is to operate with a low Q-factor (quality factor, related to how fast a cavity loses energy), achieved through a loading of the cavities. It is difficult to load the output cavity without increasing loss; however, the driver section can be heavily loaded without effecting power loss. The low bandwidth is a fundamental property of the klystron and is approximately 5%, and in some cases 10%. The bandwidth that a TWT operates at is controlled by the slow-wave structure. At a high output power the gain of the TWT and klystron becomes comparable, however as the frequency reaches the edges of the bandwidth the gain decreases quite sharply, about 6 to 10dB. The efficiency of the TWT is quite good. The efficiency is also improved due to the klystrons superior bunching in the edges of the bandwidth where the TWT falters. Furthermore, the input cavities are tuneable so they can be optimised during operation, thus providing a more versatile microwave tube.

The power levels that the twystron operate at are quite high. At S and C bands the peak power levels range from 1MW to 10MW at an average power ~30kW, in the 1970s[90]. The efficiencies of this hybrid device are also very high at 30% with a peak of ~40% at the mid-band frequency. Efficiencies as high as 50% can be obtained, with the addition of a multistage depressed collector.

1.3 The gyrotron devices

Many different microwave sources employ the electron cyclotron maser (ECM) instabilities to generate/amplify microwaves, with such sources collectively known as gyro-devices. The most well know gyro-device is the gyrotron which was invented in 1964 in Nizhny Novgorod by A.V. Gaponov-Grekhov, A.L. Goldenberg, V.A. Flagin, B.K. Yulpatov[21]. The gyro-devices have many advantages over conventional devices, especially in the millimetre and sub-millimetre wavelength range, as the power output by a gyro-device can be many orders of magnitude greater than an equivalent conventional device. The reason for these advantages are the inherent

fast-wave characteristics as mentioned in Section 1.1.2. In a gyrotron, electrons gyrate in an external longitudinal magnetic field. The gyro-devices amplify or generate microwaves based on the electron cyclotron resonance instability, which is described in Chapter 2. The growth is either through a convective or absolute instability[91] where the wave grows while propagating with the beam (convective) or where the wave grows in time at the same place (absolute).

The reason a gyro-device has a higher power at high frequencies is because conventional devices use a slow-wave structure for the beam-wave interaction and gyro-devices do not require this. The size of the SWS is dependent on frequency so when the wavelength goes down to the millimetre level the SWS becomes exceedingly small, which will cause R.F. breakdown when the power level reaches a certain level. While in gyro-devices, the interactions take place in smooth waveguide, which have much larger size as compared to the SWS when operating at the same frequency. For almost every conventional linear beam device there is a gyro counterpart. The class of gyro-devices includes the gyro-monotron, gyro-travelling wave tube, gyro-backward wave oscillator, gyroklystron, gyrotwystron and many others.

1.3.1 The gyromonotron

A gyromonotron is more commonly known as a single cavity gyrotron. The gyrotron has a simple configuration of a smooth-bore waveguide as the interaction and an uptappered waveguide after this radiating out a microwave window. Self-oscillation inside the cavity stimulated by an electron beam generates microwaves with a feedback loop, occurring from reflections at the end of the cavity, acting to increase and maintain the oscillation. The electron beam is usually produced through a Magnetron Injection Gun which generates an annular beam. The gyromonotron operates with a single non-tuneable frequency. The operating frequency range is from 10GHz up to 1THz[92,93,94]. Powers produced by gyromonotrons are very high producing MW's of powers even at sub-millimetre wavelengths with efficiencies of up to 70%[95].

1.3.2 The gyrotron backward wave oscillator

The gyrotron backward wave oscillator (gyro-BWO) is an efficient source of high-power frequency-tuneable coherent radiation. Microwaves are generated in the smooth interaction region through an absolute instability where the wave grows in time at the same position. The generated waves have a negative group velocity so they travel in the opposite direction to the electron beam propagation which is where the name "backward wave" oscillator comes from. The frequency of microwave radiation is tuneable through varying magnetic field and applied voltage (see Chapter 3 and Chapter 5). The generated microwave can be coupled out either at the downstream of the tube by using a reflection at the upstream region radiating through a microwave window or by using a side-coupler at the upstream region.

The early studies into gyro-BWO's were conducted in the 1960's in Russia since this time it has been extensively studied.[96,97,98,99]

1.3.3 The gyrotron travelling wave tube

The gyrotron travelling wave tube (gyro-TWT) is a microwave amplifier capable of large gain with high efficiency. The operation of the gyro-TWT is through a convective instability inside a smooth interaction region. A seed signal is injected through an input coupler before the interaction region and the amplified signal is radiated out of a microwave window after an uptapered waveguide. A common concern for gyro-TWT design and operation is stimulating a parasitic gyrotron and/or gyro-BWO interaction. This device can operate over a large frequency bandwidth because no resonant structure is used.

Recent studies have shown that bandwidth can be increased by using a tapered magnetic field and a tapered interaction circuit[100,101].

1.3.4 The gyroklystron

The gyroklystron is an amplifier based on the gyrotron and klystron principles. They were originally invented for radar applications, for example two phase-matched

Ka-band gyroklystrons powering a megawatt radar that tracks objects orbiting the earth[102]. More recently applications have evolved in accelerators and radars. To show the relative difference in powers between gyroklystrons and klystrons between 1998 and 1999 operating at X-band a gyroklystron was developed that had 75MW peak power[103] while at the same time a comparative klystron was developed that achieved 50MW peak power[104]. Whilest the gyroklystron works more efficiently at high frequencies and is also able to operate at high powers than a klystron, when operational at 200kW in the Ka-band, the noise output is still comparatively the same as that of a klystron[105]. The gyroklystron employs both the bunching mechanism of the gyro-devices, (see Chapter 2, Section 2.4.3), and the klystron concept of using multi-cavities to increase the efficiency of bunching the electron beam, thus power, and then extracting the microwave output through an output cavity. This operates as an amplifier and high powers have been reported. The input R.F. signal at the input cavities azimuthally bunches the annular electron beam. The bunching occurs through ballistic bunching then velocity modulation, like the klystron, occurring through interaction with the R.F. fields in the cavity. The extraction of the R.F. is at the end of this tube. The gyrokylstron can work with many cavities which increase its gain but to explain the operation of the gyroklystron it is simpler to explain it with two cavities only. The first cavity bunches the electrons in the azimuthal direction through energy modulation directed by the input R.F. signal. In the second cavity these bunches excite R.F. radiation which is extracted from it. The advantage of a gyroklystron over a conventional klystron is that the cavity dimensions can be scaled easier than a klystron and so a gyroklystron is able to operate at high frequencies with more ease and a higher power.
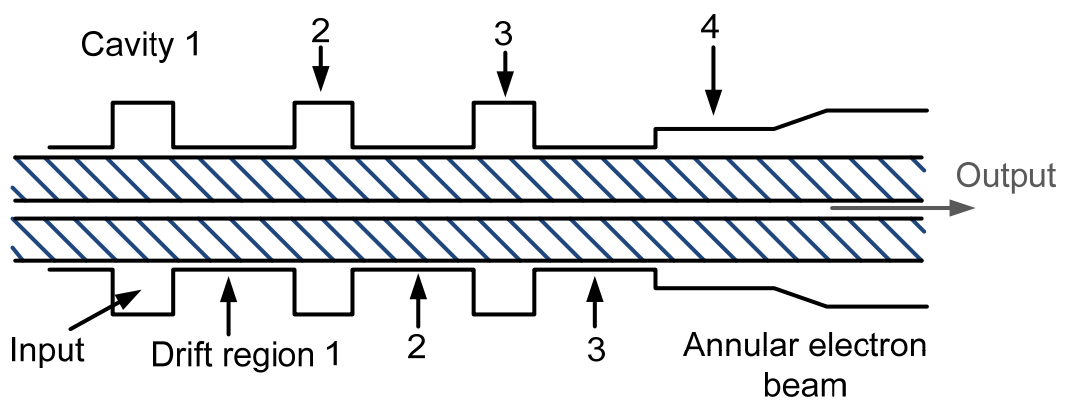
Figure 1.6: Schematic of a four-cavity gyroklystron.

In a gyroklystron, the axial and transverse dimensions of the cavity can be much larger than a wavelength, since the electrons are travelling in a cylindrical path, and are not a linear beam. There are some similarities between the gyroklystron and the gyro-TWT i.e. both employ the ECM instability and are amplifiers however the gyroklystron has a smaller bandwidth but larger output power than the gyro-TWT. Gyroklystrons have a much greater power-handling ability than klystrons but efficiency is lower due to the fact that only the transverse electron energy can be converted to RF power.

1.3.5 The gyrotwystron

The merits of the klystron, high efficiency and gain, and TWT, large bandwidth, can be achieved in one device - the twystron - and the same can be said of the gyrotwystron. The difference between the twystron and gyrotwystron lies with their electron trajectories - where the gyrotwystron uses a rotating electron beam, the twystron uses a linear beam - and in the formation of the electron bunches. The gyrotwystron bunches electrons azimuthaly, whereas the twystron bunches them transversely. The geometry of the gyrotwystron is an annular or rotating electron beam travels through an interaction region where RF is input through the input cavity. There is then a drift region and then a slightly tapered output waveguide. This type of setup mitigates breakdown problems (at high powers) associated with gyroklystrons. Through replacing the output cavity with an output waveguide much higher power can be handled. The electrons are bunched in the first cavity and excite modes in the output waveguide.

There is another configuration of gyrotwystron that has recently been investigated – the "inverted gyrotwystron". This consists of the gyro-TWT input section, a waveguide, then a drift region and an output cavity. The advantage for this is the travelling-wave input with drift region would induce higher harmonic content in the electron current density allowing harmonic operation. First suggested by Guo[106] the theory of this device is presented by Nusinovich[107]. This device also is known by another name the phase-coherent harmonic-multiplying inverted gyrotwystron or

phigtron[108,109,110]. The phigtron has the ability to be a high average, high-peak power amplifier at millimetre-wavelengths with good efficiency, high gain with medium bandwidth. In one example, efficiency as high as 35%, outputs ~400kW and saturation gain of 43dB[111] was reported. Another device shows very high gain-bandwidth performance of 1.3% bandwidth, 33dB peak gain and at 31.8GHz[109].

This combines the bunching mechanism of the gyroklystron with the output stage of the gyro-TWT. This results in the merits of both devices, the large gain and efficiency of the gyro-klystron with the bandwidth of the gyro-TWT, being present within one device. The ideal application for this is in radars which require a large bandwidth amplifier with large gain and in accelerators where high-power millimetre wave devices are required. More than one cavity can be used for bunching which increases the efficiency, just as the gyroklystron.

1.4 Overview on W-band sources

There has been renewed interest in the W-band frequency range due to the many applications that exist and more recently there has been a surge in high frequency applications. There are W-band sources being developed in almost all capable devices. This section presents a selection of W-band sources that are of importance, however there are many others available that are not listed but can be found in an extensive annual report by Thumm.[112] The fast-wave devices are given preference here with some additional results from slow-wave device and solid-state sources. The fast-wave devices have been operating at the highest frequencies for a long period of time but recent slow-wave sources have been able to push the frequencies higher due to advances in micromachining.

Many single frequency gyrotrons exist within this frequency range that can produce very high powers and at very high efficiency. One example is at CPI[113] with a 94.9GHz gyrotron using a single stage depressed collector (SDC) has been developed to give 50% efficiency and 0.12MW power at TE_{62} mode impressively operating at CW.

A 10kW average power gyroklystron[114,115] and gyrotwstron[116] have been demonstrated by NRL. The gyroklystron obtained this power due to 11% RF duty factor with a 92kW peak power operating at the TE_{01} mode. The bandwidth was 420MHz and efficiency at 33.5% at 94GHz. In a joint effort between the Institute of Applied Physics and Gycom in Nizhny Novgorod, a W-band gyroklystron which operates at the TE_{02} mode to produce 342kWs of peak output power[117] was demonstrated, a world record at the time it was published. This device was driven by a 75kV 18.3A electron beam. A gyrotwystron that demonstrated a high peak power, 50kW, at 93.9GHz with a 925MHz half width maximum (~1% tuning range) has been built by NRL[118].

Klystrons can provide a good bandwidth at W-band, however the average power is relatively low, but with high peak powers. For example, one such device is a W-band klystron with an extended interaction region (EIK). This is able to produce ~1kW peak power at 95GHz at 10% duty cycle (more than 1kW at a lower duty cycle) corresponding to 100W average power. The bandwidth of this source is relatively good for the klystron devices at 2.2% (2GHz).

A gyro-TWT[119] operating at W-band at 95GHz through a joint collaboration between CPI and Varian is able to produce impressive results with 6kW output power at a modest efficiency of 5% over a bandwidth of 3% which are relatively low results for this class of microwave source. The results can be explained by the use of a beam current which is 60% of the designed value.

W-band oscillators are summed up in two main areas - the powers they can produce and the tuning range. Generally one device will satisfy one of these conditions but not both. This makes the gyro-BWO presented in this thesis unique, the advantages of which can be seen in Figure 1.7 where this gyro-BWO is compared against similar world-wide sources.

1.5 Research pursued in this thesis

This work presents the results of gyro-BWO through theoretical, numerical and
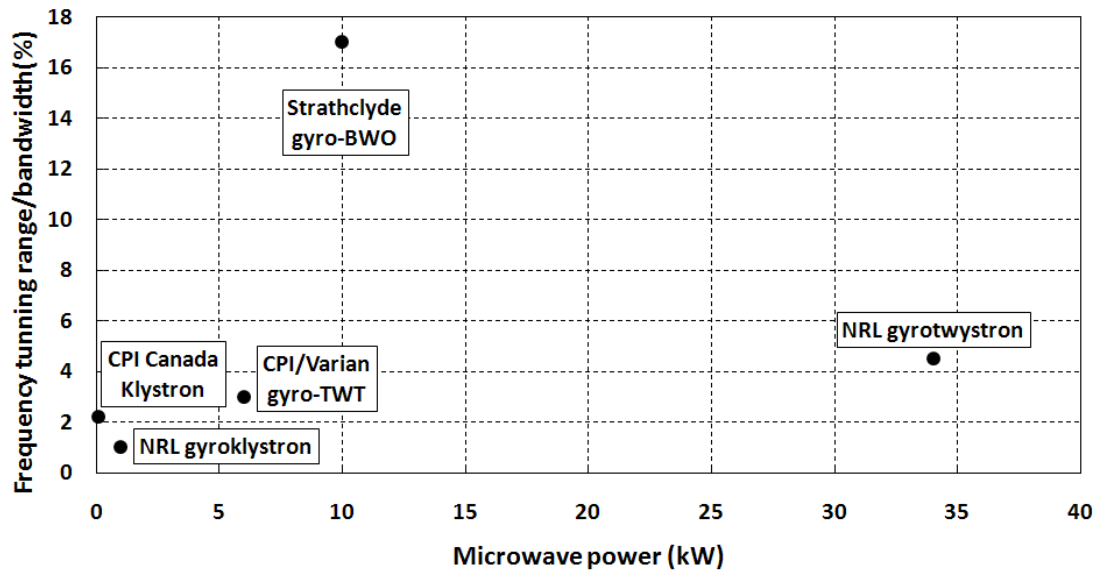
Figure 1.7. Performance of current W-band microwave sources with the gyro-BWO designed, simulated, constructed and operated as presented in this work.

experimental means. This microwave source operates in the W-band frequency range adding further difficulty to the experimental construction due to the small size of all the dimensions and tolerance sensitivity. Many sources have been created in this microwave region however the unique point of this device is a wide frequency tuning range while maintaining high efficiency and high CW power. There are many applications for high-power millimetre wave gyro-devices[120]. Specific applications requiring a device with high-frequency, wide frequency tuning range, high CW power with good efficiency are electron spin resonance[121], material processing[122] and military defence[123]. In defence applications a tuneable source is useful for jamming radar signals as the frequency required is not always known. Furthermore, amplifier sources capable for wide bandwidth at high power require a frequency tuneable ~10kW source[124] for which the gyro-BWO would be ideal.

As shown in Figure 1.7 the current state-of-the-art W-band sources can either provide high powers but at the cost to frequency tuning range/bandwidth or large tuning range/bandwidth at the cost of power.

The aim of this thesis is to provide a device that can satisfy both demands in frequency tuning range and power. To do so required two special aspects to be made:

a waveguide with a helical corrugation of the inner surface and a cusp electron gun.

The interaction region in this gyro-BWO is a corrugated waveguide with a long length with small diameter making the construction of this very demanding. A novel cusp electron gun generating an axis-encircling electron beam has been analysed through numerical simulations using two proven electron beam codes, MAGIC and Opera-3D. The interaction region has a helical corrugation on the inner surface and dispersion characteristics of this obtained from a vector network analyser are compared to numerical and analytical calculation. Two solenoids, one producing very large DC field of 2.1T, have been designed, optimised and fabricated. The microwave device was constructed and within this thesis the experimental results are given for both the electron gun and gyro-BWO.

A summary of each chapter is given here.

Chapter 2:
The theory of waveguides and electromagnetic waves is discussed within this chapter starting with the basic circular waveguide theory. The interaction between a microwave and electron beam is discussed. Instabilities which lead to microwave generation/amplification are explained within this chapter with a focus on the electron cyclotron maser, a topic of great importance to the gyro-device operation.

Chapter 3:
Within this chapter waveguides with a helical corrugation of the inner surface are introduced. Such an interaction region is analysed in many different ways starting with analytical theory from which the design parameters of the corrugation are decided. This naturally leads to the numerical simulation of the helically corrugated waveguide as a double confirmation of the designed geometry. The two methods of finding the various properties of a waveguide (dispersion, electric field pattern etc) are enough verification to construct the waveguide. The complicated geometry and small size meant construction was challenging and the various issues that arose are described in detail. The 4-period proof-of-construction-method and final 34-period

helical waveguides were constructed and analysed experimentally with the dispersion characteristics and transmission loss presented. Finally this chapter concludes with a comparison between the various methods of analysing the waveguide, with further numerical simulation results in MAGIC, and draws conclusions about the verification of the constructed waveguide.

Chapter 4:

Within this chapter is the theory of electron beams, electron guns and emission mechanisms. General electron beam physics is discussed as a starting point for the more evolved theory of electron beam transported through a cusp magnetic field. The various electron gun types are described along with the differing emission processes with a focus on thermionic emission as this is the type employed by the cusp electron gun. The various details of the cusp electron gun are presented first the general over view of the gun and why one would choose to operate with this over similar electron guns and the historical details starting with invention following to recent advancements in cusp electron guns. This chapter finishes with a discussion of the mode selective properties specific to the axis-encircling electron beam and explains why these are important for harmonic waveguide interaction.

Chapter 5:

This chapter presents the design and numerical simulation of the cusp electron gun, used as the driving source for the gyro-BWO. The design factors are first introduced with a brief discussion of the optimisation of the design, a key element in electron gun creation. The simulation of the designed diode in the 3D PiC code MAGIC is presented with the optimised beam trajectories, average alpha, alpha spread and axial velocity spread given. The desired application of the electron gun requires operation over a range of magnetic field strengths, alpha values and beam voltages so the simulated values of the electron beam over those ranges is described. The 3D simulation suite Opera-3D was used to confirm the validity of the MAGIC simulations and electron gun design.

Chapter 6:

The details of the experimental construction, except interaction region which is in chapter 3, are described and, where suitable, analysed. First, the electron gun with a new cathode is shown with the construction details given. Following this are the two solenoids with the various problems that they create described and the cooling method explained. Furthermore, the experimentally measured magnetic field profile is given and compared to the simulated values. Within this chapter the many elements of the pulsed power system are described in both theory and experimental details including: the double cable Blumlein, voltage divider and spark gap switch. The full pulsed power setup with circuit diagram and scaled technical drawing are shown.

Chapter 7:

Presents the experimental results of the cusp electron gun and gyro-BWO. Starting with analysis of the voltage pulse used to accelerate the electron beam. Following is the diode current showing the regime of operation of the emission process and the variation of the emitted current with heater power. The transported electron beam current can then be found with the application of the magnetic fields. Then through the use of a scintillator the electron beam profile can be captured using a long exposure camera. The analysis of the electron beam profile allowed determination of the average diameter and velocity ratio, alpha, value for various values of the reverse coil current. These results were compared against simulated and analytically calculated values. A summary of the performance seen in the electron gun compared to the current state-of-the-art cusp electron guns created worldwide are presented. The chapter concludes with microwave pulse measurements from the gyro-BWO and an estimation of the frequency and power of the pulse.

Chapter 8:

Presents a brief summary of the results gained within this thesis alongside a look at the future work to be carried out.

There are many different results contained within this thesis throughout the many

chapters. Listed below are some points of importance presented for convenience.

These are the main points reported in this thesis.

Key results obtained from this work are:

I. Dispersion equations for the helically corrugated waveguide were derived.

II. Various methods were used to find the dispersive characteristics of a helically corrugated waveguide. Firstly, the coupled dispersion equation was solved analytically. Then a numerical simulation package was used to find the dispersion of the waveguide.

III. The helically corrugated waveguide was fabricated with high accuracy and dispersion characteristics found through a vector network analyser.

IV. Numerical simulations were developed to model the cusp electron gun.

V. Two solenoids, one operating at a very large DC current, were constructed with cooling issues resolved.

VI. Both solenoid magnetic field profiles were measured experimentally.

VII. A cusp electron gun capable of operating at high frequency was constructed and experimentally tested producing an axis-encircling beam.

VIII. The gyro-BWO was operated experimentally producing microwave radiation.

1.6 Summary

This chapter has detailed the history behind vacuum tube technologies and introduced some fundamental microwave devices. These devices range from the magnetron to the more recently invented gyrotron and the subsequent gyro-devices. The relevance of the W-band gyro-BWO to the vacuum electronic devices has been shown with the applications and performance compared to similar devices given. The chapter closes with a brief summary of each chapter highlighting the main points of each.

Chapter 2.

Theory of Guided Waves and

Beam-Wave Interaction

2.1 Introduction

The ability to transport microwaves along a bounded system with low loss has enabled many applications. Invented in the 1930's, the original waveguides were of rectangular and circular form, although many different modifications have been made to these shapes including slotted[125], corrugated[126], spiral[127] and Bragg[128] waveguides. The purpose of changing the geometry of the waveguide is to give the system special properties, such as preserving mode purity (slotted, spiral and helically corrugated waveguides), to couple to non-fundamental modes (helically corrugated and slotted waveguides), to gain more desirable properties, for example increased bandwidth and efficiency through changing the dispersion of the waveguide (helically corrugated waveguides) and to act as a microwave mirror (Bragg waveguides). This chapter will discuss the theory of electromagnetic waves and the waveguides that guide them with in-depth analysis of waveguides with a helical corrugation of the inner surface. The interaction between an electron beam and microwave or waveguide mode is also discussed within this chapter. This interaction can take many different forms such, as the Weibel and Cyclotron Resonance Maser instabilities. When coupling occurs, the electron beam can transfer, or take, energy from the waveguide mode through a beam-wave interaction, allowing amplification or generation of high power microwaves.

2.2 Electromagnetic waves

Maxwell's equations are a fundamental set of equations that describe both electrostatics and electromagnetic waves of which are considered one of the most important scientific advances in history. These equations, shown by equations (2.1)-(2.4), are summarized in the 19th century by James Clerk Maxwell[129] from 3 previous laws with a slight modification to Ampère's Law. In using these equations, the basis of electromagnetic theory can be obtained. By time-stepping methods the solution to these equations can be numerically achieved. Many simulation software have been written based on this method to solve complex electromagnetic problems.

Gauss's Law $$\nabla \cdot \mathbf{D} = \rho$$ (2.1)

Gauss's Law for magnetic fields $$\nabla \cdot \mathbf{B} = 0$$ (2.2)

Faraday's Law $$\nabla \times \mathbf{E} = -\frac{\partial \mathbf{B}}{\partial t}$$ (2.3)

Ampère-Maxwell Law $$\nabla \times \mathbf{H} = \mathbf{j} + \frac{\partial \mathbf{D}}{\partial t}$$ (2.4)

Where $\mathbf{E}$ is the electric field, $\mathbf{B}$ is magnetic field flux density, $\mathbf{D}$ is electric displacement field, $\mathbf{H}$ is the magnetic field, $\mathbf{j}$ is the volume current density, ρ is charge density and t is time. In these equations bolded parameters indicate vectors.

Also, in a linear material the following constitutive relations for displacement and magnetic flux density are:

$$\mathbf{D} = \varepsilon \mathbf{E}$$ (2.5)

$$\mathbf{B} = \mu \mathbf{H}$$ (2.6)

Where $\varepsilon = \varepsilon_r \varepsilon_0$ is the permittivity of the media where ε_r and ε_0 are the relative permittivity of the medium and permittivity of free space respectively, $\mu = \mu_r \mu_0$ is the permeability of the media where μ_r and μ_0 are the relative permeability of the medium and permeability of free space respectively.

The wave equation ((2.7) and (2.8)) can be derived[130] from Maxwell's equations.

$$\nabla^2 \mathbf{E} = \varepsilon \mu \frac{\partial^2 \mathbf{E}}{\partial t^2}$$ (2.7)

$$\nabla^2 \mathbf{B} = \varepsilon \mu \frac{\partial^2 \mathbf{B}}{\partial t^2}$$ (2.8)

The generalised wave equation for propagation in free-space can be found when $\varepsilon_r = 1$ and $\mu_r = 1$. For many applications microwaves have to be bounded within conductive walls and so a waveguide of some form must be used.

2.2.1 Introduction to waveguides

Waveguides are of great importance to electromagnetic wave applications as they can transport waves with low loss of power. It was in 1897 that Lord Rayleigh[131]

proved mathematically that microwave transport through a waveguide was possible. However, it was not until 1932 that George C. Southworth re-examined the waveguide concept and started experimentally confirming the theory. In 1936 Southworth presented experimental proof of this concept. At the same meeting, W.L. Barrow of MIT gave a paper presenting experimental confirmation of wave transport through a circular waveguide. Both these pioneers had independently contributed to waveguide theory. A more detailed study of the history of waveguides has been published by Packard[132]. Co-axial transmission lines are useful in that they can transport high bandwidth microwaves and are generally flexible and useful for many applications, such as domestic use and test equipment.

2.2.1.1 Circular waveguides

Circular waveguides are used throughout the gyro-devices and in many other microwave devices. This form of waveguide is useful for manufacturing purposes as turning a copper pipe is simpler than machining a rectangular hole. Furthermore, in applications such as radar antenna circular waveguide is absolutely necessary. The circular waveguide geometry can be seen in Figure 2.1. It is beneficial to use the polar coordinate system when dealing with a circular system, and as such, the fields are represented in terms of r, ϕ and z, with the Cartesian equivalent given as equations (2.9) and (2.10).

$$x = r\cos\phi \tag{2.9}$$

$$y = r\sin\phi \tag{2.10}$$

The generalised wave equation in a waveguide is given by equation (2.11) when propagating along the z direction.

$$\left(\nabla_t^2 + (\mu\varepsilon\omega^2 - k^2)\right)\begin{pmatrix} E_{0z} \\ H_{0z} \end{pmatrix} = 0 \tag{2.11}$$

Where $k = \sqrt{k_z^2 + k_c^2}$ is the EM wavenumber, k_z is the axial wavenumber and k_c is the cut-off wavenumber. ∇_t^2 is the transverse part of the Laplacian operator,

$\nabla_t^2 = \nabla^2 - \dfrac{\partial^2}{\partial z^2}$.
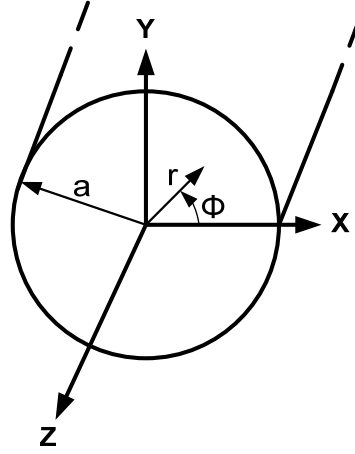
Figure 2.1. Circular waveguide geometry. Here *a* is the inner radius of the waveguide wall.

The solutions of the wave equation are an infinite number of waveguide modes. They are generally split into three categories: TE (*Transverse Electric*), TM (*Transverse Magnetic*) and TEM (*Transverse Electric and Magnetic*). The TE mode has no electric field in the *z* direction, but does have a magnetic field component. The TM mode has no magnetic field in the *z* direction but an electric field component. The TEM mode has neither an electric or magnetic field component in the *z* direction and does not exist in a regular waveguide, but rather in a co-axial system, due to such a mode not meeting the boundary conditions in waveguides. When characterising these modes it is common to use two indices *m* and *n* which represent the number of variations in the azimuthal and radial directions respectively..

Electric and magnetic components of a TE$_{mn}$ waveguide mode in a circular waveguide mode can be derived[133] as shown in equations (2.12) and (2.13). The radial dependence of the fields is given by the Bessel functions, J_m, and their derivatives.

$$E_{0,z} = 0 \tag{2.12}$$

$$H_{0,z} = A J_m\left(\frac{\zeta'_{mn}}{a} r\right) e^{\pm im\phi} \tag{2.13}$$

$$\boldsymbol{E}_{0,t} = -\frac{i\mu\omega a^2}{\zeta'^2_{mn}}\left(\hat{k} \times \nabla_t H_{0,z}\right) \tag{2.14}$$

$$\boldsymbol{H}_{0,t} = \frac{ika^2}{\zeta_{mn}'^2} \nabla_t H_{0,z} \tag{2.15}$$

Where ζ_{mn}' is the nth zero of the derivative of the mth Bessel function and A is the vector potential.

For a TM$_{mn}$ mode the field components are

$$E_{0,z} = A J_m \left(\frac{\zeta_{mn}}{a} r \right) e^{\pm im\phi} \tag{2.16}$$

$$H_{0,z} = 0 \tag{2.17}$$

$$\boldsymbol{E}_{0,t} = \frac{ika^2}{\zeta_{mn}^2} \nabla_t E_{0,z} \tag{2.18}$$

$$\boldsymbol{H}_{0,t} = \frac{i\varepsilon\omega a^2}{\zeta_{mn}^2} \left(\boldsymbol{k} \times \nabla_t E_{0,z} \right) \tag{2.19}$$

Where ζ_{mn} is the nth zero of the mth Bessel function

A circular waveguide can support both the TE and TM modes as these meet the boundary conditions. The cut-off wavenumber in a cylindrical waveguide can be found through equations (2.20) and (2.21) for a TE and TM mode, respectively. A plot of the first four Bessel functions is shown in Figure 2.2.

$$k_c = \frac{\zeta_{mn}'}{a} \quad \text{(TE mode)} \tag{2.20}$$

$$k_c = \frac{\zeta_{mn}}{a} \quad \text{(TM mode)} \tag{2.21}$$

The cut-off angular frequency can be calculated through equations (2.22) and (2.23) for the TE and TM modes respectively.

$$\omega_c = \frac{c\zeta_{mn}'}{a} \quad \text{(TE mode)} \tag{2.22}$$

$$\omega_c = \frac{c\zeta_{mn}}{a} \quad \text{(TM mode)} \tag{2.23}$$

The cut-off frequencies allow determination of the mode order within a circular waveguide. The first two modes are the fundamental TE$_{11}$ then the TE$_{21}$ modes. The electric and magnetic field patterns for the TE$_{21}$ mode can be seen in Figure 2.3. The two azimuthal variations means this is a mode with $m = 2$.
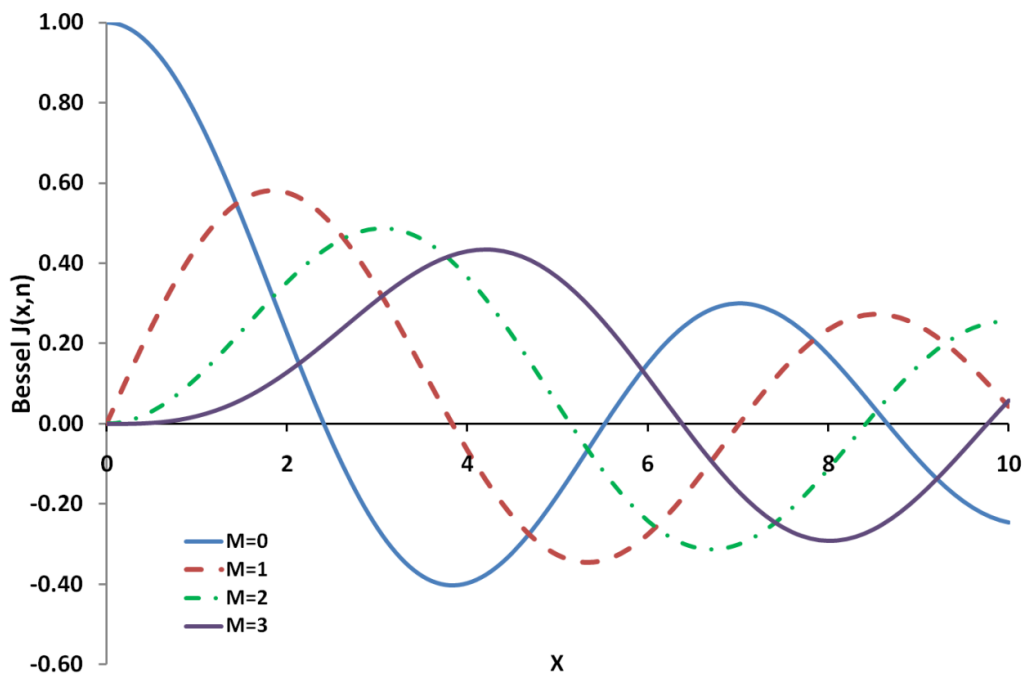
Figure 2.2. The first four Bessel functions.

Radial Electric Field   Radial Magnetic Field

(a)   (b)
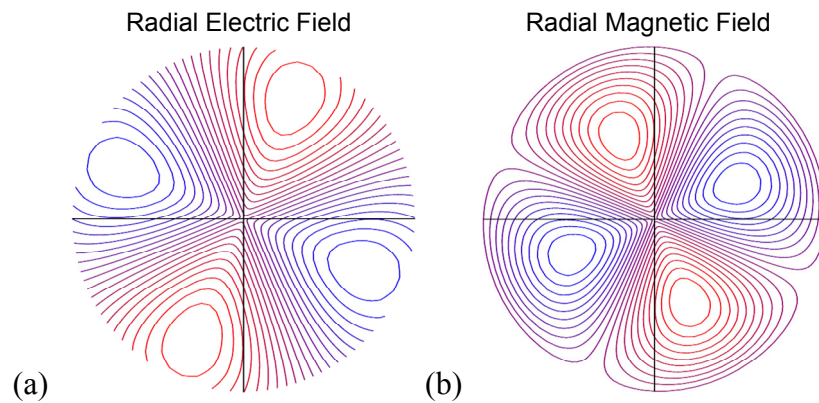
Figure 2.3. Electric and magnetic field matters for the TE_{21} mode in a circular waveguide Showing (a) electric field and (b) magnetic field.

2.2.2 Polarisation

The polarisation of an electromagnetic wave is the direction of its electric field. It is convenient to start with the simplest case, the plane wave. It is possible for two waves to travel together at the same time, oscillating around the same axis. When these oscillations occur at the same time they are said to be in phase. Also, the surface over which the fields are in phase is known as the wave front. A plane wave is one which is travelling along an axis, *z*, with plane fronts parallel to each other and

a monochromatic wave whose E field is oscillating parallel to the *x*-axis. This can be described as the real part of this expression

$$\boldsymbol{E} = \hat{x} E_0 \exp\left[i\left(\omega t - kz\right)\right]$$ **(2.24)**

Where E_0 is the amplitude of the wave, and $\hat{x}$ is the *x* direction unit vector.

The plane wave has the same amplitude at any point with the same *z* coordinate i.e. any line parallel to the *x-y* plane. This field is a solution of the wave equation in (2.7).

The first form of polarisation is the linearly polarised plane wave. This is a wave where the electric field vector is always parallel to one direction hence either in the positive or negative direction depending on the time of observation. This can be decomposed into two plane waves in *x* and *y* directions.

$$\boldsymbol{E} = \left(\hat{x} E_{0x} + \hat{y} E_{0y} \right) \exp\left[i\left(\omega t - kz\right)\right]$$ **(2.25)**

Where E_{0x} and E_{0y} are the amplitudes of the electric field in the x and y directions respectively and $\hat{y}$ is the *y* direction unit vector.

The resultant vector has an angle θ to the x-axis as given by

$$\tan\theta = \frac{E_{0y}}{E_{0x}}$$ **(2.26)**

When the polarisations of the two waves are out of phase different complicated polarisations can be found. An example of this is the electric field shown by equation (2.53).

$$\boldsymbol{E} = \hat{x} E_0 \exp\left[i\left(\omega t - kz\right)\right] + \hat{y} E_0 \exp\left[i\left(\omega t - kz + \left(\pi / 2\right)\right)\right]$$ **(2.27)**

When two polarisations are 90° out of phase which gives a circularly polarised plane wave. This can be defined as a wave that travels along a *z* axis with a field *E* and a constant length E_0 but the resultant vector is constantly changing direction in a fixed position. In the fixed point in space the field vector $\boldsymbol{E}$ rotates around this point with an angular velocity ω as time passes.

The other form of polarisation is a randomly polarised plane wave. This is also

known as the un-polarised plane wave, and is defined as a plane wave with a direction of oscillation that is randomly changing with time. This sort of polarisation occurs from most visible light sources (not lasers) as they contain many different atomic or molecular de-excitations causing the randomisation of the motion of the emitted light.

2.2.3 The phase and group velocities

The phase velocity of an electromagnetic wave is the velocity at which the phase propagates down a waveguide. It is more clearly seen in Figure 2.4 that when a wave, $A - B$, moves to position $A' - B'$ through a distance, C, the point $A - A'$ actually moves through a larger distance $c / \sin(\theta)$ making the phase velocity, v_p, greater than the speed of light. However, the actual velocity of the wave travelling down the tube is the group velocity, v_g, which must be less than the speed of light, c.
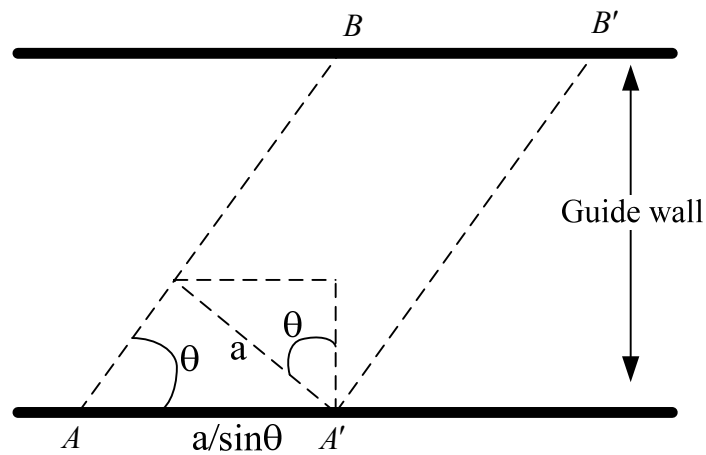
Figure 2.4. Velocity of electromagnetic wave in the waveguide.

The relationship between group velocity, v_g, and phase velocity, v_p can be given as

$$v_p = c \sin \theta \tag{2.28}$$

$$v_p v_g = c^2 \tag{2.29}$$

From the dispersion relationship, the group and phase velocities can be found through equations (2.30) and (2.31), respectively.

$$\mathrm{v}_g = c\sqrt{1 - \left(\frac{\omega_c}{\omega}\right)} \tag{2.30}$$

$$\mathrm{v}_p = \frac{\omega}{k} \tag{2.31}$$

2.2.4 Losses

In regular waveguides, microwaves lose power as they propagate along a waveguide through ohmic losses. The walls of standard waveguides (not those with superconducting walls) have a conductivity and, so electric fields can penetrate a distance into the walls, known as the skin depth, δ_s, which is dependent on the wavelength of the microwaves and material properties of the waveguide.

$$\delta_s = \frac{1}{\alpha} = \sqrt{\frac{2}{\omega\mu\sigma_m}} \tag{2.32}$$

Where α is the attenuation constant and σ_m is conductivity of the medium.

This power transfers into heating of the waveguide walls, since the electromagnetic wave induces currents along the walls. At the surface of the waveguide, the electric field in the conductor, E_c, is related to the eddy current density by Ohm's law, $J = \sigma_c E_c$ where σ_c is the conductivity of the conductor. Eddy currents are a well known effect where a conductor is near a changing magnetic field and this causes a flow of current. The losses in a waveguide are dependent on cross-sectional area, waveguide length, group velocity of the wave, the ratio of operating frequency to the cut-off frequency of the waveguide and the conductivity of the waveguide walls.

The losses in a waveguide are useful to know as they affect the output power. It can be advantageous to introduce losses to waveguides, for example a microwave sever.

2.3 The dispersion relation

In order to characterise waveguides, the dispersion equation is a relationship between angular frequency ω of a wave and its axial wavenumber k_z. Dispersion occurs as a

result of the variation of refractive index as a function of frequency in a media, as famously shown by passing white light through a prism to generate a rainbow of colours. Through analysis of the dispersion of a waveguide, the cut-off frequency, along with the waveguide modes, can be found. In a circular waveguide, the lowest order mode is the TE_{11}. The dispersion relation also provides the phase and group velocity at any frequency for any mode.

In a circular waveguide, the electromagnetic mode can be plotted though equation (2.33). The dispersion diagram of two waveguide modes with lowest cut-off frequencies in a circular waveguide can be seen in Figure 2.5. In this figure, the speed of light dispersion line is also shown. This is calculated through (2.34).

$$\omega^2 = c^2 k_z^2 + c^2 k_\perp^2 \tag{2.33}$$

$$\omega = c k_z \tag{2.34}$$
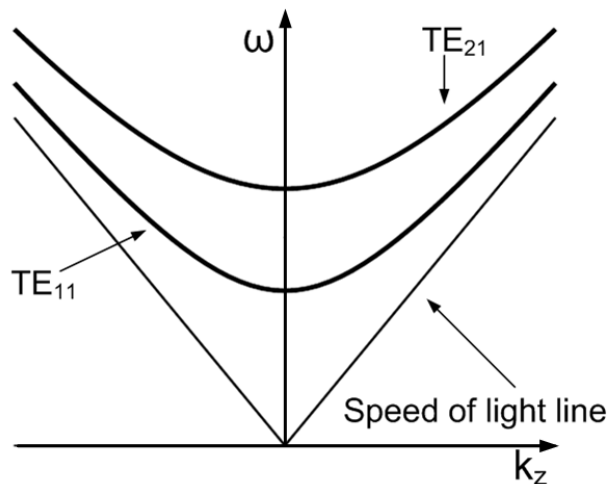
Figure 2.5. Dispersion diagram of a cylindrical waveguide. The fundamental TE_{11} and TE_{21} waveguide modes are shown along with the speed of light line.

Through plotting this, interactions can be tuned through changing electron beam properties or applied magnetic fields until the electron beam line and electromagnetic mode intersect.

2.4 Beam-wave interaction

Energy is extracted from a bunched electron beam in most microwave devices. The

bunching is critical to the devices usefulness as this creates coherent microwaves and allows for a net gain of energy transfer from the electron beam to microwave signal. Some devices, like the klystron, use a conductive mesh with an oscillating voltage applied to it to bunch electrons as the electrons cannot pass when the voltage is applied and can when they are not. The electrons are forced to "wait" until they pass which results in only bunches of electrons passing the mesh. Other devices bunch the electrons in the interaction region itself which takes away the requirement for such a mesh and reduces the complexity of the microwave source. The electrons bunch through two instabilities - the Weibel[134] and the Electron Cyclotron Maser (ECM) instabilities. Although these two coexist in the similar setups, one will dominate depending on the phase velocity of the electrons. Under similar conditions[135] it is found that the ECM instability is dominants when $v_p/c > 1$ and the Weibel mechanism is dominant when $v_p/c < 1$. The difference in the electron beam bunching is that while the ECM instability bunches the electron beam azimuthally the Weibel mechanism bunches the beam axially. The ECM is the instability employed in gyrotron devices and Weibel is more relevant to astrophysics[136] and laboratory plasma experiments. These two efficient bunching mechanisms are used in different devices to a great effect and have enabled a whole range of high power microwave sources.

2.4.1 Electron beam dispersion

Dispersion characteristics apply to an electron beam as well as electromagnetic waveguide modes, as previously discussed. Calculation of the electron beam dispersion line allows tuning of microwave interactions and allows determination of various properties of the interaction such as growth rate and tuning range/bandwidth. The electron beam dispersion of a cyclotron is given in equation (2.35). This dispersion includes the harmonic number, s, of the electron beam as this beam can be at higher harmonics to couple to waveguide modes.

$$\omega = k_z v_z + \frac{s\Omega}{\gamma} \qquad (2.35)$$

Where $v_z = v_t / \alpha$ is the axial velocity of the electrons, v_t is the transverse velocity

of the electrons, α is the velocity ratio alpha, $\Omega = eB_0 / m_0\gamma_0$ is the cyclotron frequency and $\gamma = 1 + (eV / m_0c^2)$ is the Lorentz relativistic factor.

The electron beam dispersion line can be calculated along with the waveguide modes, as shown in Figure 2.7a, and points of intersection show possible interaction where the cyclotron-resonance condition $\omega \cong \Omega / \gamma$ is satisfied. Through tuning parameters such as electron beam voltage and alpha as well as the applied magnetic field the electron beam line can be moved until the desired interaction is achieved. The coupled waveguide dispersion can be calculated which considers the interaction between the beam and waveguide mode to allow determination of the growth rate of interaction. The solution of the coupled dispersion is of the form $\omega = \omega_r + i\omega_i$ where ω_r gives dispersion properties and ω_i gives growth rate which appears only when the cyclotron-resonance condition is met. This also introduces an area of concern for microwave sources known as Doppler broadening, shown in Figure 2.7b. This occurs when the electron beam has an axial velocity spread resulting in the beam line becoming thicker as k_z increases. This effect reduces efficiency the vacuum tube and show multiple points of interaction between the electron beam and waveguide mode.

2.4.2 Dispersion characteristics of gyro-devices

The gyro-devices vary in their applications and configurations and the interaction of the electron beam to the waveguide mode easily differentiates each device. The dispersion profiles of three of the most common gyro-devices are shown in Figure 2.6. In the gyro-TWT the electron beam interaction is at the grazing or near-grazing condition operating on the $k_z > 0$ slope as the amplifier operated with an absolute instability. The gyro-BWO operates with the electron beam line intersection the waveguide mode on both the $k_z > 0$ and $k_z < 0$ slopes however the absolute $k_z < 0$ instability tends to dominate the convective instability and sets up a standing wave inside the cavity assuming there is a feedback mechanism. The gyrotron operates close to cut-off as detailed by this figure. The gyrotron has a single frequency of operation.
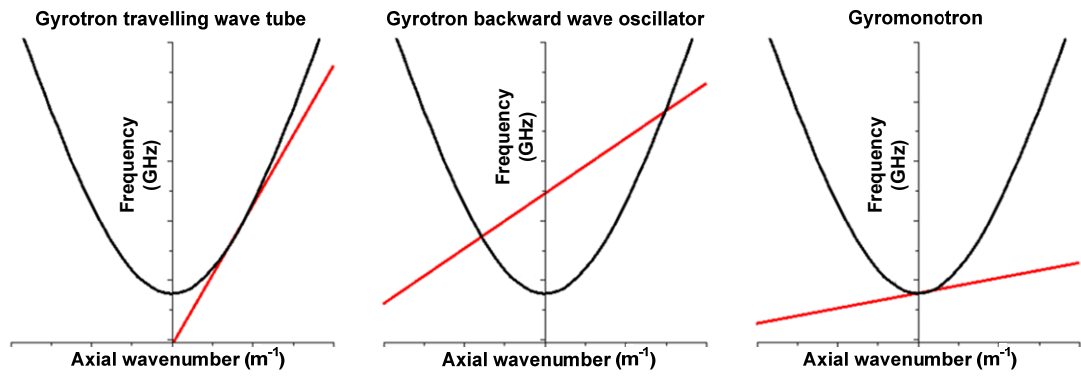
Figure 2.6. Dispersion diagrams for three gyro-devices these are from left to right the; gyrotron travelling wave tube; gyrotron backward wave oscillator; gyromonotron.
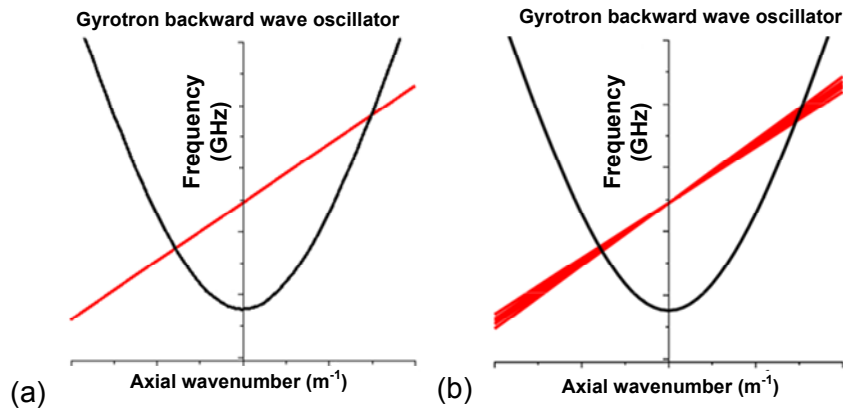
Figure 2.7. Uncoupled dispersion diagram of gyrotron backward wave oscillator with (a) the waveguide and electron beam dispersion lines presented and (b) the effect of Doppler broadening on the electron beam dispersion line.

2.4.3 Electron cyclotron maser instability

To understand the electron cyclotron maser (ECM) instability the positions of the electrons under the influence of an R.F. electric field has to be considered. Two assumptions are made about the electron motion: firstly, the electrons rotate counter-clockwise around a set point; and secondly, to make the situation simpler we are using a reference frame moving along with the electron in the z direction due to the fact that the ECM instability only extracts energy from transverse momentum of the electrons.
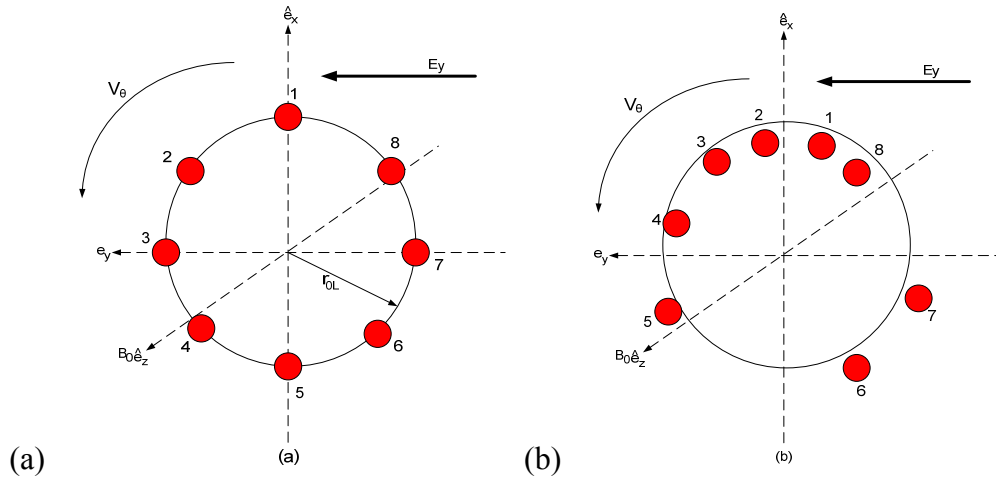
Figure 2.8. Positions of electrons in phase space in the time-frame of the electric field showing the electrons in their (a) un-bunched state and then after some time (b) azimuthally bunched.

In general in a gyro-device, two kinds of electron beams are used for ECM interactions i.e. an annular small-axis electron beam from a Magnetron Injection Gun (MIG) and an axis-encircling beam from a cusp or Pierce gun with a magnetic kicker. The electrons rotate around an applied magnetic field. Initially, they distribute uniformly around in the transverse phase space as seen in Figure 2.8a. The radius of the ring is given by the initial Larmor radius, r_{0L}, at the initial perpendicular velocity, $v_{0\perp}$, as is evident in equation (2.36).

$$r_{0L} = \frac{v_{0\perp}}{\left(\dfrac{\Omega_0}{\gamma_{0\perp}}\right)} \qquad (2.36)$$

Where $\gamma_{0\perp} = \left(1 - v_{0\perp}^2 / c^2\right)^{-1/2}$ is the initial relativistic factor and $\Omega_0 = eB_0 / m_0$ is the nonrelativistic cyclotron frequency.

It should be mentioned at this point that the velocity mentioned here is the perpendicular velocity, i.e. the electrons velocity around their axis. Essentially it is the velocity perpendicular to the direction of the beam as a whole (i.e. perpendicular to the axial direction). The other velocity mentioned is the parallel velocity, which is the axial velocity. Suppose an electric field applied to this electron ring in the y direction as shown in Figure 2.8 and is given by equation (2.37).

$$E_y(t) = \varepsilon_o \cos(\omega_o t)\hat{y} \qquad (2.37)$$

Where

$$\omega_o = \frac{s\Omega_o}{\gamma_{o\perp}}$$ (2.38)

The electric field given in equation (2.37) has the same frequency as the electron cyclotron frequency and its harmonics are shown in equation (2.38). This electric field would affect the motion of the electrons and so electrons 8, 1 and 2 in Figure 2.8 will lose energy to the field. The energy they lose is kinetic energy, so their perpendicular velocity will decrease and hence their γ must decrease. For these electrons, if their relativistic factor decreases, then their relativistic cyclotron frequency will increase as seen in equation (2.86). Electrons 3 and 7 are not affected in average by the electric field, as they have no velocity in y direction and they are only travelling in the x direction. However, electrons 4, 5 and 6 will gain energy from the electric field as they travel in the opposite direction from it. Electrons 4, 5 and 6 will therefore have increased kinetic energy and relativistic factor, and hence a lower relativistic cyclotron frequency. Electrons 8, 1 and 2 will spiral inwards from the ring as their relativistic cyclotron frequency will increase and from equation (2.86) they must of course have a smaller Larmor radius. The opposite occurs for electrons 4, 5 and 6. Particle 5 will experience a significant decrease in its cyclotron frequency, as it has a large y velocity component. If electrons 8, 1 and 2 are decelerated by the field, the electrons on the opposite side of the ring 4, 5 and 6 are accelerated by the field. This process will thus lead to phase bunching, as when one electrons cyclotron frequency decreases another at the other side of the beam will increase and therefore they will move closer together. In Figure 2.8b, the electrons in the orbit after a few cycles can be seen and the bunching effect of them is evident. This is due to the effect of the electric field on them and the relativistic dependence on the cyclotron frequency. In the situation given, there would not yet be a net exchange of energy. For an exchange in the energy to occur, the frequency of the electric field needs to be slightly greater than the relativistic cyclotron frequency.

$$\omega_o \geq \frac{\Omega_o}{\gamma}$$ (2.39)

If the frequency is slightly greater than the relativistic cyclotron frequency it satisfies equation (2.39), then the electrons traverse a space angle of less than 2π in a wave

period of $2\pi / \omega_0$. This means the electrons have an orbit less than the orbit of the wave so they will slip behind the wave. This therefore sets the bunching of the electrons in the upper half of their orbits. Since a majority of the electrons are in the upper plane, they will move in the same direction and hence will move in the same direction as the electric field, thus giving up kinetic energy to it as shown in Figure 2.8b.

2.4.4 Weibel Instability

As previously discussed, energy can be extracted from a rotating electron beam through azimuthal and axial bunching of the electrons. The axial bunching mechanism is called the Weibel mechanism[137], and is named after E. S. Weibel. This instability occurs through the axial movement of electrons and is caused by the $v_\perp \times B_1$ Lorentz force where $v_\perp$ is the electrons perpendicular velocity component, with respect to the wave vector and B_1 is the wave magnetic field. The electrons that lead the electric field by $\pi / 2$ advance in the z direction and the opposite is true for electrons that lag by $\pi / 2$. This means the electrons start to bunch together in the opposite phase of the electric field. If the cyclotron rotation is set to be slightly faster than the field rotation a net extraction of energy can be obtained.

2.5 Summary

This chapter has discussed the fundamental theory behind waveguides. Throughout the proceeding chapters the equations used can be linked back to the theory presented within this chapter. Starting with the most fundamental theory the waveguide was introduced with an emphasis on circular guides. The topic of polarised microwaves was briefly explained and this is of vital importance to the forthcoming discussions. The electron beam and waveguide dispersions were introduced. It is through the dispersion profiles of these waveguides that the theory of a waveguide with a helical corrugation of the inner surface is derived. This chapter ended with an explanation of the interaction between waveguide modes and electron beams. The two possible instabilities that exist in gyro-devices, the ECM and Weibel, were described. This

chapter set out the base theory behind smooth waveguides in preparation for the more complicated topic of helically corrugated waveguides.

Chapter 3.

Design, Manufacture and Testing of the Helically Corrugated Waveguide

3.1 Introduction

The interaction circuit of any microwave device is very important because it determines microwave modes, frequency, power, bandwidth etc. The design and testing of the interaction region for the W-band gyro-BWO, the helically corrugated waveguide, is discussed within this chapter. The analytical and numerical methods are shown with the optimised waveguide geometry given. The construction of this waveguide is described in detail with the minor problems encountered explained and the solution presented. The measured results obtained though using a vector network analyser (VNA) of the microwave transmission, reflection and phase evolution of the waveguide are given later in the chapter. Finally the results of the different methods employed i.e. analytical calculations, numerical simulations and experimental measurement of the waveguide dispersion characteristics are compared and analysed.

3.2   Previous research at the University of Strathclyde using helically corrugated waveguides

The University of Strathclyde has been at the forefront of helically corrugated waveguide research due to being co-inventors of the concept with the Institute of Applied Physics in Nizhny Novgorod in Russia. Originally the intention was to use this type of waveguide to provide a modified dispersion profile in gyrotron devices but another application has evolved in microwave pulse compression. The requirements for microwave pulse compression are that the output power should be many times that of the input power and the helically corrugated waveguide changes the group velocity of the microwave in a pulse in order to reduce the width of the pulse and in doing so increase the power. In both of these fields, results unobtainable by other methods are found and a world record in pulse compression as well as impressive gyro-TWA/gyro-BWO results have been achieved.

The original theory paper on this subject was written by G. G. Denisov et al. in June 1998[145] entitled "gyro-TWT with a Helical Operating Waveguide: New Possibilities to Enhance Efficiency and Frequency Bandwidth". The paper gives the first theory and theoretical results for a gyro-TWT using a helically corrugated interaction

region. The theoretical results of the helical gyro-TWT are compared against the conventional gyro-TWT and it is found that the helical gyro-TWT had over ~20% bandwidth and ~30% efficiency. These very impressive results showed that this new waveguide has very attractive properties and since this paper a few experiments using these waveguides have taken place. The experimental verification of the previous simulations was reported in December 1998[138]. The main conclusion of this paper was that the authors were able to achieve an output power of 1MW at 9.2GHz with a gain of 23dB and efficiency of 20%. Another paper from the joint groups was published in March 2000 by V. L. Bratman et al.[139] entitled "High-Gain Wide-Band Gyrotron Travelling Wave Amplifier with a Helically Corrugated Waveguide". This paper gives the experimental results of a gyro-TWA and here gives the measured bandwidth of the device. The results gained are that at 9.4GHz the peak power is 1.1MW, efficiency of 29%, saturated gain 37dB, linear gain 47dB and a bandwidth of 8.4 to 10.4GHz which is 24% of the central frequency. The results of a gyro-TWA were presented in 2004 at the ICMMT conference[140] operating between 8.4GHz and 10.4GHz. This had an electron beam of 185keV and current 7.5A with a RF output of 220kW, with 16% efficiency and 21% bandwidth. The latest papers to be published on this subject were in May 2005[141] and this paper gives the results of a gyro-BWO using a helical waveguide working in X-Band. The results gained from this were at 8.575GHz a maximum power of 62kW, efficiency of 16.5%, and bandwidth between 8.0-9.5GHz which is 17% of the relative frequency. After this the next work reported by Strathclyde was in 2006 by W. He et al. which investigated a gyro-BWO through simulations[146]. These simulations, performed through the 3D PiC code MAGIC, showed that ~8.6GHz the power of ~64kW could be realized with an electron beam of 185keV and 2A.

Pulse compression work in Strathclyde employs helical waveguides to provide the idealized dispersion needed to compress a pulse to high power. The helical waveguide is used so that essentially one end of the pulse moved back relatively whilst the other end of the pulse moves forwards and the two meet in the middle so the pulse is shorter in width and larger in amplitude. The first paper released on this, in March 2004[142], gives the theory behind the novel pulse compression method and

also results of the proof-of-method experiment carried out. In this work the output pulse could be 10 to 20 times in peak power of the input pulse with an efficiency of more than 50%. This compared well with the theoretical results. The next paper published is the April 2005 paper[143] these results are compared between theoretical simulations and experimental results. It was demonstrated that the frequency-swept BWO pulse was effectively compressed, resulting in about a 3-fold peak power increase, with a maximum power of 1.8GW generated

3.3 Helically corrugated waveguide theory

A waveguide with a helical corrugation on the inner surface couples two partial rotating waves to produce an idealized dispersion profile. The interaction between electron beam and ideal dispersion should occur with axial wavenumber close to zero with a large frequency tuning range in comparison with smooth-bore waveguide. When interaction occurs with low k_z the effect of velocity spread on the interaction efficiency is lowered due to the $k_z v_z$ term appearing in the electron beam dispersion line. The two partial rotating modes coupled are a near cut-off mode (A) with small axial wavenumber and a travelling wave (B) with large wavenumber. In the following discussion modes A and B are a TE_{21} and the first spatial harmonic of the TE_{11} mode respectively. The B wave rotates against the helix and is perturbed in the similar manner to a periodically loaded waveguide, creating spatial harmonics of the wave at intervals of $\pm 2\pi / d$ which is $\bar{h}$ and where d is the period of the corrugation.

Coupling between the waves A and B will occur when the axial and azimuthal wavenumbers meet the Bragg resonance conditions given in equations (3.1) and (3.2).

$$m_A + m_B = \bar{m} \tag{3.1}$$

$$h_A - h_B = \bar{h} \tag{3.2}$$

Where m_A and m_B are the azimuthal mode index of wave A and B respectively. h_A and h_B are the axial wavenumber of mode A and B respectively. $\bar{m}$ is the azimuthal index of the helical waveguide and $\bar{h}$ is the axial number of the Bragg periodicity.

When the corrugation amplitude of the helical waveguide, l, is small compared to the operating wavelength and the waveguide is long enough then the method of perturbation[144] can be used in order to deduce the field structure and dispersion characteristics of the helically corrugated waveguide. Also, the ratio of corrugation amplitude, l, to the mean waveguide radius, r_0, should be much smaller than 1, $l/r_0 \ll 1$.

The surface of the helix can be shown in cylindrical coordinates r, φ, z as

$$r(\varphi, z) = r_0 + l \cos(\bar{m}\varphi - \bar{h}z) \tag{3.3}$$

A three-fold helix, shown in Figure 3.1, is used to couple a TE_{21} and the first spatial harmonic of the TE_{11} mode. If higher harmonic operation is required then the order of corrugation is increased, for example changing to a five-fold helix as shown in Figure 3.1b. It should be noted that the spatial harmonic modes only exist within a waveguide that has an axial periodicity. The helical corrugation has periodicities in both the azimuthal and axial directions as shown in Figure 3.2.
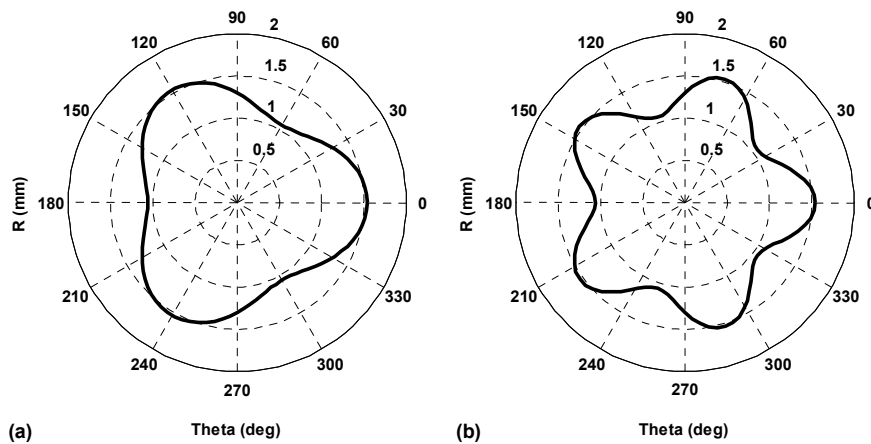
Figure 3.1. Cross-sectional profile of a helically corrugated waveguide with different aximuthal indexes showing (a) a three-fold and (b) a five-fold corrugation.

The dispersion of a helical waveguide is unique, as shown in Figure 3.3 taken from Ref. 144, and is ideal for a wide-band gyro-device. At a higher ω, the dispersive effect is closer to the TE_{21} mode and so the eigenmode tends to follow the conventional TE_{21} mode. Conversely at the lower frequency end of the eigenmode,

the dispersion follows the TE$_{11}$ mode. The dispersion creates two eigenmodes, one "operating" and the higher frequency "spurious" mode labelled W$_1$ and W$_2$ in the following discussions. The interaction between electron beam and helical dispersion occurs with the operating eignmode. There are many spatial harmonics of the helical dispersion two are shown within the figure the fundamental labelled (0), and first, (1).
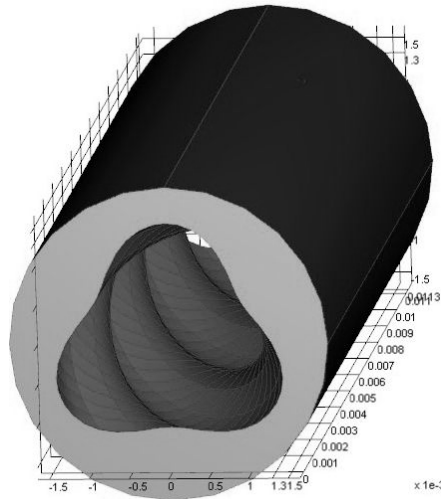
Figure 3.2. A 3D representation of the helical waveguide body showing both the axial and azimuthal periodicity of the corrugation.
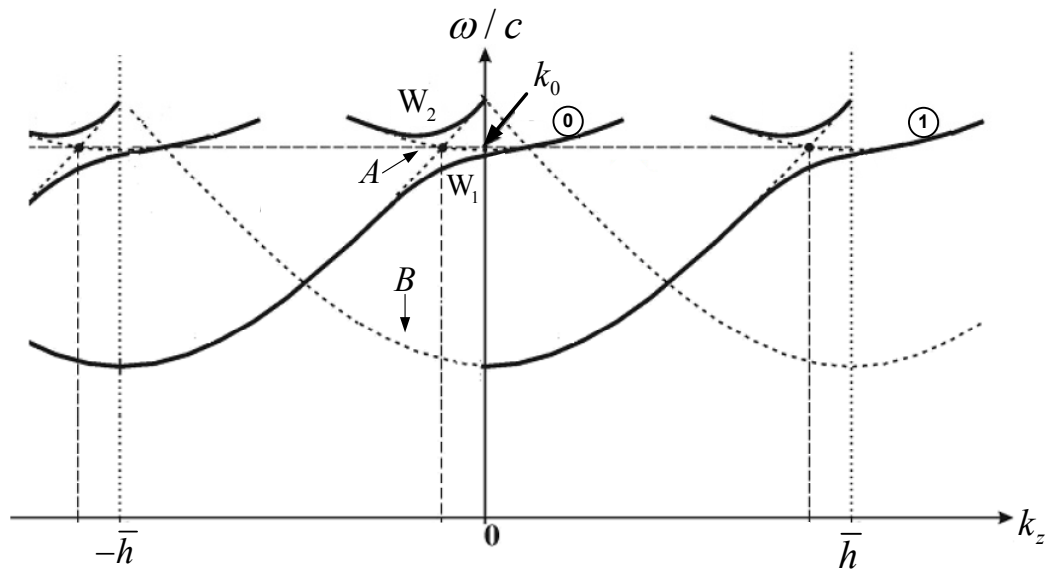
Figure 3.3. Schematic dispersion diagram of a helical structure showing the spatial harmonics.

51

Interaction occurs at the intersection between mode A and mode B. The following equations describe the two unperturbed waveguide dispersions.

$$(\omega/c)^2 - k_0^2 - h_A^2 = 0 \tag{3.4}$$

$$(\omega/c)^2 - k_{0_B}^2 - \left(h_{B_1} + \overline{h}\right)^2 = 0 \tag{3.5}$$

Where k_0 and k_{0_B} are the cut-off wavenumbers for the A and B modes respectively and $h_{B_1} = h_B - \overline{h}$.

At the point where these two lines intersect the dispersion curved can be approximated as a parabola and a straight line described by the following equations

$$2k_0\delta - h_A^2 = 0 \tag{3.6}$$

$$k_0\delta - \left(h_{B_1} + \Delta_g\right)h_0 = 0 \tag{3.7}$$

Where $\delta = (\omega/c) - k_0$ and $\Delta_g = \overline{h} - h_0$ are the frequency and geometrical mismatch[145] respectively and these are shown in, Figure 3.4. Also, $h_0 = h_B(k_0)$.
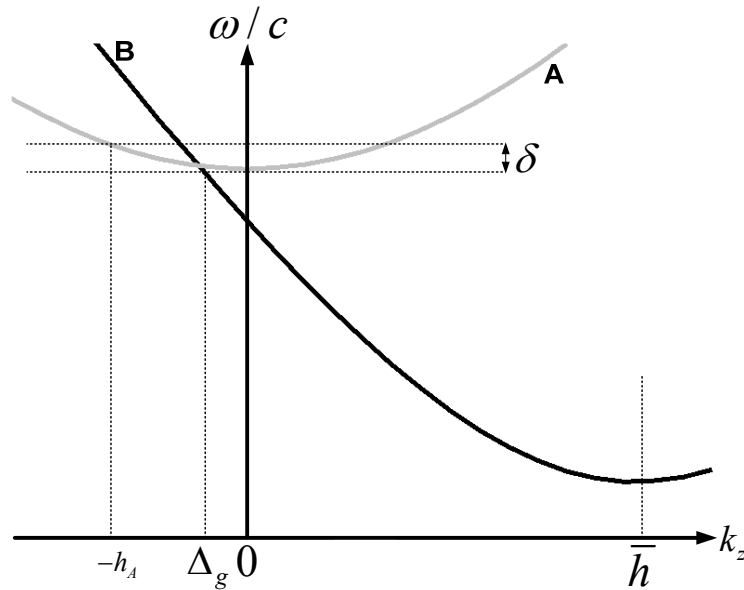
Figure 3.4. Dispersion diagram detailing A and B modes as well as various parameters used throughout the helical theory.

Supposing two partial waves can be shown using two equations in (3.8) and (3.9).

$$E = E_A(r)\left(a_+e^{-ih_Az} + a_-e^{ih_Az}\right)e^{i(\omega t - m_A\varphi)} \tag{3.8}$$

$$E = E_{B_0}(r)b_0e^{-ih_Bz}e^{i(\omega t + \omega_B\varphi)} \tag{3.9}$$

Where a_+ and a_- are the amplitude of the co- and counter-rotating mode A wave respectively and b_+ is the amplitude of the co-rotating mode B wave.

The amplitudes of the two partial waves $a\mp$ and b can be considered as functions of z which are described by a set of coupled wave linear differential equations[146], and given in equations (3.10) and (3.11).

$$\frac{d^2f}{dz^2} + 2k_0\delta f = 2\sigma k_0 b \tag{3.10}$$

$$ih_0\frac{db}{dz} + \left(k_0\delta - h_0\Delta_g\right)b = \sigma k_0 f \tag{3.11}$$

Where $f = a_+(z) + a_-(z)$, and the coupling coefficient[147] σ is given in equation (3.12) which is scaled to k_0.

$$\sigma = \frac{1}{2r_0^3k_0^2}\frac{\zeta_A'^2\zeta_B'^2 - m_Am_Br_0^2\left(k_0^2 + k_{z1}k_{z2}\right)}{\sqrt{\left(\zeta_A'^2 - m_A^2\right)\left(\zeta_B'^2 - m_B^2\right)}} \tag{3.12}$$

Where ζ_A' and ζ_B' are the first differential Bessel root corresponding to the A and B mode respectively, $k_{z1} = \left(k_{0_A}^2 - k_{0_B}^2 + \bar{h}^2\right)/2\bar{h}$ and $k_{z2} = \left\{\left(k_{0_A}^2 - k_{0_B}^2 + \bar{h}^2\right)/2\bar{h}\right\} - \bar{h}$ as shown in Figure 3.3.

When the equations in (3.10) and (3.11) are analysed by searching for eigenwaves of the form e^{-ihz} the dispersion equation can be found as (3.13).

$$\left(k_z^2 - 2\delta\right)\left(k_z - \Delta_g + \delta/h_0\right) + 2\sigma^2/h_0 = 0 \tag{3.13}$$

In this equation the parameters Δ_g, h_0 and σ are scaled to k_0.

The dispersion of the helical waveguide mode changes with the addition of the electron beam line. The full coupled equation can allow the coupled wave dispersion and the growth rate of interaction to be calculated through the same methods as previously discussed. The full derivation of these equations can be found in previous

literature[145]. The 5th order beam-wave coupled equation for the helically corrugated waveguide is

$$\left[\left(k_z^2 - 2\delta\right)\left(k_z - \Delta_g + \frac{\delta}{h_0}\right) + \frac{2\sigma^2}{h_0}\right]\left[k_z - \frac{\left(\delta - \Delta_H\right)}{\beta_{z0}}\right]^2$$
$$= C^3 \left(k_z - \Delta_g + \frac{\delta}{h_0}\right)\left(1 + \frac{2s}{\alpha_0^2 \beta_{z0}}\left[k_z - \frac{\left(\delta - \Delta_H\right)}{\beta_{z0}}\right]\right)$$

(3.14)

Where $\Delta_H = \left(s\omega_{H_0} - \omega_0\right)/\omega_0$ is the relative frequency mismatch, $\beta_{z0} = \beta / \sqrt{(1+\alpha^2)}$

is the relative longitudinal velocity and $\beta = (1/\gamma)\sqrt{(\gamma^2 - 1)}$ is a relativistic velocity

factor. A Pierce parameter[145], C, is used to determine how strong the electron beam

has coupled to the wave. This is given through equation (3.15).

$$C = \left(\frac{4\hat{I}\rho}{\gamma_0 N_A \beta_{z0}}\right)^{1/3}$$

(3.15)

Where $\hat{I} = eI / mc^3$, $N_A = J_{m_A}^2 \left(\zeta_A'\right)\left(\zeta_A'^2 - m_A^2\right)$, $\rho = \frac{\beta_{\perp 0}}{\beta_{z0}} J_s' \left(s\beta_{\perp 0}\right) J_{m_A - s}\left(\hat{r}_g\right)$ is the

scaled guiding centre of the electrons, where $\hat{r}_g = k_0 r_g$, r_g is the guiding centre of

the electrons and $\beta_{\perp 0} = \beta\alpha / \sqrt{(1+\alpha^2)}$ is the relative velocity in the transverse

direction.

The operating frequency of interaction is found by setting $C = 0$ which gives

equation (3.13) and then plotting the electron beam dispersion given in equation

(3.16).

$$\omega = c\left(\Delta_H + k_0 + k_z\beta_{z0}\right)$$

(3.16)

The dispersions of the helically corrugated waveguide and the electron beam

cyclotron mode are shown in Figure 3.5a. The coupled dispersion equation is plotted

in Figure 3.5b.

3.4 Waveguide design and dispersion through analytical and numerical methods

In order to design and manufacture a waveguide that has the most ideal properties
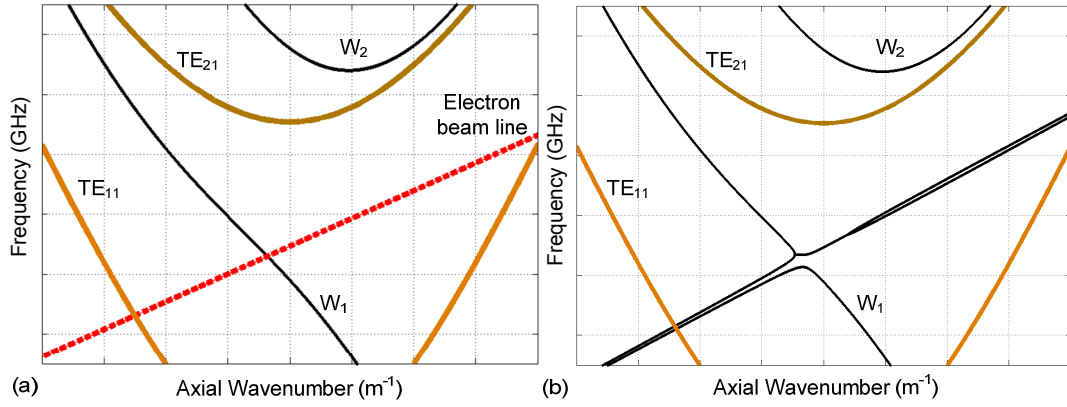
Figure 3.5. Dispersion diagrams for a helically corrugated waveguide showing (a) uncoupled dispersion (solid line) with the electron beam line (dashed line) and (b) coupled dispersion.

such as high output power, large tuning range and high efficiency it is necessary to calculate the waveguide dispersion and growth rate of the beam-wave interaction. A helically corrugated waveguide has both an axial and azimuthal periodicity, by adjusting parameters such as the corrugation amplitude and period the resultant dispersion curve is changed and therefore an optimal interaction between the electron beam and microwave mode could be achieved. It is through analytical optimisation and combined with numerical simulation of the beam-wave interaction using MAGIC that the optimised corrugation parameters and waveguide geometry were decided. This is for specific electron beam parameters such as electron beam current and accelerating voltage as well as the applied magnetic field. The optimised parameters that will give rise to efficient interaction in the frequency band from 84 to 104 GHz are shown in Table 3.1.

Parameter	Value
Average radius (mm)	1.3
Corrugation amplitude (mm)	0.24
Corrugation Period (mm)	3.75
Current (A)	1.5
Alpha	1.65
Voltage (kV)	40
Magnetic field strength (T)	1.82

Table 3.1. Parameters for a helically corrugated waveguide optimized for an interaction at ~94GHz.

A photo of the optimised waveguide is shown in Figure 3.6. Several methods were employed to calculate the dispersion of the waveguide. By using analytical calculation, numerical simulation (CST Microwave studio and MAGIC), and experimental measurement (vector network analyser) the dispersion property of the waveguide was obtained. These three methods proved to be highly reliable and in excellent agreement.
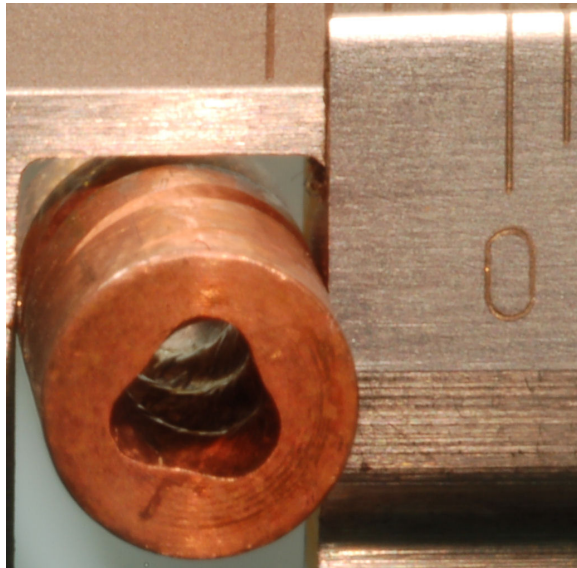
Figure 3.6. Photo of a W-band helically corrugated waveguide compared against a vernier caliper scale.

3.4.1 Analytical calculation

The theory of perturbation can be used to analyse the wave coupling characteristics so that the dispersion equation for the helically corrugated waveguide can be derived. The analytical calculation of the helically corrugated waveguide dispersion provides a distinct dispersion profile. The dispersion profile is calculated through equation (3.13) and the dispersion of a helical waveguide with properties given in Table 3.1 is shown in Figure 3.7 compared alongside the TE_{21} and 1st spatial harmonic of the TE_{11} smooth-bore waveguide modes. Noticeable here is that this dispersion curve has a different profile than the perfect dispersion shown in Figure 3.3. The difference arises because the equation used in the calculation contains some approximation and thus is only truly correct in the area between the two waveguide modes.
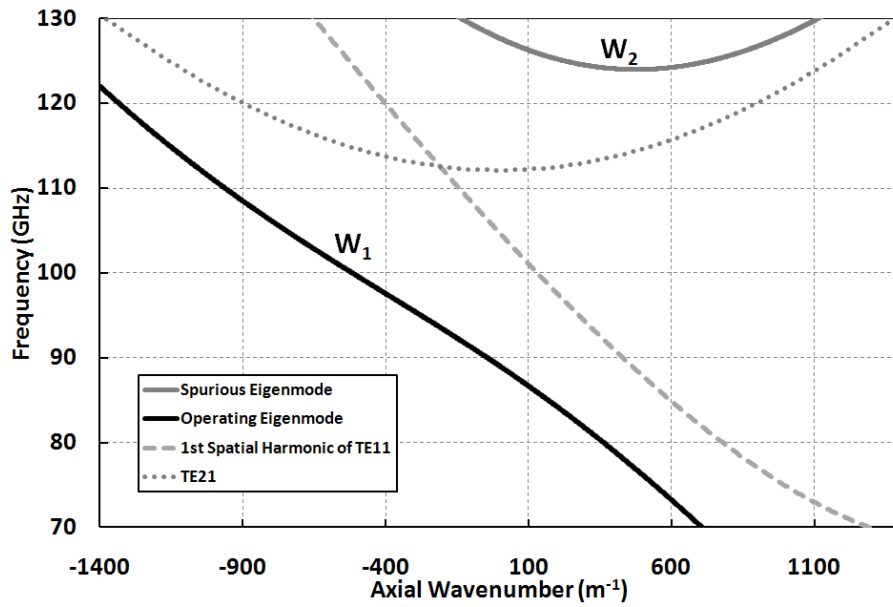
Figure 3.7. Dispersion diagram showing partial wave TE_{11} and TE_{21} and the eigenwave W_1 and W_2 as a result of resonant coupling.

The coupling between electron beam and the eigenwave waveguide modes in the helical waveguide region is described by equation (3.14). Solving this equation therefore gives rise to the coupled electron beam cyclotron mode and eigenwave mode as shown in Figure 3.8. The growth rate of the interaction can be calculated from the imaginary solution of the coupled dispersion equation and is shown in Figure 3.9. In order to get a clearer image of the interaction that takes place Figure 3.10 shows the growth rate overlaid on the uncoupled dispersion diagram to show the specific interaction point.
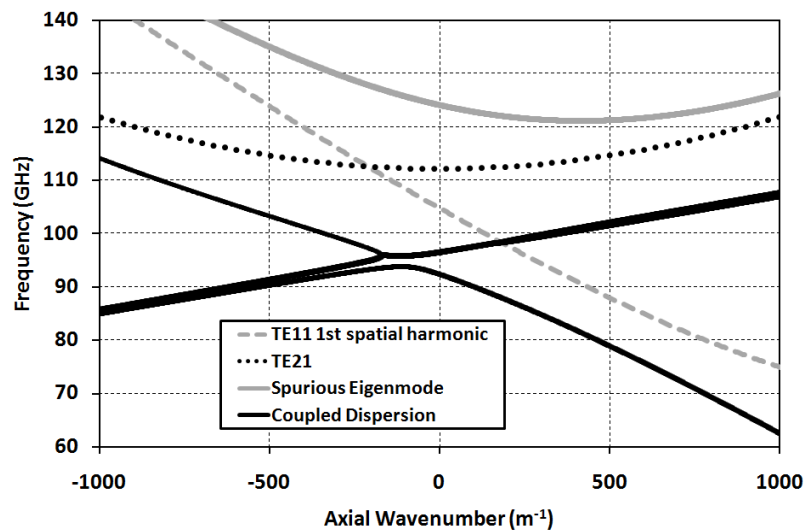
Figure 3.8. Coupled helically corrugated waveguide dispersion with an interaction at ~94GHz.
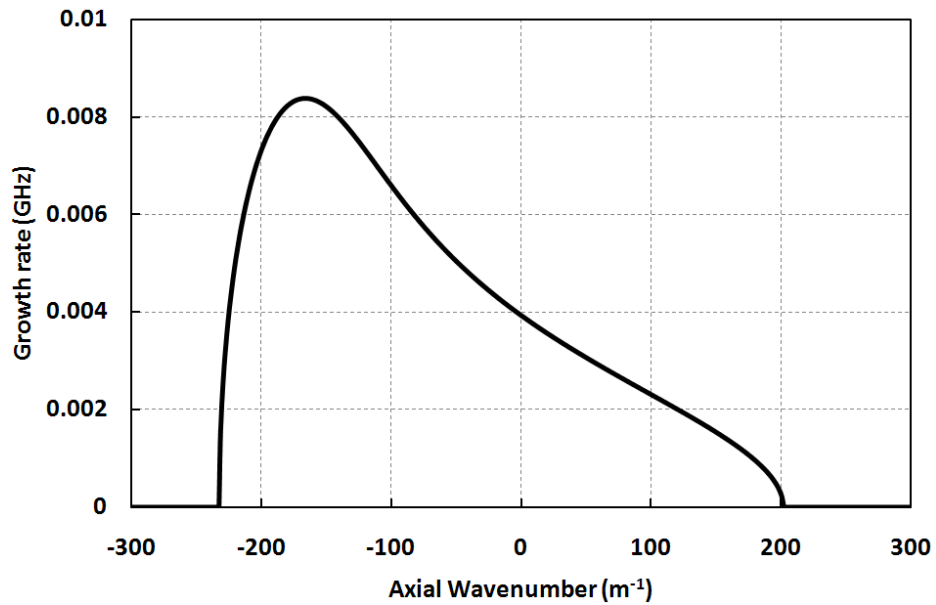
Figure 3.9. Growth rate of the gyro-BWO interaction at ~94 GHz when using a magnetic field of 1.82T.
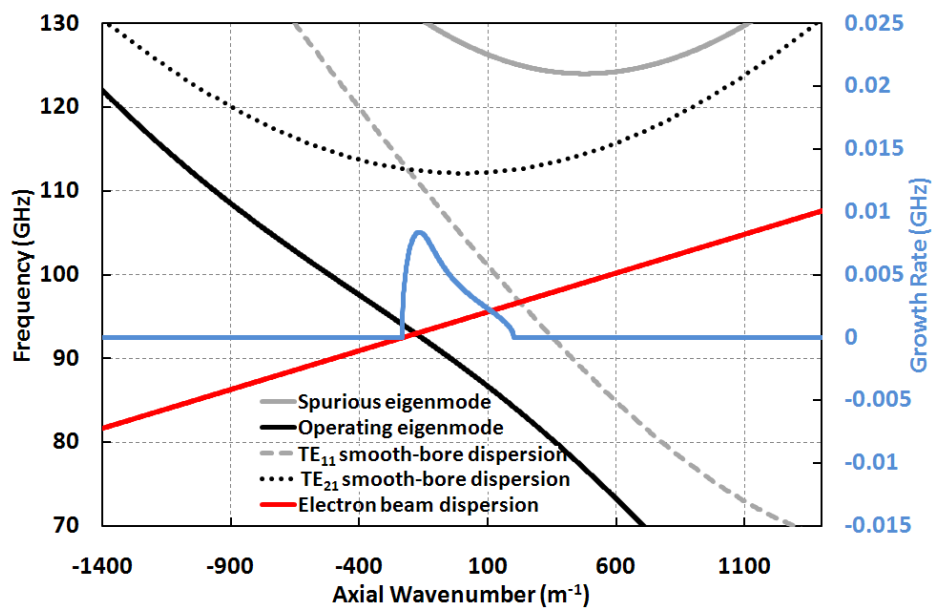
Figure 3.10. Growth rate compared against the helically corrugated waveguide dispersion at an interaction ~94GHz.

3.4.2 Simulation of the helically corrugated waveguide dispersion using CST Microwave Studio

The 3D electromagnetic simulation suite CST Microwave Studio[148] can be used to simulate the S-parameters and phase evolution through a helical waveguide.

Therefore it can be used to numerically calculate the dispersion of a helically corrugated waveguide through the same method used when performing vector network analyser measurements. Two ports were defined, one to introduce radiation and the other to let radiation pass without reflection. The simulation setup is shown in Figure 3.11. This radiation was injected with linear polarisation so an elliptical polariser was used to convert it from linear to circularly polarised radiation. After this a tapered helically corrugated waveguide was used to transition from a smooth-bore to a helically corrugated waveguide to reduce reflections associated with a sharp change in geometry. A four period helically corrugated waveguide was simulated as this allows one to measure the dispersion and electric fields with a lower run-time. The length of four periods of helical waveguide was chosen as the phase evolution would be large enough to allow a clean dispersion profile to be obtained.
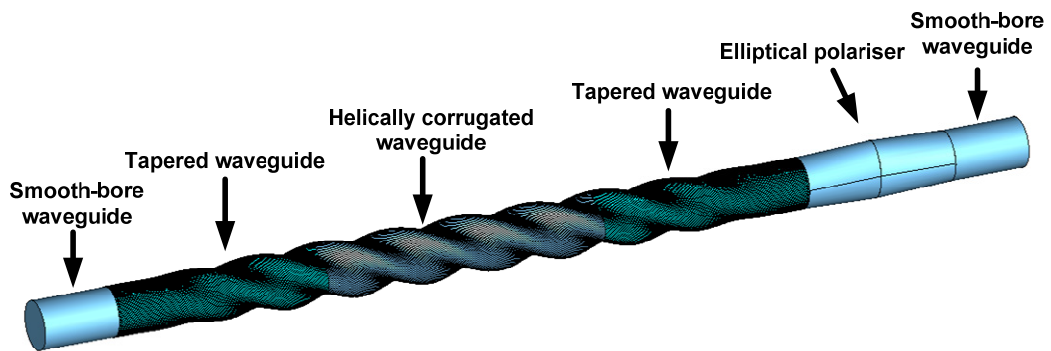
Figure 3.11. Simulation setup used to obtain the dispersion of the helical waveguide using CST Microwave Studio.

In the simulation the background material was a perfect conductor with everything else represented as vacuum. The electric and magnetic field pattern allows one to deduce the waveguide mode at a specific point along the waveguide. The distinctive eigenmode pattern is evident with a TE_{11}-like mode in the E_x component and a TE_{21}-like mode evident in the B_z mode.

Dispersion characteristics were found through an evaluation of the phase evolution through the helically corrugated waveguide, which is shown in Figure 3.13. The phase has 360 degree jumps along the frequency range as is characteristic with phase measurements. The continuous phase function can be extracted through

59
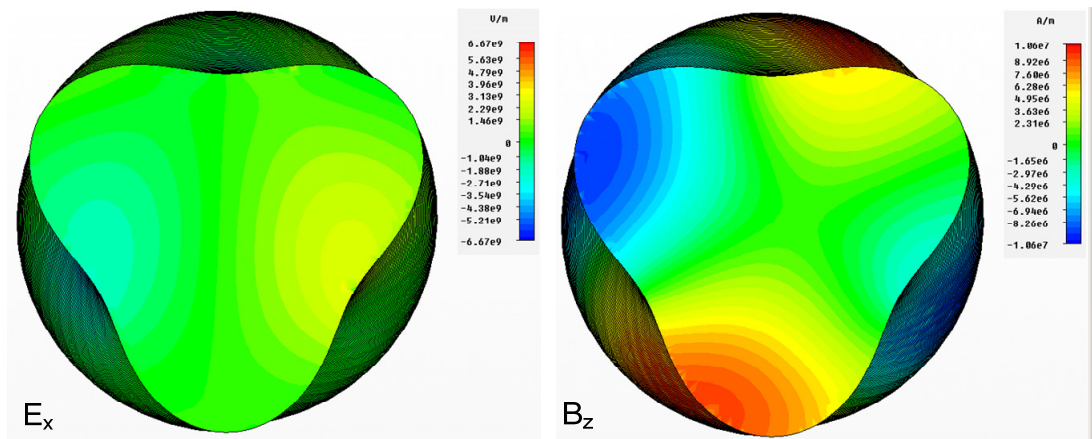
Figure 3.12. Electric and magnetic field profile captured at a cross-section of the helically corrugated waveguide.

computational analysis of the measured phase. After this the phase, in radians, can be converted to axial wavenumber through $\Delta k_z = \Delta\phi / L$. The dispersion can then be found through a phase measurement of the components already outlined and then measuring the phase again but without the helix present. This gives a measurement of the phase in the helix only.
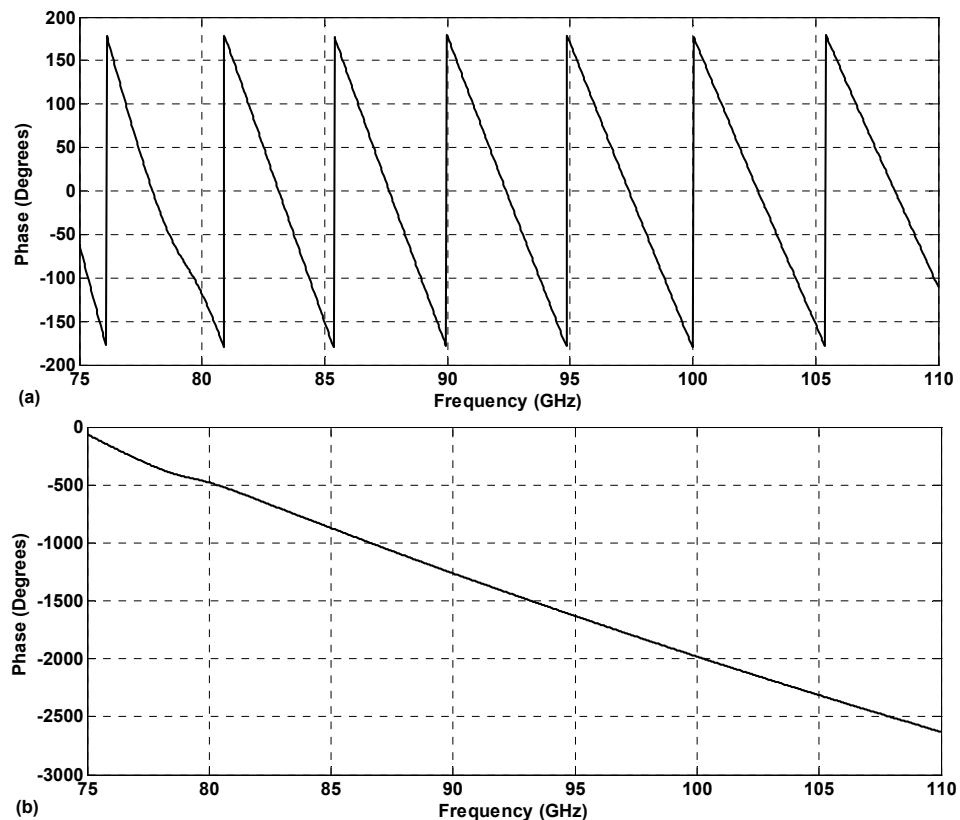
Figure 3.13. Phase output from CST Microwave Studio (a) the raw phase output and (b) the continuous phase evolution through the helical waveguide and elliptical polariser.

The phase measurement in Figure 3.13 was transformed to be frequency as a function of k_z and is shown in Figure 3.14 which is the data set of phase as a function of frequency in the simulated dispersion for the 4-period helically corrugated waveguide. This dispersion shows a good agreement with the analytically calculated dispersion. When the injected radiation has an angle of -45 degrees (relative to the vertical elliptical polariser) then the circular polarisation after the elliptical waveguide rotates in same direction as the ripples of the helically corrugated waveguide, hence the name "co-rotating mode". Thus the radiation travels along a waveguide of constant radius so the dispersion should be similar to a smooth-bore waveguide of the same average radius.
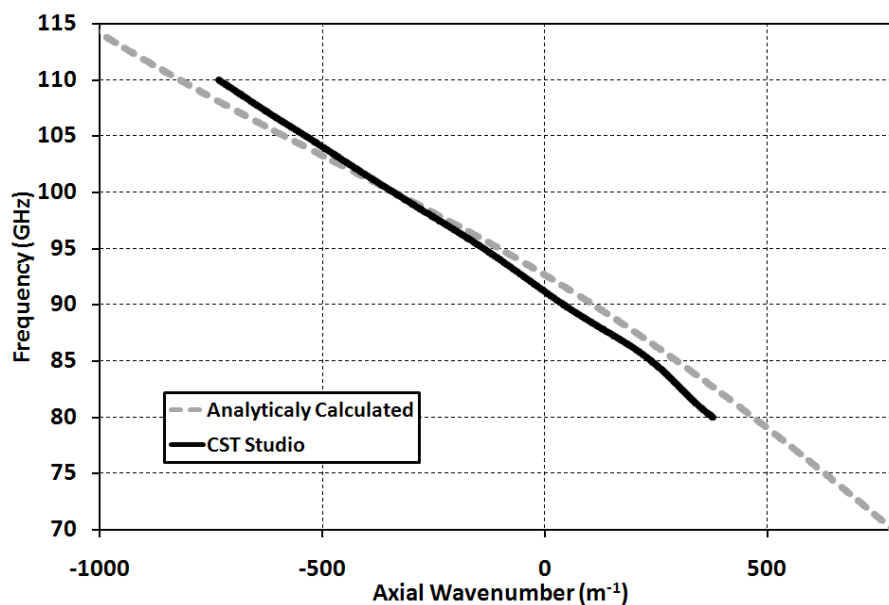
Figure 3.14. Numerically simulated dispersion of the 34-period helically corrugated waveguide using CST Microwave Studio compared against the analytically calculated dispersion.

The numerically calculated dispersion of the co-rotating mode can be seen in Figure 3.15 with the analytical calculation of the 1st spatial harmonic of the TE_{11} mode. The good agreement between the two dispersions allows one to be confident that the method employed in the CST microwave studio simulations is accurate.

3.5 Construction of the helically corrugated waveguide

A waveguide with a helical corrugation on the inner surface operating in the W-band
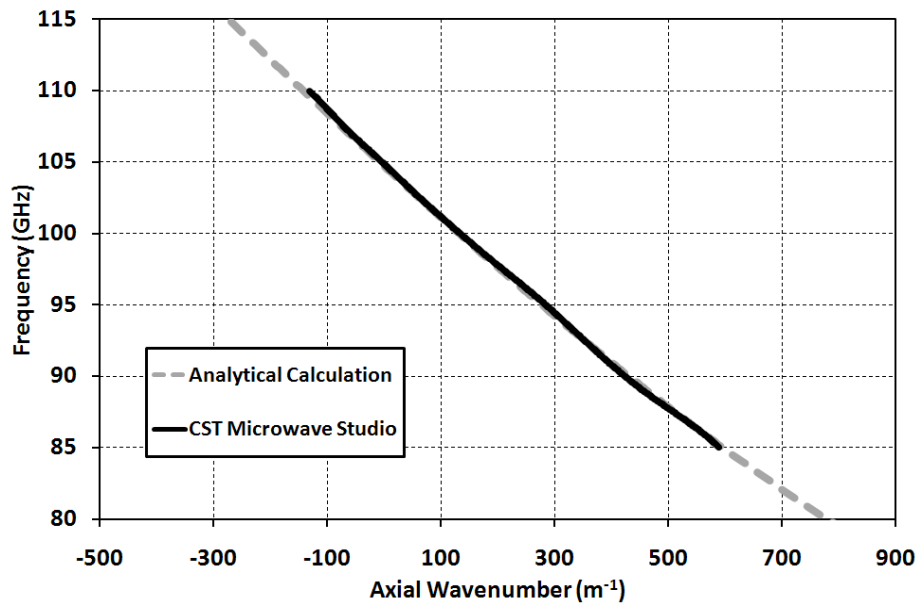
Figure 3.15. Numerically simulated dispersion of the co-rotating waveguide mode of the 4-period helically corrugated waveguide compared against the analytically calculated dispersion.

frequency range requires a sophisticated construction process due to the complex geometry, small dimensions and tight tolerance of the machining. When these waveguides are produced at lower frequencies, for instance at X-band[145,149] there is less sensitivity to manufacturing tolerances than when they are machined at W-band. As the wavelength is ~3mm small imperfections in shape and irregularities on the surface of the waveguide would cause losses or imperfect dispersion characteristics. Previously these waveguides have been manufactured through twisting a waveguide with the characteristic 3-clover shape. This is not an ideal way of producing the desired shape as the wall has to be relatively thin to allow twisting of the body hence reducing the solidness of the waveguide body and there is less control over the corrugation shape and period. Another proposed method of producing this shape is to drill out the helical corrugation in a solid copper cylinder. Due to the cross-sectional shape, the drill dimension is very small compared to the length required to be drilled. Therefore, due to the vibration of the tool bit machining with the required tolerance would be extremely difficult. After careful consideration electroplating the waveguide was chosen as the method of construction. This process involves creating a former, electroplating copper on top of this and then removing the former. Two different methods to make the former were used due to problems that arose during the construction of the longer 34-period helical former.

For proof-of-principle tests a 4-period helical waveguide was constructed. A 3D model of the negative former was produced in Opera-3D, Figure 3.16a. The geometry was cut out of a plastic rod by a computer controlled laser, shown in Figure 3.16b. The large cylinder on the left of the former is used so that this could be held during the electroplating process.

(a)   (b)
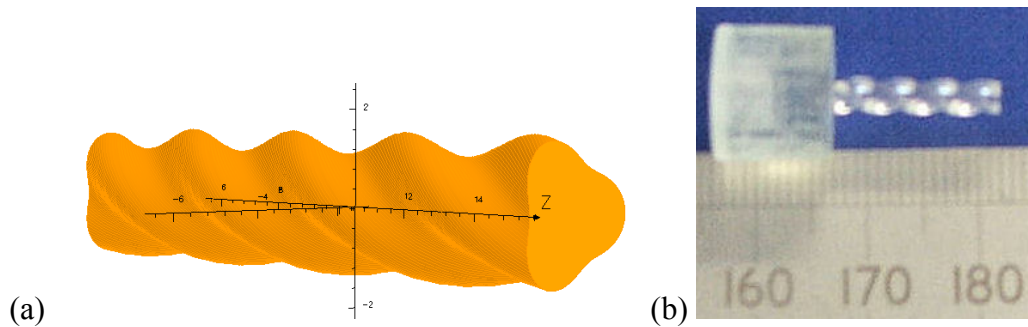
Figure 3.16. Plastic helical waveguide former in two states: (a) computer model and (b) constructed plastic former. The constructed plastic former has a large cylinder attached to it which was required for construction.

The electroplating process requires a conductive surface so the plastic former was plated with gold, about 5 microns thick. The gold also acts to stop oxidisation of the surface of the waveguide. After this the gold-plated body of the former was electroplated with copper of 4mm thickness. The plastic former was then removed through heating in a vacuum oven. The copper waveguide was immersed in a solution, Dichloromethane, to remove any excess plastic. The dispersion of the 4-period helical waveguide was measured by a VNA and the loss was found to be larger than expected and attributed to problems with the construction method. After dispersion measurement the waveguide was cut open with a section of the body removed as shown in Figure 3.17b. An optical microscope was used and it was seen that this process had left the gold layer with holes and cracks with some plastic remaining on the surface. The shape and dispersion characteristics for this method were found to be in good agreement with the calculated and simulated values and an end-on view can be seen in Figure 3.17a with a internal view shown in Figure 3.17b.

From the beam-wave interaction simulation of the helical waveguide showed the gyro-BWO required an interaction length of 34-periods for optimal microwave

output. The total length needed was 34-periods. Two tapered section should be used at each end of the helical waveguide.

| (a) | (b) |
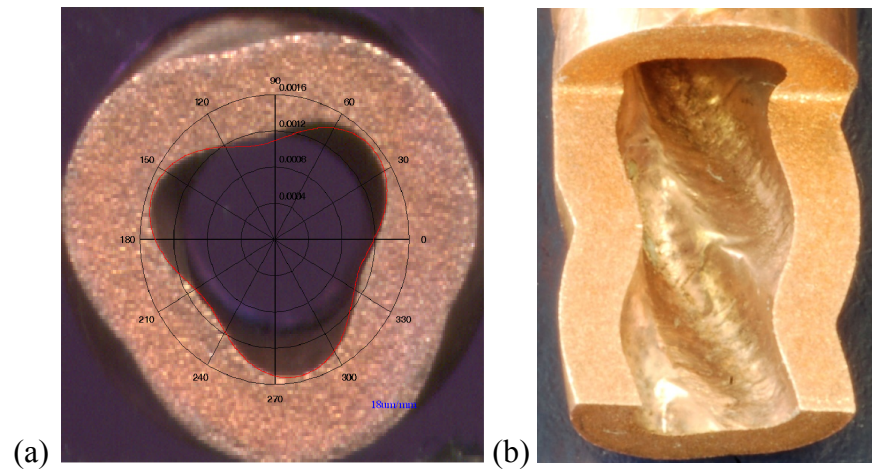
Figure 3.17. Two views of the four period helically corrugated waveguide used in analyzing the constructed geometry for errors. The two views are (a) the face of the helical waveguide shown against the ideal shape (b) surface of the helical waveguide with a section of the body removed.

It was found that the plastic used for the former is not self-supporting over the long length of the former. An aluminium former was machined as this has an increase in strength over the plastic and is conducting so removed the requirement for plating with a conductive material. A former was produced through machining with a 4-axis CNC through first producing a computer model of the 34-period negative former, shown in Figure 3.18a. A photo of the constructed aluminium former is shown in Figure 3.18b. The surface of the aluminium former is highlighted in Figure 3.18c showing no visible defects. To remove the aluminium the waveguide can be soaked in acid and then "Bright dipped", using a mixture of nitric and phosphoric acid at near boiling point, to remove any excess aluminium.

The helically corrugated waveguide after the electroplating can be seen in Figure 3.19 with the ripples of the helical corrugation shown on the outer surface of the former. This picture shows the waveguide before machining to final dimensions. The outer surface of the helical waveguide was machined to a cylinder shape with diameter of 12mm.
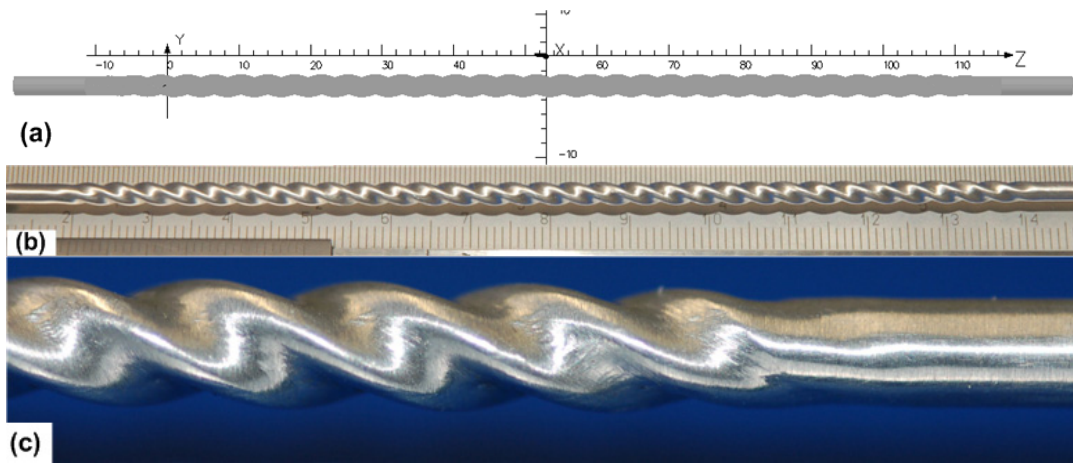
Figure 3.18. Aluminium former for the construction of the helically corrugated waveguide shown views are (a) computational model of the helical former (b) constructed 34-period helical former and (c) enlarged helical former showing the surface finish.

Figure 3.19. Photo of the constructed 34-period helically corrugated waveguide.

3.6 Elliptically deformed waveguide polariser

A waveguide with a helically corrugated inner surface requires a circularly polarised wave rotating in the opposite direction of the helix itself in order for the wave to be perturbed by the corrugation. An elliptical polariser can be used to convert linearly polarised waves into circular polarised waves. In order to perform diagnostics of wave properties in the interaction region using a vector network analyzer the elliptical polariser is required as the VNA outputs linearly polarised waves. Of course the polariser can be used at the output end of the device so that the wave can be converted back to linearly polarised waves.

A linearly polarised wave can be split into two waves in perpendicular directions which travel in the same phase and if a phase shift is introduced between the electric

field components then one can introduce a rotation to the combined component of the waves. The correct phase shift needed to produce circularly polarised waves is $\pi/2$. In a circular waveguide the wavenumber in the x and the y direction is the same $k_x = k_y$ however when the geometry of the waveguide is elliptical $k_x \neq k_y$. So the cut-off frequency of the wave is different in the x and the y direction as the waves pass through the elliptical waveguide thus one wave has larger phase velocity than the other in the polariser.

When discussing elliptical polarisers it is useful to compare this to a circular waveguide as seen in Figure 3.20. When a linearly polarised wave (E_r) travels through each of these waveguide, at 45 degrees, it can be resolved into two components of equal amplitude (e_x and e_y). The two components of the wave experienced the same waveguide with a different size. The elliptical waveguide is shown as two circular waveguides one encompassing the minor axis and one encompassing the major axis. Each of the two components of the wave then act as if they are propagating through one of these circular waveguides. Since the wave has a different cut-off frequency in each circular waveguide, there will be a phase shift between the two waves when propagating through the polariser.
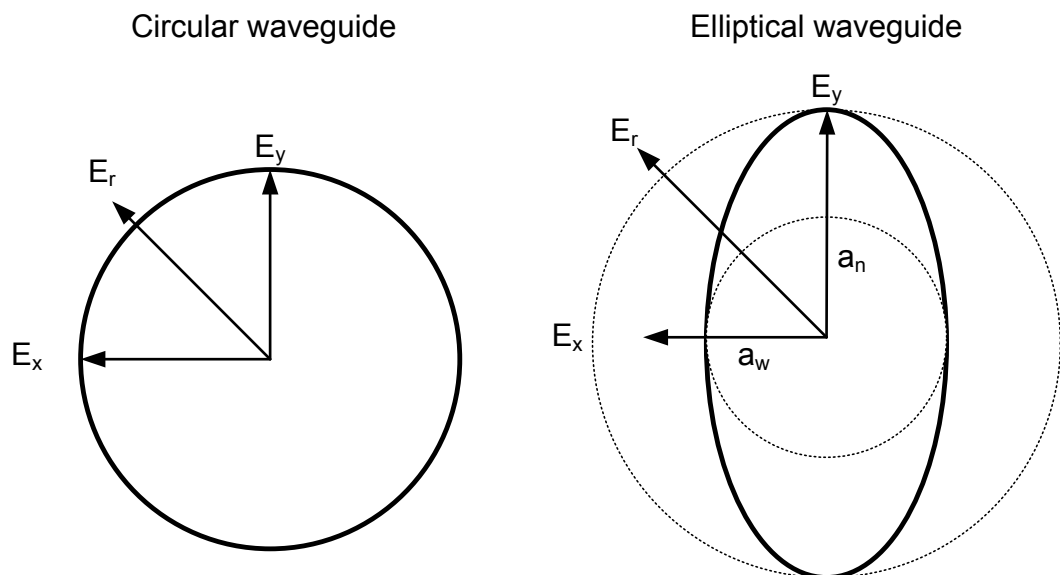
Figure 3.20. Schematic representation of an elliptical polariser using a double circular waveguide model.

The dominant, lowest order, waveguide mode in the elliptical polariser is the TE_{11} mode. The wavelength through a waveguide is

$$\lambda_g = \lambda_0 / \sqrt{1 - (\lambda_0 / \lambda_c)^2} \qquad (3.17)$$

Where the cut-off wavelength is $\lambda_c = 3.412a$ for a TE_{11} mode, a is the radius of the waveguide.

So for the TE_{11} mode this becomes equation (3.18).

$$\lambda_g = \lambda_0 \sqrt{1 - (\lambda_0 / 3.412a)^2} \qquad (3.18)$$

In an elliptical waveguide the wavelength is different for the E_x and E_y. The wave E_1 propagates through the waveguide of radius a_w, wavelength is given in equation (3.19) and the other wave with radius a_n, wavelength is given by equation (3.20).

$$\lambda_{g1} = \lambda_0 \sqrt{1 - (\lambda_0 / 3.412a_w)^2} \qquad (3.19)$$

$$\lambda_{g2} = \lambda_0 \sqrt{1 - (\lambda_0 / 3.412a_n)^2} \qquad (3.20)$$

The phase shift of the waveguide with length L is

$$\psi = 360° L / \lambda_g \qquad (3.21)$$

The phase shift of the wave E_1 is given by equation (3.22) and the E_2 by equation (3.23).

$$\psi_w = 360° L / \lambda_{gx} \qquad (3.22)$$

$$\psi_n = 360° L / \lambda_{gy} \qquad (3.23)$$

Therefore, the phase shift of the ellipse is

$$\psi_e = \psi_w - \psi_n \qquad (3.24)$$

Then substituting equations (3.22) and (3.23) for the phase shift of each axis and equations (3.19) and (3.20) for the wavelengths gives a total equation for the phase shift

$$\psi_e = 360° L \left(\frac{\sqrt{1 - (\lambda_0 / 3.412a_w)^2} - \sqrt{1 - (\lambda_0 / 3.412a_n)^2}}{\lambda_0} \right) \qquad (3.25)$$

3.7 Waveguide measurement

There are two types of network analyzers used to measure the dispersion of a waveguide; a Scalar Network Analyzer (SNA) and a Vector Network Analyzer (VNA). The former measures the magnitude of the electric field and the latter measures both magnitude and phase of the microwave field as it is passed through a device under test (DUT). A SNA takes a microwave signal and passes it through a diode detector which turns this into an output voltage that is proportional to the magnitude of the signal, shown in Figure 3.21.
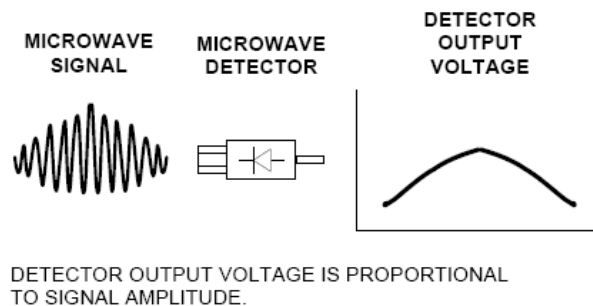
Figure 3.21. Scalar network analyser and its microwave detection.

A VNA provides more information than the SNA and is therefore a more powerful tool. Phase information can be used in diagnostics such as measurement of the dispersion of a device.

3.7.1 Experimental setup

A vector network analyzer (model 37397D) was used to measure microwave properties of the helical waveguide. It has a full measuring frequency band from 65-110GHz. The way in which these frequencies are realized is through two local oscillators which output a 20GHz signal to each test port. On the end of each test port is a frequency multiplying unit which can multiply the signal by up to 5 times. This unit can be exchanged with others to reach higher frequencies, up to 500GHz currently.

A VNA receives a high frequency signal that is then down-converted to a lower

frequency signal by an intermediate frequency (IF) through a process called Harmonic Sampling or Harmonic Mixing. The lower frequency signal is then read by a tuned receiver. This method has the following advantages; greater dynamical range and lower sensitivity to interfering signals.

The phase of the signal is measured against a reference signal, as shown in Figure 3.22, which is split from the original test signal before it enters the device. This way the difference in phase from the original signal can be found and thus the phase difference in the device can be seen. Phase is measured in degrees here where the maximum and minimum limits are +/- 180.
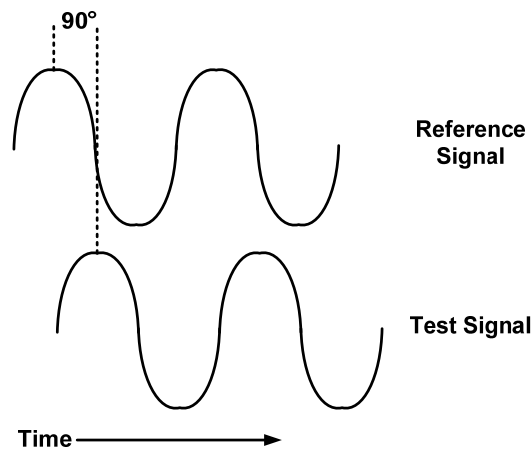
Figure 3.22. Phase measurement used in a Vector Network Analyzer.

Phase is an important property to measure as parameters such as optical path length, wavenumber, dispersion can be obtained by knowing the phase as a function of frequency. To measure the optical path length through a device under test (DUT) equation (3.26) is used.

$$\theta_2 - \theta_1 = k_{z_2} z - k_{z_1} z \qquad \qquad \textbf{(3.26)}$$

Where θ_2 is the phase with DUT, θ_1 is the phase without DUT, k_{z_2} is the axial wavenumber at highest measurement frequency, k_{z_1} is axial wavenumber at lowest measurement frequency and z is the optical path length.

The phase output from a VNA looks like a saw tooth wave as after the wave has

reached +180 it jumps back down to -180. Therefore, to calculate the actual phase this must be interpolated to give a correct phase curve.

The transmission and phase measurements were carried out to determine the performance of the helical waveguide. The reference plane of the VNA's calibration is set at the end of the VNA port so a rectangular waveguide is attached to the port. The VNA output is in a rectangular waveguide so a rectangular to circular waveguide converter was used to convert into the circular waveguide of 1.3mm radius. After this an elliptical polariser was used to convert the linearly polarised microwaves to circularly polarised ones which are perturbed by the helically corrugated waveguide. An elliptical polariser was used afterwards which converted circular polarised waves back to linearly polarised waves.
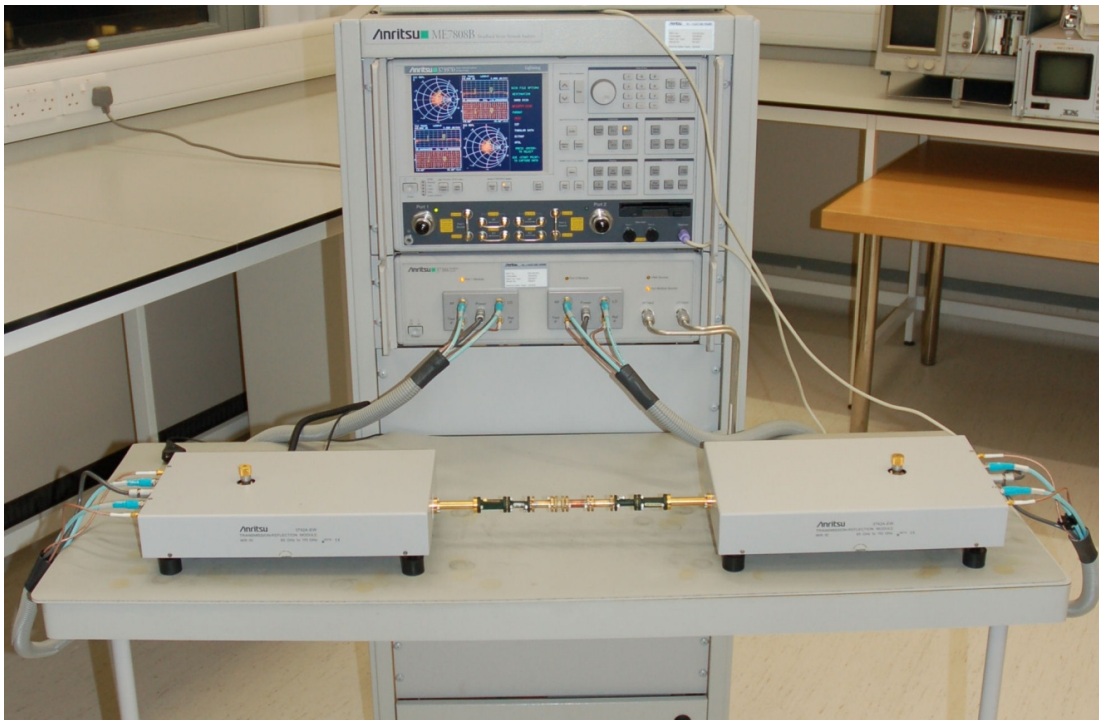
Figure 3.23. Photo of the experimental set-up for measuring the microwave properties of the helically corrugated waveguide. Using Antrisu 37397D VNA.

The full experimental setup can be seen in Figure 3.23 and Figure 3.24.

3.7.2 Measured results of the helical waveguide

The output of the VNA gives many different parameters such as smith charts,
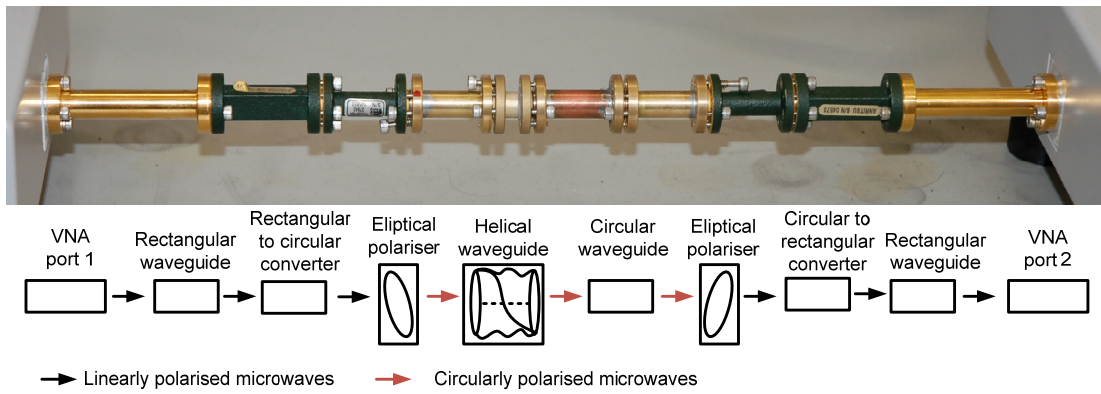
Figure 3.24. Microwave components used in the VNA measurement of the helically corrugated waveguide. Shown is the test setup for the 4-period helical waveguide.

S-parameters, phase, time-domain but it specifically the S-parameter and phase information that are used in this analysis. The S-parameters can be used to find the transmission loss in the helical waveguide and the phase can be used, with computational work, to find the dispersion characteristics. A typical phase output from the VNA can be seen in Figure 3.25 where the phase measurement is given between the -180 and 180 degree scale so in order to find the phase through the device this can be combined to give a straight phase measurement.
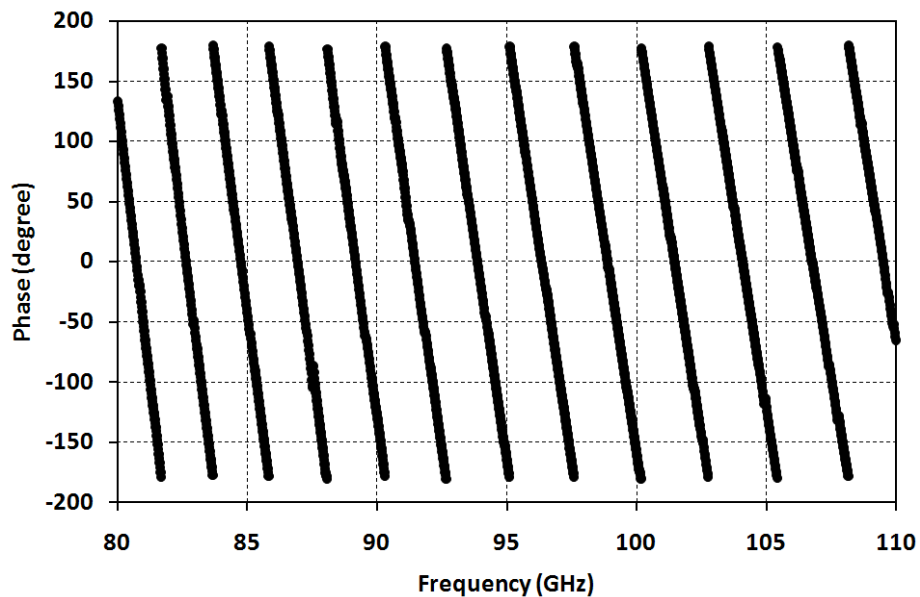
Figure 3.25. Typical vector network analyser output showing phase measurements.

The performance of the elliptical polarisers was measured by the VNA in the following way. If they are aligned in the same direction (the long axis of one ellipse is in the same direction as the other) then the waves should have a $\pi/2$ phase difference, i.e. become a linearly polarised wave again. In principle the $\pi/2$ shift is only true for one frequency therefore it always has a useful bandwidth Therefore, there should be low transmission loss over a set frequency band if both of the polarisers are made perfectly. In Figure 3.26 the frequency range of operation for the elliptical polarisers can be seen to be between ~84GHz - 105GHz this is where the conversion to circularly polarised radiation is most true.
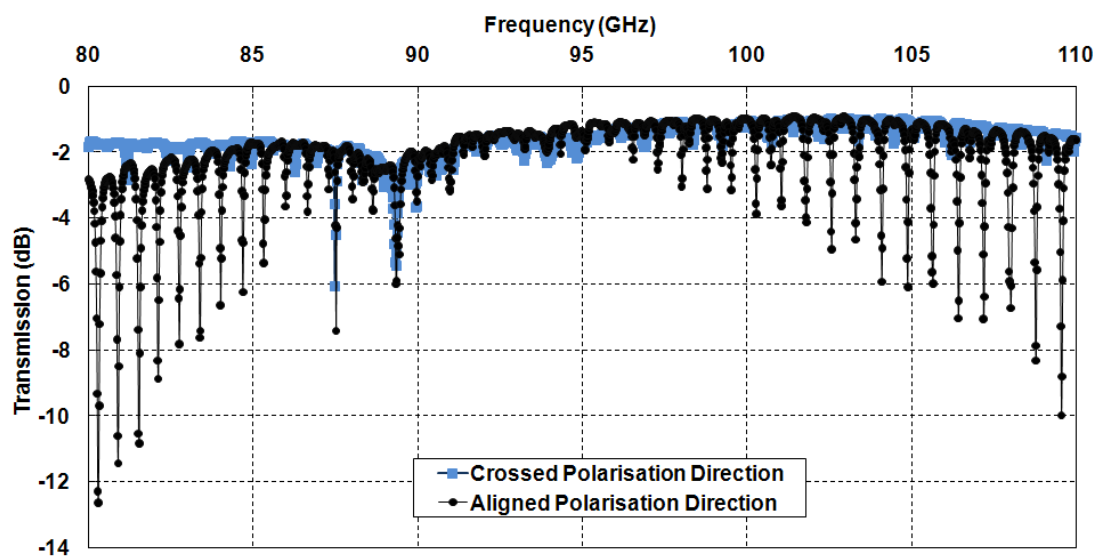
Figure 3.26. Transmission measurement through elliptical polarisers in both crossed and aligned direction.

The dispersion characteristics of the helically corrugated waveguide were measured by finding the phase with and without it present in the system. The difference in axial wavenumber was found through the equation $\Delta k_z = \Delta\phi / L$. The dispersion of its wave was measured and shown in Figure 3.27. By changing the direction of the elliptical polarisers with respect to the direction of the linearly polarised wave while keeping the two polarisers in crossed configuration a co-rotating wave can be generated. This radiation sees a constant radius of waveguide when it passes through the helical waveguide and so will give the same dispersion as a smooth-bore waveguide. The dispersion plot for the co-rotating mode is shown in Figure 3.28.
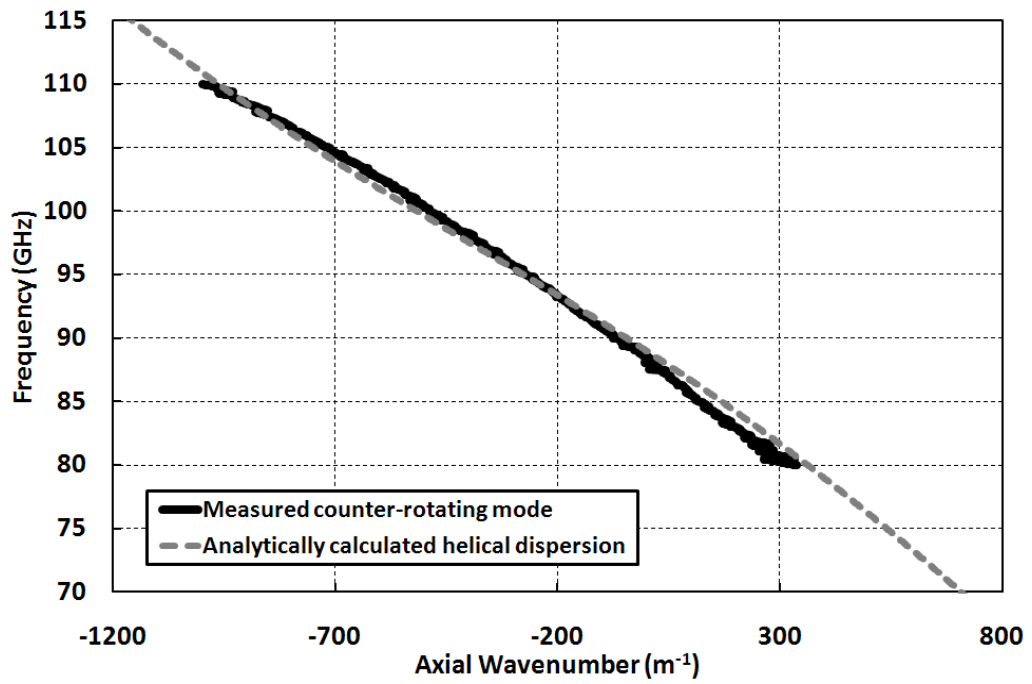
Figure 3.27. Measured dispersion of a counter-rotating wave in the 4-period helically corrugated waveguide with the analytical calculated helical waveguide mode.
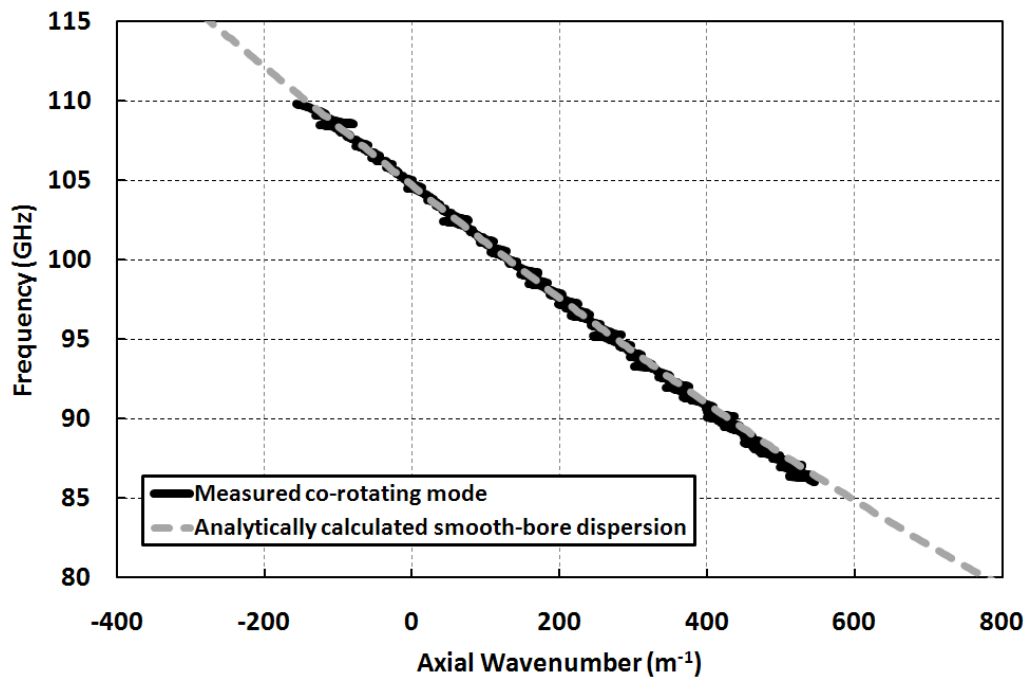
Figure 3.28. Measured dispersion of a co-rotating wave in the 4-period helically corrugated waveguide with the analytical calculated TE_{11} smooth-bore waveguide mode.

The measured helical waveguide transmission loss was found to be ~1dB through the important 84-104GHz range which was also measured and is shown in Figure 3.29.
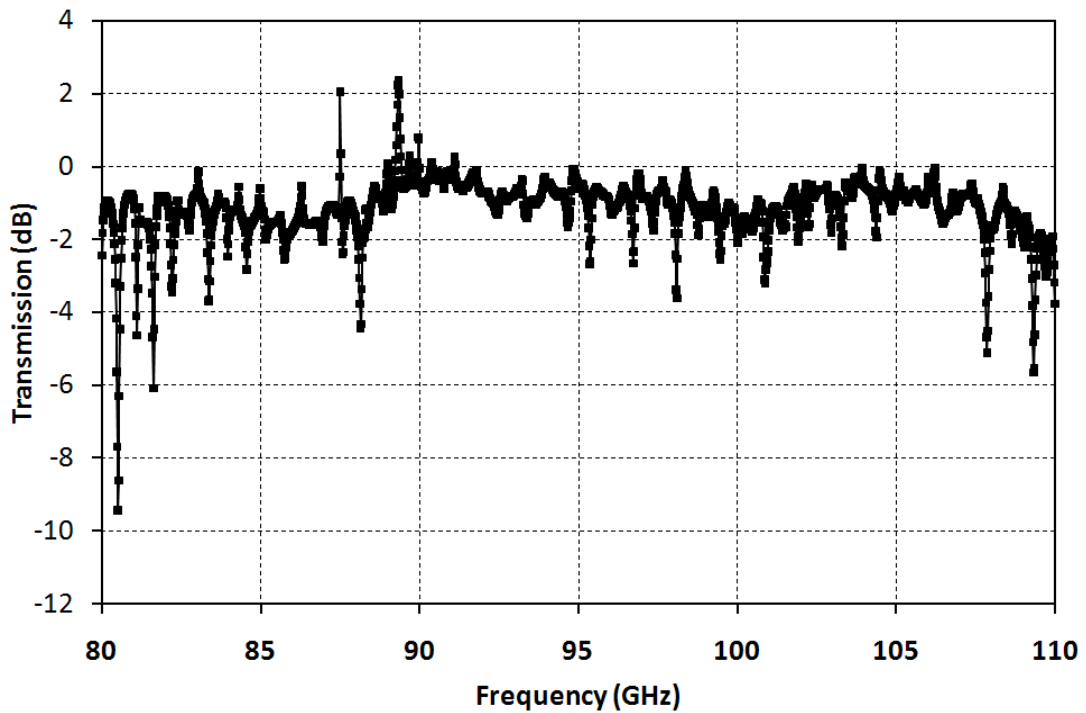
Figure 3.29. Transmission loss through the 4-period helically corrugated waveguide.

Although the measured dispersion of the 4-period helical dispersion was in excellent agreement with calculation, the transmission loss was higher than expected for such a length. However, when the surface of the helical waveguide was examined through an optical microscope there are three obvious problems that can be seen: holes in the gold layer were evident (Figure 3.30a), some plastic droplets were still on the surface (Figure 3.30b) and scratches on the inner surface (Figure 3.30c and d). These were the reason behind the larger than expected transmission loss.

A different manufacturing process was used when the 34-period helical waveguide was manufactured. It was seen that the errors in the plastic former were caused by the gold plating and also material choice. So the material chosen for the 34-period former was changed to aluminium. The transmission loss for the 34-period helical waveguide was much improved over the 4-period helical waveguide and is shown in Figure 3.31. The aluminium former was directly machined by a 4-axis CNC machine and now the loss was found to be ~0.6dB over the frequency range 88-100GHz.
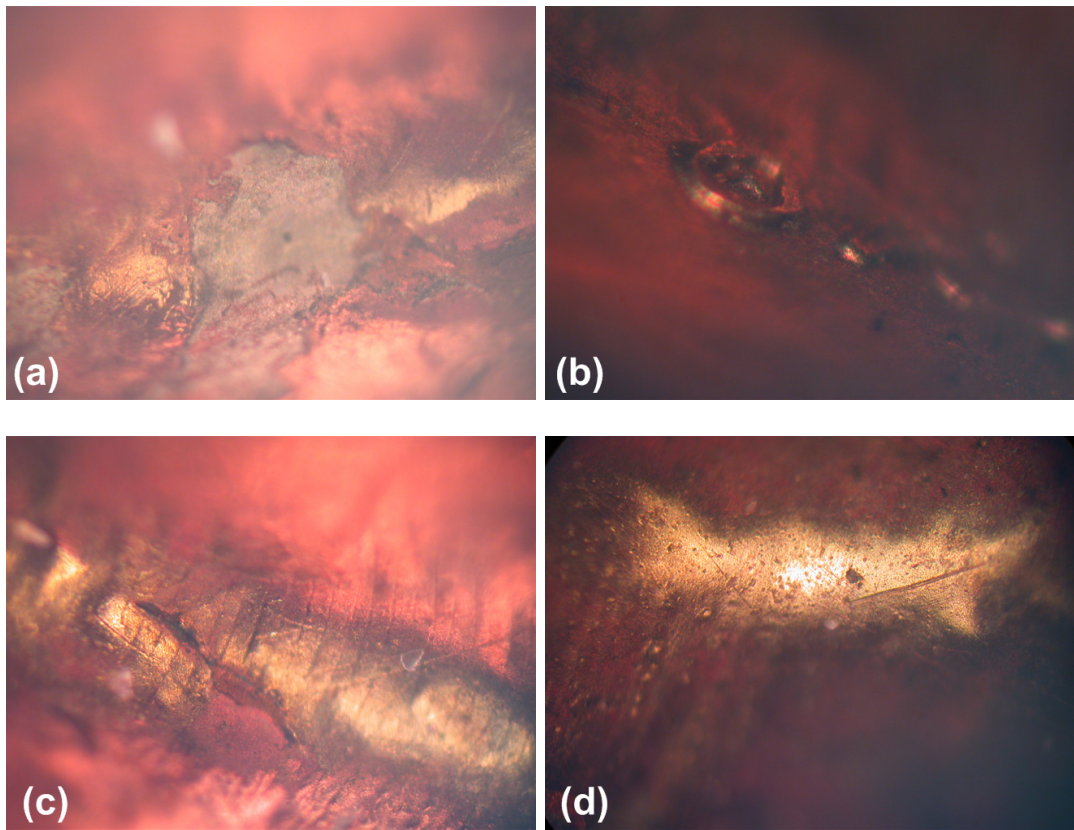
Figure 3.30. Surface of the helically corrugated waveguide showing in (a) holes of the surface (b) plastic droplets, (c) and (d) cracks along the surface.
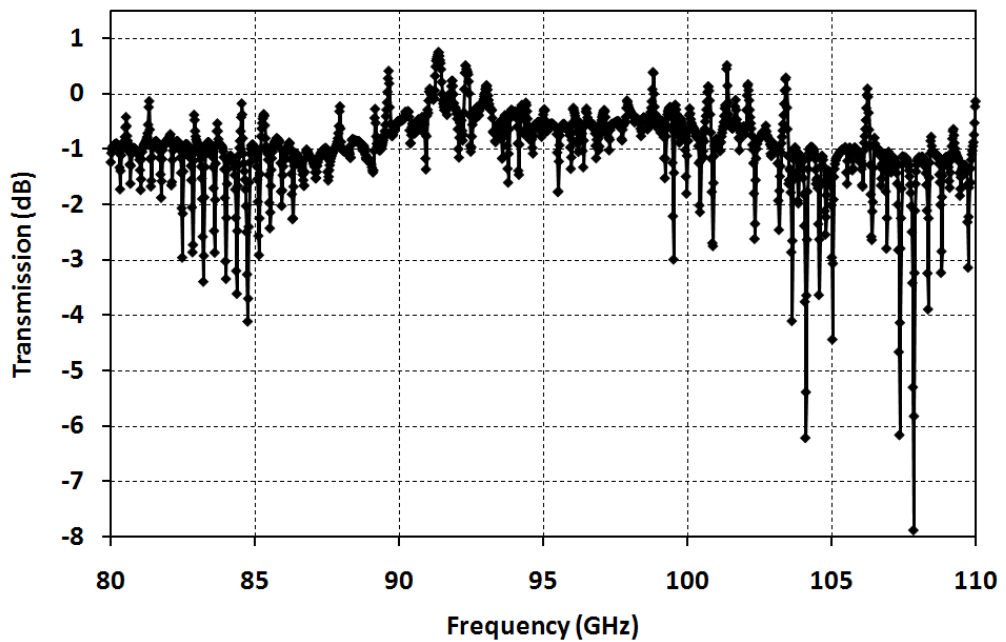
Figure 3.31. Transmission loss through the 34-period helically corrugated waveguide.

The dispersion characteristics for this 34-period helically corrugated waveguide were found through the same method as described previously. The measured dispersion of the helical waveguide is shown in Figure 3.32. For comparison the dispersion calculated using analytical methods is also shown in the same figure. The dispersion of the co-rotating mode of the wave is shown Figure 3.33 and as expected this matches exactly with the smooth-bore analytically calculated dispersion.
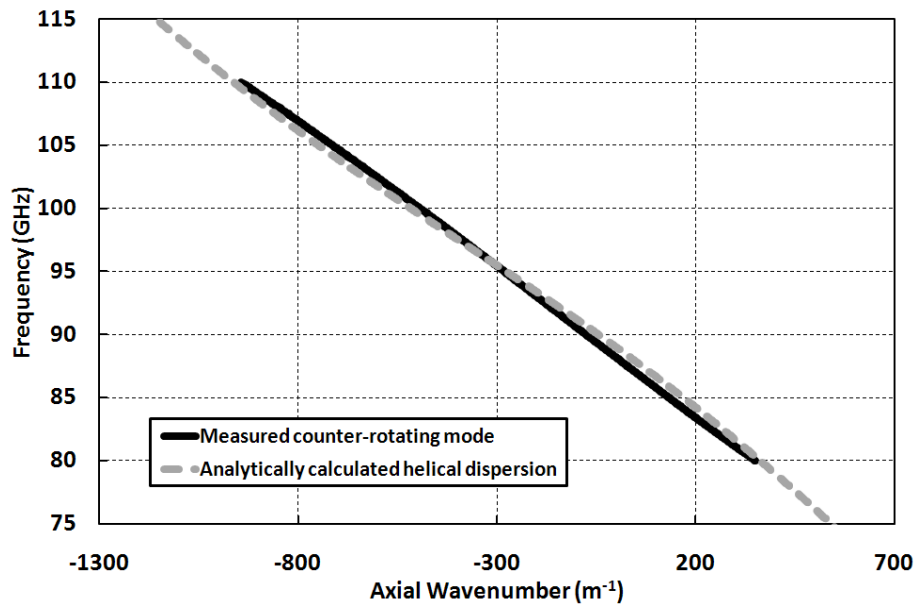
Figure 3.32. Experimentally measured 34-period helical waveguide counter-rotating wave dispersion with the analytical calculated helical waveguide mode.
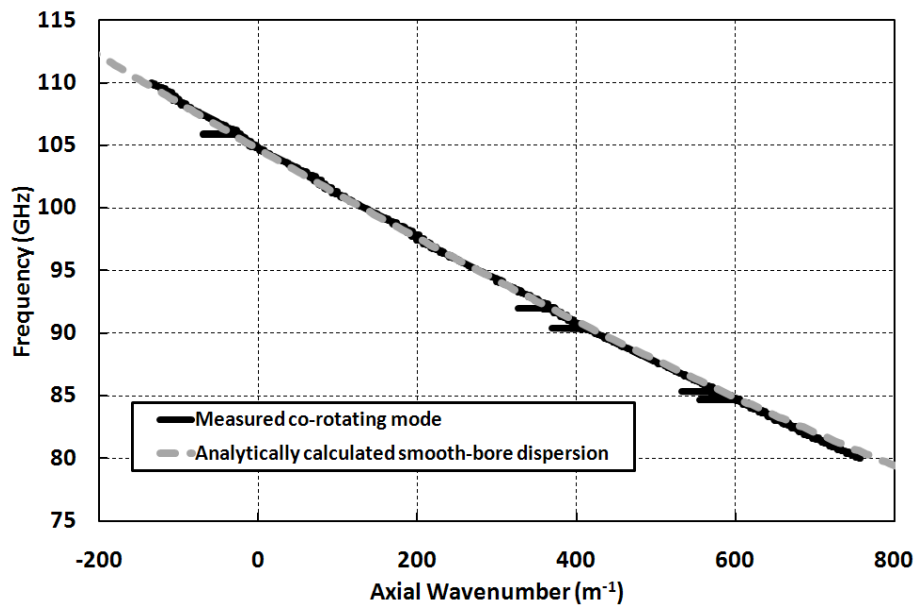
Figure 3.33. Experimentally measured 34-period helical waveguide co-rotating wave dispersion with the analytical calculated TE_{11} smooth-bore waveguide mode.

3.8 Comparison of results

The results obtained give a good indication that the helix is machined quite accurately. It is important to compare all the results obtained to see the difference in the methods employed in analytical calculation, numerical simulation and experimental measurement. Comparison between the results achieved using the MAGIC simulation and CST Microwave Studio simulation, analytical calculation and VNA measurement can be seen in Figure 3.34.
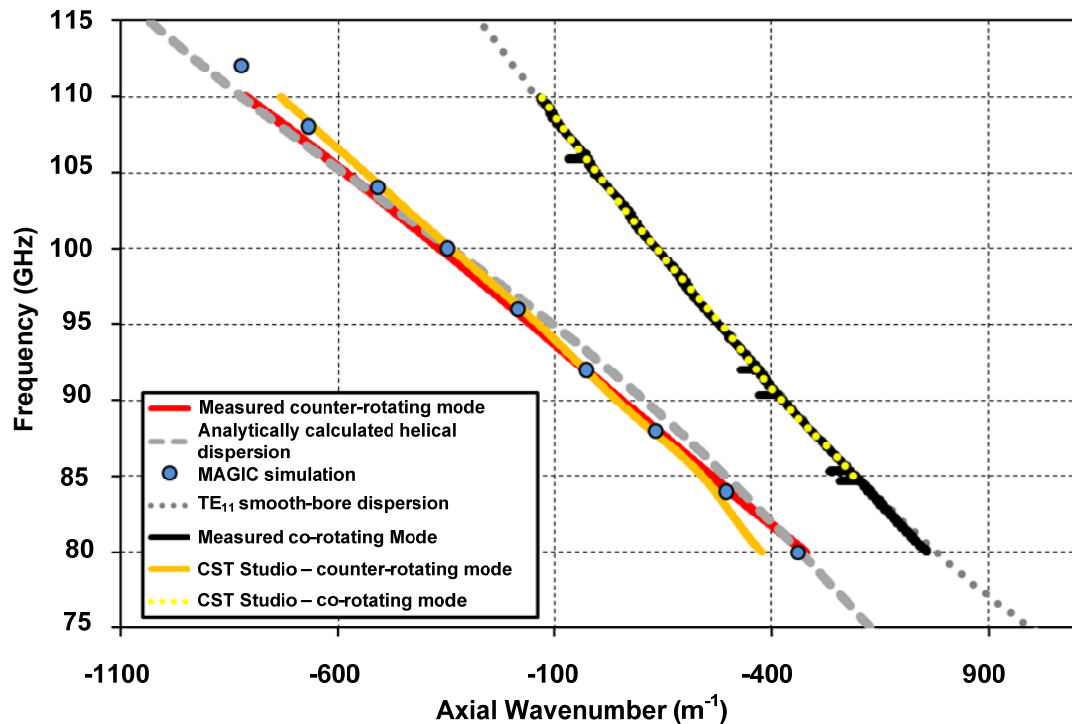
Figure 3.34. Dispersion characteristics measured through various methods including: numerical simulation using both MAGIC and CST Microwave Studio, analytical calculation and experimental measurement.

The results obtained show that the measured dispersion agreed with both analytical calculation and numerical simulation. At lower frequency analytical data had some discrepancies. The reason might be that the elliptical polarisers were not optimised at lower frequencies.

3.9 Discussion

In this chapter the helically corrugated waveguide, used as the interaction region in

the gyro-BWO, was investigated. The parameters of the corrugation were first found through analysis of the dispersion profile. The analytical calculation used some approximations in the dispersion equations so verification of the dispersion profile was performed through numerical modelling the helical waveguide in CST microwave studio. The results of this agreed with analytical theory to a good degree although deviations exist. The helically corrugated waveguide was constructed and the method of construction was optimised with an acceptable waveguide successfully fabricated. The phase evolution through the helical waveguide was measured using a VNA and the converted to give the dispersion profile. The transmission loss of ~0.6dB through the helically corrugated waveguide was a very positive result as the waveguide was relatively long in length. The comparison between the different methods of dispersion measurement showed excellent agreement between the constructed and calculated waveguide dispersions. The methods employed in this chapter allow one to be very confident that the constructed helically corrugated waveguide will perform as expected in the gyro-BWO experiment.

3.10 Summary

In this chapter the topic and theory of waveguides with a helical corrugation of the inner surface was introduced. The theory behind the waveguide dispersion and beam-wave coupling was described. The dispersion profile of this waveguide type was analytically calculated in order to produce coupling in the W-band frequency range. The parameters of waveguide corrugation were chose in order to produce coupling at a centre frequency of 94GHz and it was found that this gave a 15% tuning range. Numerical simulations confirmed the analytical calculated waveguide dispersion and allowed commission of the construction of the waveguide. The constructed waveguide was originally 4-periods which was measured to produce the desired dispersion profile. The final 34-period waveguide measured to produce a dispersion profile that had excellent agreement to theory and simulation with a low transmission loss. The main result of this chapter was to make an interaction region suitable for beam-wave interaction in the gyro-BWO.

Chapter 4.

Generation of Electron Beams

4.1 Introduction

In vacuum electronic devices, there are three important parts that define the performance of the tube i.e. magnetic field, the interaction region and the electron beam. The interaction region provides the waveguide modes that the electron beam can couple to, and its geometry defines a cut-off frequency, which in turn limits what frequency can be produced within it. The magnetic field is used to constrain the motion of the electrons through the interaction region and change how fast they gyrate, thus allowing tunability of the output frequency in gyro-devices. The electron beam transfers kinetic energy to the microwave energy. The many properties of the electron beam define the power, efficiency and frequency of the output. This chapter introduces the properties of the electron beam that define the quality of the beam and discusses the various electron guns that produce these beams, with an emphasis on the novel cusp electron gun employed in the gyro-BWO.

4.2 Electron beam parameters

There are many different parameters of the electron beam that are important in theoretical calculations. This section will explain some of these parameters.

Larmor radius, guiding centre and cyclotron frequency: Charged particles travelling in the presence of a magnetic field will be constrained by the magnetic field which is described by the Lorenz force equation with the electric field component removed.

$$\boldsymbol{F} = q\left(\mathbf{v} \times \boldsymbol{B}\right) \tag{4.1}$$

Where $\mathbf{v}$ is the velocity of the particle and q is the charge of the particle.

The force on the particle is perpendicular to the velocity so the modulus of the velocity is constant and so the mass, m, is constant too.

$$\mathbf{v} = \left|\mathbf{v}\right| = const \tag{4.2}$$

$$m = const \tag{4.3}$$

The constant mass means that equation (4.1) can simplify to equation (3.13) for the motion of the electron. This equation leads to the rotational motion in a magnetic field, called the cyclotron frequency ω_g and is given by equation (3.14).

$$\frac{d\mathbf{v}}{dt} = \frac{q}{m}(\mathbf{v} \times \mathbf{B})$$

(4.4)

$$\omega_g \equiv \frac{q}{m}B = \frac{\eta B}{\gamma}$$

(4.5)

Where η is the electron charge-to-mass ratio.

The circle the electron orbits around is called the *Larmor circle*, the radius of this is the *Larmor radius* given through equation (4.6), the centre of the Larmor orbit is called the *guiding centre*.

$$r_L = \frac{m\mathbf{v}_\perp}{|q|B}$$

(4.6)

Magnetic compression: When a particle is emitted from the cathode surface the radius is generally very much larger than the final radius of the beam and the method used to reduce the radius is through magnetic compression, which usually takes place in a diode with an anode aperture. The anode aperture leads to beam divergence as the anode aperture acts as a divergent lens. The compression method is magnetic compression where the magnetic field constrains the motion of the electron beam. When the magnetic field increases the electron beam will reduce in Larmor radius at the same rate as shown in equation (4.6). This allows for a large amount of beam compression which is described by the radius of the initial emitted electron beam against the radius of the electron beam at the maximum magnetic field. This is called the *magnetic compression ratio.*

4.3 Production of electron beams

Through different methods, electrons are produced by a cathode and through an applied magnetic field they then are turned into a beam, solid or pencil, and by the action of an electron field they accelerate and radiate and are used in many different applications. Of particular interest here is an electron beam which interacts with

electromagnetic modes that exist within waveguides. Various properties are useful for these beams such as: high-power, high-brightness and high-current density. The method for producing electron beams with one or more of these properties are through the different cathode types and emission regimes.

4.3.1 Electron emission regimes

In order to produce an electron beam, the electrons on the cathode surface must gain enough energy to escape the potential barrier of the surface. This barrier is dependant on the work function, ϕ_w, of the material. To produce a beam, a large amount of electrons must escape the cathode surface. Various methods of emission include space-charge limited, temperature limited and field dominated. The difference between these regimes is what governs the resulting beam, for instance in the temperature limited regime the current is determined by the heat applied to the cathode surface, in the space-charge limited regime this is where the space-charge of the electron beam can stop the flow of current and so determines the output current.

Electron emission in the space-charge limited regime is commonplace in microwave tubes. When a voltage is applied to a cathode surface, and the anode is grounded, the potential difference between the two creates an electric field. When electrons are emitted with a large current, they can form a negatively charged cloud in front of the cathode, as there is not enough accelerating potential to remove the current quickly enough. This depresses the potential at the cathode, when compared to an electron-beam free condition. When the emitted current to applied voltage ratio is large enough, the potential will reduce to zero or negative where the electrons would cease to be emitted or reflect back to the cathode respectively. The current of this emission is described by the Child-Langmuir equation $I = PV^{\frac{3}{2}}$ where V is the potential difference between cathode and anode and P is the perveance of the diode. The perveance is a factor used to describe how much space charge affects the electron beam.

4.3.2 Thermionic cathode

Electrons can escape the surface of the cathode at temperatures above absolute zero, since the kinetic energy of particles is temperature dependant. As the ambient temperature increases, the electrons kinetic energy increases and can be higher than the potential barrier of the surface. This type of emission is called thermionic emission, called such from the term thermal. To produce this emission, a heating coil is wrapped around the emission material which delivers the required thermal energy. The current density produced through this method is described by the Schottky equation.

$$J = A_T T^2 \exp\left(\frac{139 E_T^{0.5} - 11600 \phi_w}{T}\right) \tag{4.7}$$

Where A_T is a characteristic constant of the material, T is the cathode temperature in degrees Kelvin and E_T is the electric field normal to the surface in kilovolts per centimetre.

High currents can be produced through a low work function of the emission material with a high cathode temperature. Cathode materials can have an artificially lowered work function through doping the cathode with a different material - for instance using a tungsten cathode doped with barium. However, care must be taken to reduce the contact between this cathode and another material as the barium can migrate away from it. Also, high current densities reduce the lifetime of the cathode.

4.3.3 Photo cathode

It was realised in the early 1900's that when photons are incident on a surface, they can transfer enough energy to the electrons to eject them from this surface. Firstly described by Einstein in 1903, then more comprehensively by Spicer in 1958, this effect is used in photomultipliers. The frequency of the photon required to release the electron can be described by equation (4.8). This shows that to assist this process the work function of the cathode material should be low and frequency of the incident photons, ν, should be high.

$$hv = \phi_w + E_{k_{\max}} \tag{4.8}$$

Where h is Plank's constant and $E_{k_{\max}}$ is the kinetic energy of the ejected electrons.

The cathode is negatively charged and coated with a photo-sensitive material, typically an alkali metal with very low work function. The current produced is described by equation (4.9).

$$i(hv) = I_0(hv)[1 - R(hv)] \frac{\alpha_{PE}(hv)}{\alpha_c(hv)v + \dfrac{1}{L(hv)}} P_E(hv) \tag{4.9}$$

Where $I_0(hv)$ is the incident energy of light of photon energy hv, $R(hv)$ is the light reflectivity from the surface of the solid and $\alpha_c(hv)$ is the absorption coefficient of the solid, $\alpha_{PE}(hv)$ represents the part of the absorption where electrons are excited above the vacuum and have a possibility to escape, $P_E(hv)$ is the probability of escape of electrons reaching the surface with sufficient energy to escape and $L(hv)$ is the escape or scattering length of the electron.

4.3.4 Pseudospark based electron beam source

Many applications require a high brightness, high current density electron beam source and one such solution is utilization of a Pseudospark discharge. The Pseudospark is an axially symmetric self-sustained intense current gas discharge. This discharge has a high current density 10^4A/cm^2 at a di/dt of 10^{12}A/s over 20ns. The name occurs from the comparable properties of the hollow cathode discharge to a high pressure spark. A hollow cathode discharge can be observed under a low pressure of 50-500mTorr and in a special cathode geometry that has a hollow structure such as a cylindrical or slit shaped hole. When operating at a certain pressure then there can be a negative glow inside the hollow structure (slit or hole) of the cathode. A hollow cathode discharge occurs from the hollow-cathode effect. The current of this glow is found to be orders of magnitude larger than a similar plane cathode. The geometry consists of two or more plane-parallel electrodes with a circular central hole. During the hollow cathode discharge many electrons are

accelerated by the applied high voltage and the high electric field across the electrode gap. A high brightness, high current density electron beam can be extracted from this discharge with application of an applied voltage. This can produce a low energy very high intensity electron beam source useful for pulsed power application[150]. There is no requirement of an external applied guide magnetic field.

This source has been operated at the University of Strathclyde previously by H. Yin et al.[151,152]. Recently[153] this source was used for millimetre wave generation using a three-gap Pseudospark beam able to produce an electron beam of up to 680 A with a brightness as high as 10^{12}Am^{-2}rad^{-2}. No guide magnetic field was used and a beam transport of 10% was observed. These tests provided the highest simultaneous electron beam current density (10kAcm^{-2}) and brightness (10^{11}-10^{12}Am^{-2}rad^{-2}) compared to all other sources. The operation of this source at W-band frequencies has produced microwaves. Further experiments are planned operating in the sub-millimetre range up to 200GHz and 390GHz using a reflex klystron and BWO respectively.

4.4 Electron guns

There are many different ways of generating electron beams. Some electron guns create a solid electron beam, while others create a pencil beam whose trajectory can be kicked into a helical path. These electron guns have been extensively studied so only an outline of operation is described here. A new electron gun is also introduced in this chapter, the novel cusp electron gun, which is the main topic of interest in this thesis. The electron gun aims to solve a problem of how to selectively interact with harmonic waveguide modes.

4.4.1 Magnetron Injection Gun

The Magnetron Injection Gun (more commonly denoted as the MIG) is most commonly used in gyrotrons and produces an annular electron beam where the electrons have small cyclotron orbits. The electrons are produced from an annular emitting ring, which is heated to obtain emission. The axially symmetric magnetic
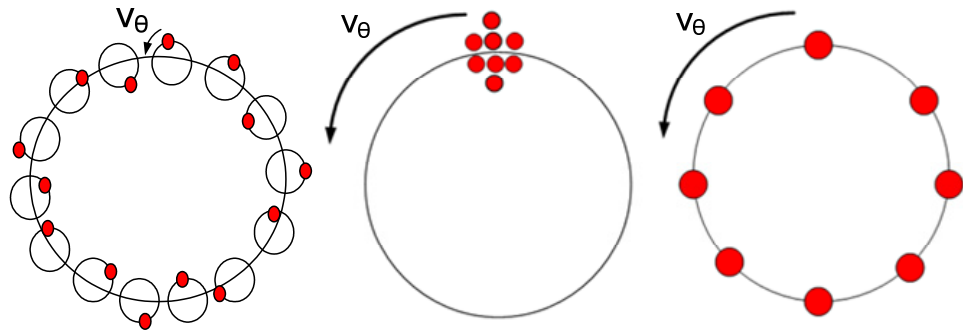
Figure 4.1. Schematic diagram of the electron beams produced from (a) Magnetron Injection Gun (b) Pierce gun with kicker and (c) cusp electron gun.

field focuses the electron beam into the interaction region. A schematic diagram of the electron beam generated through a MIG can be seen in Figure 4.1a. This electron gun is operated in the temperature limited regime to reduce the velocity spread on the beam. The output electron beam can be seen in Figure 4.1a. A typical configuration of a MIG gun can be seen in Figure 4.2.
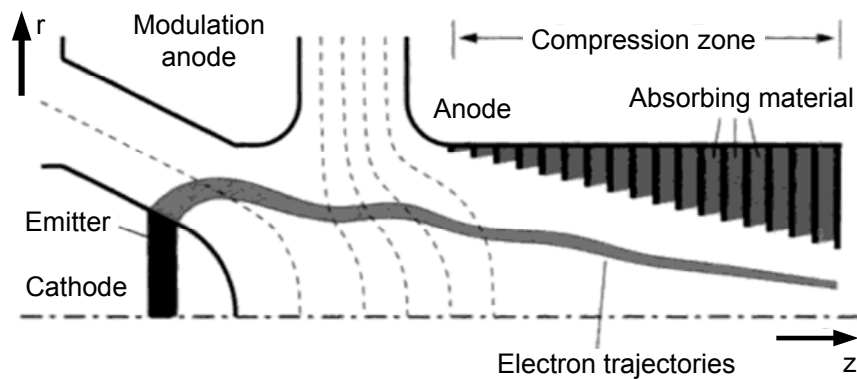
Figure 4.2. Schematic diagram of a Magnetron Injection Gun in a typical gyrotron type microwave source.

4.4.2 Pierce gun

The electron gun used in almost all linear-beam (O-type) devices is called the Pierce Gun named after J.R. Pierce. A circular thermionic emitting surface is used, in conjunction with focusing electrons, known as Pierce electrodes and designed through a method set out by J.R. Pierce[154]. The electrodes are used to shape the equi-potentials that are distorted by the presence of the electron beam for focusing the

beam. Without the beam present, these equi-potentials would be straight and equally spaced. When the electron beam is emitted, the electrons repel each other and cause the beam to diverge outwards changing the equi-potentials. If the electrodes are shaped such that the equi-potentials stayed straight with the beam present, then the beam would no longer diverge and a high quality beam could be obtained. The electrodes can be rotated towards the anode which straightens the equi-potentials when there is a beam. The angle between the electrode and the beam edge can be adjusted. When that angle reaches 67.5 degrees, this straightens the equi-potentials for a space-charge limited beam. Electrodes operated at this angle are called Pierce electrodes.

4.4.3 Cusp electron gun

While the previous electron guns described are the most common type used in microwave sources, these are not the ideal choice for a CW gyro-device operating at harmonics. In order to couple to harmonic waveguide modes, conventional electron guns cannot be used, as they produce beams that couple strongly to other waveguide modes, discussed further in Section 4.9. In order to produce the desired coupling, an axis-encircling electron beam must be used. A Pierce gun can produce an axis-encircling electron beam when a magnetic kicker is used. While the kicker usually operates in pulsed mode operation using this gun for continuous wave is hard to do due to the difficulty in producing the CW kicker magnet. A novel cusp electron gun can be used to create an annular axis-encircling electron beam, shown in Figure 4.1c. An axis-encircling beam is ideal for harmonic operating, as the mode-selectivity nature of such a beam requires that the harmonic number is equal to the azimuthal index of a waveguide mode for effective beam-wave coupling[155], leading to a reduced possibility of parasitic oscillations. Furthermore, due to the high power of the spent electron beam, an annular-shaped electron beam is desirable for: beam energy recovery using a depressed collector and reducing the energy density on an electron dump. The different types of microwave sources require different electron beams to drive the beam-wave interaction. Some of these include: a Magnetron Injection Gun or Pierce gun. However, sources have recently been invented to produce very high frequencies in the W-band and THz region, due to the many

desirable applications in this field. To operate at these high frequencies, many devices find it advantageous to operate at harmonics and conventional electron guns cannot effectively drive this interaction as they can couple to parasitic lower order modes. This electron gun uses a non-adiabatic magnetic field reversal to create an axis-encircling annular electron beam. This beam will have good mode selectivity, be ideal for energy recovery and continuous wave operation. Also, due to the relative simplicity of design it would be ideal to use at W-band (75-110GHz) frequencies, where the dimensions are of millimetre scale.

Initially, transport of an electron beam through opposing magnetic fields (so called 'magnetic cusp') was investigated in the 1960's[156,157] for plasma heating applications. Schmidt described a threshold for magnetic mirroring and the effects on the electrons after they have passed the cusp region, namely azimuthal rotation around the central axis of symmetry, due to conservation of the electrons canonical momentum. Ever since then, continuous efforts and progress have been made through both theoretical analysis and experimental study in the generation of the cusp-based electron beam sources[158,159]. Despite these theoretical and experimental studies over the decades, it was not until 1983 that a cusp electron gun was first used in microwave sources, specifically in a magnetron[160]. Recently, gyro-devices have begun to adopt cusp guns as their electron beam sources notably in lower frequency harmonic gyro-devices[161].

4.5 Electron beam dump

In microwave sources there is never perfect conversion of the electron kinetic energy to the growing wave. As a result, this can leave a significant amount of kinetic energy within the spent electron beam after the beam-wave interaction. The problem arises of how to effectively dispose of this spent beam. The choice is either an electron beam dump before the window or a depressed collector. The former simply captures the spent beam directly, while the latter extracts the energy from the beam, in order to increase the overall efficiency of the source. This requires two things: first the trajectories of the electrons must be managed, so that they do not interfere with the maximum extraction of R.F. energy; and secondly the beam can not impact the

walls of the collector with a very large current density, otherwise, the collector may not be able to adequately remove the heat. In such a case, the surface can vaporise, which will contaminate the vacuum. Another issue is that the spent electrons create X-rays through Bremsstrahlung, so safety becomes a concern. Lastly, there is a possibility of creating secondary electrons that can travel back through the beam tube, potentially damaging the cathode or anode.

4.6 Energy recovery

Microwave sources at the higher end of the frequency scale suffer from poor interaction efficiency. However, through a sophisticated design of the collector, energy can be recovered from the electron beam, increasing the overall efficiency of the source.

The effect of this can be quite dramatic and a study found[162] that for a gyro-BWO using a helically corrugated waveguide interaction region the efficiency can improve from ~15% to ~42% with a depressed collector energy recovery system.

4.7 Space-charge forces

In order to understand and predict the trajectories of electron beams the effect of electric and magnetic fields on the electrons must be known. When two of more electrons are in close proximity they exert a force on each other. An electron beam is a situation where a very large number of electrons are transported along a path and each electron will have a complex force exerted on it from the adjacent electrons. One of the main points to note is that the focusing force of the applied magnetic field can almost cancel the repulsive electric force. This allows electron beam transportation even relativistic beams at high currents. Another point to note is that it is through the field of the beam that there is a limitation on the current one can transport along a beam tube, known as the space-charge limit. This occurs from the axial electric field of a beam and can stop propagation of a high-current beam as the space-charge decelerates the electron beam when it becomes comparable to the kinetic energy of the beam.

This discussion considers an ideal cylindrical beam with azimuthal symmetry and an infinite extend in the direction of propagation. The beam has a uniform density n_0 which drops to zero at r_0, the edge of the beam. The beam-generated field varies linearly with radius due to the uniform density in the beam. The radial magnetic force is $-qv_z B_\theta$ and has a magnitude equal to β^2 times the electrical forces at all radii, where $\beta = v/c$ is the ratio of particle velocity to c. The radial electric field can be derived[163] to be equation (4.10) while the magnetic field is can be derived to be given in equation (4.11) which come from .

$$E_r = \frac{qn_0}{2\varepsilon_0} r \tag{4.10}$$

$$B_\theta = \left(\frac{\mu_0 qn_0 v_z}{2} \right) r \tag{4.11}$$

However, a more realistic condition is with a variable density through the beam. The following set of equations described the various forces for an electron beam with a varying density in the radial direction, $n(r)$. The electric field is described from equation (4.12), the magnetic field in y direction from equation (4.13), the magnetic field in θ direction is from equation (4.14) and the radial magnetic field force is from (4.15).

$$E_x(x) = \frac{q}{2\pi\varepsilon_0 r} \int_0^r 2\pi r' dr' n(r') \tag{4.12}$$

$$B_y(x) = \frac{qv_z\mu_0}{2\pi r} \int_0^r 2\pi r' dr' n(r') \tag{4.13}$$

$$B_\theta = \left(\frac{\beta}{c} \right) E_r \tag{4.14}$$

$$F_r(magnetic) = -\beta^2 F_r(electric) \tag{4.15}$$

4.8 Electron beam transport through a cusped magnetic field

In this section, two models are described. The first is the ideal cusp model, which explains an ideal magnetic field transition - one that switches from one direction to the other in a step function. However, this is not the most accurate representation of a

magnetic cusp as this cannot be achieved in experiment. This falls to the non-ideal cusp model, which described the magnetic reversal as a smoother transition.

Some assumptions need to be taken into account before the theory can be explained:

- The cathode is circular, and is centred on an axis of symmetry.
- The emitted electron beam is hollow and accelerated in the cathode-anode region.

4.8.1 Particle motion in cusped geometries

The derivation of these equations is performed in cylindrical coordinate system (r,θ,z) and the magnetic field is assumed to have no azimuthal component, i.e. $B_\theta = 0$. This field can be formed from the vector potential, $A(0, A_\theta, 0)$. The motion of a particle moving through this field is described by the Hamiltonian, H, of a particle moving in the $r-z$ plane given in equation (4.16). The field is also axially symmetric, so, $\partial V_\theta / \partial \theta = \partial V / \partial \theta = 0$.

$$H = \frac{P_r^2}{2m} + \frac{P_z^2}{2m} + \frac{1}{2m}\left(\frac{P_\theta - qrA_\theta}{r}\right)^2 + qV \qquad \textbf{(4.16)}$$

Where V is the scalar potential, P_r, P_z and P_θ are canonical momentum in the r, z and θ directions, respectively.

The Hamiltonian can be re-written due to axial symmetry, $\partial A_\theta / \partial \theta = \partial V / \partial \theta = 0$, in terms of the effective potential $\psi(r,z,t)$.

$$H = \frac{P_r^2}{2m} + \frac{P_z^2}{2m} + \psi \qquad \textbf{(4.17)}$$

Where

$$\psi = \frac{1}{2m}\left(\frac{P_\theta - qrA_\theta}{r}\right)^2 + qV \qquad \textbf{(4.18)}$$

In a static field, with no scalar potential, V, at any z the effective potential, ψ, is only a function of r (as the field does not change with time). Also, as $r \to 0$ and $\psi \to \infty$ for a non-singular field distribution. Only "trapped" or "confined" particles

are considered here, as these will rotate around the potential well, whereas the particles that escape this potential well are not considered. In order for these particles to become trapped, there must be a minimum of the effective potential for there to be a potential well. Therefore, the derivative of the potential $\psi(r)$ must be zero so that there is a turning point.

$$\frac{d\psi}{dr} = -\left(\frac{P_\theta - qrA_\theta}{mr}\right)\left(\frac{P_\theta}{r^2} - q\frac{\partial A_\theta}{\partial r}\right) = 0 \tag{4.19}$$

There are two conditions that can satisfy equation (4.19), which are shown in equation (4.20) and (4.21).

$$\frac{(P_\theta - qrA_\theta)}{r} = 0 \tag{4.20}$$

$$\frac{P_\theta}{r^2} + q\left(\frac{\partial A_\theta}{\partial r}\right) = 0 \tag{4.21}$$

The angular momentum is described through equation (4.22). When comparing the momentum to the conditions above, it can be seen particles that meet equation (4.20) are not axis-encircling as, $v_\theta = 0$.

$$P_\theta - qrA_\theta = mv_\theta r \tag{4.22}$$

Particles must meet this condition before and after the cusp. Through the cusp region the magnetic field flux, given in equation (4.23), changes amplitude.

$$\Phi(z,R) = 2\pi RA_\theta(z,R) = \text{const} \tag{4.23}$$

Where Φ is magnetic flux and R is the radius of the circle of motion, shown in Figure 4.3.

It is shown from these equations that a particle travelling off-axis in one region can then encircle the axis in another region. The value of A_θ is related to magnetic flux through equation (4.23) and so when passing through the magnetic field reversal condition (4.22) is no longer satisfied. When the magnetic field changes polarity (or direction) then $A(r) = -A_0(r)$ and $B(r) = -B_0(r)$, where the suffix 0 represents the uniform magnetic field region at $z \to -\infty$. The off-axis particle that meets equation (4.20), with a velocity described in equation (4.22), must have $v_\theta = 0$. When passing through the cusped magnetic field the potential, A_θ, will change sign. As there is a

conservation of canonical angular momentum, when the particle passes through this region equation (4.22) must always be satisfied. The only way this can be met is that m, q, r or v_θ must change sign; however, since m, q and r must be always positive quantities, only the latter parameter, v_θ, must change from zero to some value requiring electron motion around the axis of symmetry. This shows why passing through the cusped magnetic field region gives the particles rotational velocity. It should be noted that canonical angular momentum is given as equation (4.24).

$$P_{canonical} = P + qA \qquad\qquad \textbf{(4.24)}$$

The difference between the off-axis and the axis-encircling electron beam can be seen in Figure 4.3 (a) and (b) respectively taken from Ref. 156.
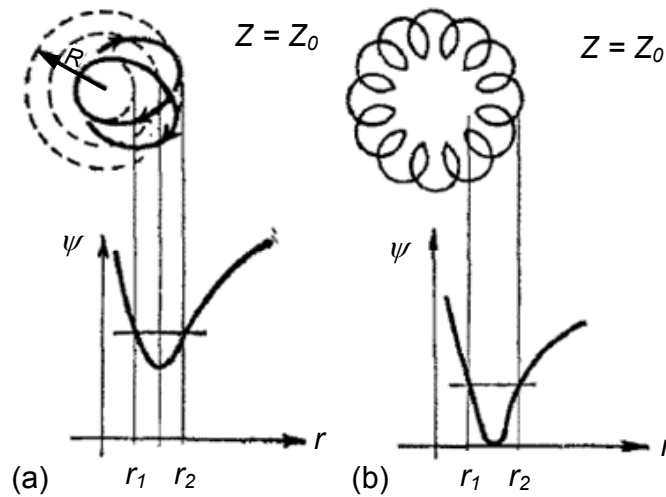
Figure 4.3. Motion of particles in both the (a) "off-axis" particles and (b) "axis-encircling" particles cases.

The smallest radius the particle can approach the cusp region at is r_0 and is found through equation (4.25).

$$E = \frac{1}{2m}\left(\frac{P_\theta^2}{r_0^2} \right) \qquad\qquad \textbf{(4.25)}$$

At the uniform field region at $z \to -\infty$, with a particle injected at a radius of r_{inj}, the particle will move axially, with a canonical momentum P_θ given by equation (4.26).

$$P_\theta = q\rho A_0 = \frac{1}{2}q\rho^2 B_0 \qquad (4.26)$$

The particle velocity in this region is $v = const$, and so, r_0 is then obtained from (4.25) and (4.26) with substituting $E = (1/2)mv^2$ to give

$$r_0 = \frac{1}{2}\left(\frac{qr_{inj}^2 B_0}{mv}\right) = \frac{1}{2}\left(\frac{\rho}{r_{cy}}\right)r_{inj} \qquad (4.27)$$

Where r_{cy} is the cyclotron radius.

The energy of particles encircling the axis cannot be less than equation (4.28) where (4.21) is satisfied at $r = R$.

$$\psi_{min} = \frac{1}{2m}\left[\frac{P_\theta}{R} - qA_\theta(z,R)\right]^2 \qquad (4.28)$$

The axial magnetic field is

$$B_z = \frac{A_\theta}{r} + \frac{\partial A_\theta}{\partial r} \qquad (4.29)$$

So by combining equations (4.21), (4.28) and (4.29), the minimum energy of the particles can be shown to be

$$\psi_{min} = \frac{q^2 R^2 B_z^2}{2m} \qquad (4.30)$$

The maximum distance the electrons can travel before being either reflected back (due to a magnetic mirror effect) or trapped (gain azimuthal rotation as stated before) is z_t - the maximum distance for any electron for the constants of motion. This is found from equation (4.28).

$$mv = \frac{P_\theta}{R} - qA(z_t, R) \qquad (4.31)$$

Where $R(z)$ is found from equation (4.21) for a given $A(r,z)$.

The minimum velocity of a particle injected into a magnetic field, B_0 is given by equation (4.32), which is obtained from equation (4.31).

$$v_{crit} = \frac{qr_{inj}^2 B_0}{2r_{inj}m} + q\frac{r_{inj}}{2m}B_0 = \frac{qr_{inj}B_0}{m} \qquad (4.32)$$
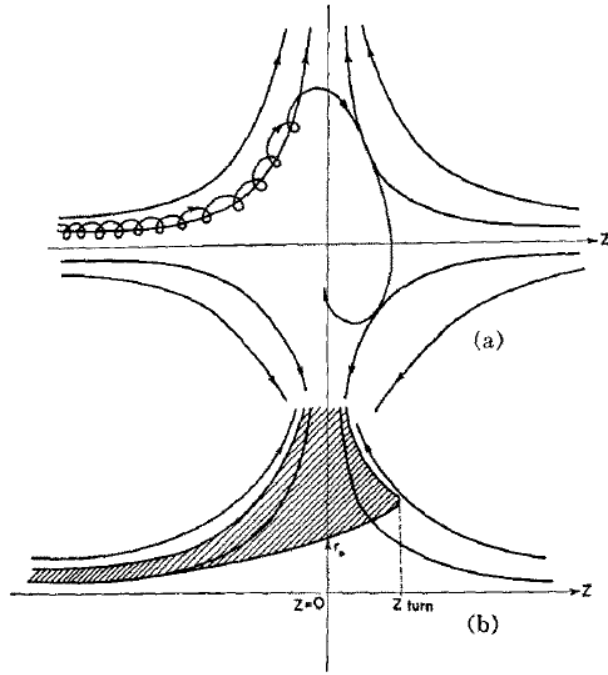
Figure 4.4. Particle motion in a cusped magnetic field.

4.8.2 Derivation of alpha value

The value of alpha can be found through calculation by equation (4.33) when the magnetic field at the cathode B_{cath}, the cavity B_{cav} and the radius of the cathode r_{cath} are known.

$$m_0 \gamma r_{cath}^2 \dot{\theta} - \frac{e r_{cath}^2 B_{cath}}{2} = -\frac{e r_{cav}^2 B_{cav}}{2} \tag{4.33}$$

In an axis-encircling electron beam, $\omega_0 = \dot{\theta} = e B_{cav} / \gamma m_0 = V_\perp / r_0$, therefore it can be shown that alpha can be found from

$$\alpha = \frac{v_\perp}{v_z} = \sqrt{\frac{-r_0^2 \eta^2 B_{cath} B_{cav}}{\gamma^2 v^2 c^2 + r_{cath}^2 \eta^2 B_{cath} B_{cav}}} \tag{4.34}$$

The radius of the electrons at the cavity magnetic field region can be calculated by using equation (4.35).

$$r_0 = \frac{r_{cath}}{\sqrt{-B_{cav} / B_{cath}}} \tag{4.35}$$

4.8.3 Transfer of energy, coherent off-centering and beam envelope

The transfer from axial to azimuthal velocity in the cusped magnetic field is described in a paper by Rhee and Destler[158]. The derivation of the Lagrangian in an electromagnetic field starts from the theory of special relativity. The general form for the non-relativistic Lagrangian is given in equation (4.36). When a particle travels through an external electromagnetic field it is affected by the potential, Φ, and therefore the potential energy of the electron is given by equation (4.36).

$$L = T - V \tag{4.36}$$

Where T is kinetic energy and $V = e\Omega$ is Potential energy.

It is important at this point to define the magnetic field step used in the calculations, which can take the form of either an "ideal" cusp or a "non-ideal" cusp. The "ideal" cusp is a step function, which transfers from one direction to the other with an infinitely small cusp transition, while the "non-ideal" cusp uses a more realistic approximation, where there is a smooth rise in magnetic field. The magnetic field as a function of axial position is therefore given in equation (4.37) with the corresponding potential in equation (4.38).

$$B_z = B_{z_0}\left[1 - 2u(z)\right] \tag{4.37}$$

$$A_\theta = \frac{rB_{z_0}}{2}\left[1 - 2u(z)\right] \tag{4.38}$$

Where u is the Heaviside unit step function, B_{z_0} is cavity magnetic field

While some are able to use this as an approximation to the experimentally produced field when the cusp transition is very small, the magnetic field profile is obviously not a very realistic one to achieve, and so a more realistic approach is the non-ideal cusp model. The magnetic field for this is more of a smooth rise and as such the magnetic field is described by equation (4.39) with corresponding potential in equation (4.40).

$$B = B_{z_0}f(z) \tag{4.39}$$

$$A_\theta = \frac{rB_{z_0}}{z} f(z) \tag{4.40}$$

Where $f(z)$ is an arbitrary function with the property that $\lim_{z \to \pm\infty} f(x) = \mp 1$.

The ideal cusp case, whereby the transition between directions of magnetic field is approximated by a step function, is considered here. The initial conditions used are that all the electrons come from the same point, the radius of the cathode, and there is no radial electric field at the cathode. The Lagrangian equation is solved for the theta component and then, by using the initial conditions, this is simplified to an equation for the z component (4.41) where $\delta(z)$ is the Dirac delta function.

$$\ddot{z} - \frac{\omega_c^2}{2} \left[r^2 (1 - 2u) - r_0^2 \right] \delta(z) = 0 \tag{4.41}$$

Finally, to transform this equation to give velocity, it must be integrated using the condition in equation (4.42). Also, it should be noted that the integral of the Dirac delta function is 1.

$$\frac{d}{dt} = v_z \frac{d}{dz} \tag{4.42}$$

This gives the equation which states that the velocity after the cusp, v_{z2}, is equal to the velocity before the cusp minus the imparted azimuthal velocity given to the electron beam. Noticeable here is that the velocity is not dependant on the radial position of the electron as it passes through the cusp region.

$$v_{z2}^2 = v_{z1}^2 - r_0^2 \omega_c^2 \tag{4.43}$$

This equation shows that there must be a threshold velocity for the electrons for which they have to exceed or are reflected through the magnetic mirroring.

$$v_{zth} = r_0 \omega_c \tag{4.44}$$

The "non-ideal" cusp model is the more realistic model, which can describe some undesired effects that occur when the electron beam passes through the cusp region. In this model, the magnetic field now takes the form of equation (4.45) with the resultant potential given in equation (4.46).

$$B = B_{z_0} f(z) \tag{4.45}$$

$$A_\theta = \frac{rB_{z_0}}{z} f(z) \tag{4.46}$$

Where $f(z)$ is an arbitrary function with the property that $\lim\limits_{z \to \pm\infty} f(z) = \mp 1$.

There are assumptions made here that $r \cong r_0$ (investigating the central ray only) and $r / r_0 \omega_c \ll 1$. The Largrange equations can be described as equations (4.47)-(4.49).

$$\dot\theta = \frac{\omega_c}{2}(f - 1) \tag{4.47}$$

$$\ddot{z} + \left(\frac{\omega_c r_0}{2}\right)^2 (f - 1)\left(\frac{df}{dz}\right) = 0 \tag{4.48}$$

$$\ddot{r} + r_0 \left(\frac{\omega_c}{2}\right)^2 (f^2 - 1) = 0 \tag{4.49}$$

The axial velocity as a function of distance, z, is

$$v_z(z) = \frac{r_0 \omega_c}{2}\left[(2\eta)^2 - q^2\right]^{\frac{1}{2}} \tag{4.50}$$

Where $\eta = v_0 / r_0 \omega_c$ and $q = 1 - f$.

Then substituting equation (4.50) into (4.49), and using $d/dt = v_z(d/dz)$, produces a description of the radial velocity gained through the cusp transition.

$$\dot{r} = \int_0^2 \frac{\omega_c}{2} \frac{f^2 - 1}{\left[(2\eta)^2 - q^2\right]^{1/2}} \frac{dq}{f'} \tag{4.51}$$

The function $f(z)$ is given through equation (4.52) which requires knowledge of the actual experimentally found magnetic field to find ζ_{scale}, a scaling factor used to fit the experimental and theoretical magnetic fields.

$$f = -\tanh\frac{\eta}{\zeta_{scale}} \tag{4.52}$$

After the cusp transition, it is found that the all the particles suffer an off-centering of the guiding orbits once they pass the cusp transition region as shown in Figure 4.5 and described by equation (4.53).

$$\Delta R = \frac{\dot{r}}{\omega_c} = \frac{\zeta_{scale}}{2} \sin^{-1} \frac{1}{\eta} \tag{4.53}$$
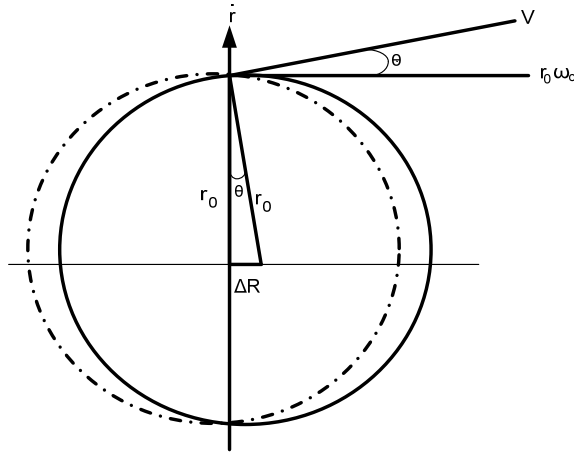
Figure 4.5. Electron beam position before (solid line) and after (dashed line) the cusp transition highlighting the off-centering of the guiding centre caused by the cusped magnetic field.

The electrons which have an off-centering of the particle orbits would also have then a beam envelope as shown in Figure 4.6 where the period of the envelope, λ, is

$$\lambda = \frac{2\pi v_{z2}}{\omega_0} = \frac{2\pi \left(v_{z1}^2 - r_0^2 \omega_c^2 \right)^{1/2}}{\omega_c} = 2\pi r_0 \left(\eta^2 - 1 \right)^{1/2} \tag{4.54}$$
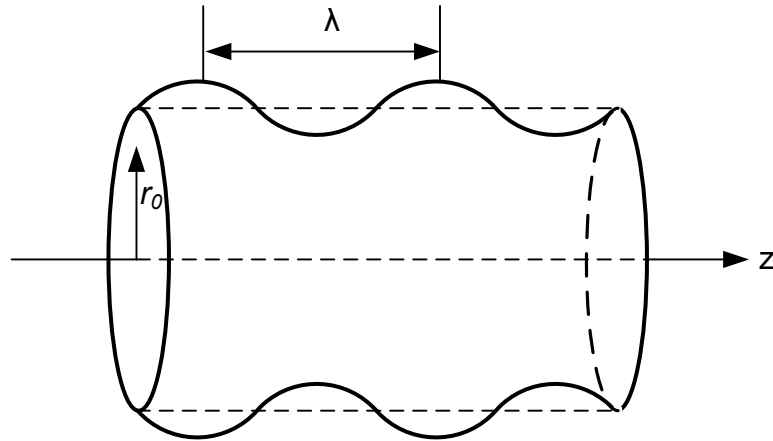
Figure 4.6. Beam envelope at the cavity side of the cusp transition showing an electron beam with a very low velocity spread but large mismatch in solenoid position.

4.9 Mode selectivity of axis-encircling electron beams

In order to preserve mode purity, it is imperative to have either a very mode selective

electron beam or another way of suppressing parasitic modes. When operating at harmonics, it is a concern that the electron beam can couple strongly to other waveguide modes, and this is true for electron beams generating through the MIG gun. An axis-encircling electron is able to be mode selective and can be designed to couple strongest to the second harmonic waveguide mode. The reasons for this are explained further through a descriptive means and then proved analytically.

The electron beam from a MIG can couple to any mode, as the electrons rotate around their own orbits and to couple to a mode they only need to change their phase. In an axis-encircling beam, the bunches form at one point in the cross section of the beam, for a TE_{11} mode, then travels around the beam. The fundamental mode in the circular waveguide is the TE_{11}, and thus has a lower frequency than the TE_{21} mode. When coupling to the TE_{21} node this has two dipoles, so the electron beam splits into two bunches which rotate relatively faster than one bunch. The electron beam splits into two bunches, due to the mode pattern of the TE_{21} mode, this is shown in Figure 4.7. These two electron bunches, for a large-orbit beam, act the same as a beam with double cyclotron frequency and thus will couple to only the second harmonic of the cyclotron mode. This means that the cusp gun has good mode selectivity, since once it couples to a mode, it will stay with that mode and not deviate.

Electron beams can have an infinite number of modes available to them for coupling, and the beam has a preference to which mode this will couple to. First, considering the mode TE_{01}[164], a coupling coefficient H_s can be defined as the energy-transfer rate of the microwave interaction and is a measure of interaction strength.

$$H_s\left(k_n r_g, k_n r_L\right) = J_S^2\left(k_n r_g\right) J_s'^2\left(k_n r_L\right) \tag{4.55}$$

Where $k_n = x_n / a$, x_n is the nth nonzero root of $J_1(x) = 0$ and J_s a Bessel function of order s the harmonic number.

This equation can be plotted as a function of $k_n r_g$ and $k_c r_L$ for $s = 1$ to 4 and is shown in Figure 4.8. This graph shows that in the limit of $r_L \to 0$ when compared to
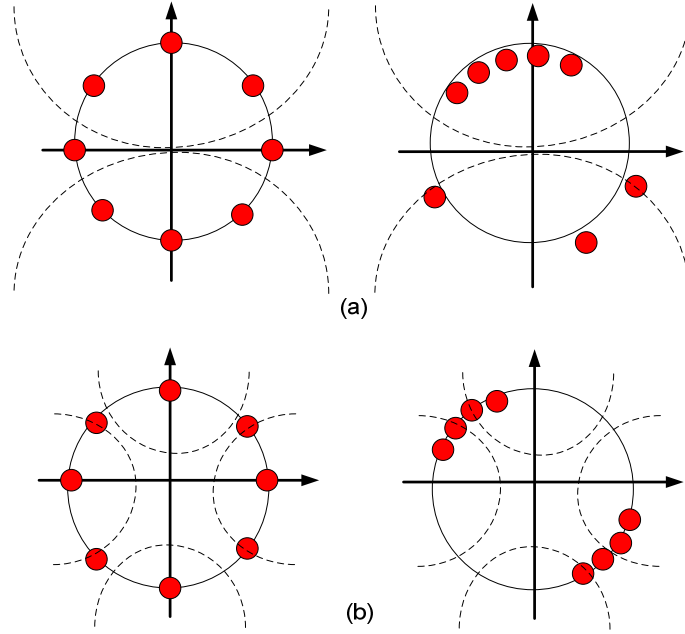
Figure 4.7. Effect of the electric field on an electron beam in the presence of the (a) TE$_{11}$ mode and (b) TE$_{21}$ mode. The left hand side shows the initial state of the electron beam and the right hand side shows the bunched electron beam. The dashed line represented the poles of the electric field.

the cavity radius, the coupling coefficient vanishes in all harmonics except $s = 1$. This shows that harmonic fields ($s > 1$ where $s = 1$ is the fundamental mode) occur due to a finite Larmor radius. Furthermore, it can be seen that if one wishes to couple to harmonic modes the electron beam should have a larger Larmor radius as when r_L increases the coupling coefficient for $s = 1$ decreases while the other harmonics increase. The radial periodicity of the electric field is the reason for the periodic dependence of the coupling coefficient on $k_n r_g$ as seen in all harmonic graphs.

When considering modes of the form TE$_{mn}$ the generalized couple coefficient equation[165] is

$$H_{sm}\left(k_{mn}r_g, k_{mn}r_L\right) = J_{s-m}^2\left(k_{mn}r_g\right)J_s'^2\left(k_{mn}r_L\right) \tag{4.56}$$

In analysing this equation it can be seen that in operation at harmonic waveguide modes it would be advantageous to use a beam with $r_g = 0$, an axis-encircling
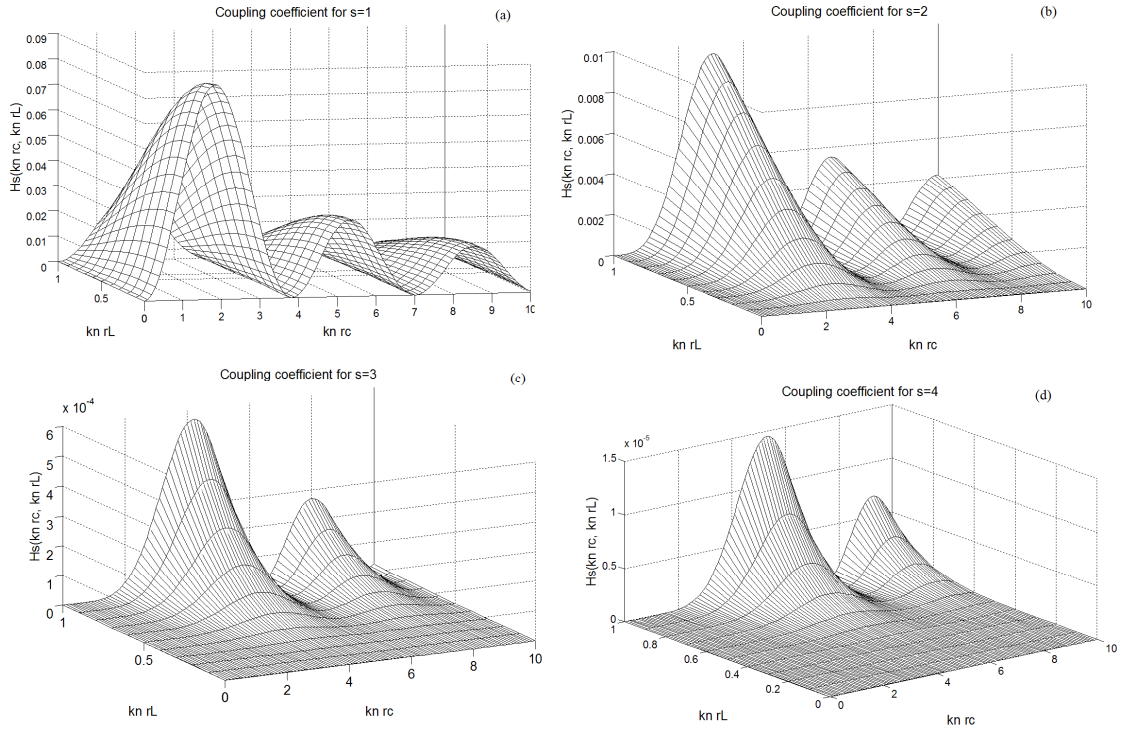
Figure 4.8. Coupling coefficient for (a) $s = 1$ (b) $s = 2$ (c) $s = 3$ (d) $s = 4$.

electron beam. This beam had very good mode selective properties as it requires that the harmonic number, s, equal the azimuthal index, m, otherwise the coupling coefficient vanishes. Furthermore, when operating at $m = s$ the strongest interaction occurs when $r_g = 0$. This can be seen from the plot of the Bessel functions. Therefore, using an axis-encircling electron beam can allow harmonic modes to be selectively coupled without parasitic modes being stimulated.

4.10 Summary

This chapter introduced the physics of electron beams from the production to transportation through a magnetic field reversal. The various methods employed to produce electron beams of differing properties were described. This chapter concluded with discussion of the cusp electron gun and explained why the electron beam produced through this gun is important for interaction in a helical waveguide operating at the 2nd harmonic waveguide mode.

Chapter 5.

Numerical Modelling of the Cusp Electron Gun

5.1 Introduction

The design of an electron gun capable of generating an electron beam which could drive the gyro-BWO is a complicated and lengthy process. This chapter discusses the numerical and analytical analysis of the cathode. The electron beam produced by a cathode is difficult to predict without accurate numerical modelling, due to the many interactions between the emitted electrons and the complicated space-charge effects. More than one code was used, in order to provide a validation of the cathode design. Also, the optimisation of this design is introduced and the final optimised geometry with corresponding electron beam properties are given.

5.2 Cusp electron gun simulations

While cusp electron guns have been simulated previously[161,166,167,168,169] - and in a few cases constructed[170] and tested[171,172,173] - this work expands on this research area to create a cusp electron gun for a millimetre-wave microwave source. The complications of the design arise through the requirement of a large magnetic field at the interaction region. Design considerations include the average diameter of the coil, which must be big enough to accommodate cooling channels through the layers, and the large magnetic field tuning range. The electron beam has to travel through the beam tube while maintaining an acceptable amount of axial velocity and alpha spreads over the full magnetic field range of $1.65T - 2.1T$. Therefore, a long, gradually tapered tube must be employed, at the diode side of the beam tube, to ensure complete beam transport at the lowest magnetic field.

This section introduces the design and simulation of the diode, with later chapters discussing diode construction and experimental results. While the design of the cathode produces an electron beam of good quality to drive the gyro-BWO interaction, it should be noted that this source has an inherent insensitivity to axial velocity spread due to the dispersion properties of the helically corrugated waveguide. Therefore, the requirement to produce an axial velocity spread lower than 10% is less important in this device compared to conventional gyro-BWO's.

5.2.1 Diode design

There are two primary goals of the design of the cusp electron gun: a) to produce a beam of suitable quality to drive the gyro-BWO over the required magnetic field range; and b) to produce a design simple enough that this could be manufactured with less complication than usual electron guns. Consideration of the construction of the diode plays an important role in the design process, as the cathode will be small radially and thus sensitive to manufacturing tolerances. The aim is that a good quality electron beam would be produced even with some imperfections in cathode shape. The gyro-BWO was previously numerically analysed[174] to calculate the predicted output in order to find the beam properties the cusp electron gun would have to produce. Through those calculations it was found the microwave output was ~10kW (CW) at ~16% efficiency when the interaction was driven by a 40kV, 1.5A beam of 1.65 alpha. The targeted performances of the electron gun and gyro-BWO are given in Table 5.1. The gyro-BWO parameters as-well-as electron beam power, voltage, current and alpha were found through beam-wave interaction simulation of the interaction region and analytical calculations of the dispersion profile. The axial velocity spread target of approximately less than 15% was chosen from previous investigation on the effect of velocity spread in helical waveguide gyro-devices[145] where the velocity spread from 0% to 15% had little effect on the device but above this value had a significant detrimental effect.

Beam parameter targets		Gyro-BWO parameters	
Beam power	60kW	Max power (CW)	10kW
Accelerating voltage	40kV	Efficiency	~16%
Beam current	1.5A	Frequency band	W-band
Alpha	~1.65	B-field range	1.65 – 2.1T
Axial velocity spread	<15%	Tuning range	85 – 105GHz

Table 5.1. Performance targets for the cusp electron gun and gyro-BWO.

Electron guns consist of a cathode, to supply the electrons, focusing electrodes and a grounded anode, to distort the electric field lines and therefore change the path of the electrons. The distortion of these lines at the anode aperture defocuses the electron

beam through a negative lens effect. The effect on the cathode electric field is small when the anode aperture radius, r_a, is small compared to the distance between the cathode and the anode, d_{ac}.

$$r_a \ll d_{ac} \tag{5.1}$$

The effect on the electric field lines is large when the condition in equation (5.2) is met. If this is true, the cathode geometry must be adjusted to compensate for the effect.

$$r_a \geq d_{ac} \tag{5.2}$$

Perveance is a parameter that describes the effect of space-charge effects on a beam and is given by the unit perv (Amp/volt$^{3/2}$). It is therefore important to investigate the perveance of the diode when the design at the initial stage of development as this can have a large effect on the beam. The perveance is only an important factor for circular diodes with apertures. In a cylindrical electron gun, perveance can be calculated[163] through

$$P = \frac{I}{V_{ac}^{3/2}} = \frac{4}{9} \frac{A_c \varepsilon_0}{d_{ac}^2} (2\eta)^{1/2} = \frac{4}{9} \varepsilon_0 (2\eta)^{1/2} \left(\frac{\pi r_a^2}{d_{ac}^2} \right) \tag{5.3}$$

Where V_{ac} is the accelerating voltage, A_c is the area of the cathode and η is the electron charge-to-mass ratio.

If the condition in equation (5.1) is applied to this equation, then it is found the effect of the perveance is low when

$$P \ll \frac{\pi \varepsilon_0 / 9}{\sqrt{2e/m_e}} = 0.6 \times 10^{-6} \tag{5.4}$$

The effect of the perveance shows how strong the negative lens effect will be. When the perveance is much smaller than 1µperv (~0.01µperv) the distortion of the equipotential is very small and this negative lens effect can be ignored. In a so-called medium perveance gun, where the perveance is closer to 1 µperv (~0.1µperv), the negative lens effect has to be taken into consideration. High perveance guns are those in which the perveance exceeds or is close to 1µperv, where the negative lens effect is strong and the design has to be changed to compensate for the effect. The cusp

electron gun is found to have a perveance of 0.1875µperv putting it into the medium perveance end.

The beginning of the design process focused on the emitting strip design and from this the focus electrodes and anode can be shaped around it. A schematic diagram of the general cathode geometry can be seen in Figure 5.1, with some dimensions highlighted that are used in this discussion. The dimensions of the emitter required are: radial thickness of the strip, the average radius and the inclination of the surface. When a very narrow strip is chosen, a high quality beam can be produced, as the magnetic field variation – one of the leading causes of velocity and alpha spread – across the emission surface can be reduced at the expense of current density. Excessive current density, $> 10 \text{A/cm}^2$, can lead to a vastly reduced cathode lifetime; therefore, the thickness of the strip is chosen to produce a current density less than this limit. In this initial design stage this value can be chosen to be approximately 8A/cm^2.
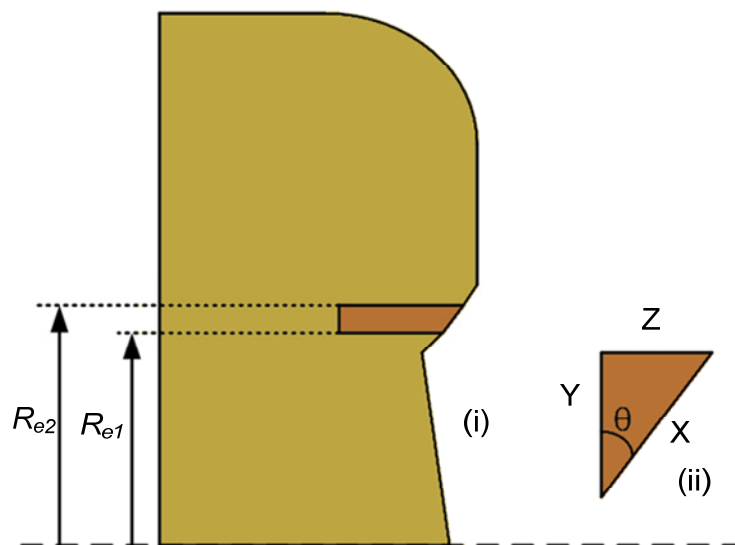
Figure 5.1. Schematic diagram of the cusp electron gun showing (i) the basic geometry of the cathode and electrodes outlining the position of the inner and our radius of the emitting strip, (ii) Close up of the emitting surface showing the dimensions needed for the area correction factor.

The emitting strip is inclined at an angle, as shown in Figure 5.1 this leads to an area bigger than just the difference between the inner, R_{e1}, and outer radii, R_{e2}. This can

be found from an area correction factor A_{CF}.

$$A_{CF} = \frac{\sqrt{y^2 + z^2}}{y} = \frac{x}{y} = \frac{1}{\cos\theta}$$ (5.5)

Where dimensions x, y, z and θ are shown in Figure 5.1.

Therefore, the area of the emitter can be found through

$$A_e = A_{CF}\pi\left(R_{e2}^2 - R_{e1}^2\right)$$ (5.6)

The average radius of the emitter can be chosen through the desired alpha value required. This is given through

$$r_c = \frac{\alpha V_0}{\sqrt{-\left(\alpha^2 + 1\right)\omega_{ca}\omega_0}}$$ (5.7)

Where $\omega_{ca} = eB_c / \gamma m_0$ and $\omega_0 = eB_0 / \gamma m_0$ are the cyclotron frequency in the cathode and cavity magnetic field regions respectively. B_c and B_0 are the magnetic fields in the cathode and cavity magnetic field regions.

Through this method, the angle of the emitter was chose to be ~35° (actual value in simulation is 33.74°) and the average radius of the cathode set at ~6mm. This gives the inner and outer radii as 5.78mm and 6.3mm respectively. The final design has the values of R_{e1}=5.79mm, R_{e2}=6.29mm, A_{CF}=1.2, A_e=0.227cm^2 and emission current density J_c=6A/cm^2.

To design the diode, a generalised shape was produced from Pierce principles[154] and from this and previous designs used at the University of Strathclyde, a new design that was better suited to the desired electron beam was produced. While another cusp electron gun has been produced at the University of Strathclyde, simply scaling this to produce an electron beam suitable for driving a higher frequency interaction would not be possible, as the space-charge effects are significantly different for this electron beam. A schematic diagram of the cathode geometry can be seen in Figure 5.2 where some dimensions changed during the design process are noted.
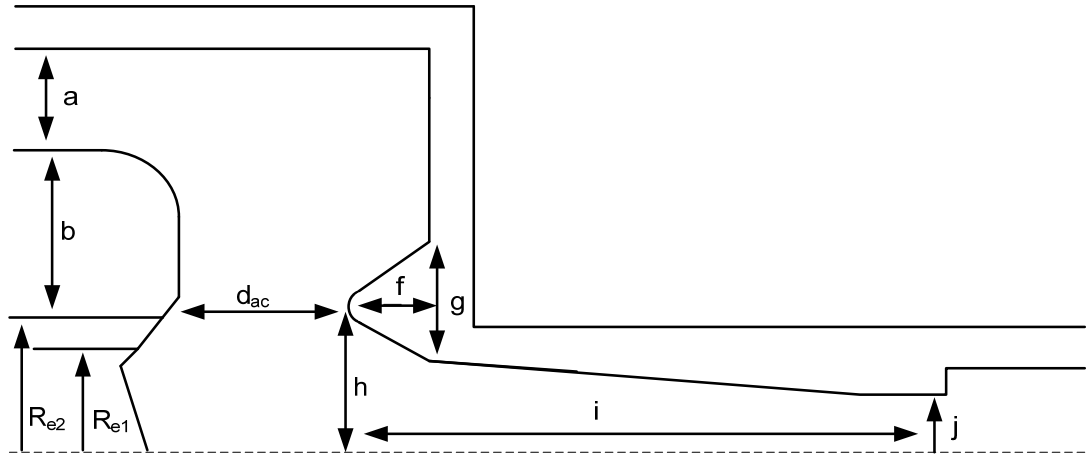
Figure 5.2. Schematic diagram of the diode highlighting dimensions used in the design.

In this design, the size of the average radius of the emitting strip is found through the equation for alpha, defined in Chapter 4 as equation (4.34). A table of the final parameters of the diode design can be seen in Table 5.2.

d_{ac}	4.48mm
Emitter strip width ($R_{e2} - R_{e1}$)	0.5mm
Angle of emitter face to horizontal	56.6^o
R_{e1}	5.79mm
R_{e2}	6.29mm
Cathode stock radius (R_{e2} + b)	17.38mm
Anode aperture radius (2f)	14.6mm
Cut-off section aperture (2j)	1.67mm

Table 5.2. Final parameters of the diode design.

5.2.2 MAGIC simulation

To model the emission of a charged particle beam with 3D geometry and the complicated space-charge effects through a purely analytical method would be very time-consuming and difficult. Numerical codes provide a fast and accurate way of modelling electron emission, transport and are especially useful in electron gun design, where many parameters have to be adjusted until an electron beam of sufficient quality is generated. The particle-in-cell (PiC) code MAGIC[175,176]. (**MAG**netic **I**nsulation **C**ode) by Mission Research Libratory has been used for many

years to simulate electromagnetics, charged particle emission and beam-wave interactions. At the University of Strathclyde, MAGIC was previously used to model a cusp electron gun used to drive an X-band gyro-TWA. The simulated electron beam results agreed very well to experimental results giving a validation of the numerical code. The MAGIC script used in this thesis is a derivative of the pervious successful numerical code.

Originating in 1978, this program was originally designed to model magnetic insulation[177]. Later, a new three-dimensional version was created to model electromagnetic pulse effects on satellites, called SOS (**S**elf-**O**ptimized **S**ector)[178]. This program was then used to model pulsed power applications[179]. This program solves Maxwell's time-dependant equations directly and by using the Yee cell algorithm[180] shown in Figure 5.3 taken from reference 180, can time-step these equations to show what the electric and magnetic fields will be at some point later in time. This is called the particle-in-cell (PiC) approach and differs to the Finite-Difference approach of other modellers such as Opera-3D.
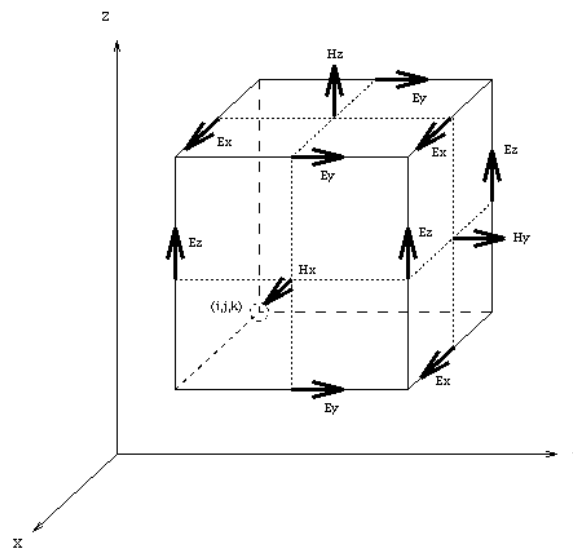
Figure 5.3. Yee cell from the Yee Algorithm.

5.2.2.1 Emission model

The code MAGIC allows different ways of emitting particles from a surface, for instance thermionic and explosive emission. As the cusp electron gun will use a

thermionic cathode, a thermionic emission process was used. In the code this can be accurately modelled using the Richardson-Dushman equation (5.8).

$$J_e = A_e T_c^2 e^{\frac{-\phi_w}{k_B T_c}} \qquad \text{(5.8)}$$

Where T_c is the temperature of the emission surface and k_B is the Boltzmann constant.

In the MAGIC script the work function is chosen to be 1.5eV – the value found for previous cathodes using a tungsten cathode impregnated with barium.

5.2.2.2 Simulation parameters

The design of the diode is constructed on a gridded system so this can lead to slight inaccuracies in the modelling when the mesh is not dense enough; however, if the system is meshed properly the results should be very accurate. The cathode can be seen in both 2D in Figure 5.4a and the full 3D version in Figure 5.4b.

(a)

(b)
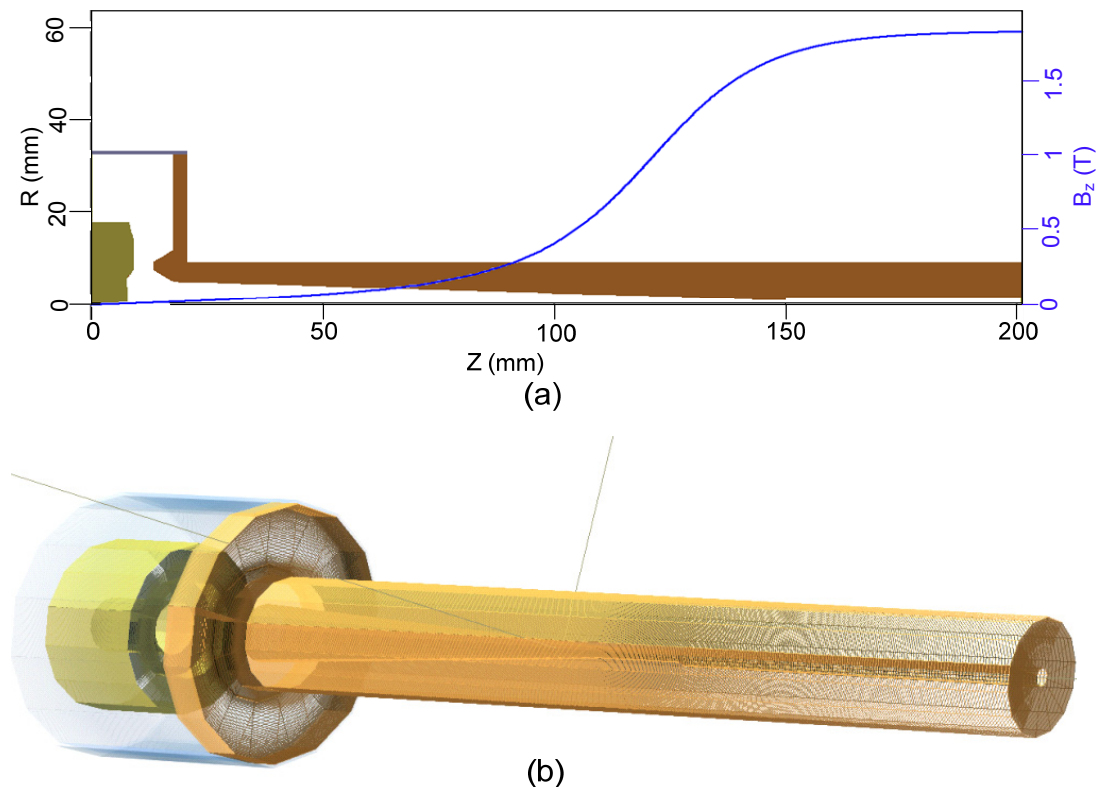
Figure 5.4. Geometry of the cusp electron gun (a) 2D image with magnetic field profile overlaid and (b) 3D image.

111

It should be noted that although the simulation is 3D, to decrease the run-time the electron beam was only emitted from 4 points around the 360 degree axis. This still yields accurate results, as the geometry is fully symmetric around the axis of symmetry, and so the results should not differ. In this figure, the magnetic field is overlaid showing the position of the cusp point in relation to the geometry of the cathode and anode. Also, the length of the tapered section down to the backstop filter can be seen here, as well as the geometry of the anode.

In Figure 5.5 a more detailed view of the focusing electrodes, anode and cathode can be seen, showing the meshing effect of MAGIC and the sizes and distance between the anode and inner electrode. It should be noted that at the cathode there are two small gaps above and below the emitting surface (coloured brown). These gaps are to stop contact between the cathode and the focus electrodes, so that the barium in the cathode does not migrate into the focusing electrodes. Such migration could cause the electrodes to emit particles and also to further reduce the conduction of thermal energy to the focus electrodes.
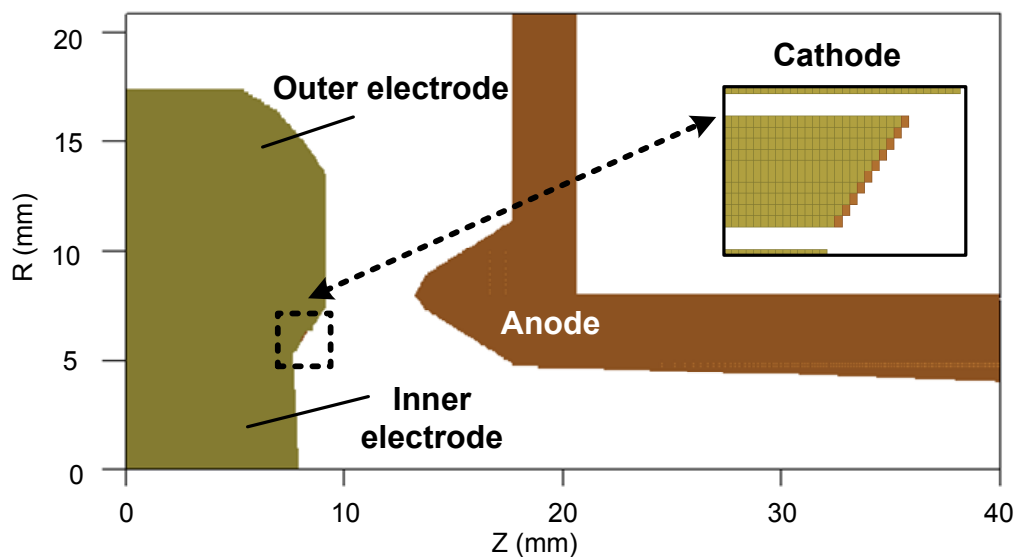
Figure 5.5. A close-up view of the diode as drawn by MAGIC.

5.2.2.3 Simulated B-field profile of magnetic coils

The magnetic coils defined in MAGIC are an approximation of a single line of coils

at an average radius. The program defines one coil position, and then through a do-loop defines each subsequent coil position for a given number of the turns. The current is defined as the current for the coil multiplied by the number of layers in the coil. The magnetic field profile is very important to the operation of a cusp electron gun as it guides the electrons along the beam tube, determines the position of the cusp and in-turn has a large effect on the quality of the electron beam. When the solenoids are designed to produce a smooth cusped magnetic field profile it was calculated that there would be a large amount of heat. In order to reduce the overall length of the coil, as well as the heat produced by the wires, two extra coils, so-called "shim coils", were added to the cavity solenoid. The shim coils sharpen the magnetic field profile and allow the total length of the solenoid to be reduced allowing a total number of turns to be reduced. The parameters used in the code to produce the required magnetic field profile can be seen in Table 5.3.

	Reverse coil	Cavity coil	1st Shim coil	2nd Shim coil
Start position	-6cm	12.3cm	12.3cm	31.6cm
Average radius	8cm	2.84cm	4.92cm	4.92cm
Wire width	2.2mm	2.2mm	2.2mm	2.2mm
Number of turns	10	103	15	15
Coil current	713.28A	3257.8A	465.4A	465.4A

Table 5.3. Properties of the solenoids defined in MAGIC simulation code.

It is important to note that while the current of the revserse coil is equal to 713.28A in practical terms, this would be 4 layers of coil with 178.32A per layer. Similarly, for the cavity coil 3257.8A is equal to 14 layers of 232.7A per layer. The shim coils are driven by the same wire as the cavity coil, and so have the same current but with only two layers, resulting in a total current of 465.4A. The shim coils reduce the length of the solenoid and it was decided that only 2 layers of 15 turns per layer were required. However, different configurations were also examined. The effect of adding different ammounts of shim coil layers can be seen in Figure 5.6.
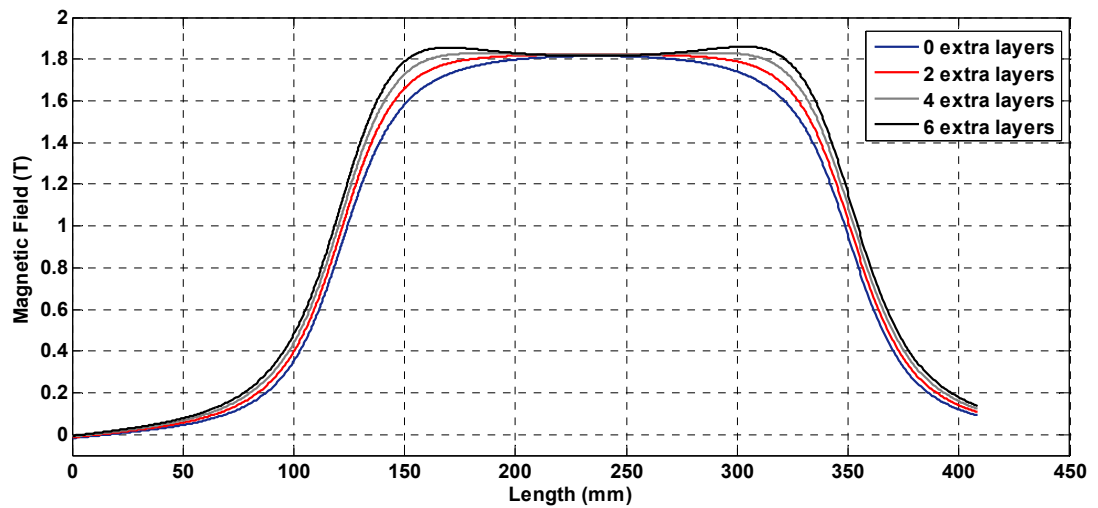
Figure 5.6. Simulated magnetic field profile using different amounts of extra layers at each end. The sharper magnetic field as the number of extra layers is evident.

These coils are described approximitly in MAGIC so a comparison with an analytical calculation of the magnetics would be prudent. The magnetic field that MAGIC produces can be seen in Figure 5.7. This is the magnetic field along the central axis of symetry and shows the smooth rise from a slightly negative magnetic field to the full field.
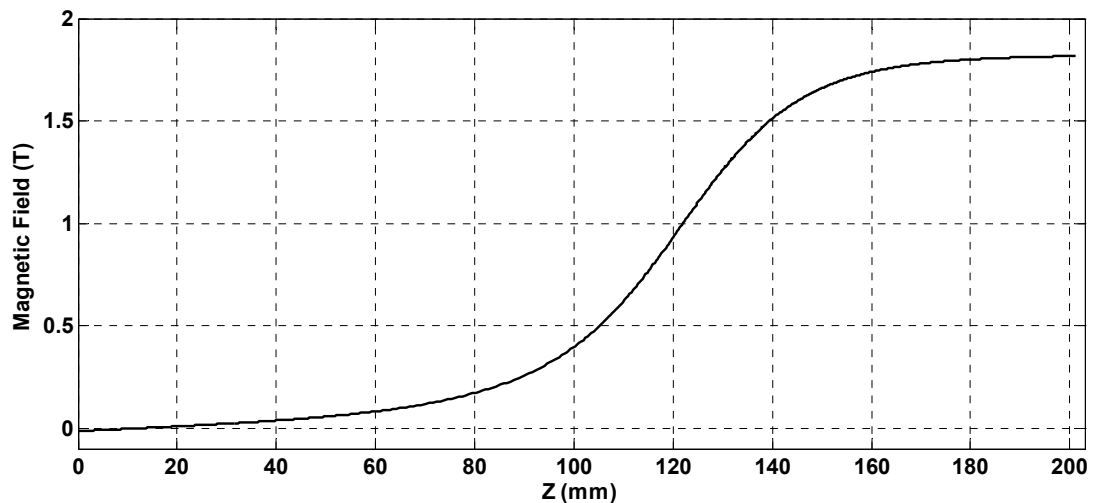
Figure 5.7. Axial magnetic field (B_{max} = 1.82 T) along axis of symmetry as calculated by MAGIC.

This magnetic field is a combination of the two solenoids. The region of the flat top has to be at least 10.75cm, to match the length of the helically corrugated waveguide. The full magnetic field profile of the solenoid is shown in Figure 5.8.

114
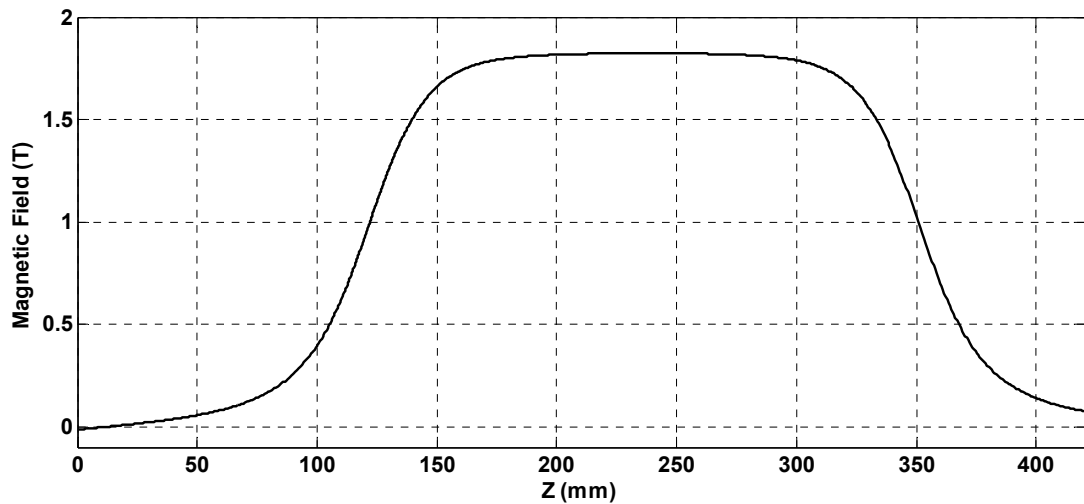
Figure 5.8. Simulated magnetic field profile of the gyro-BWO at B_{max} = 1.82 T.

The magnetic field at the cusp region, the combination of both the reverse coil and the cavity solenoid, is one adjustable factor that determins the alpha value of the electron beam at the beam-wave interaction region. The spread of magnetic field over the emission surface is one of the biggest factors that contributes to velocity spread in the electron beam. The magnetic field vector at the cusp region is shown in Figure 5.9. This shows the direction and amplitude of the magnetic field that the electrons travel through when they pass from the cathode through the anode appeture. It also shows the position of the cusp point, in this case, at 4.3mm from the middle point of the front face of the emitter.
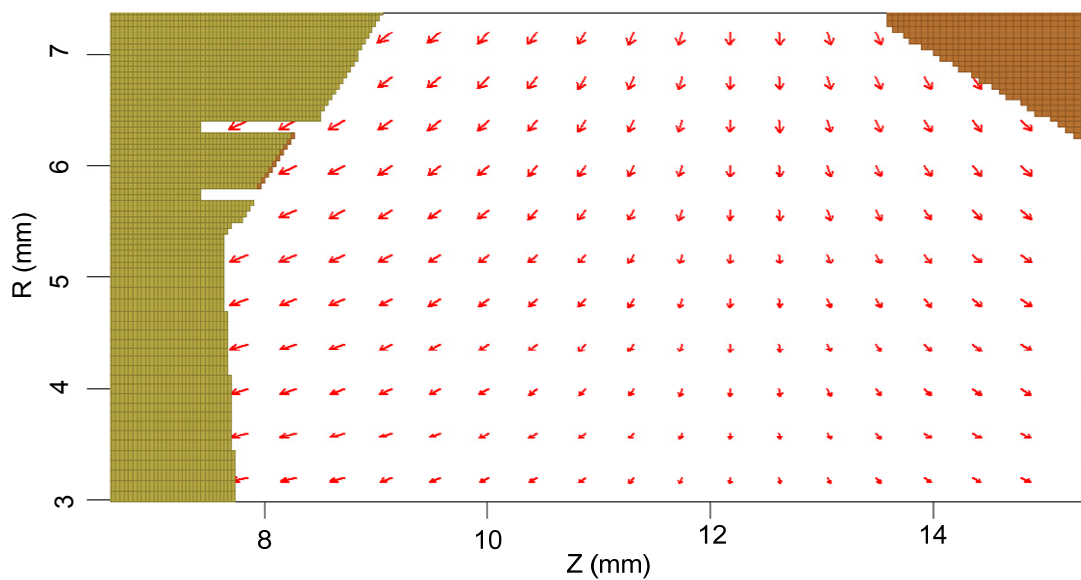
Figure 5.9. Magnetic field distribution in the cusp region.

5.2.2.4 Design optimisation

The design of the diode requires extensive optimisation of the geometries to produce a high quality electron beam. There are 0.1mm gaps above and below the emission surface increasing the difficulty of optimising the design as these are hard to adjust for. There are many dimensions of the cathode that can be adjusted in order to optimise the geometries, which are outlined in Figure 5.10. The first step is to settle upon the average radius and width, in addition to the slope of the cathode. After this, dimensions **a**, **b**, **c**, **d**, **e**, **f**, **g**, **h**, **i** and **j**, as shown in Figure 5.10, are adjusted to shape the equipotentials in order to stop the electron beam diverging. Along with the geometry of the diode, the driving current, average radius, and start and end positions of the solenoids can be adjusted to optimise the cusp position.
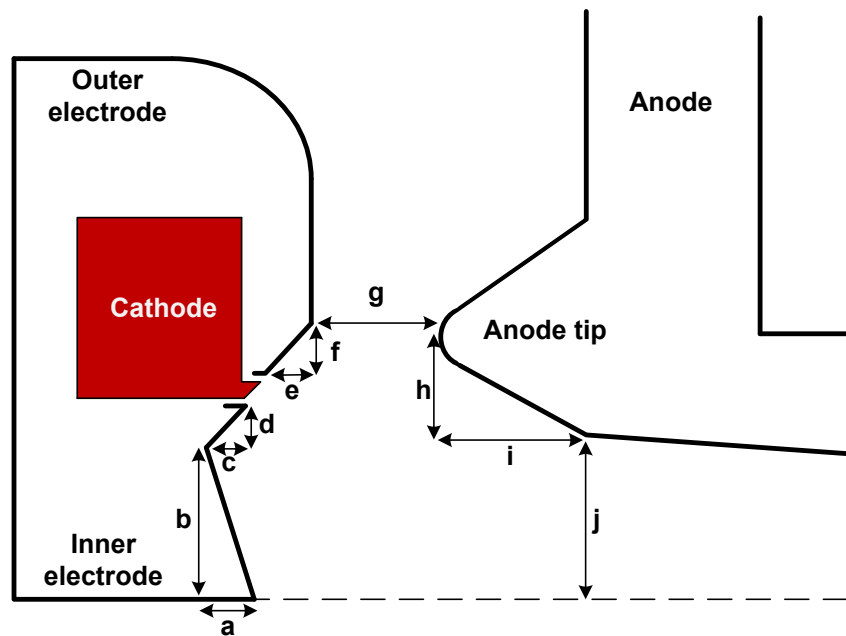
Figure 5.10. Schematic diagram of the diode geometry showing the parameters that were changed during optimization of the design.

The range of optimisation and final optimised values are given in Table 5.4. Local optimisation of each dimension can be shown by adjusting each parameter by ±0.1mm and comparing against the optimised value this can be seen for some selected parameters in Table 5.5.

Dimension denotation	Optimised value (mm)	Range of optimisation (mm)
a	0.30	0.00-0.60
b	5.44	5.30-6.00
c	0.27	0.10-0.45
d	0.25	0.10-0.45
e	0.60	0.40-0.80
f	1.01	0.70-1.30
g	4.48	2.50-5.00
h	3.23	2.00-4.00
i	4.13	3.50-5.10
j	4.80	4.00-5.20

Table 5.4. Cusp electron gun optimised values and optimisation ranges.

Dimension	Deviation from optimised value	Axial velocity spread	Alpha spread
a	+ 0.1mm	9.40%	11.85%
	- 0.1mm	8.21%	10.88%
b	+ 0.1mm	8.37%	10.83%
	- 0.1mm	9.42%	11.97%
c	+ 0.1mm	15.03%	20.56%
	- 0.1mm	10.14%	13.33%
e	+ 0.1mm	8.62%	11.01%
	- 0.1mm	8.57%	10.77%

Table 5.5. Optimisation of the dimensions of the diode.

An incorrect position of the solenoids will increase the thickness of the electron beam with a large envelope ripple. In order to reduce the difference of magnetic field over the emission surface, it is important to make sure the reverse coil has a larger radius than the cavity solenoid.

The addition of a 0.1mm gap above and below the cathode provides some additonal difficulty in generating a good quality beam. These gaps distort the equipotentials at the cathode. Additionally, the removal of the focusing electrode geometry in immediate contact with the cathode causes the edges of the electron beam to diverge, resulting in a large spread in alpha and velocity. To reduce this, the cathode is moved by 0.1 mm from the focusing electrodes, leaving part of the focusing electrode

geometry at these gaps, in order to "push" the electrons into the main electron beam and prevent them from diverging.

5.2.2.5 Equipotential surfaces and electric field enhancement

The electron beam is focused in relation with the shape of the equipotentials in the diode region. The equipotentials are changed through the shape of the focusing electrodes and the anode. The equipotential in the diode region show us how the electrons are focused by the shape of the anode and cathode surface.

The shape of the equipotentials is acting to focus the electron beam down through the anode aperture. Looking at the potentials at the emission surface, clearly shown in Figure 5.12, the equipotentials at the emission surface are almost parallel with the surface in order to reduce the velocity spread. The inner and outer focusing electrodes are used in order to produce this equipoential profile.

The electrons would stray off course without the focusing. The electrons would diverge due to the repulsive space-charge forces in the beam. The correct shape of the focusing electrodes reduces the velocity spread in the beam.
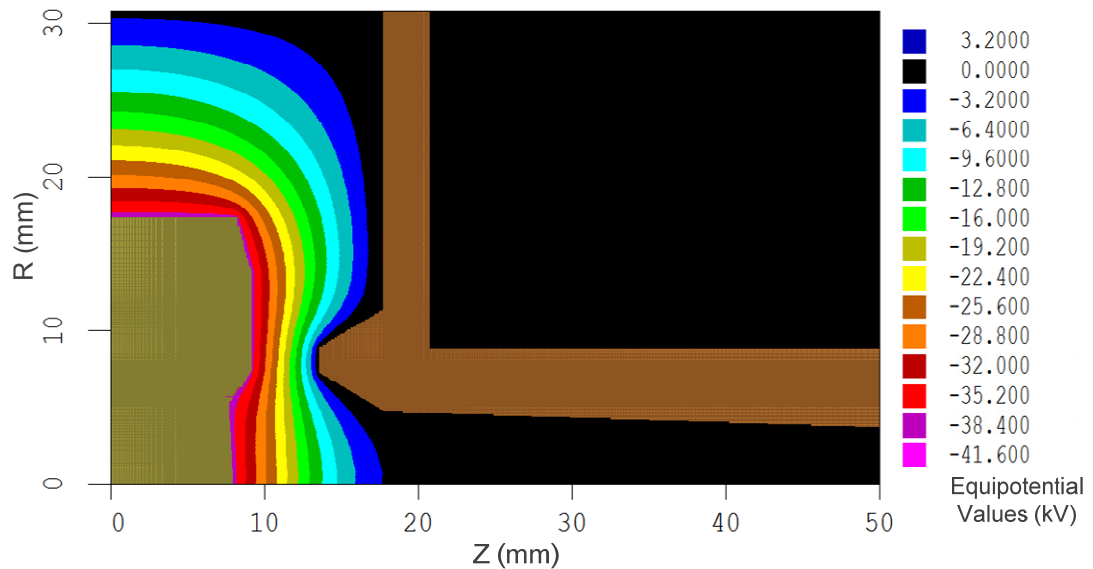
Figure 5.11. Equipotential profile in the diode region with the electron beam present.
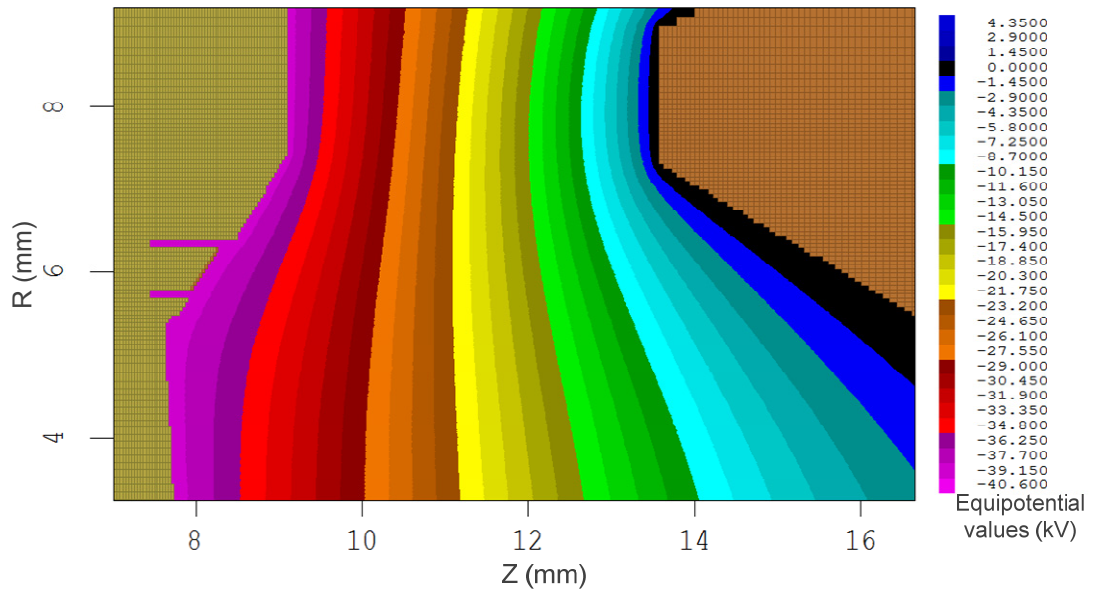
Figure 5.12. Equipotentials at the cathode surface.

The magnetude of the electric field at the cathode and anode gap is a concern for electron gun design due to the possibility of electric field breakdown. If there are sharp corners in the geometry field enhancement would increase the electric field possibly causing field emission. The electric field at the cathode surface is required to be lower than breakdown threshold in vacuum in order to ensure the cathode does not get damaged during operation. The axial electric field (E_z) when the accelerating voltage is at its maximum 40kV and the electron beam has fully passed through the tube was recorded and is shown in Figure 5.13.
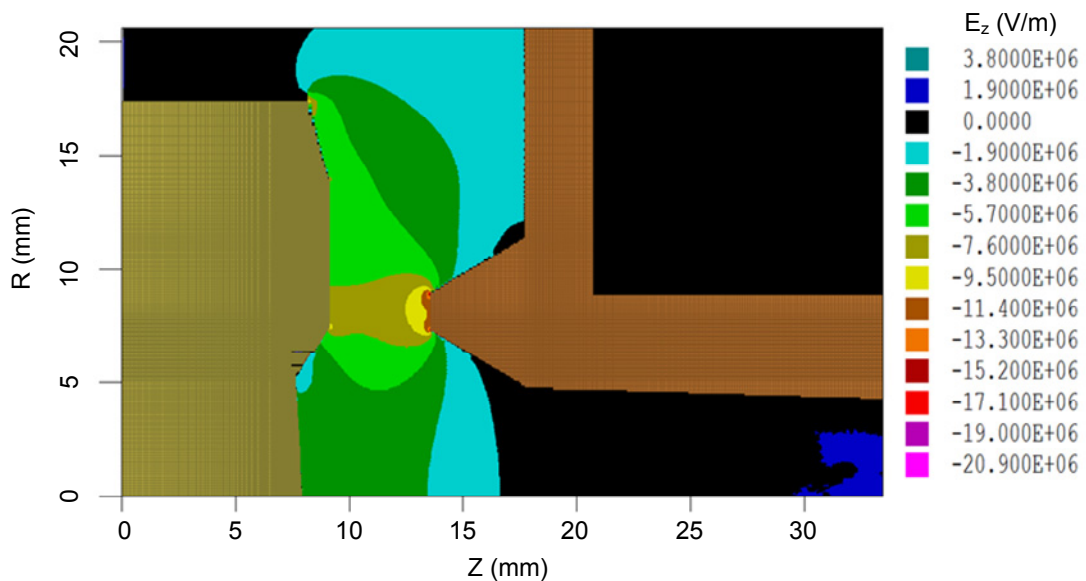
Figure 5.13. Axial electric field in the diode region.

The field shows an area around the anode tip that is larger than the recommended 10MV/cm in vacuum however this area of high electric field is most likely due to the flatness of the anode tip during the simulation. When the cathode was constructed care was taken to round and smooth the anode tip as much as possible so that there was less chance of breakdown. Areas where the electric field should be at a maximum are at the sharpe edge above the emitting surface and at the outer radius of the outer cathode. These two areas and the anode tip are highlighted in Figure 5.14. The outer electrode previously had shown a very large electric field at the outer radius as this was close to the anode in both *z* and *r* directions. This was reduced by beveling this surface, so that it had a large radius. The area just above the emitting surface shows a slight increase in electric field, but this is another area where the electric field would reduce during construction.

(a)

(b)
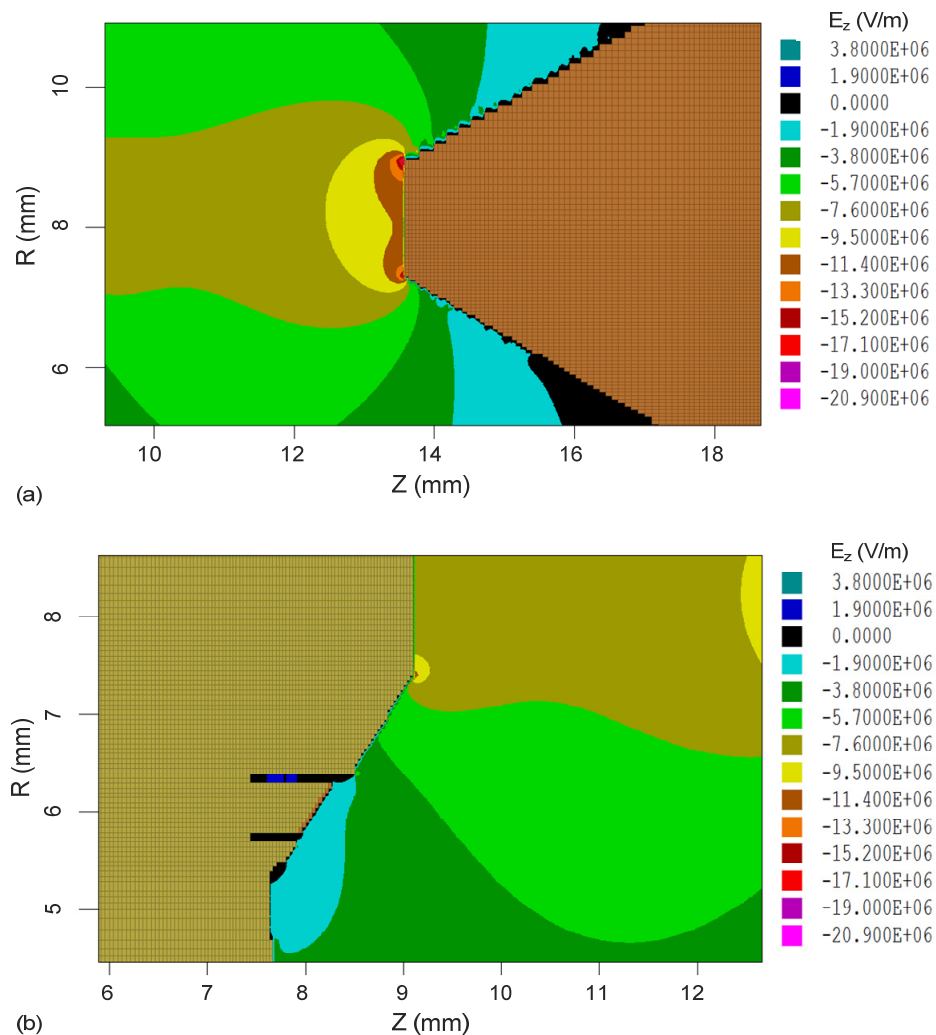
Figure 5.14. Continued on the next page.
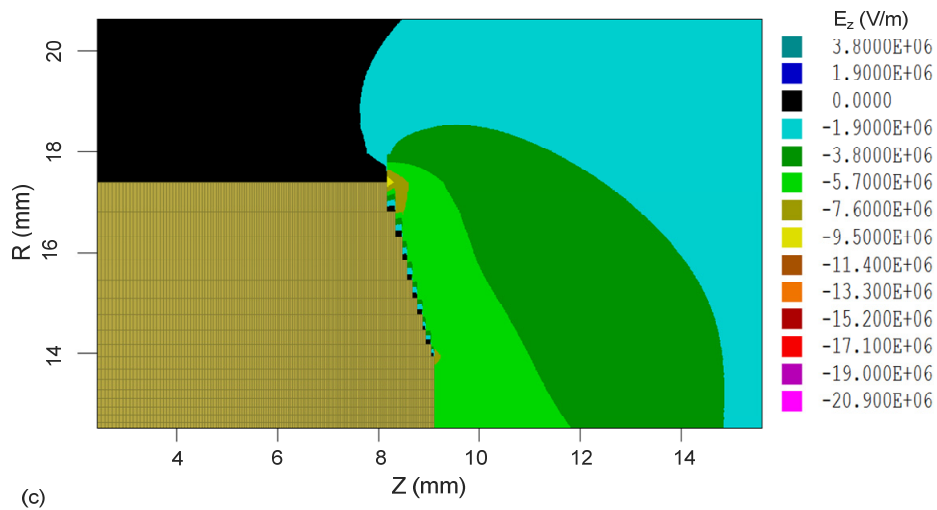
Figure 5.14. Electric field at areas of importance (a) anode tip, (b) cathode surface and (c) outer electrode.

5.2.2.6 Simulated electron trajectories

The electron trajectories after emission from the cathode are one of the most important diagnostic tools as these show if the electrons pass through the beam tube, where possible collisions occur, the thickness of the electron beam at the plateau magnetic field region and if the electron beam can pass through the backstop filter (the smallest diameter area of the tube). The electron trajectories through the diode up to downstream uniform B-field region are shown in Figure 5.15. These pictures show that the electrons pass through the waveguide geometry and form an axis-encircling beam, a view of which is clear to see in Figure 5.15b. There is an unproportional amount of reflected electrons shown in this trajectory plot. These electrons amount for less than 1mA, compared to the electron current of ~1.5A. At the end of the beam tube the thickness of the electrons can be calculated from their trajectories at the point of maximum magnetic field, shown in Figure 5.16.
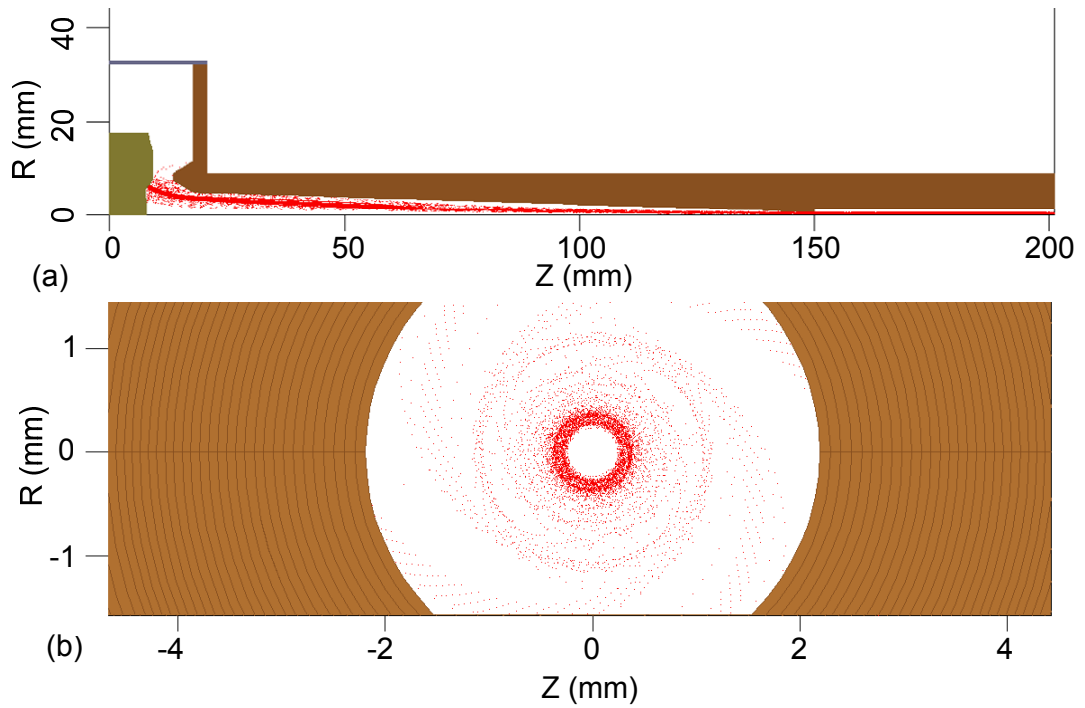
Figure 5.15. MAGIC simulated electron trajectories at 1.82T cavity field showing (a) the beam in the *r-z* plane with the full geometry and (b) cross-sectional shape at the downstream region.
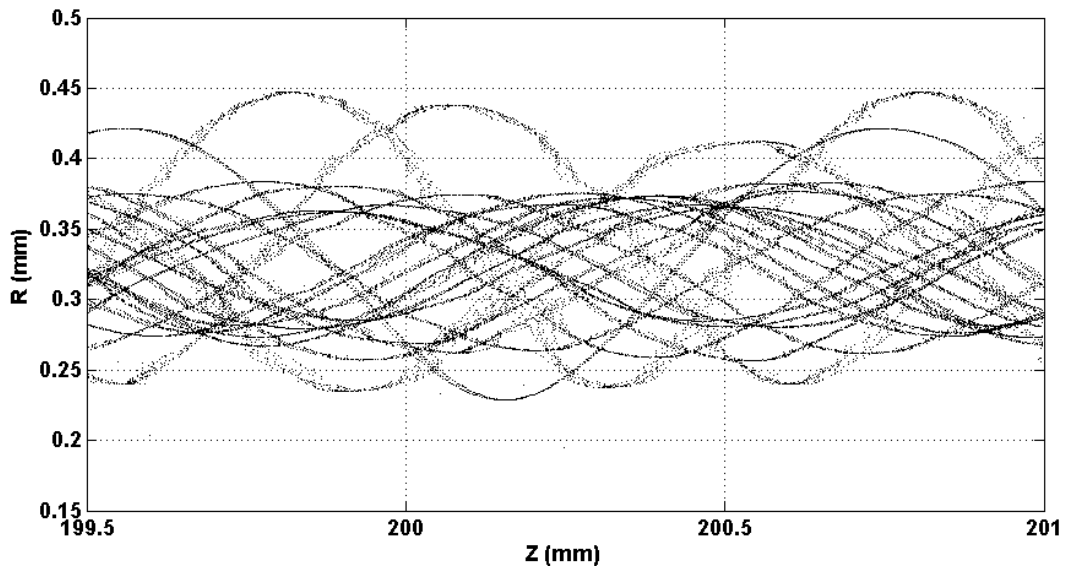
Figure 5.16. Trajectories of the electron beam at the plateau magnetic field region ($B_z = 1.82$T).

The exact properties of this beam can be seen in Table 5.6. This shows that this beam has a thickness of ~0.2mm corresponding to a spread of 60%. This spread is larger than targeted.

Minimum radius	0.229mm
Maximum radius	0.421mm
Average radius	0.325mm
Radius spread ($\Delta r / r$)	59.2%
Envelope ripple	15%

Table 5.6. Properties of the electron trajectories at magnetic field plateau region, $B_z = 1.82$T.

5.2.2.7 Electron beam current and voltage

The design of the waveguide interaction region sets the value of the electron beam current and voltage that should be generated by the cathode. Measurement of how much of these two properties are transported along the waveguide allows one to measure the beam power produced by the electron gun and compare that value to the target set for the electron gun.

In this MAGIC script an accelerating voltage pulse was applied to the cathode and focusing electrodes, as shown in Figure 5.17. This graph shows the voltage pulse rises to 40kV after ~1ns and stays steady after that time. The slow rise of the voltage is important in the MAGIC simulations to avoid effects associated with a sharp application of voltage.
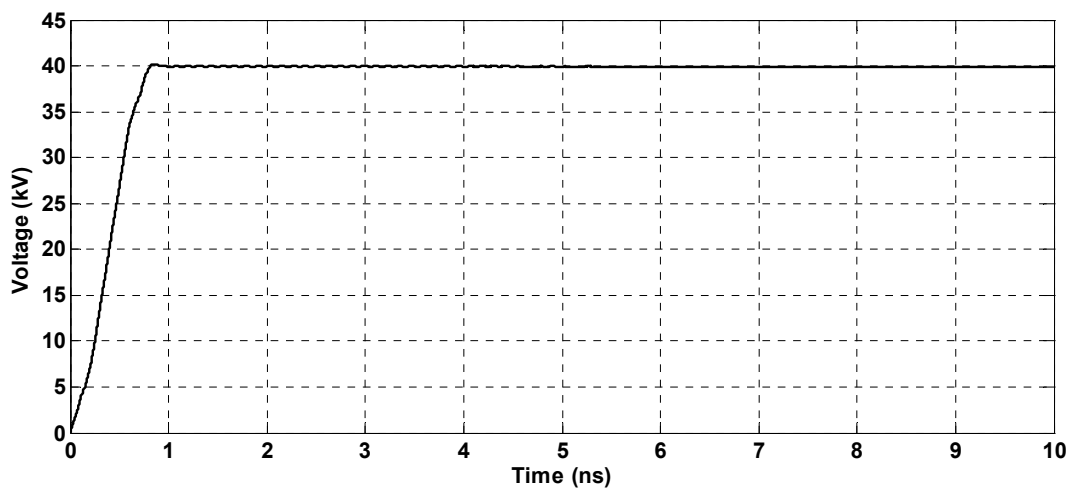
Figure 5.17. The 40kV accelerating voltage pulse produced using MAGIC.

Another diagnostic was used to measure the current emitted from the cathode, with a plot of this as a function of time shown in Figure 5.18. This current is shown for two cases, one with a gap between the emitting surface and the focusing electrodes and one without this gap. This shows how much current was emitted from the emitting surface and from inside the gap. The cathode surface emitted 1.5A after ~0.6ns, while this rises to 1.57A with the inclusion of gaps at the emitting surface, showing 0.07A is emitted inside the surface, due to electric field penetration inside the gaps.

The electron beam current at the downstream uniform magnetic field is a vital diagnostic as this allows calculation of the transported electron beam current to show what percentage of the electron beam is reflected or transmitted. This can be seen in Figure 5.19 as a function of time, showing after 10ns the transported current is 1.56A corresponding to 99.9% of the current transmitted through the tube which meets the target for the electron gun design.
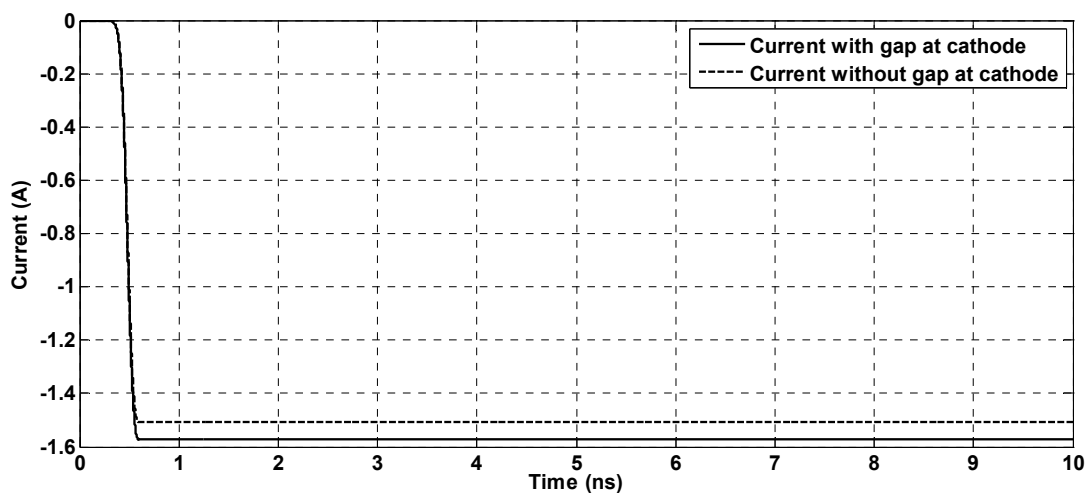
Figure 5.18. Emitted electron beam currents with and without gaps at the emission surface showing an emitted current of 1.57A and without gaps showing an emitted current of 1.5A.

As the accelerating voltage is slowly increased over 1ns, the electrons emitted over this time will have a much lower energy than designed and will thus suffer from magnetic mirroring. This causes reflection of the electron beam and an effect that does not fully stop until almost the end of the simulation time. It is worth noting that the transported current shows a larger current at an emission time of ~3.4ns and then

stays larger until near the end of the simulation time. This can be explained by the low energy electrons at the beginning of the simulation, which are slowed down, and so travel to the end of the waveguide with other electrons which have since caught up, causing a surge of electrons to impact on the diagnostic area.
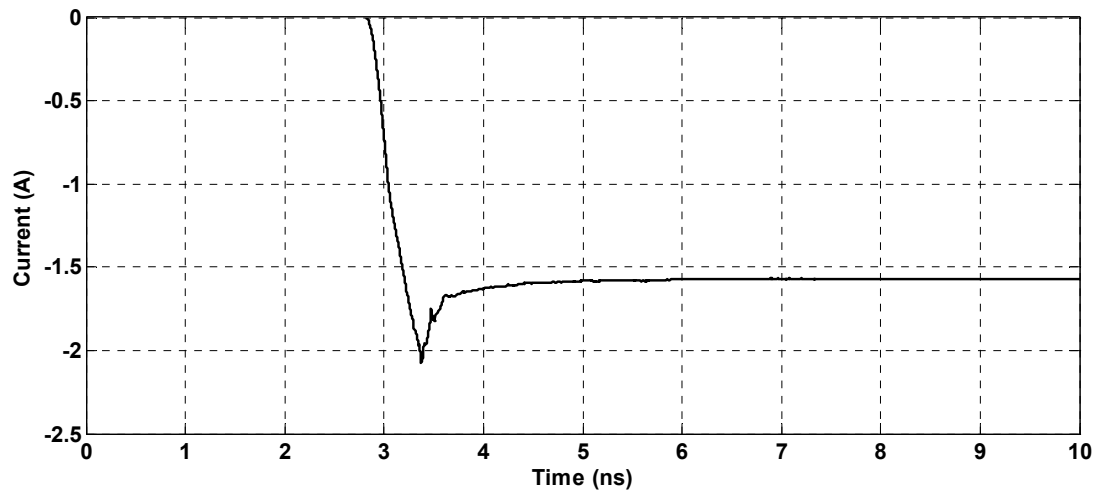
Figure 5.19. Transported current through the beam tube as a function of time showing electron current transport of 99.9% after a few ns's.

The low energy electrons emitted at during the rise-time of the applied voltage reflect due to a magnetic mirroring effect and impact on various parts of the diode, this current must be measured in order that this is not significantly high. A large reflected electron current would result in heating of the beam tube and possibly contamination of the vacuum. This measurement can be shown in Figure 5.20 with a measured current at the anode, anode cone and waveguide. The biggest current is at the anode cone which registers at 47mA; however, it is evident that these recorded currents are over a very small time period and so are not thought to be an area of concern for manufacture of the electron gun.

5.2.2.8 Pitch angle and axial velocity spread

The two parameters of the electron beam that determine the eventual interaction strength and efficiency of the gyro-BWO are the spreads in velocity ratio, α, and axial velocity. The alpha value of the electron beam is a measure of the ratio of
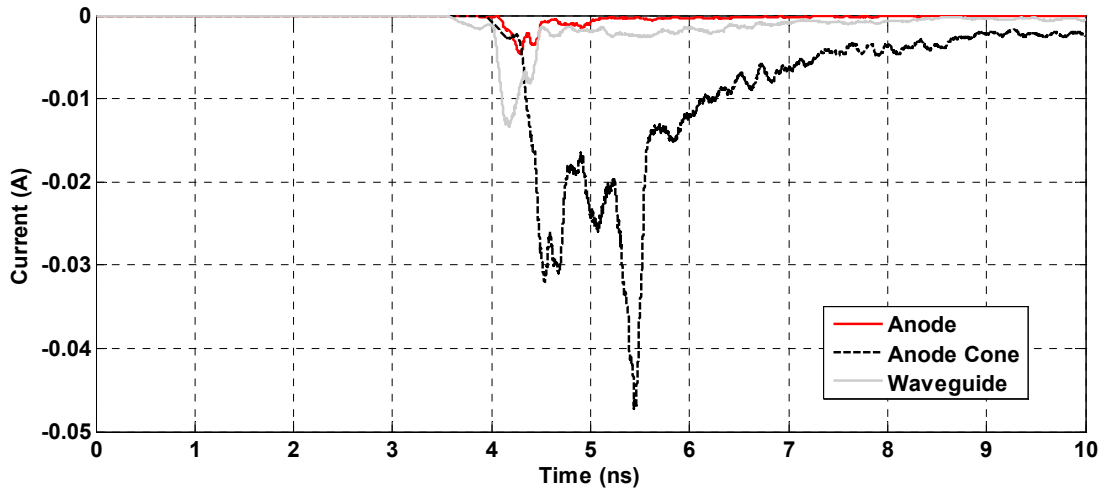
Figure 5.20. Collected electron current at various parts of the electron gun showing the low reflected current of a few tens of mA's ~5ns after the voltage is applied.

perpendicular to parallel velocity $\alpha = v_\perp / v_\parallel$. Since it is only the transverse velocity. that participates in the interaction, this is a measure of the amount of the electron beam energy that is available for the interaction. The axial velocity spread will result in Doppler shift of the electron cyclotron frequency therefore larger axial velocity spread will give rise to low beam-wave interaction efficiency.

The alpha value sought is designed at ~1.65 determined through the dispersion for the gyro-BWO and numerical simulations previously performed for high power output. The alpha value as a function of the *z*-axis was observed in the simulation and is shown in Figure 5.21. Clearly shown here is the rise in the alpha value along the waveguide tube due to the rise in magnetic field. There are two stray beam lines shown here with a very large alpha value. These are emitted from inside the cathode gap and for the purpose of these calculations are not taken into consideration when measuring the alpha value, average value and spread. The alpha value at the end of the beam tube where the magnetic field strength is 1.82T is shown in Figure 5.22.
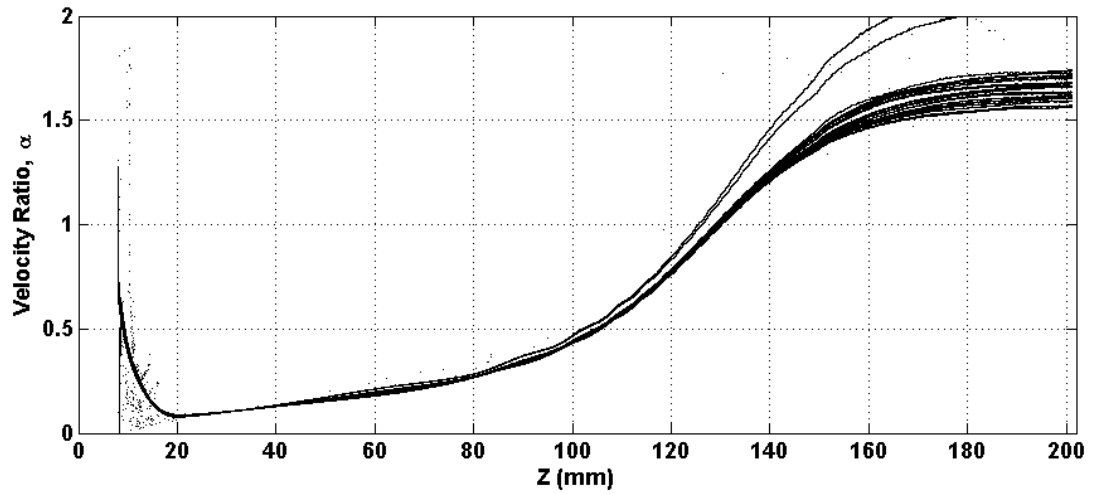
Figure 5.21. Simulated velocity ratio (alpha) of the electron beam as a function of axial position. Measured with a magnetic field at the uniform downstream region of B_z=1.82T.
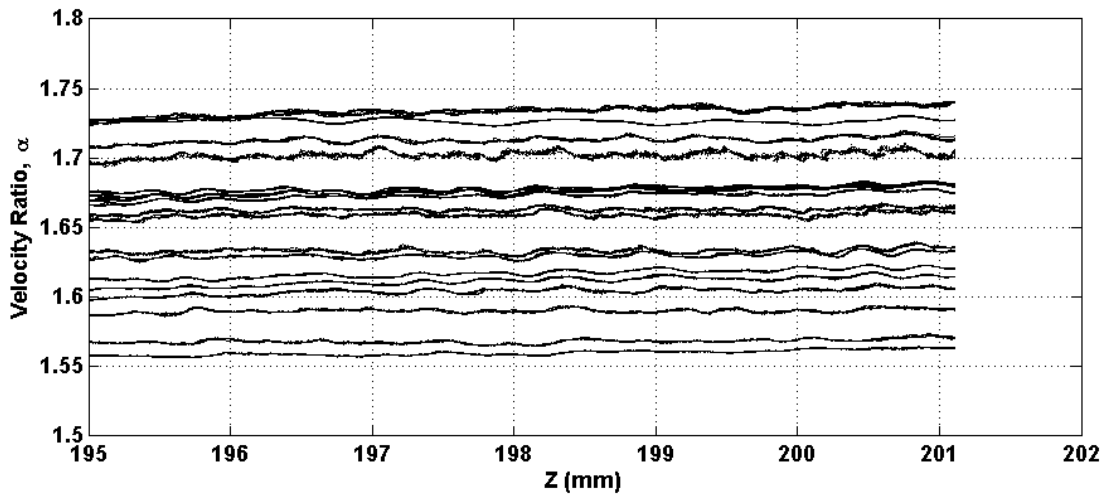
Figure 5.22. Velocity ratio, α , at the plateau magnetic field region $B_z = 1.82$T.

At this point the magnetic field is at the uniform end of the solenoid so the alpha value is also used for beam-wave interaction. This measurement was taken at a magnetic field of 1.82T and the results can be seen in Table 5.7.

Minimum alpha value	1.56
Maximum alpha value	1.74
Average alpha value	1.65
Alpha spread ($\Delta\alpha / \alpha$)	10.7%

Table 5.7. Simulated velocity ratio alpha, α, values at $B_z = 1.82$T.

127

The average alpha and alpha spreads were in-line with the targeted values. The alpha spread at 10.7% is much lower than comparable electron guns which produced alpha spreads ~30%.

The axial momentum of the electrons along the axial position is shown in Figure 5.23. This shows the two electron beamlets trajectories with a much lower axial momentum than the rest of the electron beam, with these coming from inside the gap at the emitter. If it is assumed that there is a negligible difference in electron mass from the lower and upper values of the momentum then the axial velocity spread can be found from

$$\frac{\Delta v_z}{v_{z,av}} = \frac{\Delta m v_z}{m v_{z,av}} = \frac{\Delta P_z}{P_{z,av}}$$ (5.9)

Where P_z is axial momentum, $P_{z,av}$ is average axial momentum, v_z is axial velocity and $v_{z,av}$ is average axial velocity.
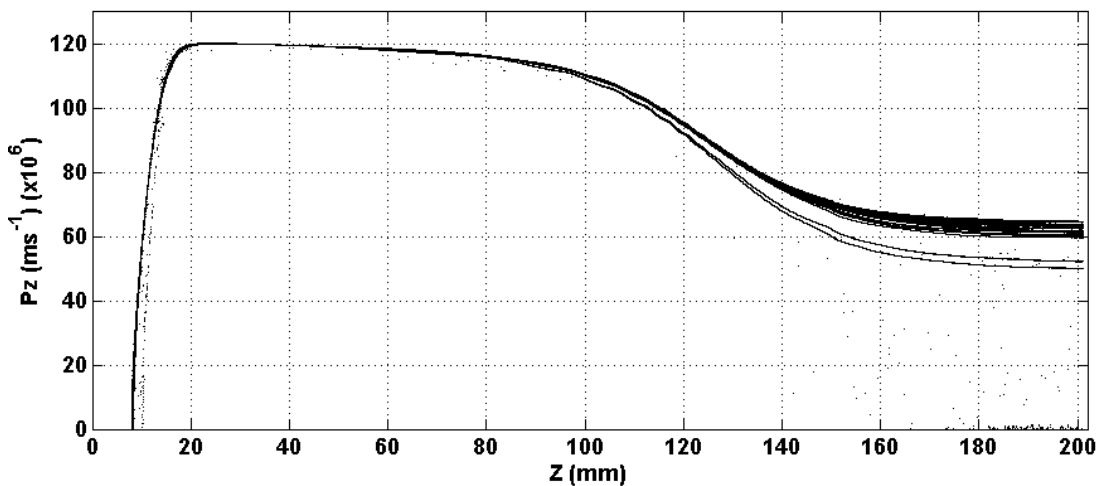
Figure 5.23. Simulated axial momentum of the electron beam as a function of axial position.

The axial momentum at the downstream uniform magnetic field region at 1.82T is shown in Figure 5.24. Analysis of this axial momentum allows calculation of the axial velocity spread and the values obtained are given in Table 5.8. The axial velocity spread is within the design target.
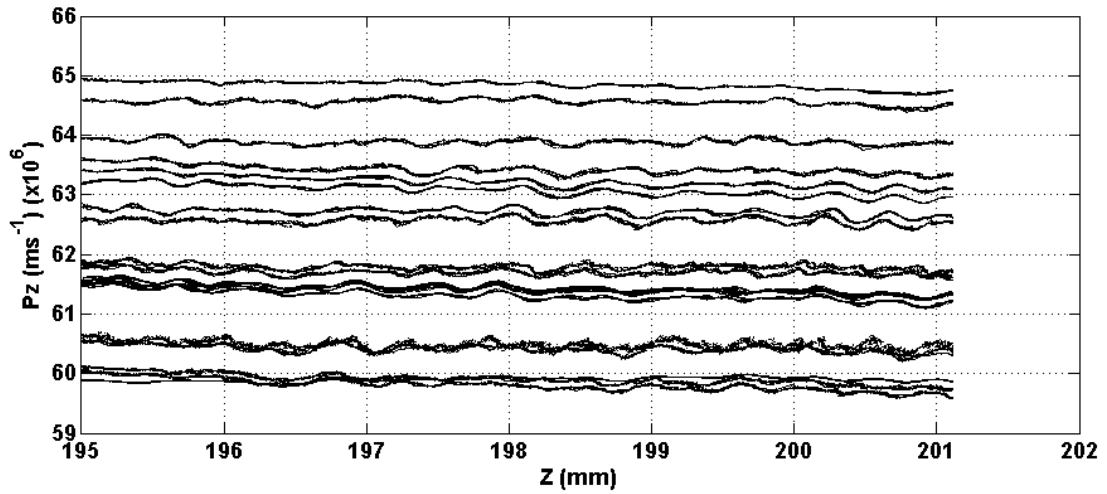
Figure 5.24. Axial momentum at the plateau magnetic field region B_z = 1.82T.

Minimum axial momentum value	59.7 $\times 10^6$ ms^{-1}
Maximum axial momentum value	64.7 $\times 10^6$ ms^{-1}
Average axial momentum value	62.2 $\times 10^6$ ms^{-1}
Axial velocity spread ($\Delta v_z / v_z$)	8.1%

Table 5.8. Values of axial momentum and corresponding axial velocity spread at the plateau magnetic field region, B_z = 1.82T.

5.2.2.9 Variation of magnetic field and different combinations of electron beam properties

The interaction frequency can be tuned through adjusting parameters of the electron beam such as accelerating voltage, alpha as well as the cavity magnetic field strength.. In order to change the alpha values of the electron beam, the magnetic field at the cathode can be changed. The alpha value as a function of magnetic field at the cathode is shown in Figure 5.25 at a fixed cavity magnetic field of 1.82T. The effect of varying the alpha value changes the electron beam dispersion line so different interaction frequencies can be achieved, this is shown in Figure 5.26.
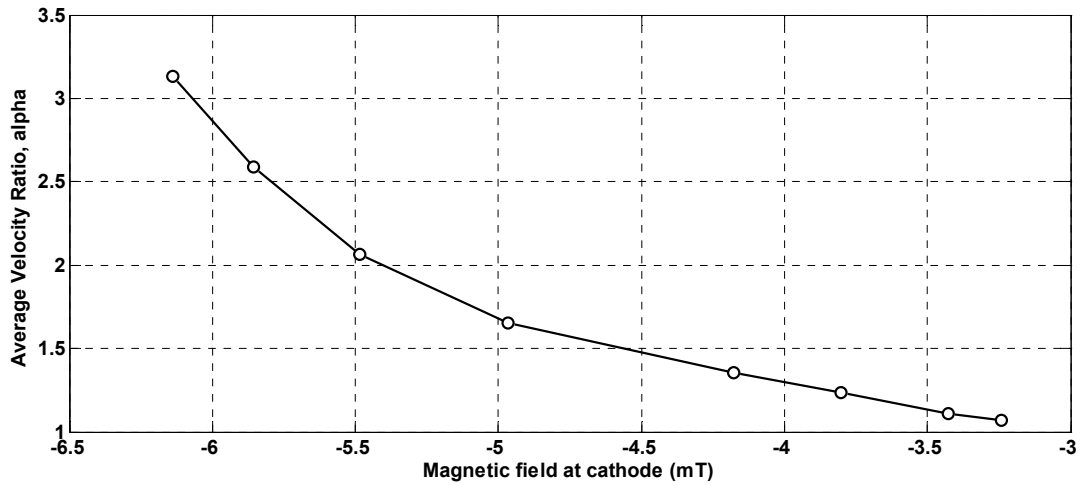
Figure 5.25. Alpha value as a function of magnetic field at the cathode surface. The cavity magnetic field is kept constant at B_z=1.82T.
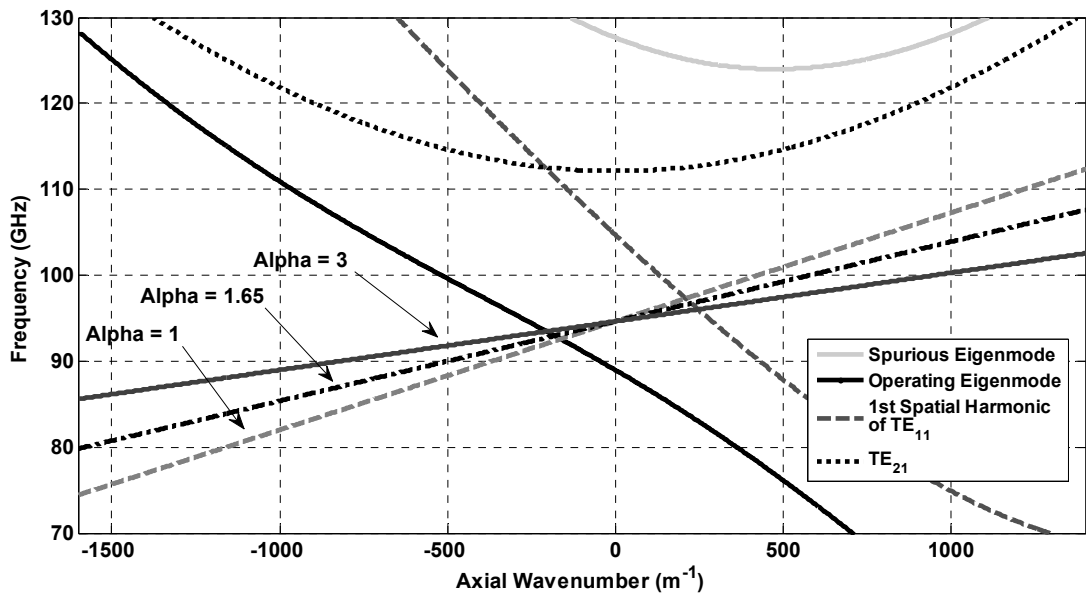
Figure 5.26. Helically corrugated waveguide with electron beam dispersion with different values of velocity ratio alpha from 1 to 3 at a fixed cavity field of 1.82T. The analytically calculated values of the circular TE_{11} and TE_{21} waveguide modes are also shown.

While the cathode magnetic field is swept in order to change the value of alpha over the range of 1 to 3, the electron beam qualities (alpha and axial velocity spreads) will be affected. This can be seen in Figure 5.27 where the plateau of the electron beam qualities is at the desired interaction parameter of -4.97mT corresponding to an alpha of 1.65.
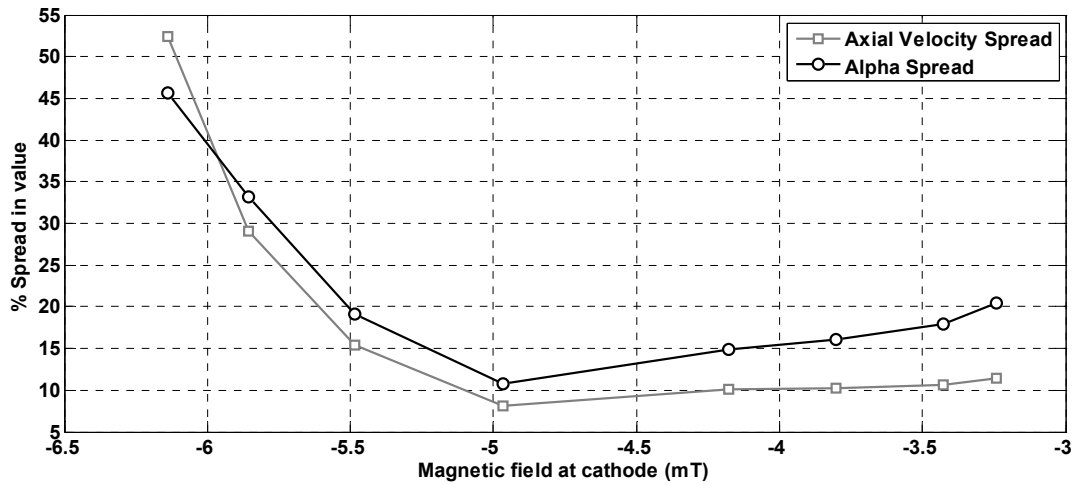
Figure 5.27. Simulated values of axial velocity and alpha spreads as a function of cathode magnetic field strength.

The designed beam voltage is 40kV but the gyro-BWO is tuneable in frequency when the voltage changes so the electron gun had to pass through the beam tube with an acceptable beam quality over a range of voltages. It was found that when the beam voltage varied from 35-45kV the large orbit beam was still fully transported to the downstream cavity region. However, with a constant magnetic field configuration the beam alpha would be different and so some adjustment in the reverse coil strength would have to be made through the range of voltages. The alpha value was 2.46 and 1.35 for 35kV and 45kV respectively.

The effect of changing the beam voltage on the electron beam dispersion line can be seen in Figure 5.28. As the voltage changes from 35kV to 45kV the interaction frequency is tuned from 92GHz to 98GHz respectively. The electron beam quality also varies over this voltage range, as shown in Figure 5.29. The plateau of the electron beam quality curve is centred on the designed voltage of 40kV showing the optimised electron gun design. Throughout the range of voltages the electron beam maintained an acceptable quality, defined as the axial velocity and alpha spreads.
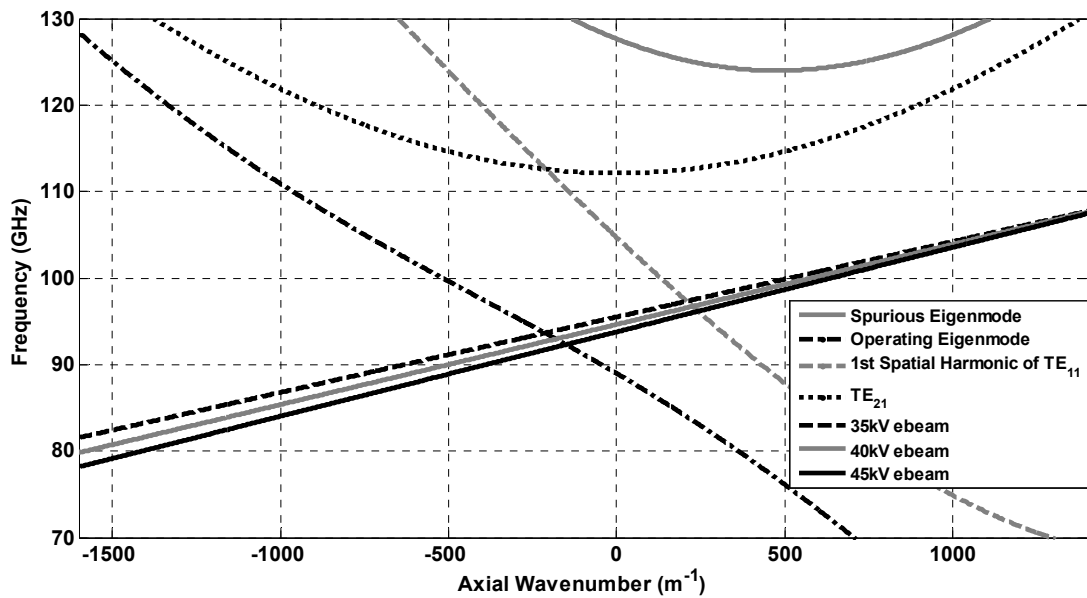
Figure 5.28. Helically corrugated waveguide dispersion against different values of the electron beam dispersion line with an acceleration voltage of 35, 40 and 45kV at a fixed magnetic configuration. The analytically calculated values of the circular TE_{21} and TE_{11} waveguide modes are also shown.
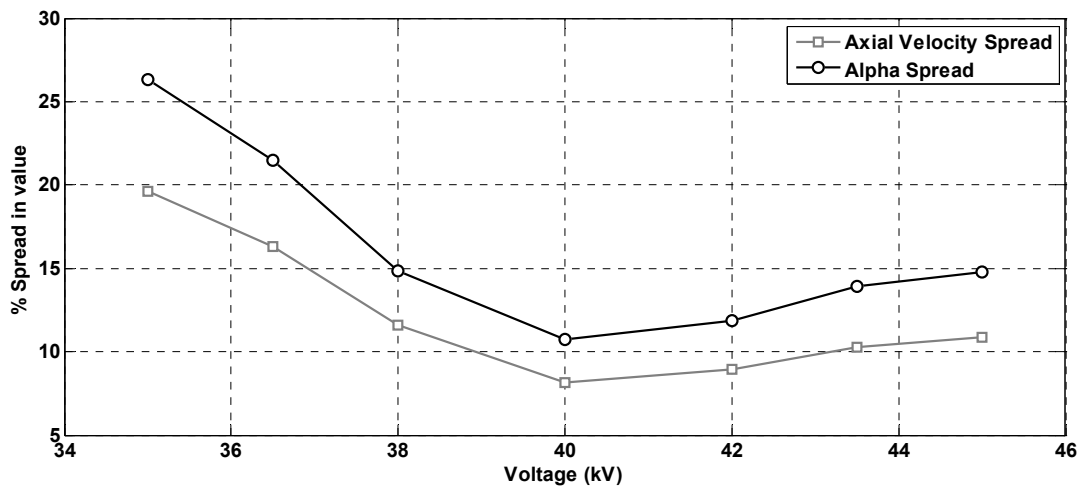
Figure 5.29. Simulated axial velocity and alpha spreads as a function of the beam voltage. The average alpha and cavity magnetic field is kept constant at 1.65 and 1.82T respectively.

If the constant alpha value is required when the voltage is changed the cathode magnetic field, and so reverse coil current, would have to be adjusted for each value of accelerating voltage. The range of cathode magnetic field that kept alpha at 1.65 with a cavity magnetic field of 1.82T is shown in in Figure 5.30.
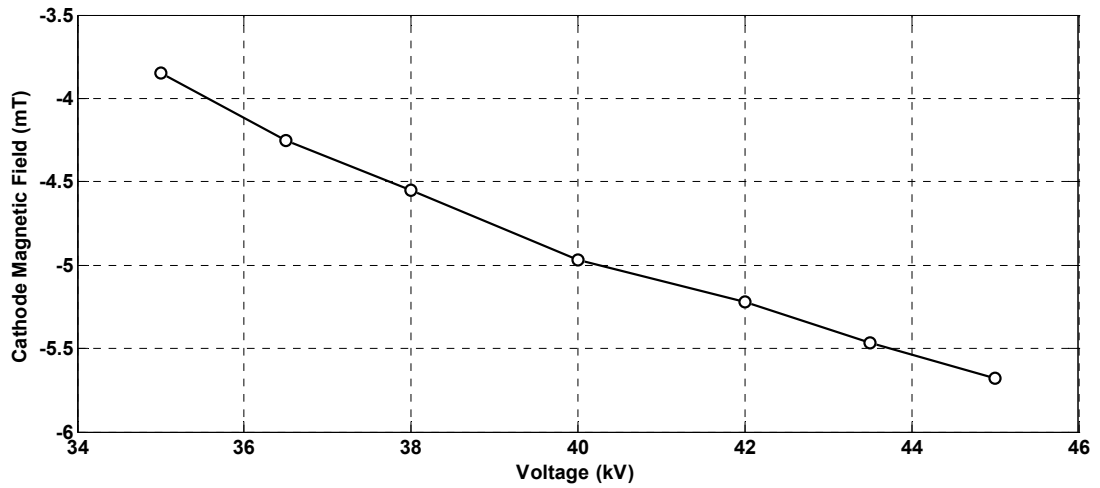
Figure 5.30. Variation in cathode magnetic field required to keep a constant alpha (=1.65) as the applied voltage is swept from 35kV to 45kV.

Changing the cavity magnetic field strength allows the frequency of interaction to be changed to any desired frequency over the full range of the gyro-BWO interaction, 85-105GHz. This has a stronger effect on the electron beam line than any other method of frequency adjustment. The dispersion for different values of cavity magnetic field strength can be seen in Figure 5.31. In this dispersion diagram, it is clear to see that the maximum achievable magnetic field strength is 2.1T as a higher magnetic field would result in stimulation of the parasitic TE_{21} mode.
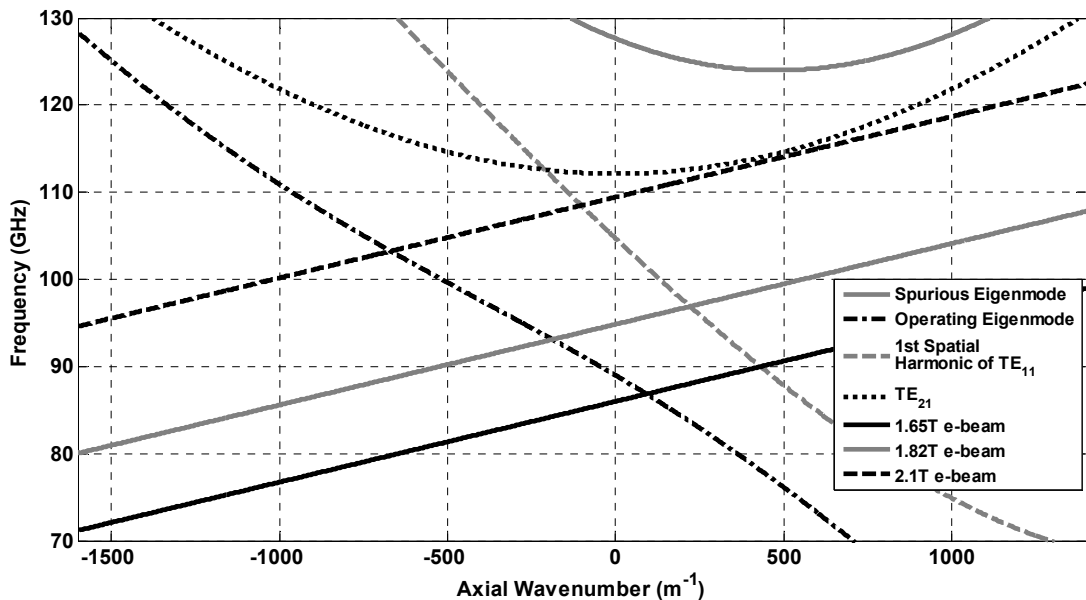
Figure 5.31. Helically corrugated waveguide dispersion against electron beam dispersion with a cavity magnetic field of 1.65T, 1.82T and 2.1T.

133

The axial velocity and alpha spreads were simulated in the operating cavity magnetic field region and is shown in Figure 5.32. Since the geometry of the cusp electron gun was optimised for the centre frequency of 94GHz i.e. at a magnetic field of 1.82T. The simulation at a different magnetic field would be an un-optimised setup so by changing some of the variables such as reverse coil position, cavity coil position and applied voltage these results can be improved.
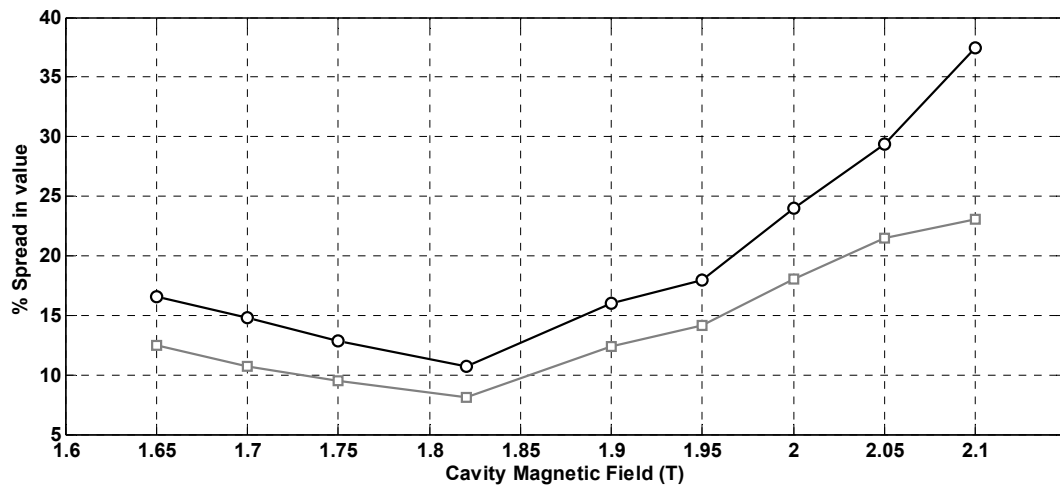
Figure 5.32. Alpha and axial velocity spreads as the cavity magnetic field is swept from 1.65T to 2.1T. The magnetic field at the cathode is adjusted in order to keep the alpha constant at 1.65.

To obtain a constant value of alpha in the gyro-BWO operating regime which required a cavity magnetic field of 1.65T – 2.1T the cathode magnetic field must be changed in accordance with the change in the cavity magnetic field. The value of the magnetic field at the cathode as a function of the cavity magnetic field required to generate an alpha value of 1.65 is shown in Figure 5.33.

5.2.3 Opera-3D simulation

To verify the simulation results from MAGIC another code, Opera-3D, was used. The electromagnetic code produced by Vector Fields called Opera-3D (**OP**erating environment for **E**lectromagnetic **R**esearch and **A**nalysis) is a program that can be used to solve many different problems and is a widely recognised accurate electron gun code. This code includes many different elements: TOSCA, ELEKTRA SCALA,
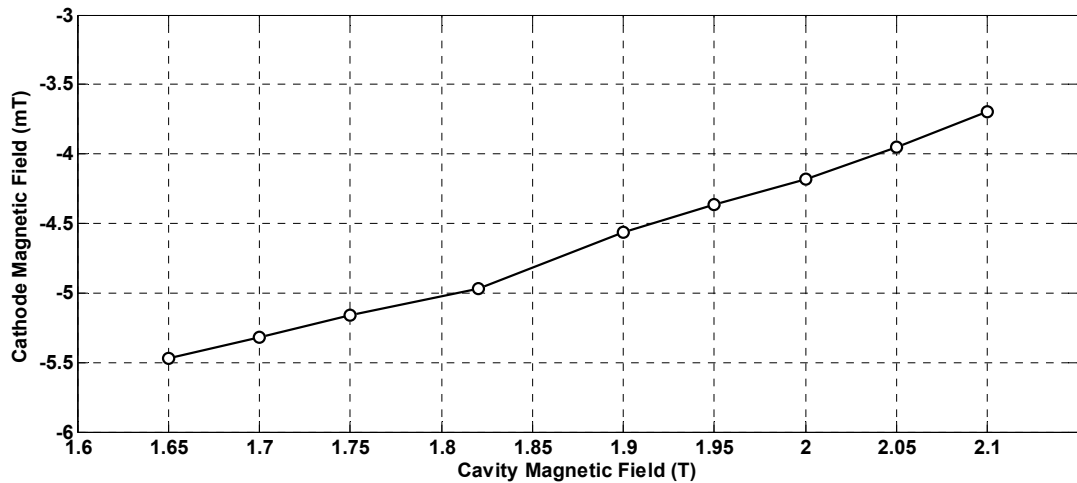
Figure 5.33. Values of the magnetic field at the cathode required to keep a constant alpha (= 1.65) as the cavity magnetic field strength is changed.

CARMEN, SOPRANO, DEMAG, QUENCH and TEMPO. The programs used within this work are TOSCA and SCALA, which are used to measure magnetic field and particle trajectories, respectively. SCALA is able to analyse charged particle beams, modelling the emission through different processes of the users choice, and the space charge effects caused by these beams. TOSCA is able to solve for magnetostatic or electrostatic fields[181] in three dimensions. This is achieved by breaking the model down into total and reduced scalar potentials, which are then, solved using finite elements.

The program can create complex models by creating solid objects, and then performing different types of Boolean operations on them, for example adding shapes together or intersecting them. The program uses a finite element mesh of first and/or second order tetrahedral shapes, the size of which are controlled by the user. This allows for perfect straight lines and well defined curves.

5.2.3.1 Simulation parameters

The Opera-3D simulation replicates the geometry that was constructed in MAGIC in order to validate those results. This is constructed in 3D using solid objects and then Boolean operations are performed to produce the desired shape. The 3D geometry can be seen in Figure 5.34. Since this geometry is fully axially symmetric a

135

10 degree segment, also shown in Figure 5.34, is simulated as if it were fully 360 degrees through symmetrical boundary conditions. This saves simulation run-time while still producing accurate results. Also, this allows for a higher meshing density as meshing the full structure with a small mesh would become a very large problem for computational solvers.
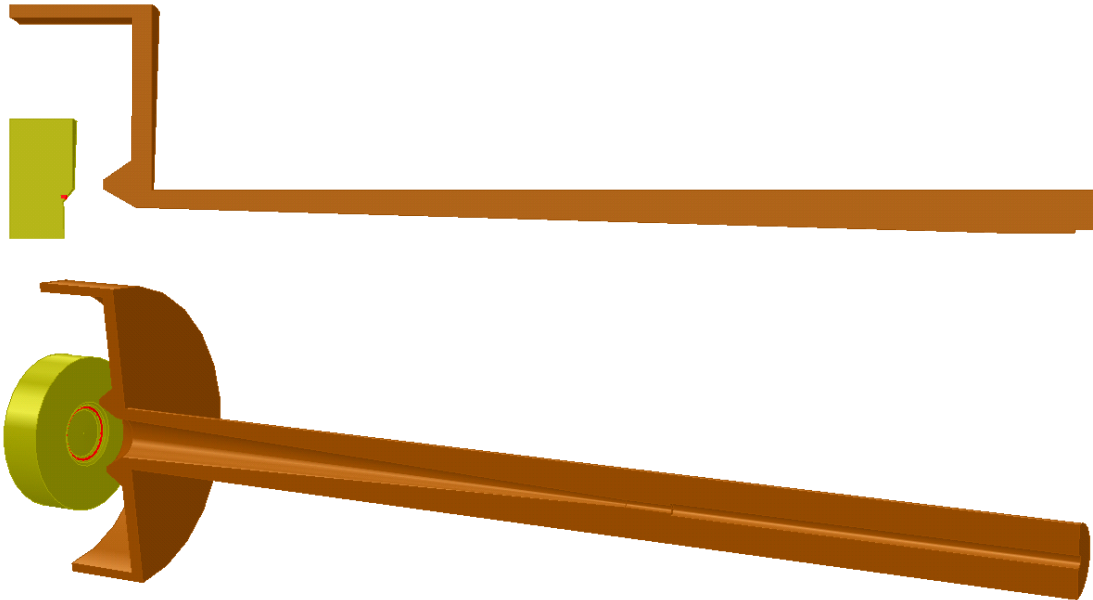
Figure 5.34. Diode geometry as represented in Opera-3D. The top view is a 10 degree segment of the 360 degree structure. The bottom view is the full electron gun with the anode and beam tube shown in half for clarity.

The emitter can be seen in Figure 5.35 with the anode (dark blue) focusing electrodes (light blue) and cathode (green) shown.

The solenoids are also displayed in Opera-3D while in other simulation programs they are hidden and the magnetic field profile is simulated by those programs only. These solenoids are build up through defining the geometry of the solenoid wires as a bulk mass, and then giving the current density through the mass. The solenoid designed in the MAGIC simulations took into consideration water channels however in Opera-3D these water channels must be ignored and the wires are assumed to be pressed against each other with no spaces between them. The geometry of the solenoids can be seen in Figure 5.36.

Figure 5.35. A detailed view of the cathode emitter with top and bottom electrodes in Opera-3D.
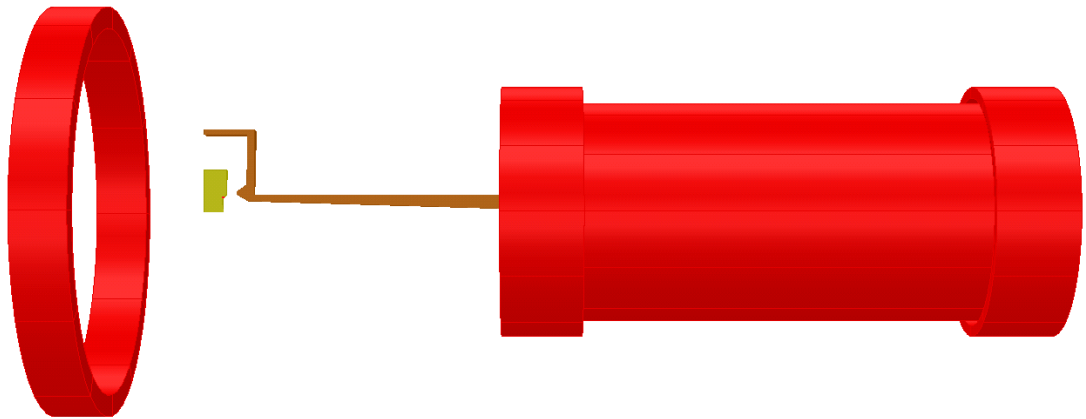
Figure 5.36. Position of solenoids in Opera-3D shown against size of the cusp electron gun.

The data used to produce these solenoids is given in Table 5.9, which comes from the solenoid simulated in MAGIC. The outer and inner radii of the coils are found throught the design for the constructed solenoid, see Chapter 6 for more details.

5.2.3.2 Simulated electron trajectories and comparision to MAGIC results

The electrons are emitted from a 10 degree segment but Opera-3D projects the electron beam around the full 360 degree axis as shown in Figure 5.37. Uniform emission is observed in this area, since the magnetic field is negative in this area,

before changing to positive. The electrons rotate after passing the cusp but the effect does not become apparent until later in the beam tube.

	Reverse coil	Cavity solenoid	1st Shim coil	2nd Shim coil
Start position (mm)	-60	123	123	316.6
Inner radius (mm)	75.6	14.1	47	47
Outer radius (mm)	84.4	44.6	51.4	51.4
Axial length (mm)	22	226.6	33	33
Current density (A/cm^2)	44.4	48.7	48.7	48.7

Table 5.9. Properties of the solenoids defined in Opera-3D simulation code.
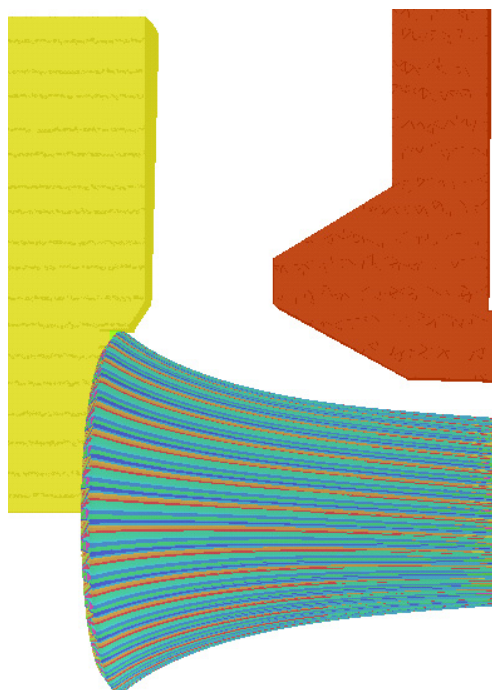
Figure 5.37. Simulated electron trajectories between the cathode and anode.

The beam trajectories at the downstream region are shown in Figure 5.38. This shows the thickness of the electron beam. The electron trajectories from only one segment of the cusp gun are shown in Figure 5.38b, which clearly shows an axis-encircling behaviour. As the magnetic field increases the electrons gyrate faster due to larger cyclotron frequency and with smaller Larmor step due to smaller axial velocity.

(a)

(b)
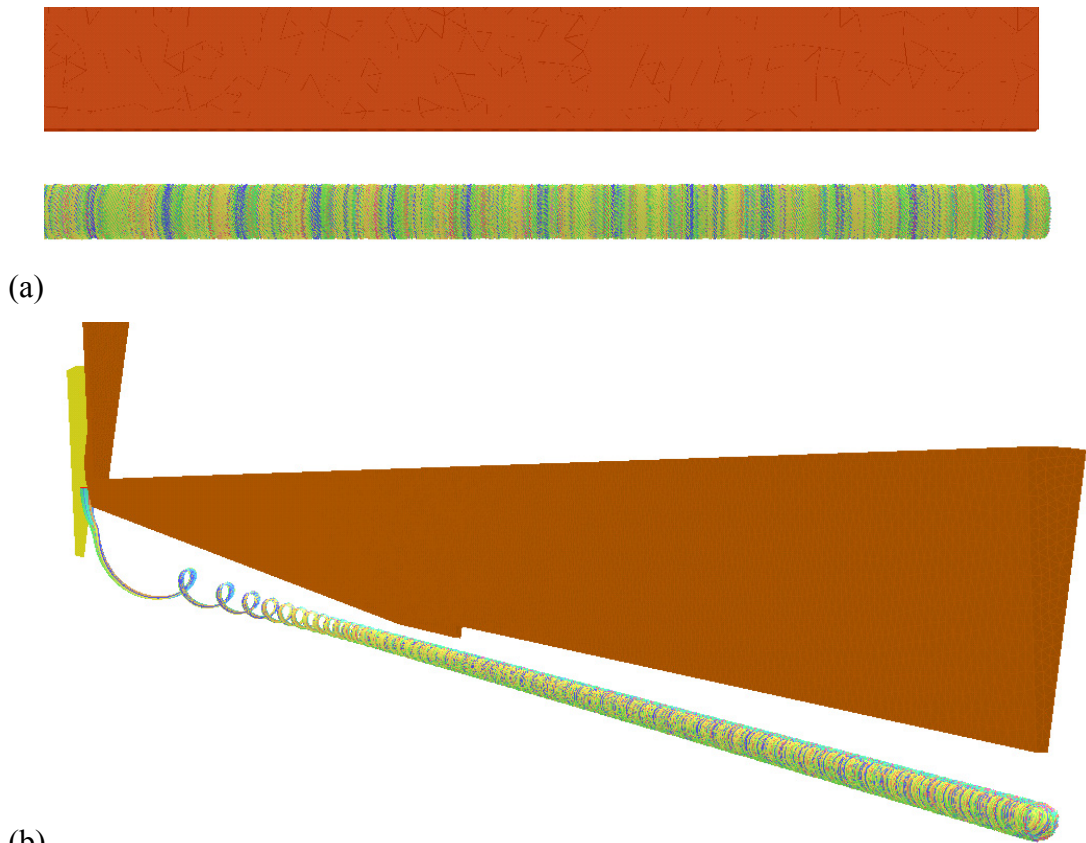
Figure 5.38. Trajectories of the electrons from the cusp electron gun as simulated in Opera-3D.

The electron beam transport through the beam tube can be found in Opera-3D by creating a circular diagnostics at the end of the beam tube and in front of the cathode Through integrating the number of electrons impacting both diagnostics, a measurement of the electron beam transport can be made. No electrons are found to be lost within the beam tube in the simulation using Opera-3D.

The properties of the electron beam at a cavity magnetic field of 1.82T and alpha of 1.65 are shown in Table 5.10. These results show that the electron beam had similar trajectories to the MAGIC simulation predictions. The average radius and radius spreads were almost the same which gives confidence in the both the Opera-3D and MAGIC simulations.

Beam properties	Opera-3D	MAGIC
Inner radius of beam (mm)	0.22	0.23
Outer radius of beam (mm)	0.41	0.42
Average radius of beam	0.315	0.325
Spread in beam radius (%)	60.3	59.2

Table 5.10. Simulated properties of the electron beam trajectory.

5.2.3.3 Axial velocity and pitch angle spread and comparision to MAGIC results

The axial velocity of the cusp electron beam was measured along the axial position and is shown in Figure 5.39. The change in axial velocity over the entire length of the beam tube shows a similar profile to that of the MAGIC simulations (Figure 5.23).
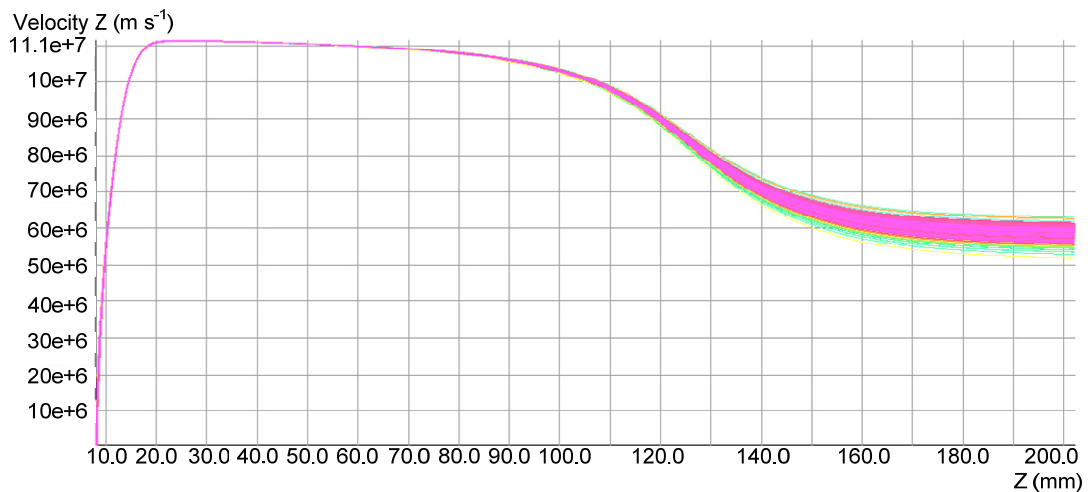
Figure 5.39. Simulated axial velocity of the cusp electron beam using Opera-3D.

In order to make a quantitative measurement of the axial velocity spread in these simulations the electron beam velocities at the uniform downstream magnetic field region has to be investigated further and this is shown in Figure 5.40.
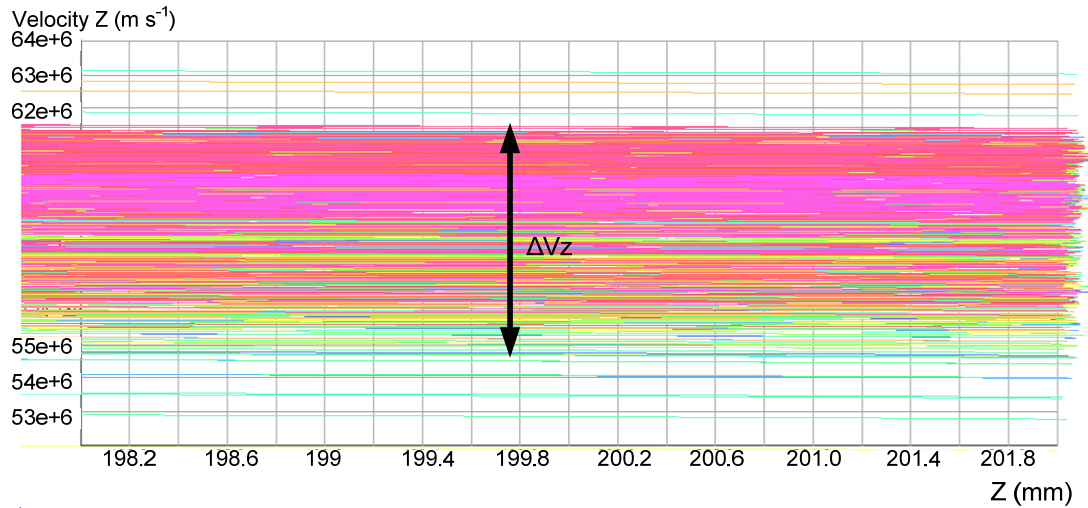
Figure 5.40. Simulated axial velocity and its spread in value using Opera-3D.

Viewing the measurement of axial velocity at the downstream region one can see that there is a very dense region of electron beam energies in-between the values of 55×10^6 ms^{-1} and 62×10^6 ms^{-1}. Out with this region are velocities for some stray electrons. One can take the dense electron beam, highlighted in this figure, as being the values used in determination of the axial velocity spread. The electron beam trajectories out with the main beam account for an insignificant percentage of the beam and can thus be ignored otherwise they artificially significantly affect electron quality values. In such measurement the axial velocity spread was calculated as 11.2% through the values given in Table 5.11. The comparative MAGIC values are given also in this table and a good agreement in the results is shown.

Beam properties	Opera-3D	MAGIC
Minimum axial velocity value	55×10^6 ms^{-1}	59.7×10^6 ms^{-1}
Maximum axial velocity value	61.5×10^6 ms^{-1}	64.7×10^6 ms^{-1}
Average axial velocity value	58.3×10^6 ms^{-1}	62.2×10^6 ms^{-1}
Axial velocity spread ($\Delta v_z / v_z$)	11.2%	8.1%

Table 5.11. Velocity ratio alpha values for the cusp electron gun at B_z=1.82T.

The simulated alpha values along the axial position of the cusp electron gun can also be measured in Opera-3D and is shown in Figure 5.41. This graph is very similar in profile to the MAGIC simulated values; (Figure 5.21). The alpha spread at the

uniform downstream magnetic field region was ascertained by measuring the alpha spread as a function of axial position as shown in Figure 5.42.
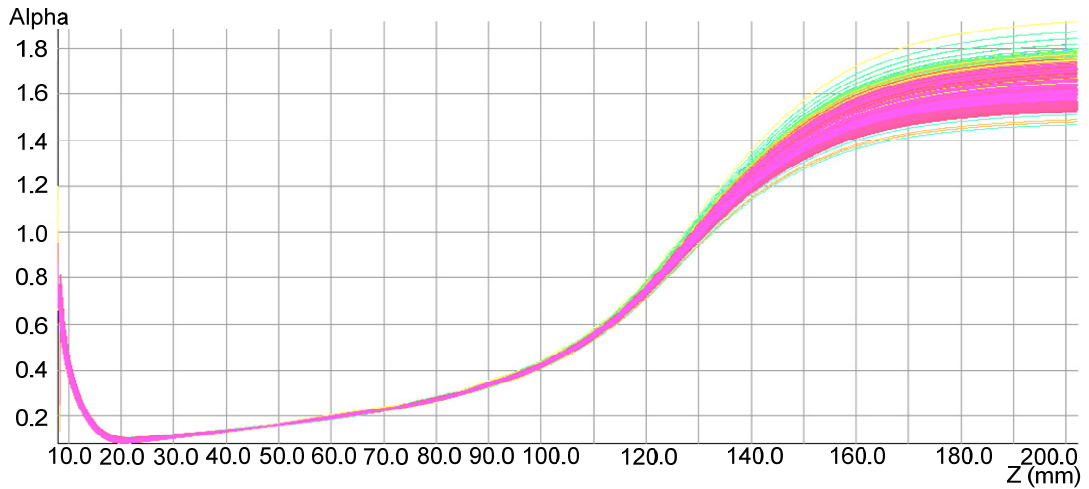
Figure 5.41. Velocity ratio alpha along the axis of symmetry of the cusp electron gun.
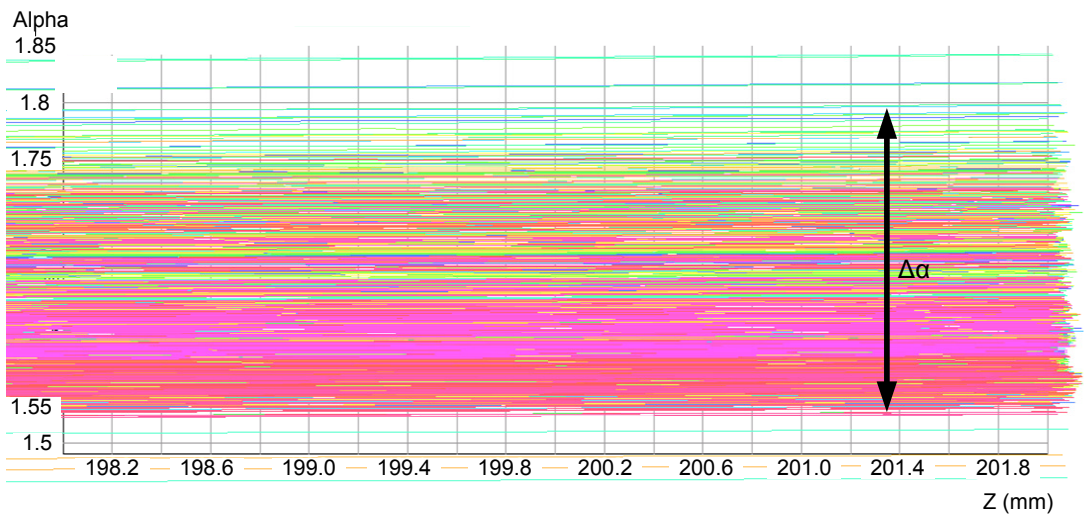
Figure 5.42. Velocity ratio alpha spread at B_z = 1.82T.

The values of alpha show a very dense region, highlighted in the figure, between the alpha values of 1.55 and 1.79. Out with this region are some stray electron beam lines which account for a few 10's of electron beam trajectories when the total amount of electron trajectory values shown is ~1750. So one can see that the stray electrons account for <1% of the total beam so they can be ignored in determination of the alpha spread. The simulated alpha spread is 14.4% at an average alpha of 1.67,

calculated using values given in Table 5.12. This agrees well to the MAGIC values of 10.7%. The current weighted alpha value is 1.66 showing that there was more electrons with a slightly lower alpha value explaining that the current weighted alpha spread would be lower than 14.4%.

Beam properties	Opera-3D	MAGIC
Minimum alpha value	1.55	1.56
Maximum alpha value	1.79	1.74
Average alpha value	1.67	1.65
Alpha spread ($\Delta\alpha/\alpha$)	14.4%	10.7%
Current weighted average alpha	1.66	N/A

Table 5.12. Axial velocity values for cusp electron gun showing the axial velocity spread.

5.2.4 Comparison between MAGIC and Opera-3D

Two particle software packages were used to verify the diode design and the electron beam generated from the cusp electron gun. The results showed a good agreement; however, differences between their results exist and a comparison between the two programs is necessary.

Beam properties	Opera-3D	MAGIC
Average alpha	1.67	1.65
Alpha spread (%)	14.4	10.7
Axial velocity spread (%)	11.1	8.1
Average radius at maximum B-field (mm)	0.315	0.324
Inner radius (mm)	0.23	0.22
Outer radius (mm)	0.42	0.41
Magnetic field at cathode (mT)	-5.02	-4.97
Electron beam transport (%)	100	99.9

Table 5.13. Simulated electron beam properties using Opera-3D and MAGIC so the programs can be compared.

The difference in electron beam transport between MAGIC and Opera-3D allows one

validation of the earlier statement that in MAGIC, the lower electron beam transport and reflected electrons is caused by an inherent effect within the code, and is not a physical effect. This results due to the slow ramp of the voltage pulse. As Opera-3D does not require this slow ramp, the electron beam transport is simulated to be the full 100%.

The two electron beam codes have been compared in past work by D. Rowlands[182] who investigated a cusp electron gun for an X-band gyro-TWT. The alpha values from MAGIC and Opera-3D were in good agreement with that of another code SURETraj. All three codes gave almost the same alpha value i.e. $\alpha = 1.17$ which was very close to the designed value of 1.2. However, as the alpha increases and decreases away from the designed value the difference between the codes increases. A similar phenomena was found for the W-band design of the cusp electron beam.
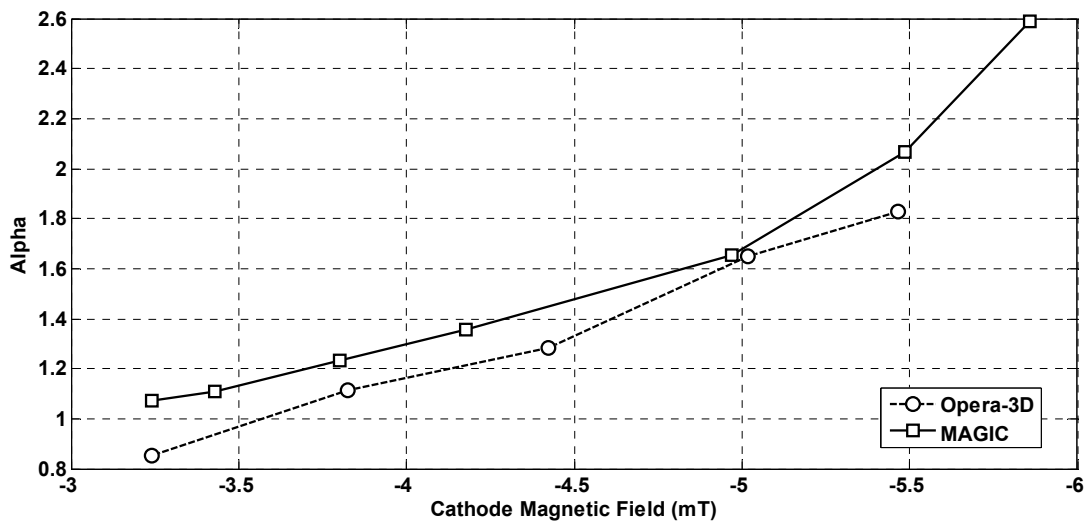
Figure 5.43. Measurement of the alpha produced by varying magnetic field at the cathode.

The magnetic field profile calculated by Opera-3D and MAGIC is shown in Figure 5.44. It is noticeable that while these profiles are in good agreement, there are some differences, particularly in the ramp up region. The discrepancies are largely caused by minor differences between the methods employed by the two programs to describe solenoids. MAGIC defines the solenoid as a series of coils separated by a certain distance while each coil is considered as a circular line of current. Therefore,

if the solenoids based in the MAGIC script were recreated in Opera, the result would not match exactly.
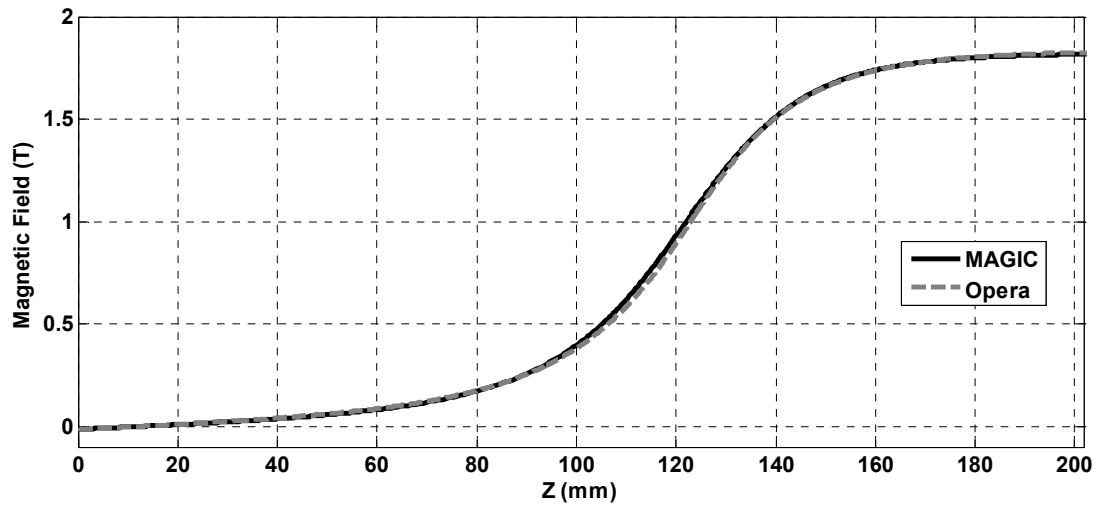
Figure 5.44. Magnetic field profile simulated by Opera-3D and MAGIC along the axis of symmetry.

Overall the two programs give very similar results although the results do not agree exactly. Each program defines geometries and other parts of the simulation in very different ways, so to recreate one program in the other is a rather hard task and minor differences will always occur. For example MAGIC simulates the experiment with the Yee cell meshing and Opera-3D uses finite element meshing. This results in the geometries being not exactly the same, resulting in differences in particle trajectories.

The main points of the simulation are shared between the programs. An axis-encircling electron beam of 1.5A and 40kV is generated through each program, with beam transport of 99.9 to 100% obtained. Additionally, the electron beam quality of alpha spread and axial velocity spread are comparable. These similarities allow one to be confident in the design of the electron gun and for construction to be undertaken, in order to confirm the simulation results. Chapter 6 will discuss the details of the construction of the gyro-BWO device; in Chapter 7 the experiment results will be presented.

5.3 Discussion

In this chapter the design and optimisation of the cusp electron gun was investigated

using the 3D PiC code MAGIC, then verified using the finite element software package Opera-3D. The simulation results of the cusp electron beam were in good agreement between both simulation methods. While the results produced in Opera-3D agreed with the MAGIC simulations over the majority of beam parameters differences existed also. The reasoning for the discrepancies between the two results stems from differences in the codes and the method used in the meshing of the geometry.

5.4 Summary

In this chapter the cusp electron gun was designed, simulated and optimised to produce an axis-encircling annular beam of 40kV, 1.5A with alpha of 1.65. The design was originally simulated in the 3D PiC code MAGIC and optimised through changing the diode geometry. The optimised design produced an electron beam with low axial velocity and alpha spreads at the centre magnetic field strength with acceptable quality over the full magnetic field tuning range. Other factors were investigated for instance the alpha tuning range of 1 to 2 and applied voltage tuning ranges. In each case the electron beam passed through the beam tube without scraping or mirroring and had an acceptable amount of axial velocity and alpha spreads. The optimised electron gun design produced an electron beam of high enough quality in order to drive beam-wave interaction within the gyro-BWO.

Chapter 6.

Gyrotron Backward Wave

Oscillator Experimental Setup

6.1 Introduction

The gyrotron backward wave oscillator design is complicated due to the quantity of parts that were produced along with the required precision of the machining. The many different components that were required and constructed include: two solenoids, a water cooling system for the solenoids, 3-axis mounting system, electron gun, heater coil for the cathode, interaction region, microwave window, vacuum system and power supply system. The full setup of the gyrotron backward wave oscillator can be seen in Figure 6.1 drawing attention to the cathode, reverse coil, cavity solenoid, interaction region and the microwave window. These components are designed in conjunction with the electron beam generated and the frequency of interaction. Presented within this chapter is the individual design of each of the components of the gyro-BWO system, referring to the main parameters that are set from research found in previous chapters. The magnitude of the magnetic field provided by the solenoids and the magnetic wire configuration is decided by results from electron beam simulations. The cathode geometry is designed through electron beam simulation, the interaction region geometry is designed through analytical and numerical calculation and the microwave window is constrained by the frequency of operation.
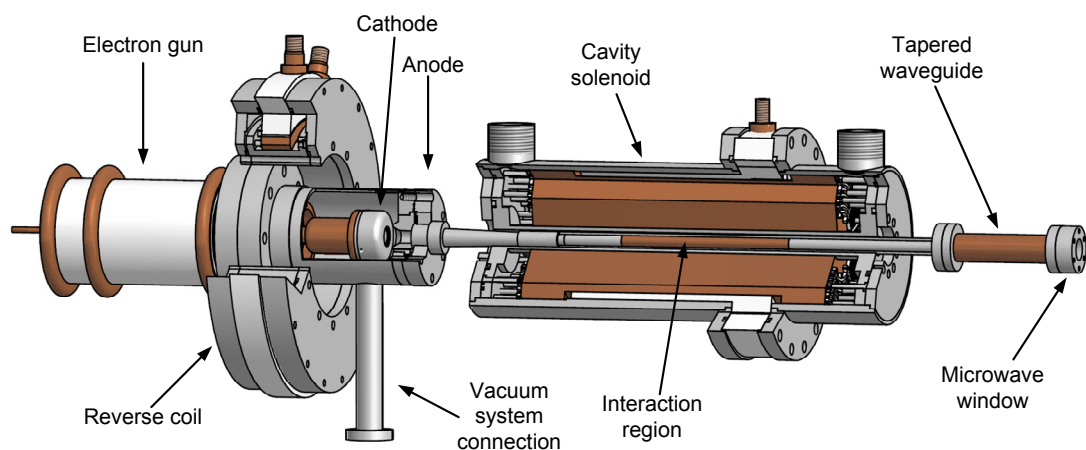
Figure 6.1. The gyro-BWO setup illustrating the main components of the device.

6.2 Cusp electron gun geometry and manufacture

Electron guns are generally very expensive to manufacture and require a lot of time

and testing to make sure they can perform as well as required. To reduce some of the cost the cusp electron gun was manufactured by modifying a previous MIG electron gun. A new cathode and anode were manufactured for this application. The design of the electron gun can be seen in Figure 6.2a. As the applied voltage is designed to be 40kV, in order to produce the required microwave output power, ceramic insulators are used to stop the possibility of electric breakdown over the surface.

6.2.1 Cathode

The cathode can be seen in Figure 6.2b and is comprised of three parts: inner electrode, emitter and outer electrode. This was designed so the focusing electrodes can be changed for multiple reasons: in order that other microwave sources can use this electron gun, to provide a way to fix any possible manufacturing errors and to replace the electrodes in case of damage. Furthermore, as the cathode has a finite lifetime it is useful to be able to replace the emitter without having to remanufacture the whole cathode.
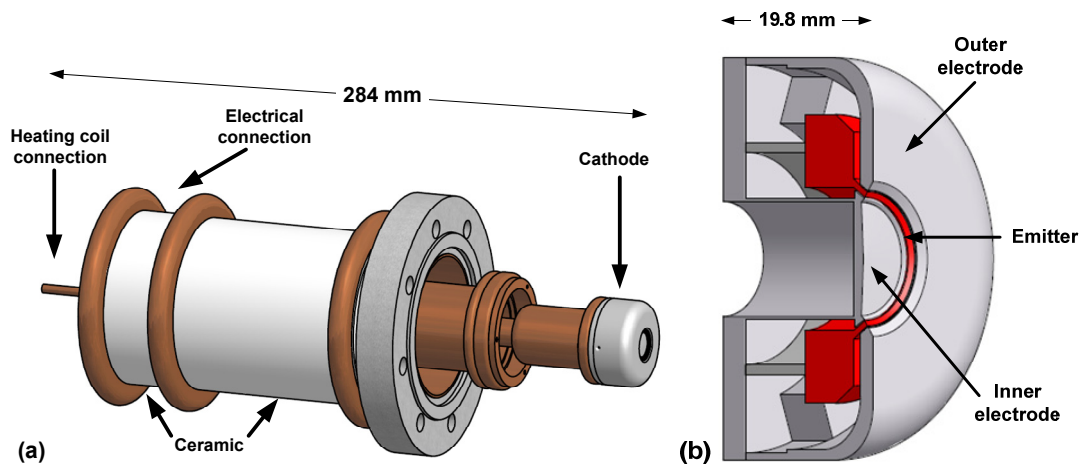
Figure 6.2. Electron gun geometry as produced by Autodesk Inventor illustrating (a) the full electron gun and (b) a cross sectional view of the cathode.

The temperature of the cathode will rise to ~1000°C during operation. A few layers of molybdenum were used to fully enclose the emitter to reduce heat radiation. These heat shields are 0.1mm thick, with dimples on the surface to reduce the contact between them and hence reduce thermal conduction. The weight of the cathode is

reduced where possible in this design as an overly heavy cathode can lead to misalignment and non-concentricity of the emitting surface with the electron gun and anode. To reduce the weight of the cathode three blocks that contain threaded screw holes to connect the cathode to the electron gun were designed so that the space in-between radially and behind them can be hollow, detailed in Figure 6.3b, reducing the weight of this focusing electrode. There are a further three blocks used which contain matching holes for location pins. Within each of these holes are small holes drilled from the outside of the focusing shield, visible in Figure 6.3a, which are used to evacuate the thread. Molybdenum was used for the components due to attractive properties such as low density, low thermal conduction and low thermal expansion rate.
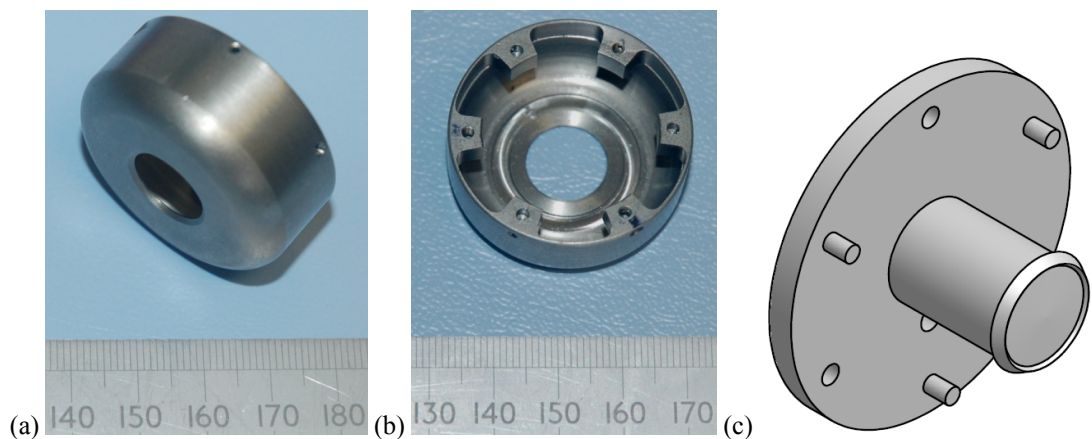
Figure 6.3. Focusing electrodes for the cusp electron gun (a) and (b) the constructed outer electrode, (c) the inner electrode.

The heating coil is wound in a bi-filar method in order to reduce the stray magnetic field produced by itself. If the coil is not wound in this way but rather as a few turns of wire wound like a traditional coil, then there would be a considerable magnetic field produced at a position close to the cathode. Through the bi-filar configuration the magnetic field can be reduced to an amnount that will not greatly affect the electron trajectories.

The magnetic field strength of the heating coil configuration was simulated using CST microwave studio[183] assuming a heating coil current of 1A. This was then optimised so that the coil would produce the lowest magnetic field and was found to
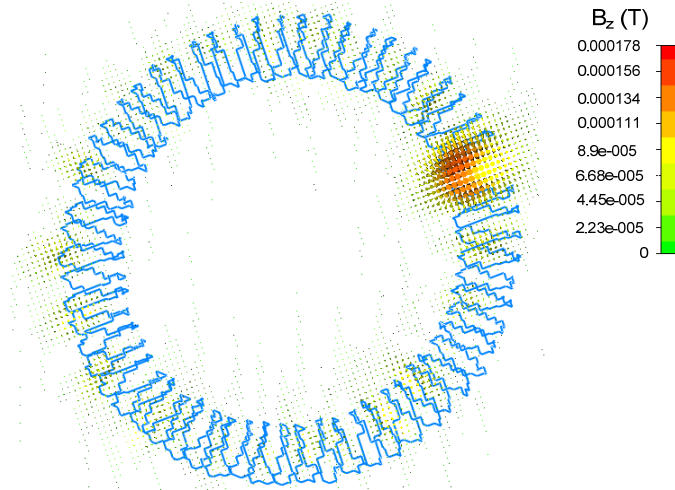
Figure 6.4. Magnetic field produced by the bi-filer configuration of the heater coil at 1A current.

be ~10^{-4}T at the cathode surface. This field is markedly lower than the field at the cathode, used to produce the electron beam, of ~10^{-3}T. The stray field can be compensated for by adjusting the reverse coil field. The wire configuration can be seen in Figure 6.5. The input voltage connection labled as +V connects to the heating coil wire that is along the central axis of the electron gun while the output voltage 0 connects to the outside of the cathode enclosure.
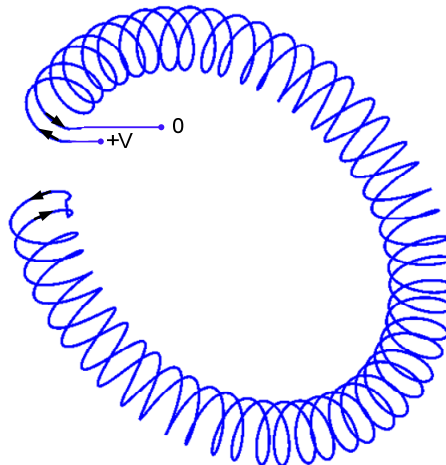
Figure 6.5. Bi-filar heating coil configuration.

The inner and outer electrodes were constructed from molybdenum. The cathode was tested under controlled conditions in order to find out what heating power was

required to increase the heating temperature to ~1000°C. The cathode during these tests can be seen in Figure 6.6, the emitter is shown glowing red hot. Also noticeable in this picture is a molybdenum heat shield directly in front of the emitter. The small dimples on the surface of the shield are used in order to reduce contact with the focusing electrodes to reduce heat conduction. Not shown in this image are the other two heat shields: one behind and one on top of the cathode.
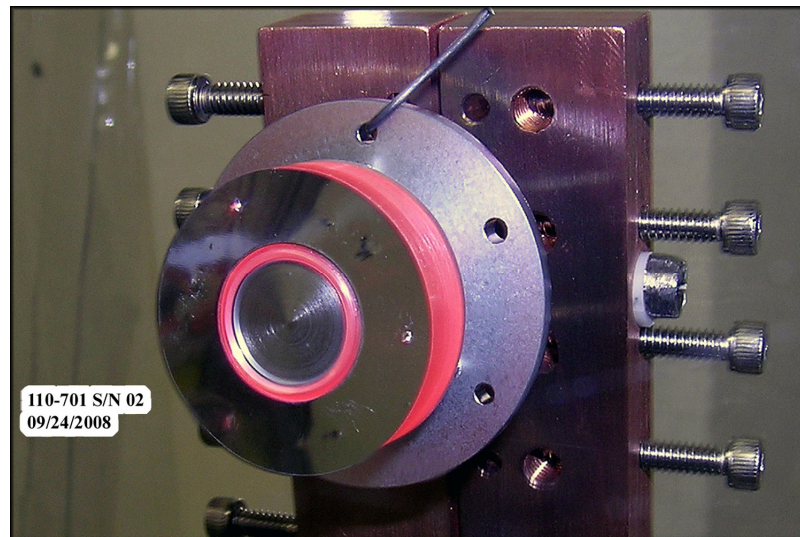
Figure 6.6. Photo of the cathode in a vacuum chamber with the emitting surface glowing red hot.

The cathode was constructed in a clean enviroment where the moisture levels are much lower than normal. The constructed electron gun can be seen in Figure 6.7 with the anode removed for clarity. The largest copper ring in this picture is for an intermediate anode, which was not used in this electron gun. The large hole in the copper just before the cathode is for access to the heater wire so the joint between the electron gun and cathode heater wires can be made. The anode is joined together with the large stainless steel flange.

Prior to the cathode being used in the experiment it had to be "activated" which is a process that involves heating the cathode to a very high temperature in order to convert the surface from having carbonates to oxides producing an oxide-coated cathode. The oxide-coated cathode is preferable due to a low work-function and low operating temperature.
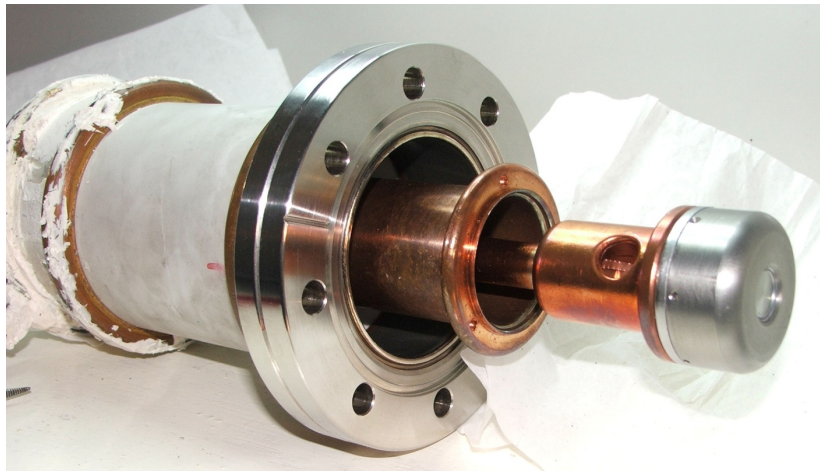
Figure 6.7. Photo of the constructed cusp electron gun.

6.2.2 Anode

The design of the anode can be seen in Figure 6.8. The anode was machined from stainless steel (grade 316) and is connected to the electron gun through eight M8 bolts equally spaced around the large Conflat Flange$^{(TM)}$ with the vacuum sealed by using copper gaskets. This piece was machined using a CNC machine to ensure the highest accuracy of the nose cone as this will ultimately decide the qualities of the electron beam. The design of the anode was to make the nose cone, shown in Figure 6.8b, changeable so alterations can be made if necessary.

(a)

(b)
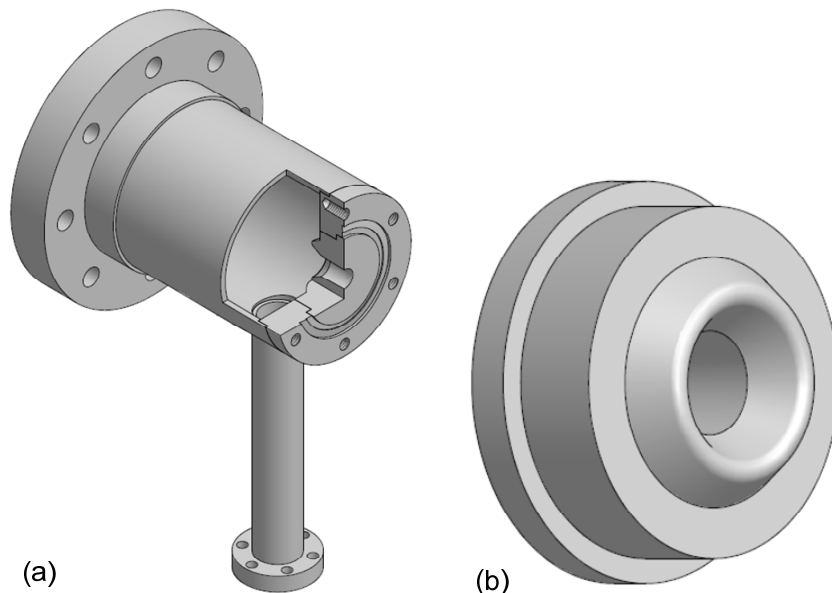
Figure 6.8. Anode as constructed in Autodesk Inventor illustrating (a) the anode with a section removed for clarity and (b) the anode cone.

When the rest of the beam tube is connected onto the anode the anode cone was firmly and tightly attached to the anode. This means that the anode cone cannot move away from the anode. This was made as a rounded cone with a taper at the top and at the bottom as shown in Figure 6.8b and then this sits inside the outer anode walls shown in Figure 6.8a.

6.3 Solenoid system

In the cusp electron gun the magnetic field profile is of primary importance as it is through this that the final beam properties: velocity ratio alpha, axial velocity and radius, of the electron beam are decided. The generation of the magnetic field is one of the more challenging aspects of the construction of this gyro-BWO system due to the very large DC currents required. The final design of both solenoids have to take into consideration cooling of the wires by reducing the output power through the addition of shim coils in the cavity coil and allow a large volume of water to pass through the wires in both coil. This is required due to the large amount of heat produced in a small volume. The design of the solenoids has to overcome the forces produced between two magnetic coils and the heat produced by the ~270A currents required to produce the maximum magnetic field. In the previous simulation of the electron gun it was stated that the solenoid wire was 2.2mm by 2.2mm square copper wire that has insulating varnish coating on the surface so that no breakdown will occur between the layers of the coils.

6.3.1 Design of cavity solenoid

In order to design the solenoids it is important to determine what problems have to be overcome in order to be able to operate the solenoid. First it is important to set out the parameters of the solenoid being built. These are given in Table 6.1. The primary problem is the heat produced by the wires. The current the wire operates at is ~260A, to give a 2.1T magnetic field, which through a wire of small cross-sectional area will give rise to large heat output and require enough water cooling especially when these wires are closely packed. In order to deduce how much heat is generated by the

Magnetic field range	1.65T - 2.1T
Layers	14
Turns/layer	103
Average diameter	5.68cm
Wire size	2.2mm x 2.2mm
Length of wire required	285.25m

Table 6.1. Properties of the cavity solenoid important for initial design consideration.

solenoid the resistance of the wire is first calculated. This has to be done through a calculation of the length of the wire. A MatLab script was written to calculate the length of solenoid wire from the average radius of each turn and total number of turns. The radius of each turn takes into account the thickness of the wire and the water channel between layers. The length of the wire, L, is found to be 285m. After this the resistance of the wire was found through

$$R = \frac{L\rho}{A}$$ **(6.1)**

Where ρ is electrical resistivity of the conductor and A is the cross-sectional area of the wire.

The current required to produce the B-field for the solenoid can then be found from Amperes law.

$$I \approx \frac{B}{\mu_0 N}$$ **(6.2)**

Where N is the turn density.

The voltage required can be found from Ohms law.

$$V = IR$$ **(6.3)**

Then from the current and resistance the power is calculated.

$$P = I^2 R$$ **(6.4)**

The results of these calculations is shown in Table 6.2 where B_0 is the maximum magnetic field strength at the cavity region. This shows that the electrical power of the solenoid required to produce a magnetic field of 2.1T is 62.3kW thus high

pressure water is required to cool the solenoid. Simulation of the cooling of the solenoid showed that with a channel of 0.4mm and 4 Bar water pressure, using Comsol Multiphysics[184] package the temperature rise of water is about 25°C at 2.1T.

	B_0=1.65T	B_0=1.82T	B_0=2.1T
Resistance (Ω)	0.99	0.99	0.99
Current (A)	211.4	228.84	262.60
Voltage (V)	209	226	260
Power (kW)	44.3	51.9	68.3

Table 6.2. Properties of the cavity solenoid calculated for consideration in the design process.

The second problem that the solenoids suffer from is strong attraction forces between the cavity solenoid and reverse coil. Through a rough calculation using the program Beam Boy[185] it was calculated that this force will be of the order 800N. Apart from this force, each turn inside the solenoid experiences an electromagnetic force due to the magnetic field it is in. To combat these forces the cavity solenoid former was machined from a solid piece of stainless steel so that the deformation and weakening of welding could be avoided. Also, the mounting structure was designed and made to withstand heavy weights as well as the magnetic force.

The coil winding configuration, as shown in Figure 6.9, is very important in the design of the solenoid as this decides how much cooling reaches each wire, the dimensions of the solenoid and therefore the magnetic field produced by the current. There is a former and on top of this the wire is wound tightly so that there is no space between turns. Inbetween these layers is a water channel of 0.4mm thickness so that the coil can be adequately cooled. The wires are kept apart through 0.5mm nylon wire along the length of the solenoid. Purposely thicker wire than the required spacing was chosen as it was found the nylon will be compressed ~0.1mm under the pressure of the tight solenoid windings. The reverse coil was configured the same way although it was much shorter in overall length.
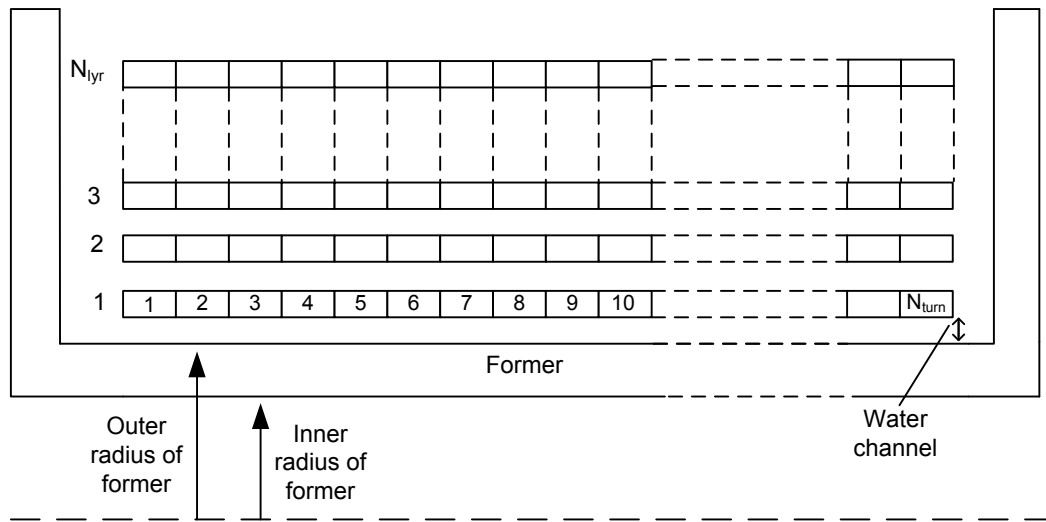
Figure 6.9. Winding configuration used in both the cavity solenoid and reverse coil.

Effective cooling of a solenoid requires: high water flow rate, large area of copper for the water to contact and low initial temperature of the water. In order to give the largest copper wire filling factor square wire was chosen over the more conventional circular wire. Using squared wire will increase the cross-sectional area of the wire hence reduce the total resistance which is essential to keep the electric power down. It was shown through simulation of the electron gun that a solenoid with small average radius produces an electron beam with the highest quality using a wire of small cross-sectional area allows the smallest average radius. However, as the cross-sectional area of the wire decreases the required electrical voltage increases and cooling the wire with pressurised water becomes more difficult. The good wire size when these factors are taken into consideration was found to be (2.2×2.2) mm^2 varnished square wire. Water channels of 0.4mm are placed between each layer of the copper wire and these channels are kept from closing through high strength nylon wire that is tied along the gaps axially. The number of nylon wires required increases as the diameter increases but the distance between each wire is kept to be around 10mm in order to keep a uniform cooling channel around the circumference of the solenoid. The simulations show that the cavity coil requires 14 layers of 2.2mm wire, 103 turns is required to provide the desired magnetic field profile. Also, a shim coil is added to each end of the solenoid of 2 layers and 15 turns per layer in order to increase the length of the flat-top region of the magnetic field so that the length of

the solenoid can be reduced hence lowering the overall electrical power. To insulate the wire from the metal former a 4mm thick polycarbonate mesh was used at both ends of the solenoid and channels were formed for water passing through the mesh.
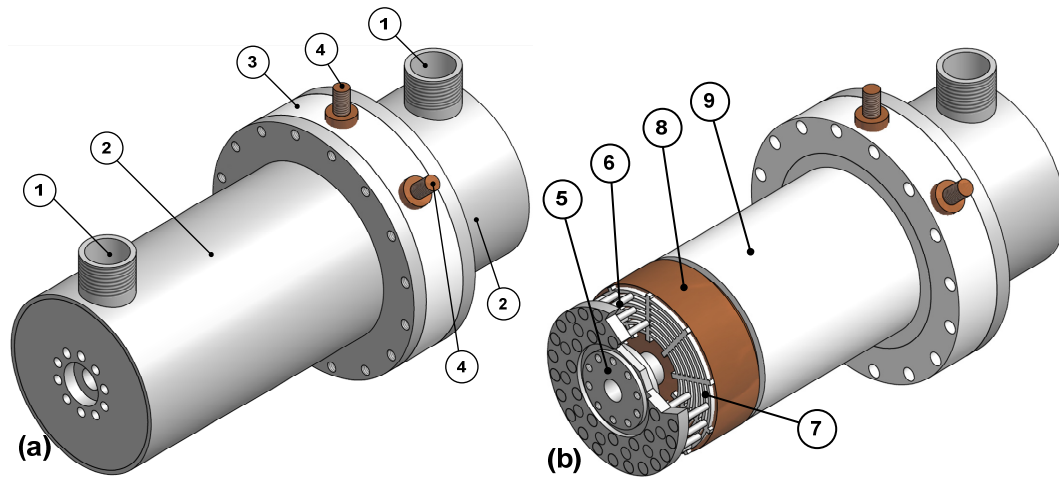
Part list: (1) Water pipe connections; (2) Outer tube; (3) Nylon insulator; (4) Electrical connections; (5) Former; (6) Clevis pins; (7) Polycarbonate Mesh; (8) Solenoid wire; (9) Nylon Insulator

Figure 6.10. Cavity solenoid as illustrated in Autodesk Inventor showing (a) full solenoid and (b) the outer flange removed for clarity.

The nylon wire was then secured to this polycarbonate mesh. The polycarbonate mesh was kept in place by being secured to clevis pins, pins with a hole at the end, that are attached to the solenoid former.

6.3.2 Design of the reverse coil

The solenoid used at the cathode side to produce the negative B-field required for the cusp electron gun operation is called the reverse coil. From simulation the reverse coil required 4 layers with 10 turns per layer, markedly different from the cavity solenoid and hence why this is given the term coil to note the small number of turns. The maximum magnetic field produced is only ~68mT with 2.8kW of heat produced so the cooling requirements are much less of an issue compared to the cavity solenoid.

As the heat produced by the reverse solenoid is much less than the cavity solenoid the water flow can be reduced through use of a 1/4inch BSP input pipe. From the

simulation, to achieve an α of 1.65, the driving current and consumed power of the reverse coil is tabulated in Table 6.4.

Layers	4
Turns	40
Average diameter	16cm
Wire size	2.2 x 2.2mm
Length of wire required	20.1m

Table 6.3. Properties of the reverse coil important for the design.

	B_0=1.65T	B_0=1.82T	B_0=2.1T
Magnetic field (mT)	50.8	61.8	67.9
Magnetic field at cathode (mT)	-5.47	-4.92	-3.69
Resistance (Ω)	0.07	0.07	0.07
Current (A)	169.8	180.8	198.9
Voltage (V)	11.9	12.2	13.9
Power (kW)	2.0	2.3	2.8

Table 6.4. Magnetic and electrical properties of the reverse coil.

The structure used for the reverse coil is shown in Figure 6.11. The winding configuration is similar to the cavity solenoid, Figure 6.9. Highlighted here is the water jacket that encloses the wires and the nylon ring that acts to force the water to travel through the small water channels between the layers of the copper wires. The reverse coil is connected to a 3-axis mounting system by use of two threaded holes welded to the water jacket, part 5 in the figure. This mounting system allows one to adjust the position of the reverse coil by small increments to ensure that the electron beam can travel through the smallest diameter part of the beam tube, the backstop filter, and to keep the reverse coil concentric with the electron gun so the magnetic field profile at the cathode surface will be comparable to the simulated magnetic field profile.
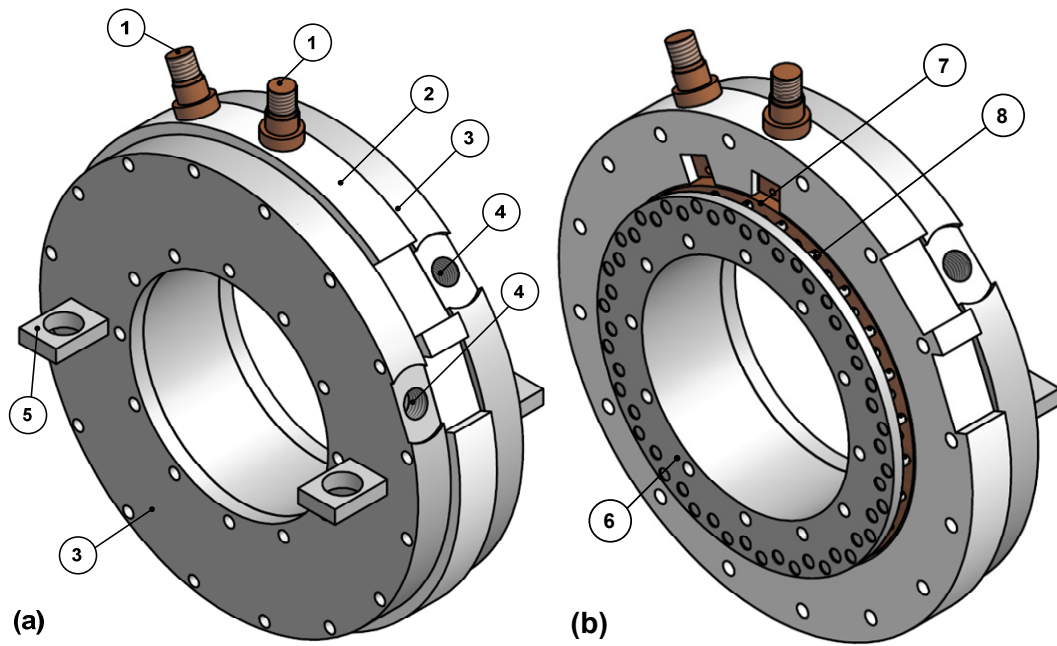
Part list: (1) Electrical connections; (2) Nylon insulator; (3) Outer Flange; (4) Water pipe connections; (5) Connection to 3-axis mounting system; (6) Former; (7) Solenoid wire; (8) Clevis pins

Figure 6.11. Reverse coil as illustrated in Autodesk Inventor showing (a) full solenoid as constructed and (b) the outer flange removed for clarity.

6.3.3 Manufacture of the solenoid system

The cavity solenoid is calculated to have a maximum electric power consumption of 62kW. The heat power is cooled through a pressurised water circulating system. It is calculated that with 4 Bar of water pressure into the solenoid and 3 litres of water per second the solenoid should be cooled. This means that the design of the solenoid has to take into consideration the high pressure water going into it, the channels between each layer of the wire cannot close up or be blocked. The solenoid has to be insulated electrically from the metal former. These are considerations taken during manufacture of the solenoid. The design produced in Autodesk Inventor can be seen in Figure 6.12. Firstly the inner tube used as a former was constructed, machined from a solid for strength without any welding to avoid the deformation associated with it. Then clevis pins were used as these have a hole at one end into which 0.5mm diameter nylon wire could be threaded into to form small channels of correct spacing
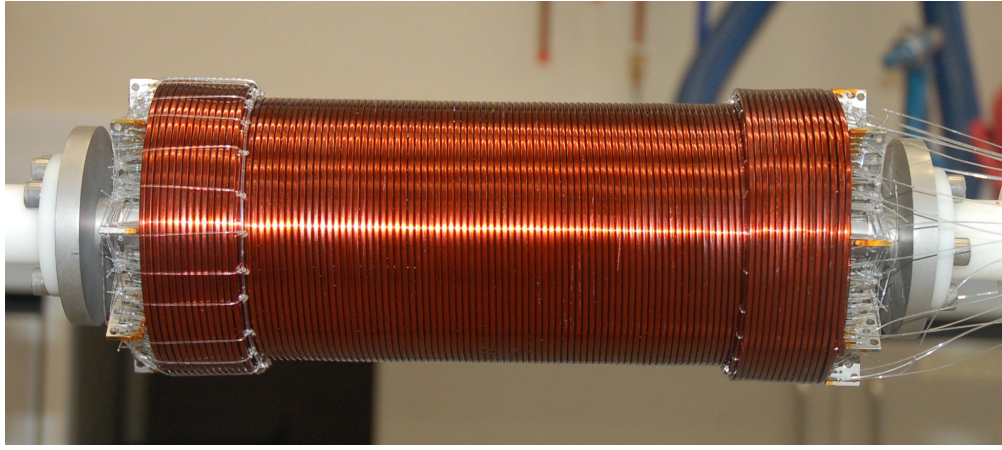
Figure 6.12. Photo of the solenoid during winding process showing the varnished copper wire and the nylon wire used to form water channels.

between copper wire layers. There was a polycarbonate mesh placed between the clevis pins and the copper wire in order to insulation and protection from the metal pins and former. Two ends of the wire were then connected into two copper electrical connections situated inside a nylon insulator. A main concern here is making sure the water can only flow through the layers of copper and not over the top of them so an insulator labelled 11 in the Figure 6.10 was used to stem the water flow between the top layer and the tube. It is essential in this design to ensure a tight fit between the coil and surrounding metal case. The constructed solenoid can be seen in Figure 6.13 with both the water hose and power cables connected.

Figure 6.13. Photo of the constructed solenoids with water hoses, power connections and 3-axis mounting system.

6.3.4 Solenoid cooling system

The solenoids require a relatively sophisticated cooling system to ensure normal operation without excessive build-up of heat. A schematic drawing of the cooling system is shown in Figure 6.14 and Figure 6.15. It should be noted that the water flows into the system through 2-inch pipe then changes to 1 inch pipe at the input of each of these drawings. Unless stated all connections here are 1 inch, designed for simplicity, and so no pressure is lost through changing pipe dimensions.
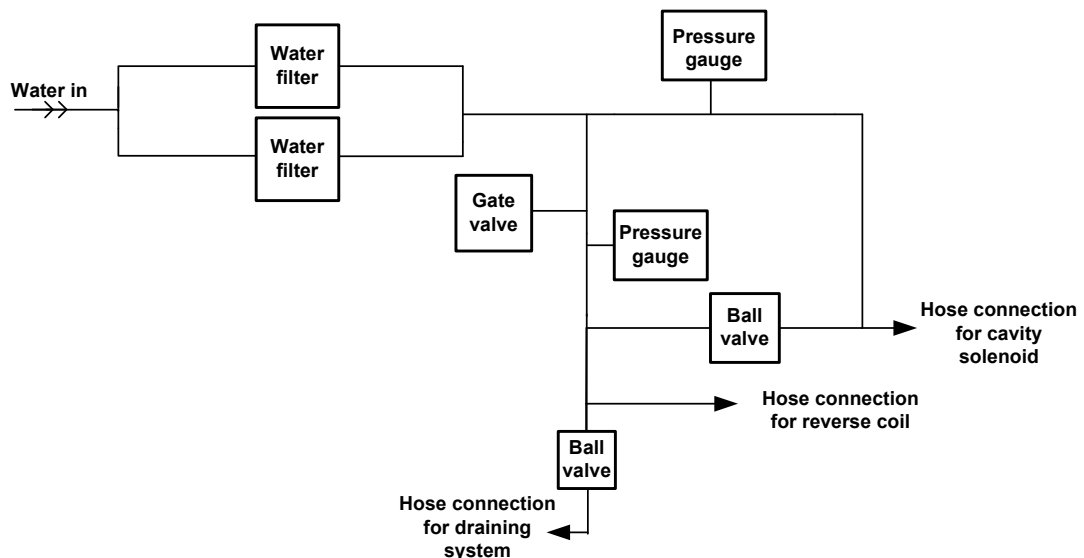
Figure 6.14. Schematic representation of the water cooling system flowing into the solenoids.

Firstly, water flows into this system from a recirculating source which is driven by a pump to ensure a large flow rate at a pressure of 4 Bar. As the gap between the layers is only 0.4mm the possibility of objects blocking the layer is of concern so two water filters are used. These are connected in parallel to ensure there is enough water flow rate through the filters. In order to split the cavity solenoid and the reverse solenoid a gate valve is used to limit the water flow into the reverse coil as this requires much less flow than the cavity solenoid. Pressure gauges are used here to measure the pressure going into both coils independently. The two ball valves are used for the draining system. One ball valve is used so that the reverse coil and cavity solenoid can be bled independently and the other ball valve is used to allow flow to a hose that

the system can be drained with. The input water system here is aiming to provide diagnostics and filters so that the perfect flow into the solenoids can be achieved.
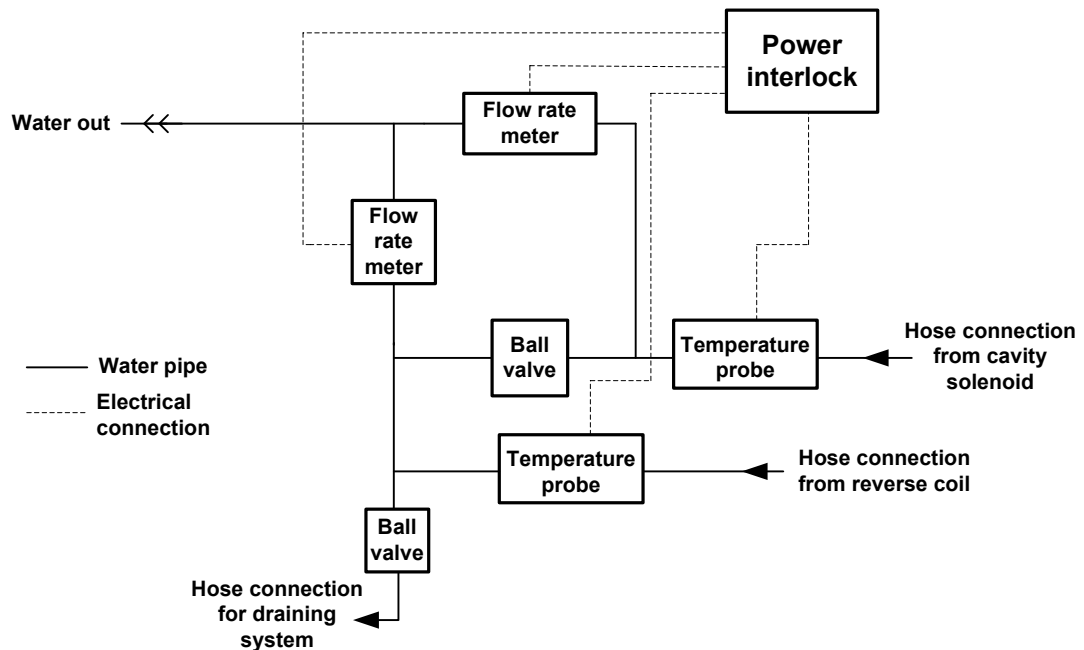
Figure 6.15. Schematic representation of the water cooling system flowing out of the solenoids.

The water that comes out of the solenoids would have a rise in temperature due to the heat generated by the coils. Therefore, two immersed temperature probes were used to measure temperature and this was read by a power interlock box. The box provided two functions: (1) displaying the temperature of the water in real time for both the reverse coil and cavity solenoid, (2) provide an interlock signal to turn off the power supply system if the temperature of the water rises above a set limit or the water pressure undergoes a set change. The ball valves are used for the same purpose as before to allow a way of draining the system.

6.3.5 Measurement of the magnetic field profile

The measurement of the magnetic field profile allows verification of how well the constructed solenoid matches the simulated solenoid. This was carried out using a Gaussmeter with an axial Hall probe, shown in. A Gaussmeter employs the Hall effect in order to measure the strength of an applied magnetic field. This probe was

kept in the middle of each solenoid and moved by small increments along the solenoid's axis of symmetry.

Figure 6.16. Axial hall probe used to measure the cavity and reverse coil's magnetic field profile.

The reverse coil requires 180A for a mid magnetic field operating range and so the magnetic field profile was measured at a driving current of 100A. The profile obtained is shown in Figure 6.17. This shows an excellent agreement between numerically simulated profile and the experimentally measured one. One issue arose during testing was a discrepancy between the driving currents used in measurement and simulation. The current into the solenoid was 100A while the MAGIC simulation that agrees exactly with this profile is at a current of 92A. This is caused by the incorrect display of the power supply.
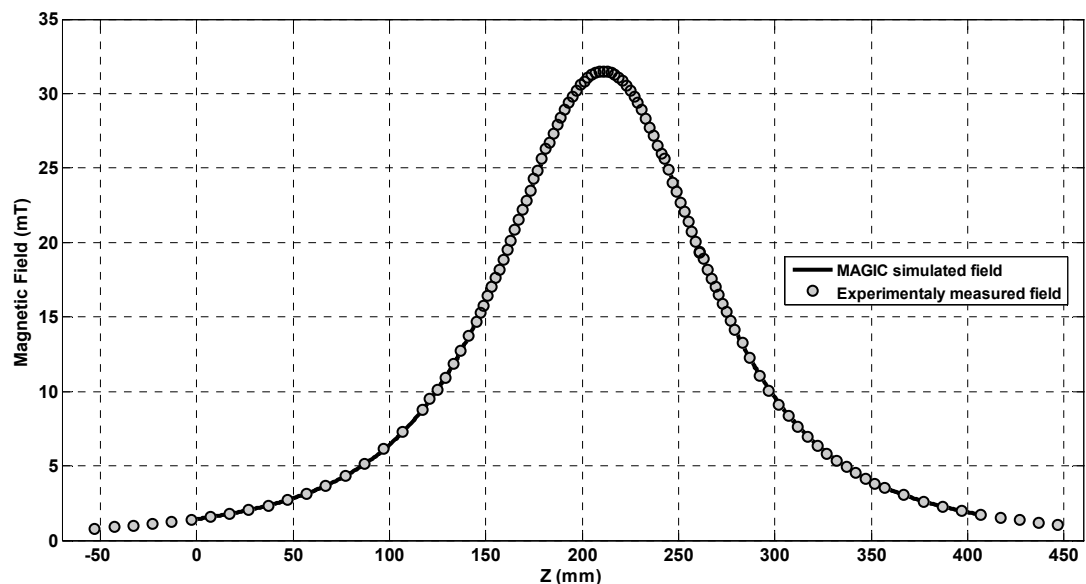
Figure 6.17. Magnetic profile of the reverse solenoid simulated in MAGIC at 100A compared against the experimentally measured magnetic field profile at ~92A.

164

The B-field profile of the cavity solenoid was performed through the same methodology. A profile at a driving current of 70A is shown in Figure 6.18. The maximum B-field at 70A was ~0.54T resulting in no significant rise in water temperature.

It was found through this measurement that the experimental profile did not match the theoretical profile. The reason for this is when the solenoid was constructed the last layer of the shim coil at the beam dump end of the solenoid was wound in the wrong direction and thus this cancels out the effect of the shim coil. Therefore the theoretical profile with only one shim coil is shown here (black line) and this shows very good agreement to experimental results. Importantly the experimentally measured profile at the cusp region (left hand side of the profile) has a good agreement to theoretical values. The length of the flat-top region (+/- 1% of the maximum value) is ~10cm while the interaction region requires 10.5cm so this should not significantly reduce the output microwave power.
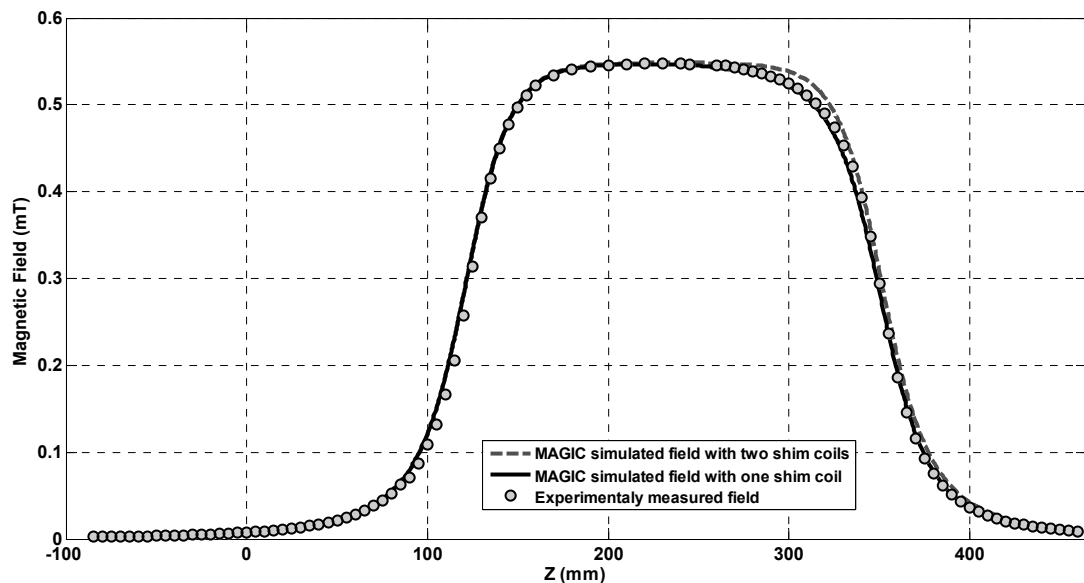
Figure 6.18. Measured and simulated magnetic field profile for the cavity solenoid at 70A.

These measurements allow one to measure where the position of the coil is inside the solenoid and from this the position of the solenoids can be adjusted to achieve the designed cusp field. In the reverse coil it was found that there was a difference of 0.7mm between the position of the wires in the real and simulated cases. For the

cavity solenoid it was found there was a difference of 2.5mm between the real and the simulated cases. The larger difference in the width of the cavity solenoid profile is most likely due to slight errors in the measurement of the Hall probe position inside the solenoid.

The magnetic field profile used by the cusp gun and gyro-BWO experiment was constructed from the measured driving currents for the reversed coil and cavity solenoid and the distance between the two coils. Each experimental magnetic field profile must first be scaled up to the real magnetic field strength from the calibration value described in the previous section. In the optimal simulation conditions the reverse coil has a current of 181.24A producing a maximum field of 61.8mT. While the cavity coil has 232.7A producing a maximum field of 1.82T. The two profiles are then combined to produce the experimentally measured cusp magnetic field. The calculated field produced by MAGIC is compared against this measured profile in Figure 6.19. Excellent agreement between the experimental and simulated cusp magnetic field profiled is observed.
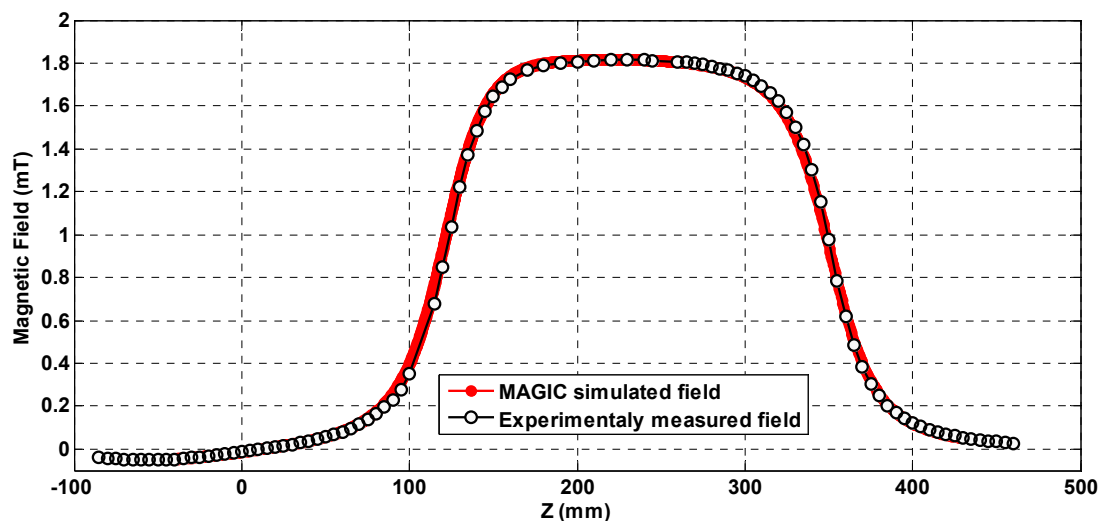
Figure 6.19. Measured and simulated cusp magnetic field profile.

6.4 Microwave window design, manufacture and measurement

A thin sapphire window, shown in Figure 6.20, was used to separate the vacuum of the interaction and the outside atmosphere. The design of this has to allow a broad

range of frequencies through the window with little transmission loss. The window is 15.44mm diameter and 1.6mm thick. Also, a gyro-BWO is relatively insensitive to window reflection as this would help the wave to grow associated with the absolute instability of the gyro-BWO.

Figure 6.20. Photo of the microwave window used in the W-band gyrotron backward wave oscillator system.

This window was also used to measure beam image described later in this chapter. So transmission of visible light is useful as shown in Figure 6.21.
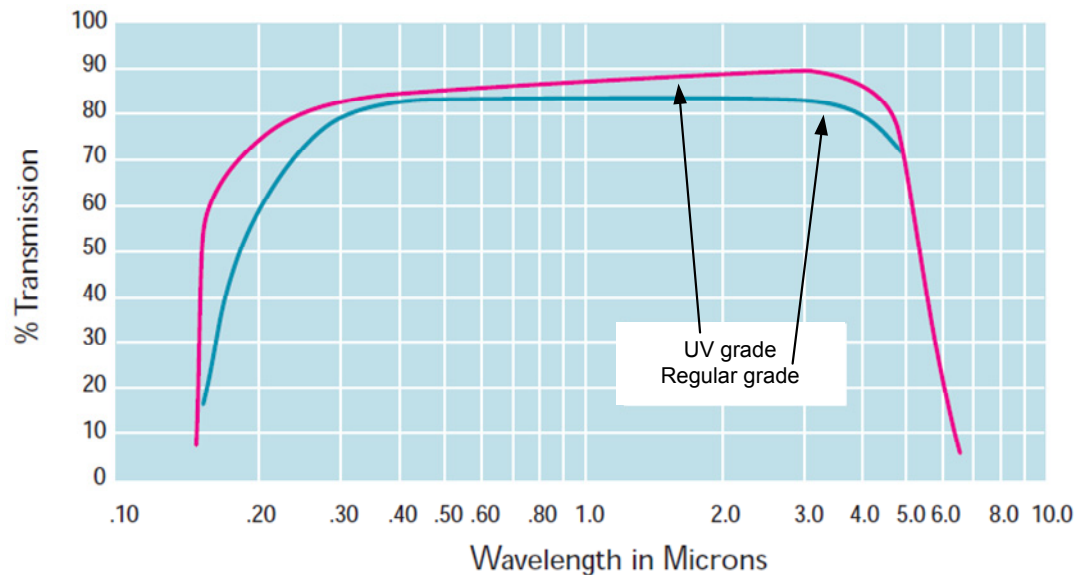
Figure 6.21. Sapphire window transmission profile over a wavelength range as provided by the manufacturer.

The microwave window is connected onto the tube through a microwave horn, the dimensions and shape of which is detailed in Figure 6.22. This horn is used to slowly increase the radius of the waveguide from 2.6mm up until the size of the microwave window 15.44mm. The length of the tapered horn is 80mm.
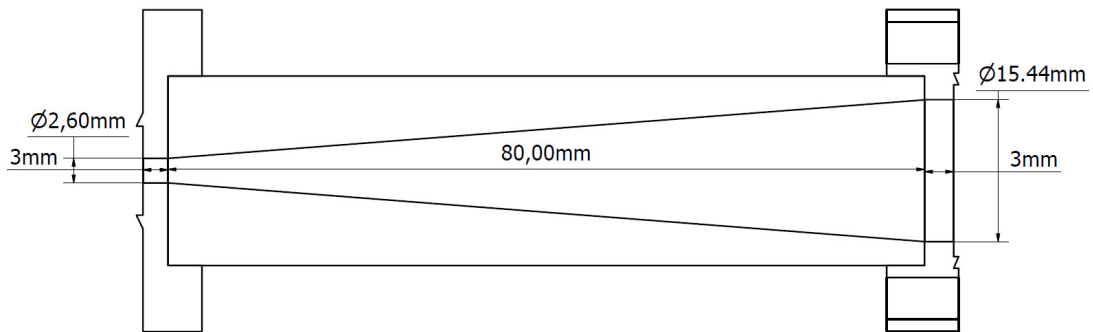
Figure 6.22. Output waveguide horn as used in the gyro-BWO.

The window is a single layer of sapphire and the thickness is known to be 1.6mm through measurement. The microwave window has discrete transmission bands due to Fabry-Pérot resonance. To design a broadband window the dielectric constant of the window material needs to be measured. Once this is known a multi-disc window for broadband operation can be designed. The transmission band is dependent on the dielectric constant of the window. To measure the dielectric constant and transmission frequency of the sapphire window a setup as shown in Figure 6.23 is used.
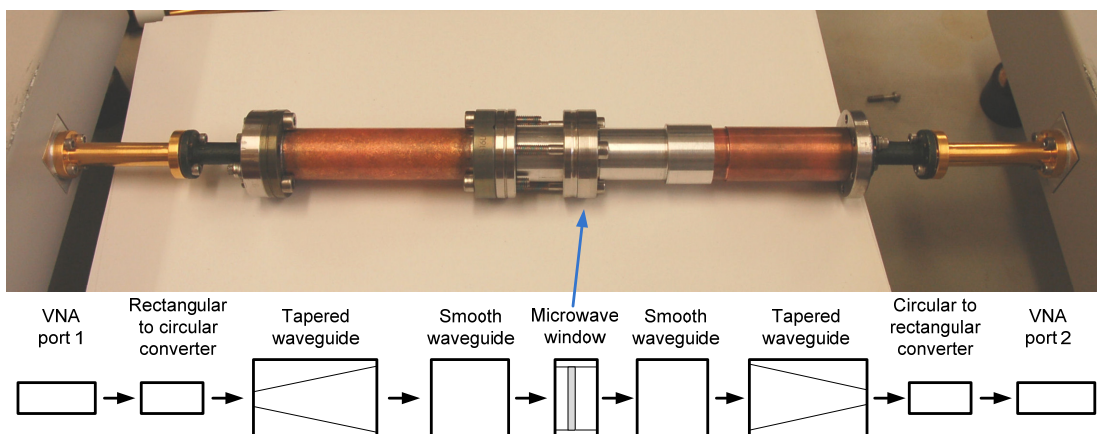
Figure 6.23. Components used during the VNA measurement of the sapphire microwave window

The microwave components listed in Figure 6.23 were used in the measurement of the microwave window using a vector network analyser. The window is separated from the tapered waveguides with two straight waveguides. The measurement uses time domain technique in order to locate and analyse microwave properties of the window. The two straight lossless waveguides connected to the window were used to make the window reflection in the time domain a clean measurement. Using time domain the location of the window can be found and then just after and before the window (i.e. two straight waveguide pieces) a gate can be set that makes the analyser measure the microwave properties just between the two locations. As the window is within these locations the reflection S_{11} measurement will provide the S_{11} profile of the window only. The S_{11} reflection measurement with time gating on is shown in Figure 6.23. This graph shows the location of one resonance at 78.3GHz. This resonance should, in theory, have another resonance at 106GHz. This does not appear in the measurement however at the end of the frequency scale near 110GHz the S_{11} parameter starts to drop showing the location of the second resonance.

The location of this resonance allows the determination of the dielectric constant of the microwave window. The dielectric constant is calculated to be 12.8. Therefore the gyro-BWO experiment should aim for an output close to this transmission peak when the single sapphire window is used. Furthermore, a multi-disc window can be designed through the addition of more layers of quartz with adjustable spacing to provide full band transmission for the gyro-BWO.
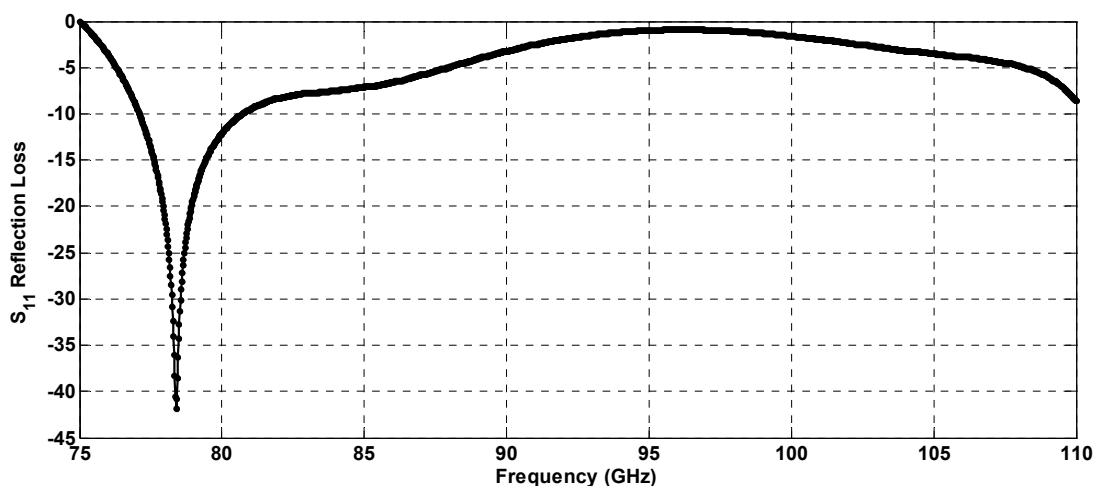
Figure 6.24. Measured S_{11} parameter of the sapphire window using a VNA

6.5 Power supply system

The gyrotron backward wave oscillator is designed to be run CW however it is initially operated in pulsed mode in order to be able to do proof-of-principal experiments and to be able to run electron beam diagnosis. The power supply therefore had to provide a pulsed output voltage of 40kV with little deviation from pulse to pulse. The supply used was a double Blumlien pulse generator[186].

6.5.1 Pulse forming line and single cable Blumlein

In order to understand the double cable Blumlien it is important to describe the single cable Blumlien and a cable pulse forming line (PFL). The PFL is a relatively simple concept and can be seen in the effective circuit shown in Figure 6.25. This system is charged through an input DC voltage, V, through a current limiting resister R_{lim} when the switch is in the open state. Then when the switch is closed the charge cable will discharge with an output of V_{out} to the load which has an impedance of Z_L.
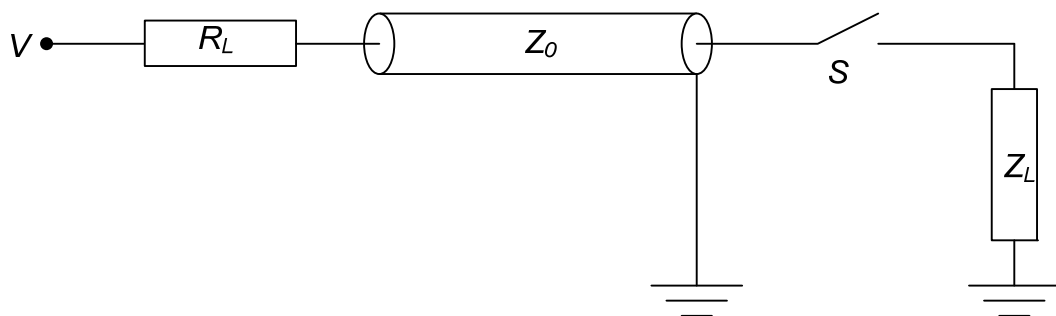
Figure 6.25. Schematic of a pulse forming line.

It is obvious therefore that the pulse length τ is a function of the cable length, l_{cab}, and the speed of the wave through this cable v_c as the longer the cable the longer it takes to discharge the voltage as given in equation (6.5). The voltage of the output is given in equation (6.6).

$$\tau = 2\frac{l_{cab}}{v_c} \tag{6.5}$$

$$V_{out} = \frac{Z_L}{Z_L + Z_0} V \qquad\qquad \textbf{(6.6)}$$

This system operates with one disadvantage that the output voltage cannot exceed the input voltage so in order to gain a large output voltage there can be excessive cost and more complication in having to operate at high voltage at the input power side of the experiment. The solution is to use the Blumlein cable pulser. The circuit diagram of the Blumlein pulser can be seen in Figure 6.26.
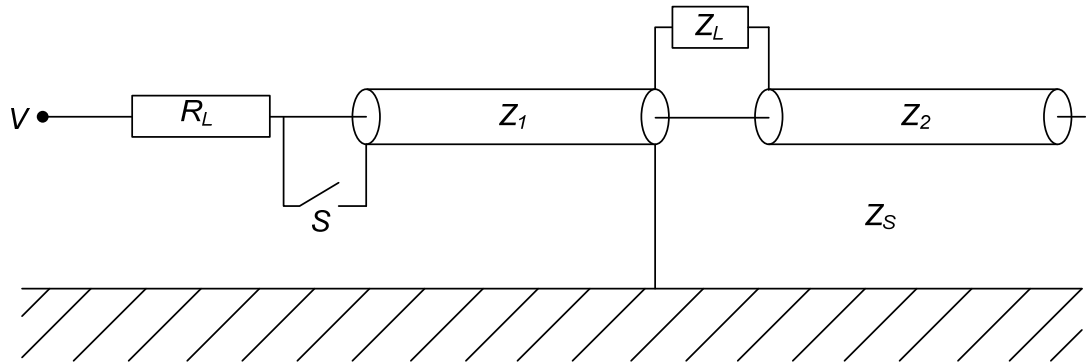
Figure 6.26: Schematic of a single Blumlein cable pulse generator.

This shows two cables of the same length with an applied DC voltage V and these can discharge to the load resister Z_L when the switch S is closed. This is a similar setup as the PFL except now it is possible to get almost twice the output power compared to the input power if $Z_L \gg Z_1, Z_2$. This can be seen in the equation for voltage given in equation (6.7) and the pulse width of this is given in equation (6.5).

$$V_{out} = \frac{2VZ_L}{Z_1 + Z_2 + Z_L} \qquad\qquad \textbf{(6.7)}$$

Although this system gives an increase in the output voltage it suffers from a connection between the 2nd transmission line and the earth that gives the impedance Z_S and this reduces the efficiency of the system, reducing the output voltage.

6.5.2 Double cable Blumlein

The next arrangement possible is the double cable Blumlein which introduces a third cable to the single Blumlein setup to produce two cable Blumleins that can now be charged in series and discharged in parallel. This allows an output of four times the

input power. The circuit for this can be seen in Figure 6.27. While it was explained that for a single Blumlein a voltage of 2V can be outputted in the double Blumlein this value can be produced between points b-c and e-d.
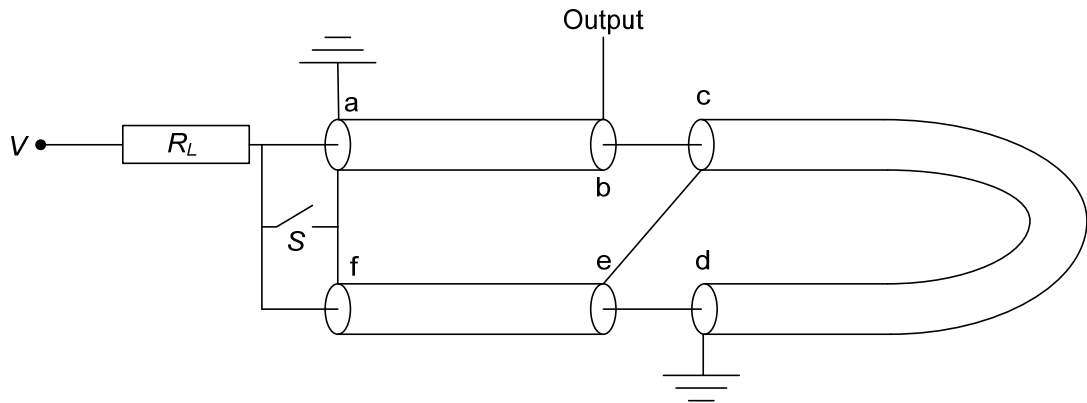
Figure 6.27. Schematic of a diagram of a double-Blumlein pulse generator.

The Blumlein can have two types of output the inverting double-Blumlein and the non-inverting double-Blumlein. The difference between these is deciding the point of earth and output. The inverted Blumlein has an earthing point at b and output at d while the non-inverting has earth at d and output at b. The inverting and non-inverting Blumlein can generate -4V and +4V respectively.

In this experiment an inverting double cable Blumlein was built and used. A schematic diagram of the pulsed power unit is shown in Figure 6.28.
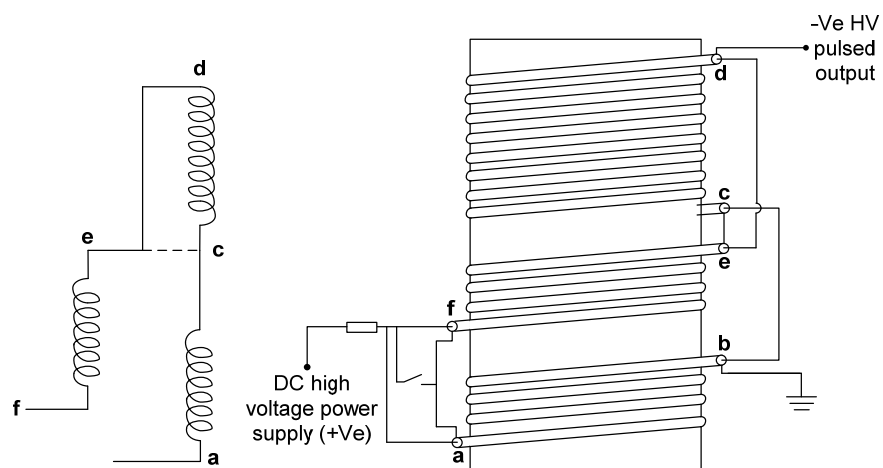
Figure 6.28. Schematic diagram of the double cable Blumlein.

6.5.3 Voltage divider

The use of high voltage signals is necessary in microwave sources but this cannot be measured directly as the voltage is too high for any measuring instrument therefore it is necessary to take a small portion of this signal to measure it. This retains the same characteristics as the original signal but has smaller amplitude. This is done through a voltage divider. The main component of this is a resister which has an inductive component L_s (self inductance) in series with itself and a capacitive element (self capacitance) C_s in parallel with itself. Also a self inductance due to the magnetic field generated through the flowing current. As an electric field is generated by the resister there is a self-capacitance. Knowing this information an equivalent circuit for the resistive voltage divider can be seen in Figure 6.29.
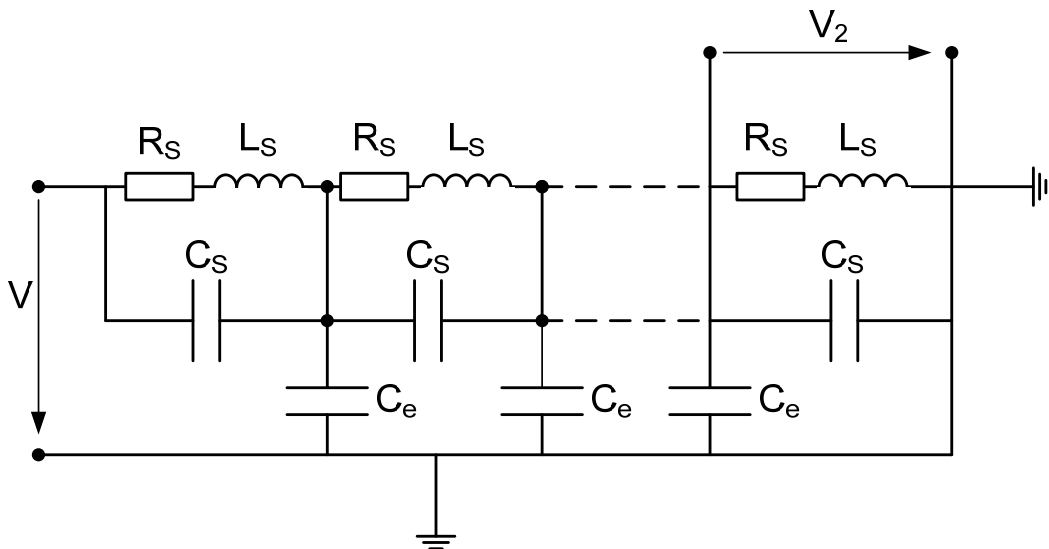
Figure 6.29. Circuit diagram of a voltage divider.

The work considers a resistive divider where the values of the resistance will decide the output voltage. The circuit diagram for this voltage divider can be seen in Figure 6.30. This shows that the output voltage, V_2, will be a function of the input voltage V and the resistance ratio.

$$V_2 = \frac{R_2}{R_1 + R_2} V \tag{6.8}$$

The voltage divider used in this experiment has a R_1 of 2.73kΩ and a R_2 of 2.72kΩ with an input voltage of 40kV and gives an output of 39.8V allowing the measurement of the voltage pulse by an oscilloscope, when using an attenuator.
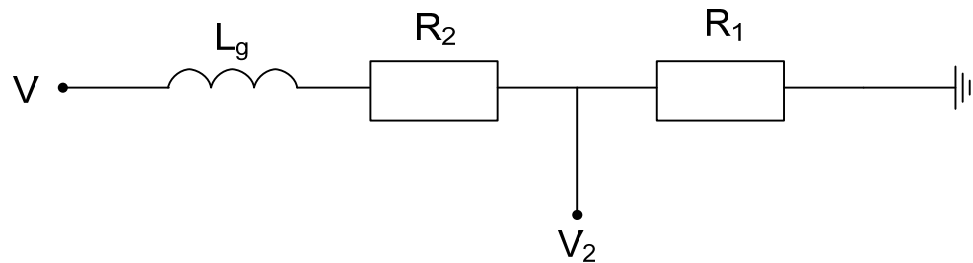
Figure 6.30. Circuit diagram of a voltage divider.

The equivalent circuit of the divider is shown in Figure 6.31(a) while a photo of the divider and the cable Blumlein are shown in Figure 6.31(b).
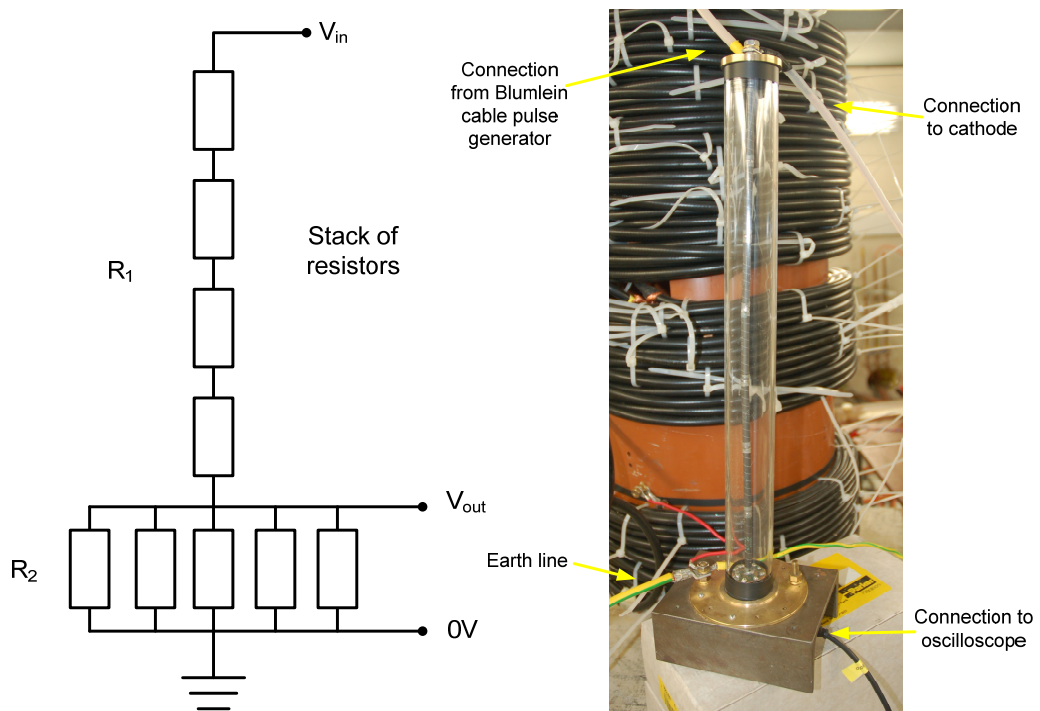
Figure 6.31. Construction of the voltage divider showing (a) a schematic diagram of the electrical circuit and (b) the constructed voltage divider.

6.5.4 Spark gap switch

The spark gap switch is a relatively simple concept yet an effective form of close

switch that gives rise to a high power voltage pulse. The basic concept is: a high voltage trigger pulse is applied to a trigger electrode which initiates an arc between electrodes. There are some different configurations of the spark gap which create the discharge. The type employed here was the mid plane spark-gap which consists of two domed electrodes, one grounded and one charged, with a trigger pin in between them. The distance between the two electrodes and the pin was set. The gas inside the spark-gap can be changed in order to change the point of break-down and common gasses include: air, SF6, argon and oxygen or a mixture of those. In a few cases liquid or solid filled spark gaps are used. The solid-filled spark-gap would be preferable when dealing with extremely high powers, ~10TW, but this would operate for a single shot as the solid is destroyed.

The circuit diagram of a mid-plane spark gap can be seen in Figure 6.32. The voltage between the gaps was adjusted through changing the resister values of R_{b1} and R_{b2}. The trigger pulse causes a discharge between the two electrodes. However, it can be operated in self-breakdown mode when no trigger pulse is used. The constructed spark gap can be seen in Figure 6.33 which had resistance values of R_{b1}=250 MΩ and R_{b2}=200 MΩ . This was operated without a trigger pulse instead operating at self-break down. The trigger system was not necessary here as the solenoids and heating power are permanently on so the only thing requiring to be triggered was the spark gap and we could get a repetitive pulse from it operating in self-breakdown mode.
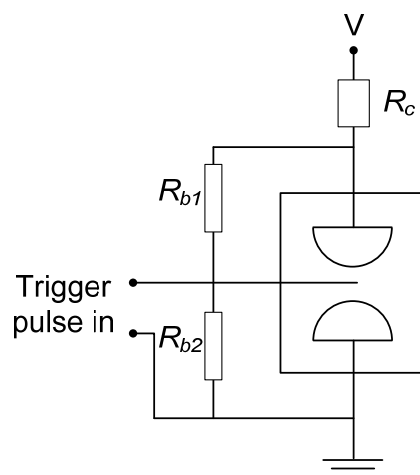
Figure 6.32. Circuit diagram for typical mid-plane spark gap.
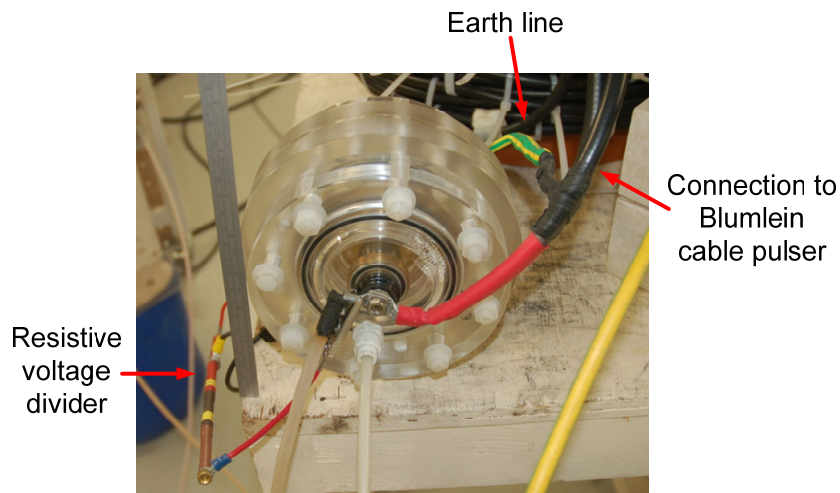
Figure 6.33. Photo of the spark gap switch used as closing switch in the double Blumlein circuit.

6.5.5 Power supply systems

The power supply system used to generate the voltage pulse for the gyro-BWO can be seen in Figure 6.34. The power supply for this experiment is a 100kV, 40mA Glassman DC high voltage power supply. This charges the cable Blumlein when the spark gap is open. By adjusting the resistive value of the two resisters in parallel with the spark gap, a desired charging voltage can be reached. Once the desired voltage is reached the spark gap would close due to voltage breakdown so that the double Blumlein would output a voltage pulse.
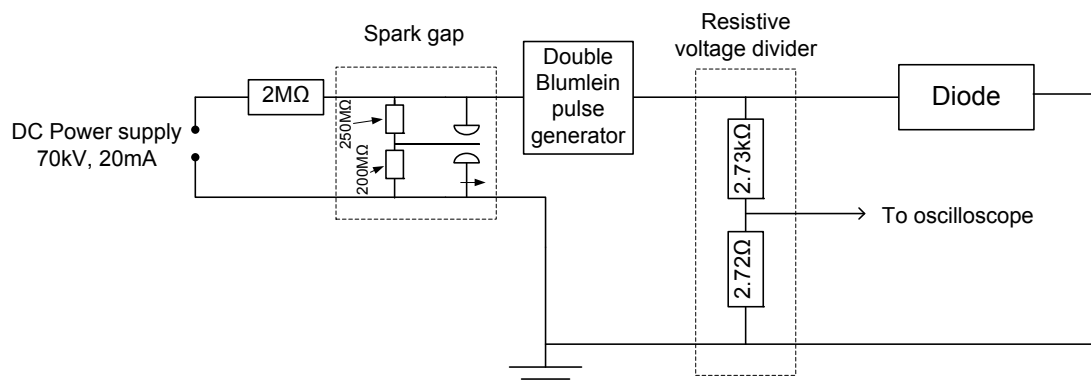
Figure 6.34. Power supply design used for the diode.

The cathode has a heater coil that requires enough current to provide enough heater power to increase the cathode temperature to ~1050°C. This requires the heater to be

operated at 10V and 10A DC, not AC as this would result in a changing magnetic field at the cathode. The electronic circuit of the heater power unit can be seen in Figure 6.35.
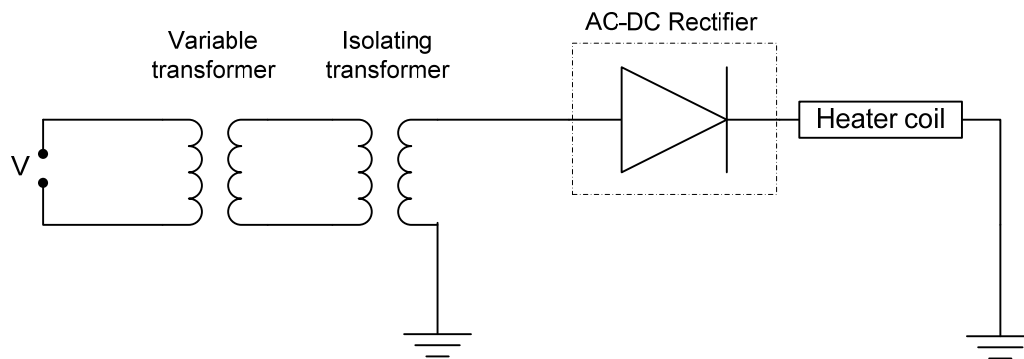
Figure 6.35. Power supply used for the cathode heater.

The construction of the power supply can be seen more visually in Figure 6.36. The size of the relative components along with their position in the setup is visible in this figure.

6.6 Safety interlock system

The generation of electron beams, microwaves and the use of high voltage power supplies requires careful consideration of the safety requirements for the experiment in the laboratory. Most of these safety systems were linked through one interlock box.

The power supplies including high current supplies and high voltage supplies are all centrally interlocked for safety. A schematic diagram of the interlock system is shown in Figure 6.37. The high current power supplies i.e. NADA, Farnell, were interlocked through temperature and pressure monitors. If the water flow-rate drops below a set level or temperature changes above a level then the monitor stops outputting a voltage to the interlock, which then switches off the high current and high voltage power supplies. In the experimental bay there is a box which links the earth line of every electrical component in the system to the earth line of the experiment bay. This box was a pneumatic interlock. When every safety check
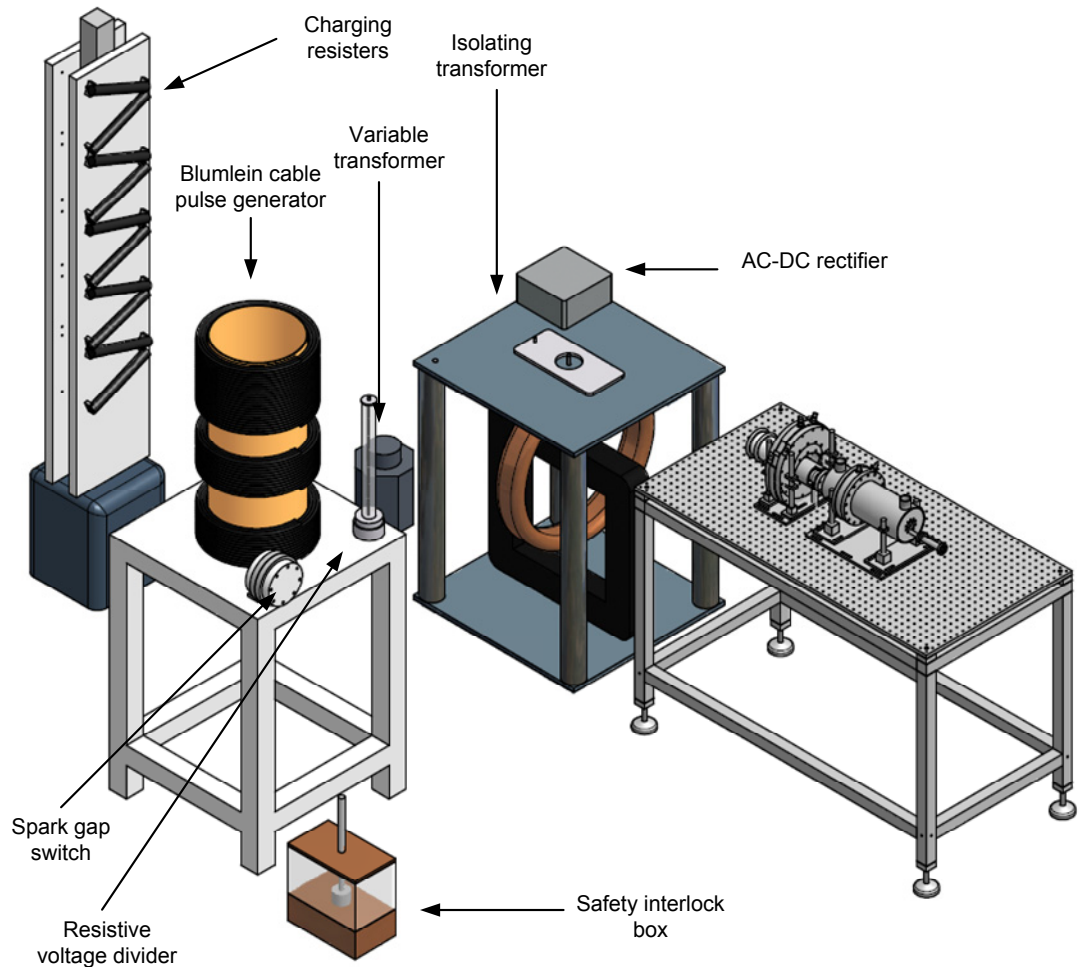
Figure 6.36. Full power supply system shown in relation to the gyro-BWO.

was passed then the earth box will lift an electrical contact and un-ground the experiment. If any one of the checks is not ok then there is an air leak stopping the pressuring of the box and automatically grounding the experiment. This also provides the function of automatically grounding the components used in the experiment when the door is open.

The area in which the gyro-BWO is enclosed is surrounded by lead in the roof, walls, ground and a movable door for X-ray shielding. The door has a pneumatical sensor at the top to ensure that the high voltage can only applied when the door is closed.
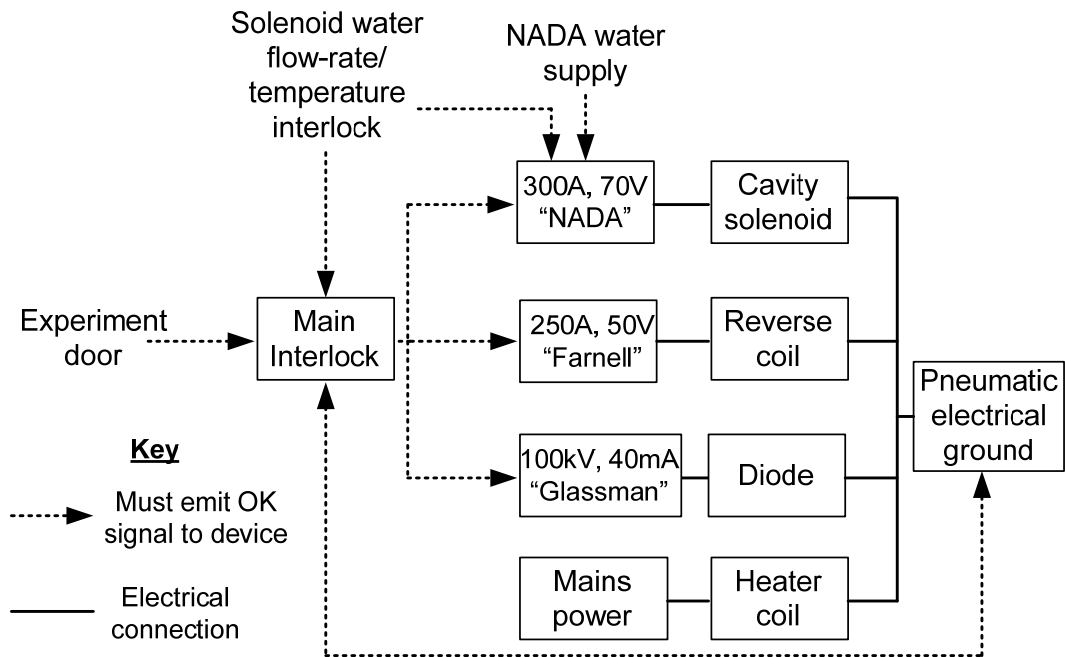
Figure 6.37. The safety interlock system. Each item has to be "true" before the main interlock will allow power on the high voltage power supplies.

6.7 Electron beam tube

The beam tube in the gyro-BWO experiment has many different features which are critical for generating the microwaves. The beam tube is detailed in Figure 6.38 with the magnetic field profile shown below. When the electrons are emitted from the cathode they travel through the anode aperture and during the electron beam compression region there is a tapered waveguide that leads to a backstop filter. When this was constructed the stainless steel tube that houses the main waveguide components is welded to the anode and tapered waveguide. The main waveguide components are then inserted into the stainless steel tube with a tight fit and pressed in place by the microwave horn component. The backstop filter is 10mm in length with a diameter of 1.67mm in order to avoid the electrons in the cathode region being disturbed by the reflected microwave. The reflected microwaves propagate back along the beam tube for extraction through the microwave horn. The position of the backstop on the magnetic field profile is detailed in Figure 6.38 and it can be seen that this field is at 1.56T - 1.7T, which is lower than the full magnetic field of the interaction. The field is required to be low so no microwaves are produced at this
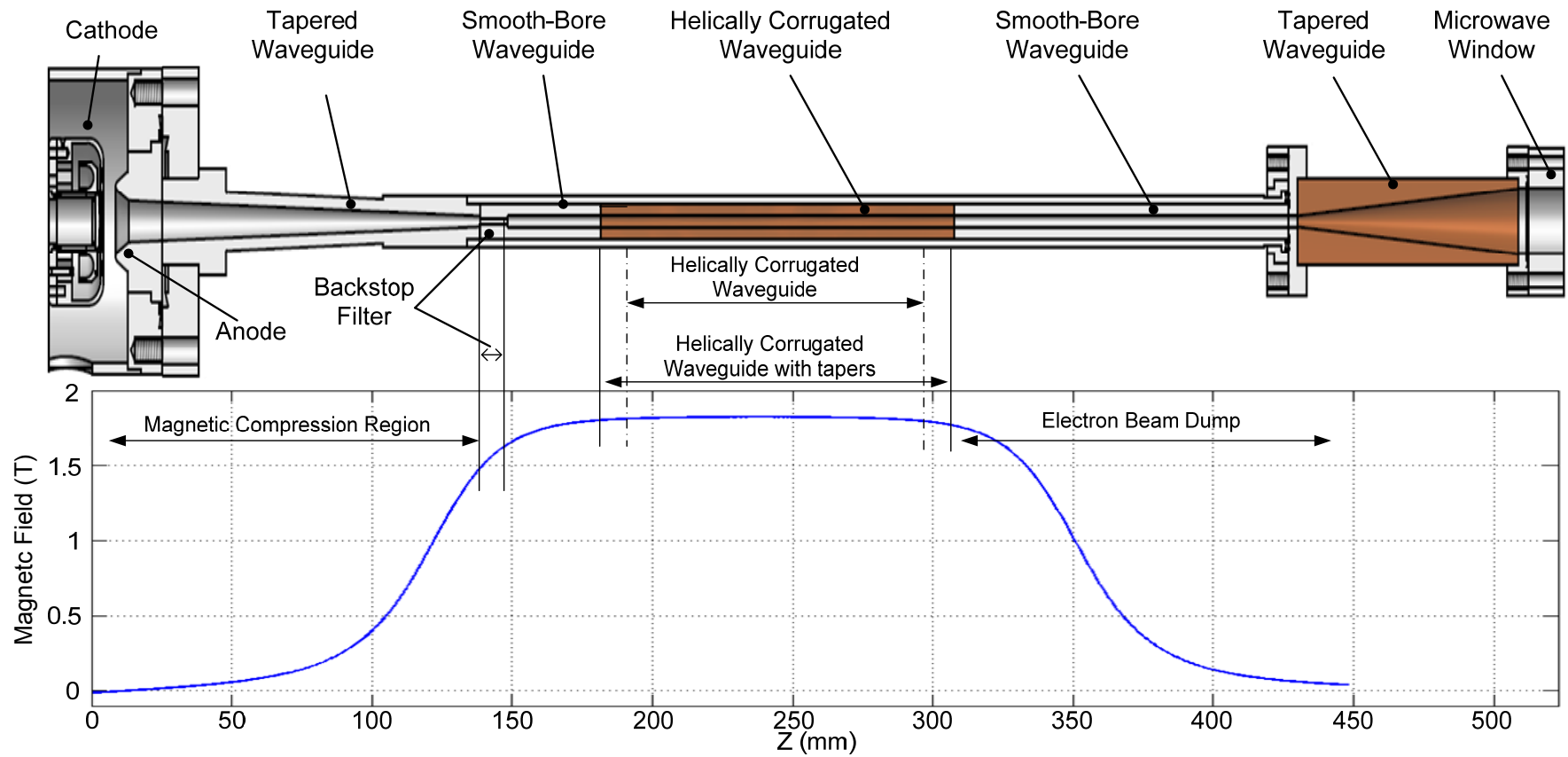
Figure 6.38. Beam tube used in the gyro-BWO experiment with the simulated magnetic field profile.

region. The long smooth waveguide after the backstop filter is used so that the helically corrugated waveguide can be situated in the middle of the maximum magnetic field region. After this there is another long smooth-bore waveguide which acts as a beam dump as the magnetic field slowly reduces in strength.

6.8 Electron beam diagnostics

The various electron beam properties of interest are velocity ratio alpha, velocity spread, the cross-sectional shape of the electron beam and current. These can all be measured through well known techniques.

6.8.1 Scintillator

The measurement of the size, shape and profile of the electron beam is most commonly performed through a witness plate technique. A thin sheet of material is placed in the beam tube perpendicular to the path of an electron beam. When the beam hits the plate this will change the appearance of it, for instance colour, or produce detectable effects such as visible or X-ray radiation. These thin sheets come in the form of Mylar sheets, films or scintillators.
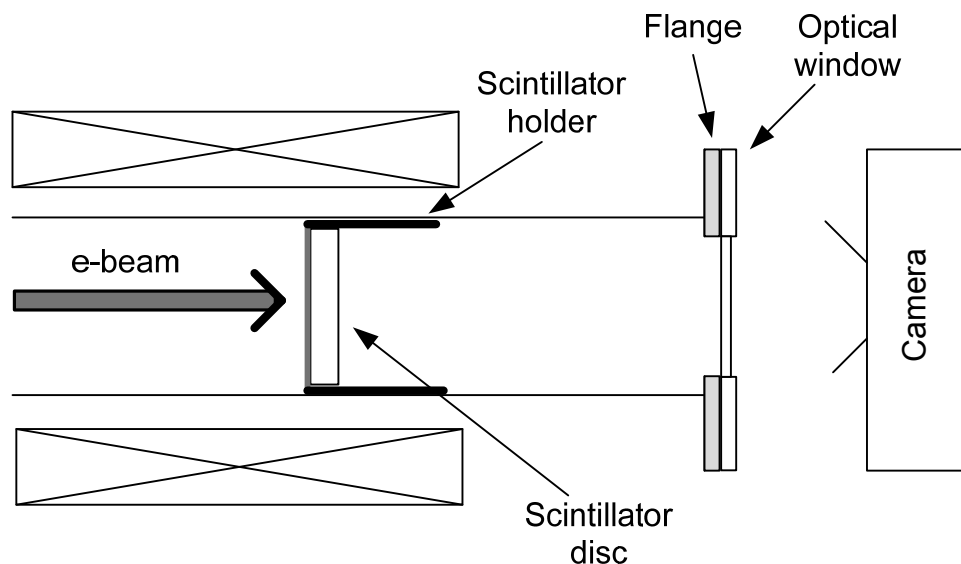
Figure 6.39. Schematic of the scintillator experimental setup.

A scintillator is a very simple concept of taking a transparent material and covering

the surface of this with a very thin coating of a scintillator powder, a phosphor, and in front of this is a thin metal sheet. The metal sheet is used for reducing the electron energy to a low ~kV level as otherwise the scintillator powder would be blasted away by the electrons. This was mounted on a tube and kept in place with another tight tube as seen in Figure 6.40.
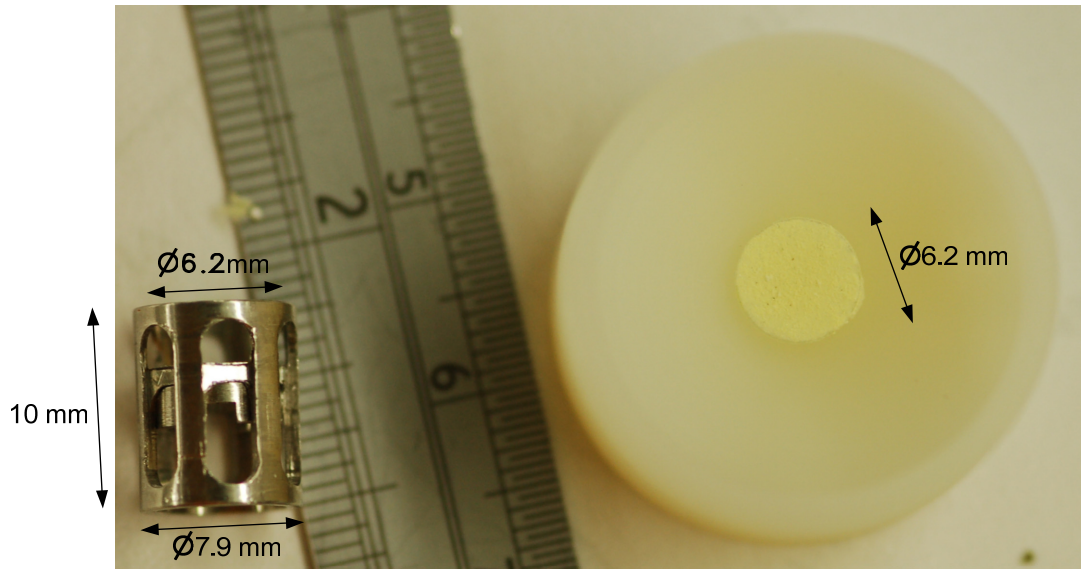
Figure 6.40. Scintillator disc, held inside a plastic ring, and a stainless steel holder for the scintillator disc and molybdenum foil.

The scintillator is then placed far into the beam tube so that it is in the region of high magnetic field so the correct beam parameters could be obtained. The light pattern is then recorded by a high resolution camera in a long-exposure mode. This allows the determination of the inner and outer radius of the electron beam thus allowing the determination of the alpha value, which can be compared with simulated values and also analytical means. This also shows the thickness of the electron beam showing how well the solenoids are positioned as incorrect placement of the solenoids results in a large electron beam ring. Therefore, this is a very useful diagnostic technique for adjusting parameters until the correct alpha and beam thickness are obtained.

6.8.2 Faraday cup

A Faraday cup is a metal cup or cylinder with a small orifice used to measure current of electrons or ions. The impacting electrons or ions hit the wall transferring the

current into a voltage signal through a resistor which can then be transferred to a measuring unit, such as oscilloscope. The design was relatively simple and a schematic of a Faraday cup can be seen in Figure 6.41. The design had to be careful to try and reduce the number of secondary electrons emitted which can increase errors in the measurement of current. When this is used to measure ions the secondary's can be reduced by coating the cup with carbon. Another way of reducing these is to specially shape the cup.
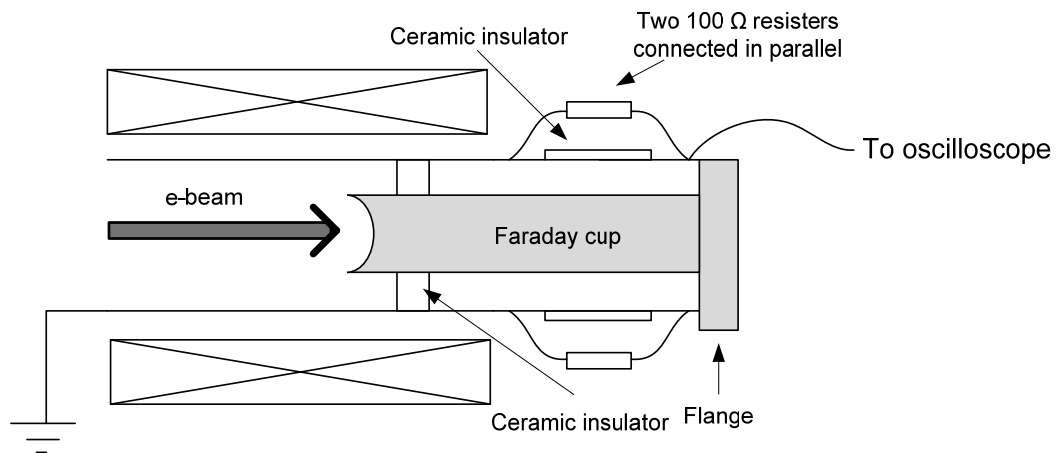
Figure 6.41. Schematic diagram of the Faraday cup experimental setup.

Due to the current induced in the Faraday cup this has to be separated from the other parts of the experiment with an insulator or insulation to avoid damaging other equipment. There are two 100Ω resistors in parallel that connect the Faraday cup to the beam tube of the experiment which is grounded.

Figure 6.42. Photo of the Faraday cup connected to a ceramic insulator which has two 100Ω resistors connecting the two sides of the ceramic insulator.

Any current measured by the Faraday cup will then pass through these to the earth line, while the oscilloscope is connected to the resistors to measure the voltage across the resistor.

6.8.3 Rogowski coil

A useful diagnostic tool is a Rogowski coil which is able to measure pulsed currents or alternating current as current produces magnetic fields and this coil can pick-up that magnetic field. Where this is most useful is to perform an in-situ measurement of the current produced by the cathode to compare against the applied voltage and output microwave power. A Faraday cup can perform this measurement but this cup will not be in-situ when microwaves are generated so the methodology used is to first measure the current with both the Faraday cup at the end of the beam tube and the Rogowski coil near the cathode. If these measurements show the same current then there is 100% current transport through the tube. This means that the output of the Rogowski coil can be assumed to be the current produced from the cathode. If these two diagnostics do not show the same current then there is less than 100% transport and so the output from the Rogowski coil should be then modified to show the current that transports to the end of the tube. The reason the coil is able to measure the current is that it is a solenoid wrapped in a torus which encircles the current to be measured, shown in Figure 6.43.
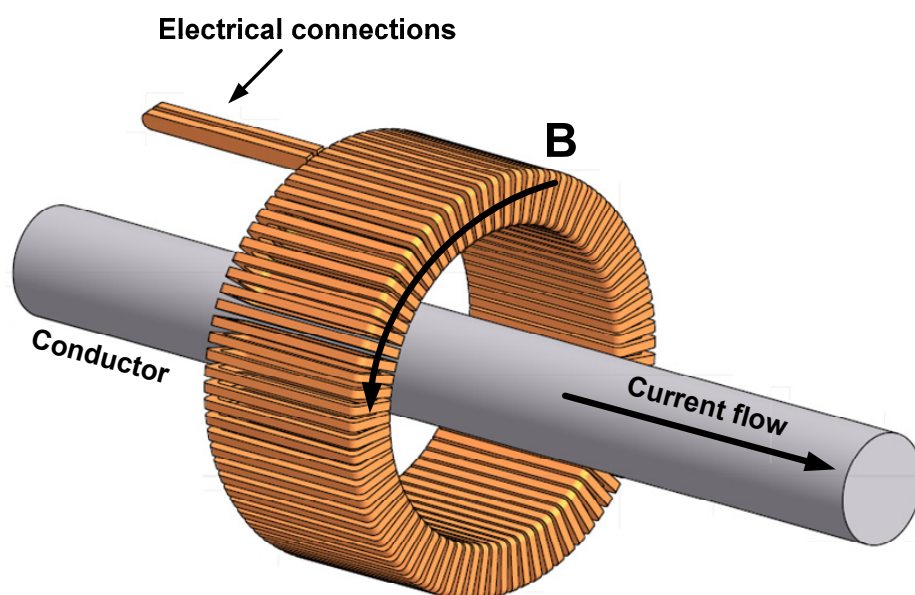
Figure 6.43. Schematic diagram of a Rogowski coil.

The changing current induces an electromotive force $-d\psi/dt$ in the coil. The voltage is proportional to the rate of change of the current and so this is connected to an integrator circuit that produces a steady signal that can be measured and this is proportional to the current to be measured.

If a coil of uniform cross sectional area, A, is considered with a constant turns per unit length n the flux can be measured by first assuming that the magnetic field changes little over one turn spacing so that the following condition is met

$$|\Delta B|/B \ll n \tag{6.9}$$

Then the total flux linkage by the coil can then by found through an integral rather than a sum over the individual turns

$$\Phi = n\oint_l \int_A dA\,\mathbf{B} \cdot dl \tag{6.10}$$

Where dl is the line element along the solenoid.

Then the order of this integration can be changed so that Amperes law given in equation can be substituted in.

$$\oint_l \mathbf{B} \cdot dl = \mu I \tag{6.11}$$

So this now means the flux can be found through

$$\Phi = nA\mu I \tag{6.12}$$

Therefore, the voltage out of the Rogowski coil can now be found through

$$V = \dot{\Phi} = nA\mu \dot{I} \tag{6.13}$$

This signal is then normally integrated so that the voltage is proportional to the current and this can be measured by an oscilloscope.

The Rogowski coil is used in the experiment as an in-situ measurement of diode current which allows electron beam current to be inferred. This has to first be calibrated with a known current then the Rogowski coil can used to allow a constant measurement of the diode current. The position of the Rogowski coil can be seen in Figure 6.44. This is connected on the earth line of the experiment so that any electron beam emitted will have to travel back along the earth line through the Rogowski coil.
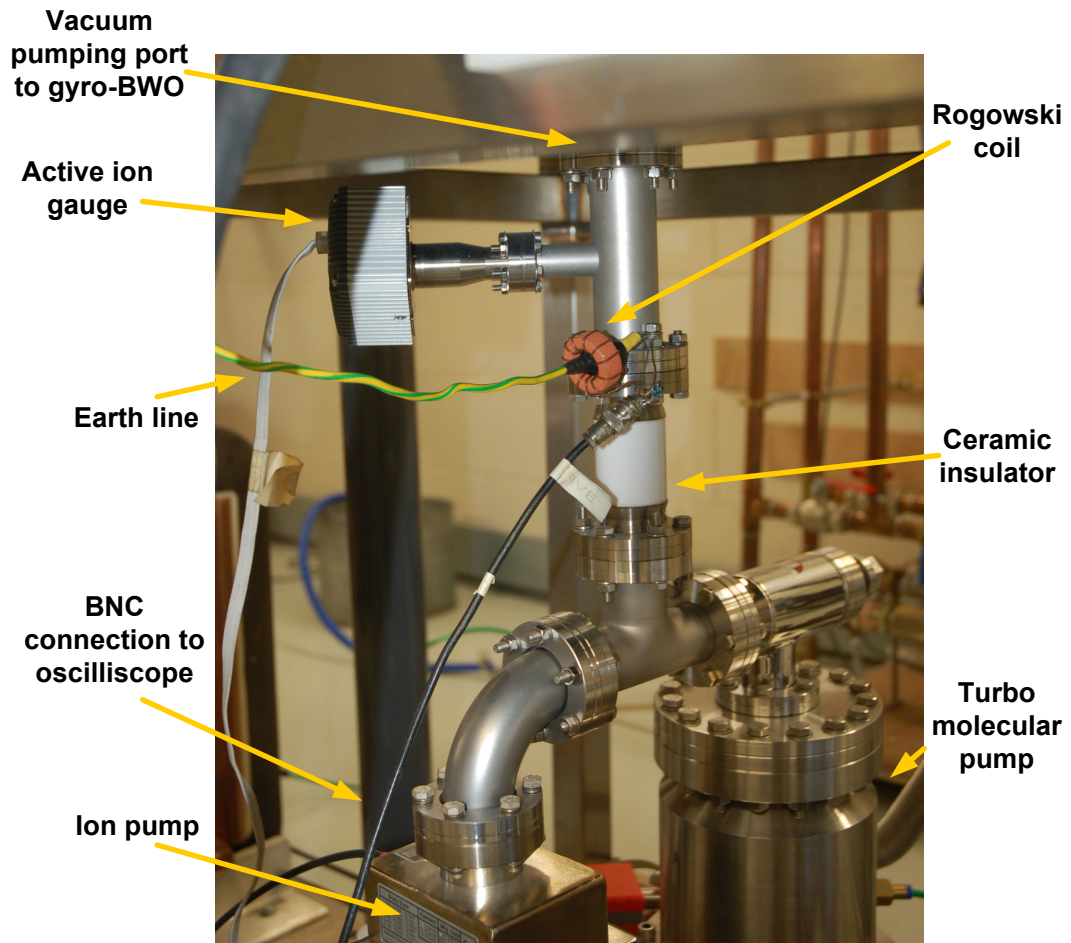
Figure 6.44. Position of the Rogowski coil on the gyro-BWO system.

6.9 Vacuum system

The vacuum system in this experiment is comprised of an ion pump, turbo molecular pump and scroll rough pump operating together. The electron beam requires a suitably evacuated tube in order to travel without many collisions with heaver particles that would inhibit flow. Also, the cathode requires an ultra-high vacuum to reduce the possibility of contamination. The system is evacuated from the diode chamber while the rest of the system is kept sealed using ConFlat flanges with copper gaskets.

A scroll rough pump is used first to remove the bulk mass of particles from the vacuum chamber and obtain a pressure of $\sim 1 \times 10^{-3}$ mBar. This pressure is low

enough to operate a turbo molecular pump that can reduce the pressure down to the required 1×10^{-9} mbar range. The turbo molecular pump is sensitive to voltage surges and is liable to stop operating in which case the diode chamber would loose vacuum due to leaks, in the seals, especially in the low vacuum region. This is the reason that an Ion pump is used to maintain the pressure as this is much more reliable.
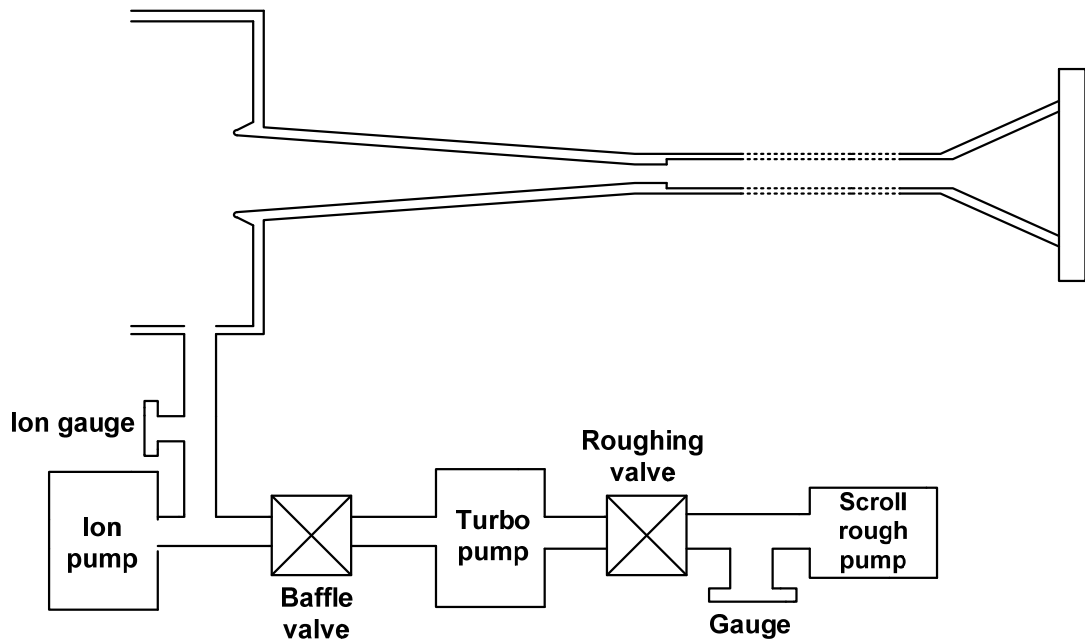
Figure 6.45. Vacuum system used for the gyro-BWO.

6.10 Overview of experiment

In this chapter the various elements that make-up the gyro-BWO have been detailed in-depth and this section presents a brief overview of the whole system. The gyro-BWO system was designed in order to produce microwave radiation at 84-104GHz in the TE_{11} electromagnetic mode. The experiment was run as "proof-of-principle" tests with an aim to later expand the research to measure broadband frequencies. The setup is shown in Figure 6.46 consists of 8 main areas: 1. Electron beam source, 2. Pulsed power system, 3. Beam transport, 4. Gyro-BWO interaction region and microwave launcher, 5. Magnetic field formation system, 6. Electron beam/microwave diagnostic system, 7. Vacuum system, 8. Environmental protection

system. The constructed setup is shown in photographic form in Figure 6.47 and Figure 6.48.

1. Electron beam source: The electron beam was produced by the thermionic cathode operated at a high temperature. The diode was driven by a pulsed signal generated by a double-Blumlein closed by a spark-gap switch in order to produce a pulse of 400ns range. (Chapters 5 and 6)

2. Pulsed power system: A double Blumlein with a spark-gap switch was used in order to produce the power for the diode. The pulsed power system was charged using a 100kV, 40mA DC power supply (Glassman). The designed output pulse was ~400ns with a rise time of 40ns. (Chapters 6 and 7)

3. Beam transport: The beam was transported from diode through the anode aperture by the combined magnetic field of a reverse coil and cavity solenoid. Further transport from the anode to the interaction region and finally to the collector was through the cavity solenoid magnetic field. Rotational velocity was imparted to the beam at the cathode-anode region due to the magnetic field reversal caused by the aforementioned reverse and cavity solenoids. Furthermore, axial velocity was converted to azimuthal velocity due to magnetic compression. (Chapters 5 and 6)

4. Gyro-BWO interaction region, microwave horn: The gyro-BWO interaction, based on the electron cyclotron maser instability, takes place in the helically corrugated waveguide (1.3mm average radius, 0.24mm corrugation amplitude, 3.75mm corrugation period and 12.75mm overall length). In the waveguide the rotating electron beam, with a significant ratio of transverse velocity to axial velocity, interacts with the eigenmode that is a combination of the TE_{11} and TE_{21} mode. The backward travelling waves are then reflected along the waveguide in the forward direction due to the step-reflector. Microwaves generated through this process are launched by a tapered output horn through a sapphire microwave window. (Chapters 3, 6 and 7)

5. Magnetic field formation system: There are two magnetic coils used in this system: reverse coil and the cavity solenoid. The former produces a negative magnetic field just behind the location of the cavity and the latter produces a strong positive magnetic field at the location of the interaction region. The driving power for the cavity solenoid was a 300A, 70V DC power supply (NADA) that consisted of 5 power supplies operating in parallel to produce the maximum 300A's. The driving power for the reverse solenoid was a more modest 250A, 50V (Farnell) power supply. Both solenoids were wound with square copper wire of 2.2mm side length in order to assist cooling. The cooling system was from pressurised re-circulating water supply. (Chapter 6)

6. Electron beam/microwave diagnostic system: The electron beam measurement system included the diode/beam voltage (measured using a resistive voltage divider), transported beam current (measured using an in-situ Faraday cup), diode current (measured using a Rogowski coil connected at the earth path of the electron beam tube), electron beam cross section profile (scintillator witness plate technique). The microwave diagnostics include wave frequency (measured using a oscilloscope), power. (Chapters 6 and 7)

7. Vacuum system: The vacuum system used was three pumps working in tandem: a scroll pump, turbo molecular pump and an ion pump. The pumping path was at the diode region of the gyro-BWO through a 1 inch pipe at the anode can. A vacuum seal was kept at the interaction region through the microwave window at the end of the microwave horn. The vacuum obtained was in the 10^{-9} mBar range. (Chapter 6)

8. Environmental protection system: The gyro-BWO was constructed and operated in a place sealed in all sides with 7mm lead walls or 44cm thick high density concrete walls. This system provides enough protection against X-rays generated by the 40kV, 1.5A electron beam. (Chapter 6)
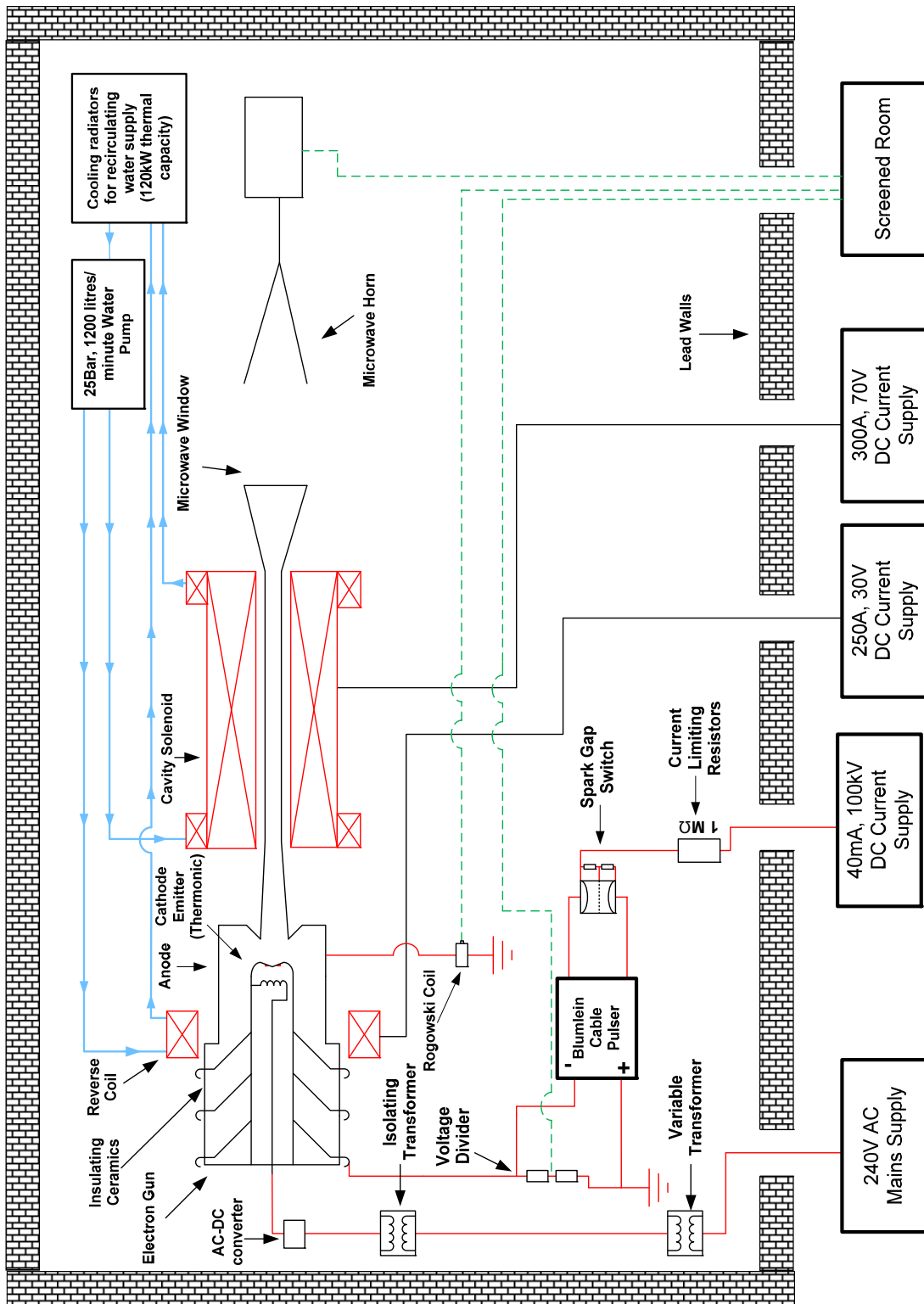
Figure 6.46. Schematic of the gyro-BWO experimental setup.
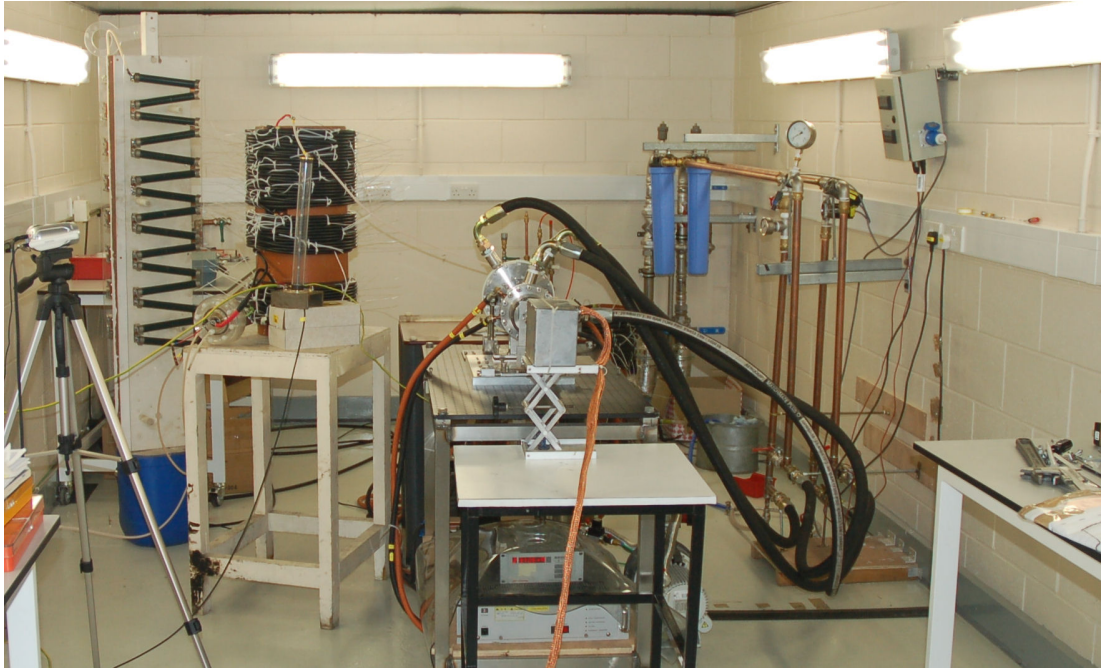
Figure 6.47. Photo of the gyro-BWO system as a whole. Included are the power supply system, water cooling and gyro-BWO.
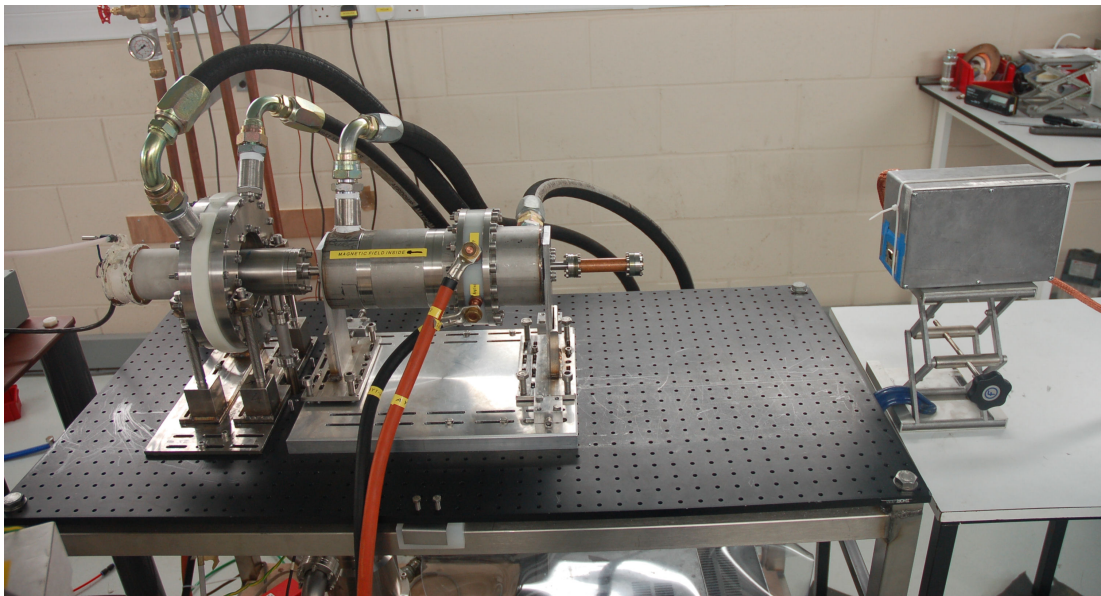
Figure 6.48. Photo of the gyro-BWO and microwave detector.

6.11 Summary

This chapter has introduced the various elements that are used for the gyro-BWO experiment. The cusp electron gun manufacturing process was described and shown.

A main point of this chapter was to show the solenoids from inital model to the final construction state. There were many parts of these solenoids which were introduced from the wire configuration to the cooling system and calculation of the heat output to the measured magnetic field profiles. Electron beam diagnostics were introduced and shown here as well from the Faraday cup to the scintillator disc which were critical for gyro-BWO experiments. The chapter concluded with the full gyro-BWO experimental setup.

Chapter 7.

Gyrotron Backward Wave

Oscillator Experiments

7.1 Introduction

In this chapter the experimental results of the gyrotron backward wave oscillator experiments are given. The first section describes the output voltage pulse from the pulsed power system. From this, the current produced by the cathode was investigated. The magnetic field was then applied, with the transported beam current measurement taken. A scintillator disc, placed inside the beam tube, recorded the cross-sectional shape of the electron beam. The form, diameter and alpha value of the electron beam was then deduced from the beam profile. Finally, microwave radiation generated by the gyro-BWO was observed and recorded. The results presented within this chapter confirmed the generation of an axis-encircling electron beam from the cusp electron gun and microwave generation from the gyro-BWO.

7.2 Beam voltage measurements

The cusp electron gun, which was previously designed and simulated (see Chapter 5), was used to drive the gyro-BWO. In order to achieve the highest electronic efficiency of beam-wave interaction and hence the microwave power, it is necessary to minimize the spreads in beam energy, axial velocity and alpha. The axial velocity and alpha spreads are dependent on: the diode geometry, emission process, emission locations, B-field profile and energy spread of the beam. Therefore the first task was to improve the pulse shape of the accelerating voltage as this would additionally affect the beam transport along the tube. A poor quality voltage pulse – e.g. one that has a slow rise-time and a varying voltage over the pulse length - will generate an electron beam of similar varying energy. This could lead to mirroring of electrons, an increase in axial velocity and alpha spreads, and resonance at more than one microwave frequency. Therefore it was important to optimise the voltage pulse before cusp electron gun experiment in order to replicate the simulated pulse used within MAGIC simulations of the diode. The optimisation aimed to reduce the rise and fall times and produce a stable voltage during the pulse.

The voltage pulse was produced by a double cable Blumlein charged by a 100kV, 40mA Glassman DC power supply. This was discharged through a closing spark gap

switch operating at self-breakdown mode. The breakdown voltage of the spark gap could be adjusted by changing the resistive dividing ratio between the first and the second gap to produce a pulse of differing magnitudes. The resulting voltage pulse was then measured using a digitized oscilloscope. The voltage pulse produced is shown in Figure 7.1. The rise-time of this pulse is ~40ns with an average voltage of ~40kV.
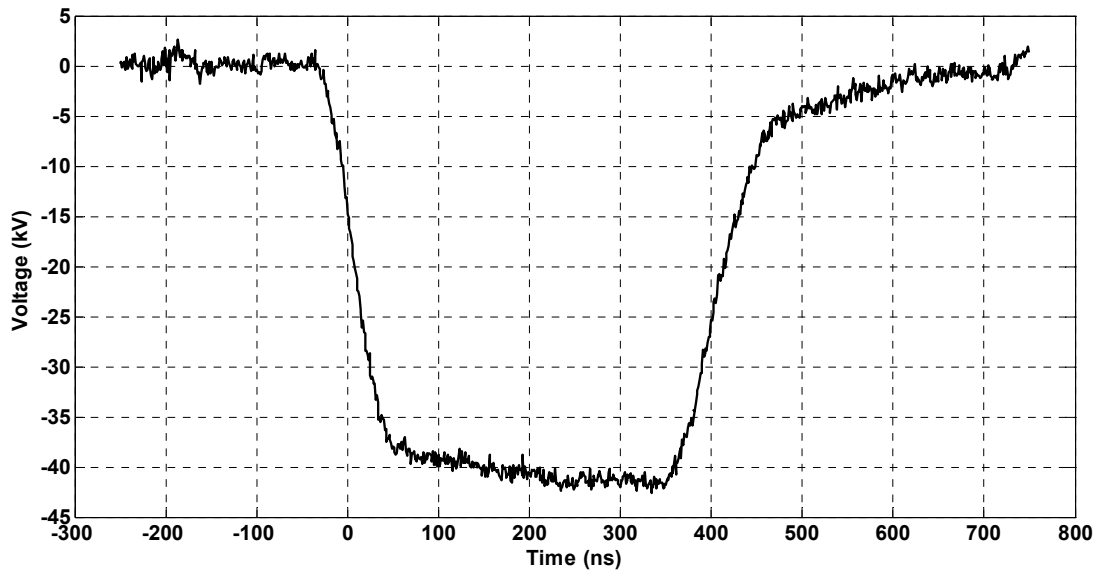
Figure 7.1. Voltage pulse used to accelerate the electron beam. The ~40kV pulse lasts for ~400ns.

The length of the pulse is ~400ns chosen to be relatively long in order to study the microwave generation over the hundreds of nanosecond time scale. Since the gyro-BWO was designed and built CW-ready, there are no inherent problems in running long pulses. The fluctuation of the voltage amplitude in the flat-top region is ~5% from the average voltage. This pulse was of good enough quality to drive the gyro-BWO and cusp electron gun.

7.3 Diode current measurements

It is imperative to measure the diode current in the gyro-BWO, in order to know the amount of emitted beam current and to observe how the cathode is performing. Later, the transported beam current can then be compared and calibrated due to the fact that there was no in-situ diagnostic of the beam current in the device. The current produced by the diode allows one to determine the emission regime of the cathode.

The normal operating regimes for the cathode are either thermionic or space-charge limited. The diode current varies depending on either the temperature of the cathode, in the thermionic regime, or the applied voltage, in the space-charge limited regime. The experimental setup used in diode current measurements was discussed in Chapter 6 and requires a Rogowski coil encircling the earth line of the device (i.e. anode and beam tube). Any electron that impacts on the beam tube will be returned along the earth line and thus be measured by the Rogowski coil. The diode current produced by the aforementioned voltage pulse is shown in Figure 7.2.

The plot displayed the current with and without the heater current power on. When there was no heater current the cathode was cold with no electrons emitted so the recorded signal was a fictional displacement current. When the heater current was sufficiently high enough for electron emission from the cathode surface ($\sim 1000^{\circ}$C) the recorded diode current would be different to the background. The difference between these two signals is the value of the real emitted current and this can be observed in Figure 7.3. The displacement current is reproducible so the real value of the diode current could always be found.
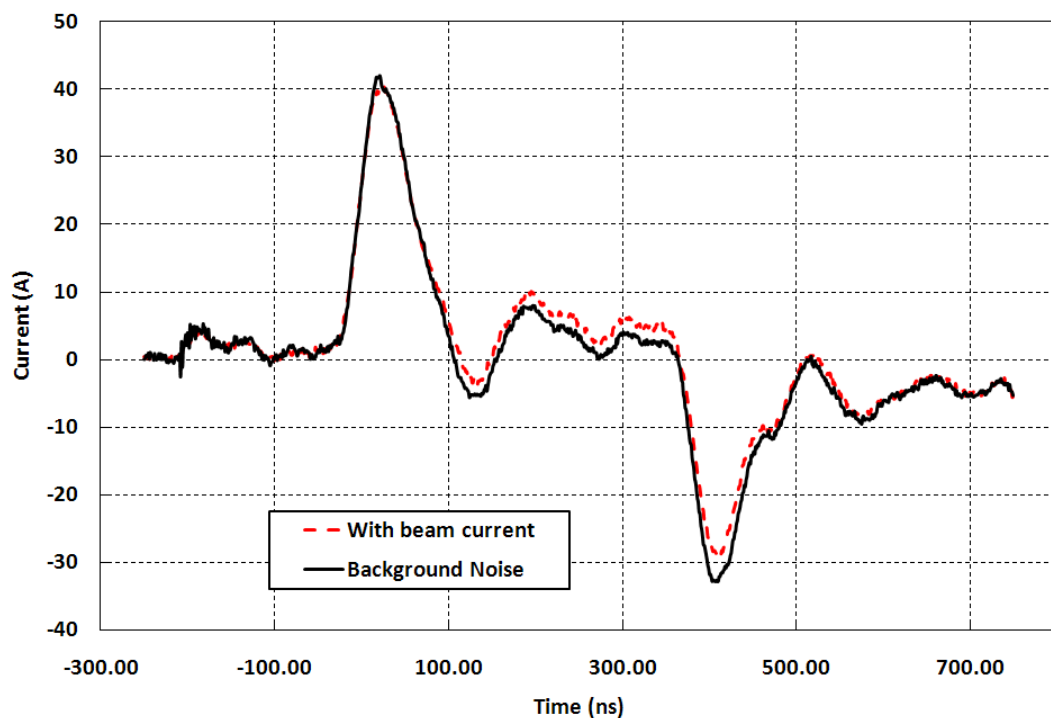
Figure 7.2. Rogowski coil measurement of the diode with no heater current (background noise) and with heater current.

Two peaks, that are much larger than the rest of the signal, are recorded at the rise and fall time of the voltage pulse. These arise from a fictional current known as the displacement current. This occurs in all diodes and is due to the application of the pulsed voltage which creates the electric field across the cathode-anode gap. The diode has a capacitance, C_d, held between the cathode, negative potential, and anode, grounded. The capacitance and time-varying voltage give rise to a displacement current, I_d, calculated through equation (7.1). This displacement current was predicted through, and derived from, Maxwell's equations[187].

$$I_d = C_d \frac{dV}{dt} \qquad \text{(7.1)}$$

This displacement current does not correspond to actual diode current so in order to view the real diode current the current in-between the two peaks should be used to calculate the average value. This displacement current is the same in both cases where the heater current is off (no electrons emitted) and on (an electron beam emitted). The current produced from the diode in this typical result had an average current of ~5A over duration of ~400ns.
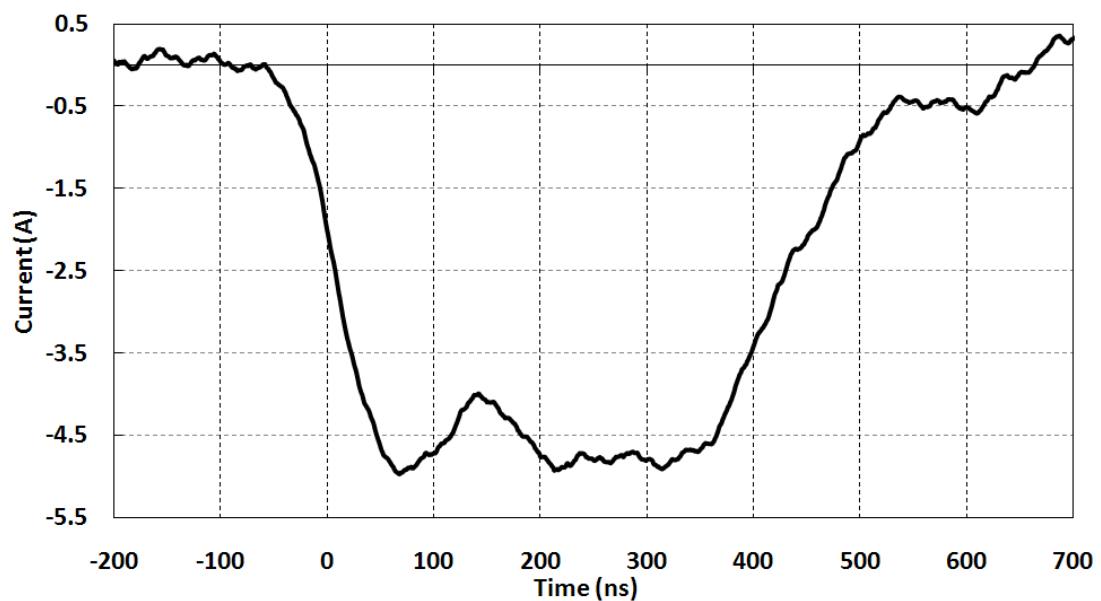
Figure 7.3. Rogowski coil measurement of the diode current.

The cathode is designed to be operated in the temperature limited regime so by adjusting the heater power one can change the cathode emitting current. The

measured diode current as a function of the heater current is shown in Figure 7.4. It is obvious that the cusp gun operates in the temperature limited regime. When operating a cathode in the temperature limited regime it is important to know the relation between the diode current vs. T, see equation (4.7).
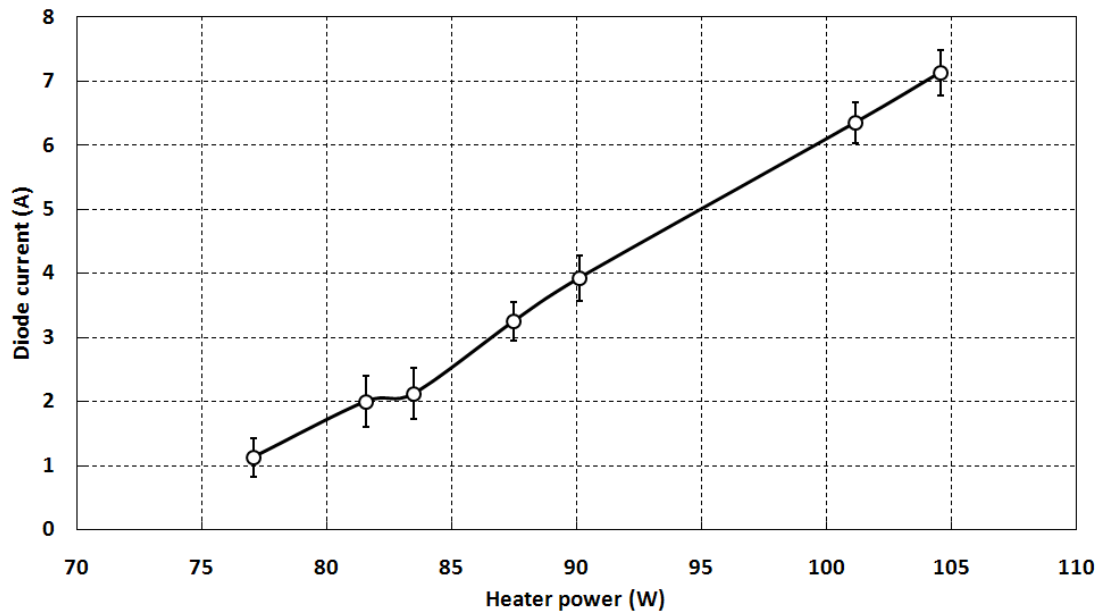
Figure 7.4. Values of emitted diode current against heater coil power.

7.4 Beam current measurements

The transported electron beam current – that which passed from the diode through the interaction region – allows one to know how much electron beam current is available for microwave interaction and to measure the electronic efficiency of the gyro-BWO. If the transported current was very low then this could be problematic for the operation of the cathode as the cathode would be required to output a larger current to compensate, reducing lifetime and increasing the risk of parasitic electron emission.

The electron beam current was measured by a Faraday cup, see Chapter 6 for full experimental details, situated at the output of the interaction region. The Faraday cup was inserted from the collector end of the beam tube and the length was set so that the cup is at the maximum magnetic field region. Calculations predict that the

diameter of the electron beam would be ~0.8mm at this region so the cup diameter of 4mm would capture all the electrons. A typical measured electron beam current waveform, at 1.5A, is shown in Figure 7.5.
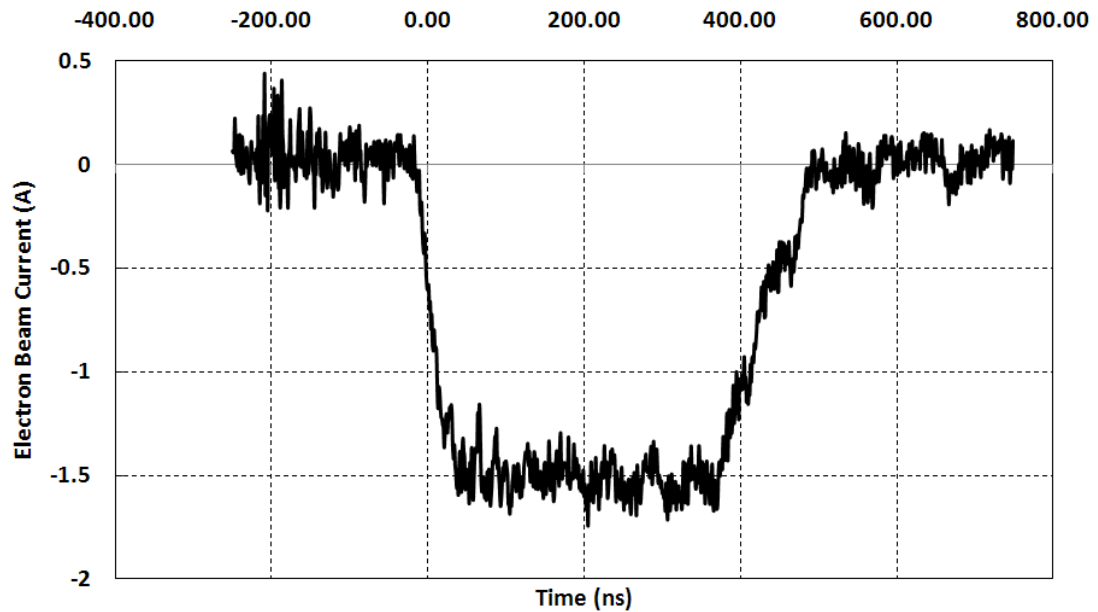
Figure 7.5. Measured transported electron beam current pulse of ~1.5A.

The electron beam current has an average current of ~1.5A with a peak current of 1.55A in this particular operation condition. The variation in beam current is +/- 3.33% comparable to the change in the applied voltage pulse of +/- 5%. For clarity the superposition of the electron beam current and accelerating voltage can be seen in Figure 7.6. It is apparent that the current pulse displays the same profile as the accelerating voltage pulse. When the diode current was adjusted from 1.5A to ~8A the observed transported electron beam current showed a limiting value of ~1.5A as shown in Figure 7.7. The measured data in Figure 7.7 suggests that the cathode was operating in the temperature limited regime up to a diode current of ~2A. When the cathode temperature was raised the electrons start to emit from the cathode-focus electrode gap giving rise to diode current but not beam current. This effect was not simulated in the MAGIC or Opera-3D simulations.
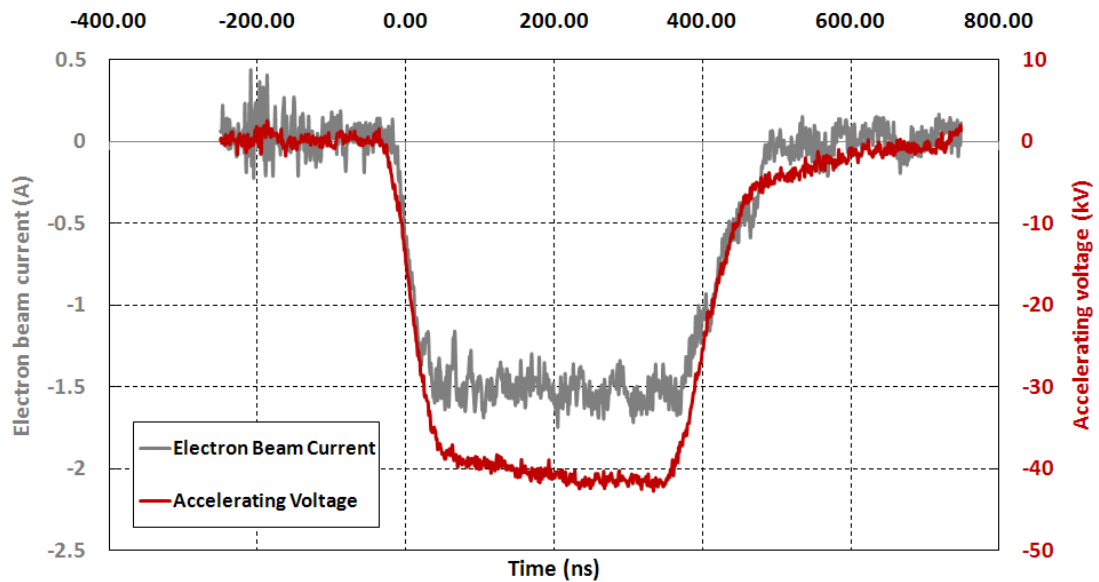
Figure 7.6. Electron beam pulse compared against the accelerating voltage pulse.
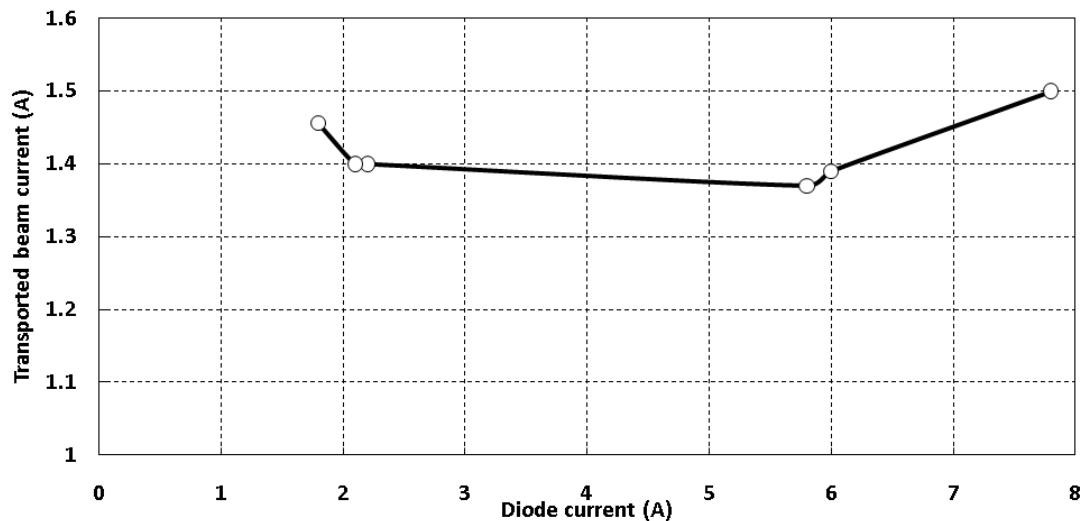
Figure 7.7. Variation of transported beam current with the diode current.

To study if the reverse coil has effect on the transmitted beam current, one should study the effect of varying values of alpha on the beam transport. As the radius of the beam is dependent on alpha, as shown in Figure 7.8, when the reverse coil magnetic field strength is increased this would cause more of the electron beam to impact on the beam tube. Increasing the reverse coil magnetic field strength would eventually stop beam transport through the beam tube. In this case the maximum beam transport was recorded to be 96% at a reverse current of 144.5A, diode current of ~1.8A. The reverse coil was 155.5A reducing the transported beam current to ~70% at a diode

current of ~2.4A. As shown in the figure the radius of the electron beam increases by a small amount with a reverse coil increase of this amount, just over 0.1mm. This means that loss of beam transport current would be mostly attributed to a change in diode current as the diode current does not stay at a stable value from shot-to-shot when the electrons start filling the gaps between emitter and focusing electrodes.
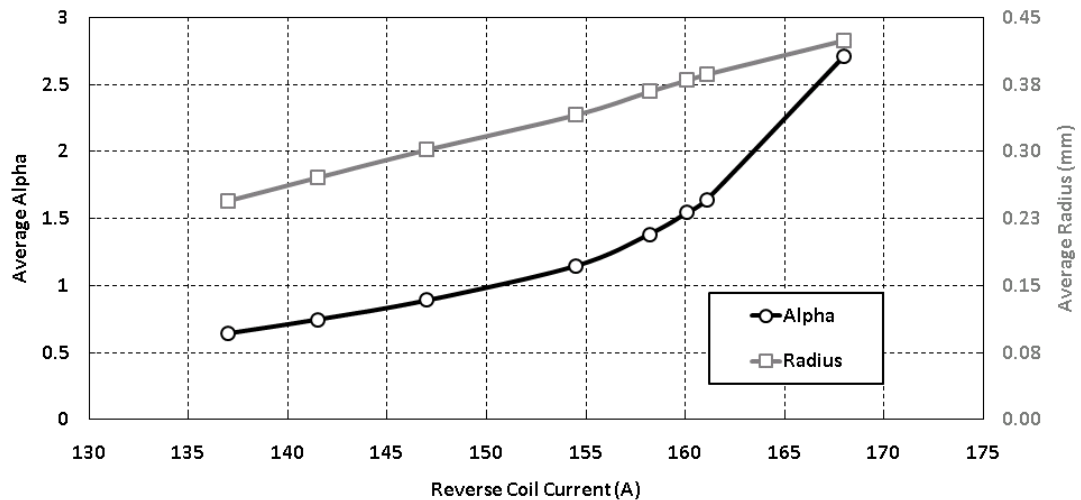
Figure 7.8. Electron beam average beam diameter compared against average alpha value as the reverse coil current changes.

7.5 Beam cross-section shape and velocity alpha measurement

The most important diagnostic for the cusp electron gun is measurement of the electron beam cross-sectional shape. The beam profile can allow one to see, clearly, if the transported electron beam is an axis-encircling or solid beam. If one can observe an electron beam ring on the scintillator disc then this proves successful generation of an axis-encircling electron beam. The setup for this experiment has been detailed in Chapter 6 Section 6.8.1. The scintillator disc was coated with a phosphor which emits photons when electrons impact on the surface. This disc was inserted 11cm inside the magnetic field so that the disc was almost at the maximum B-field, at 10% less than maximum value. A typical observed photo can be seen in Figure 7.9. While this shows a large blue ring surrounding a small white circle the image is less clear than one would expect. The red segmented circle surrounding the image was the light from the cathode passing through the gap between beam tube and the scintillator holder.
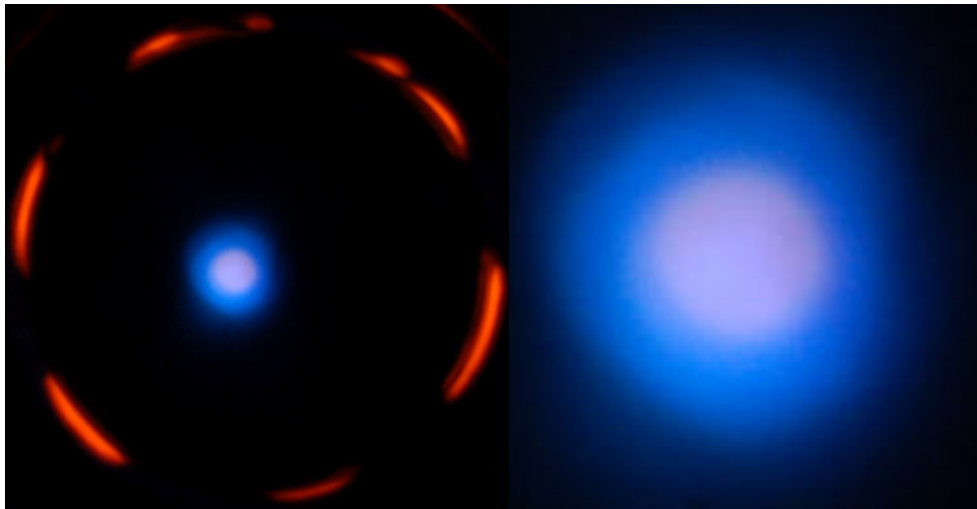
Figure 7.9. Photo of scintillator taken with a long exposure camera. The left picture shows the full recorded image and the right image shows the enlarged beam image.

The phosphor emitted blue light so through the use of photo editing tools the area of pure white light was reduced. The white area contained differing amounts of red, green and blue. It was seen that in areas around the blue ring where the light appeared white it was actually mostly blue with small amounts of red and green. The software used a colour filter to highlight areas with greater blue light intensity and reduce areas without blue light. The result was a much clearer image of the electron beam, shown in Figure 7.10, with the high intensity ring of the beam surrounded by a cloud of much lower intensity light.
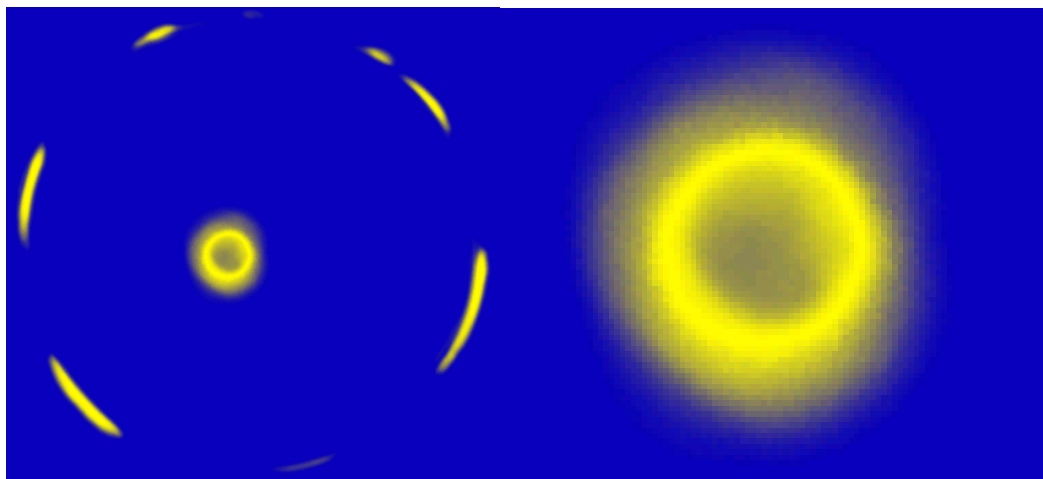
Figure 7.10. Position and the shape of the electrons on the scintillator.

One obvious problem that occurred with the measurement of these results was a high intensity white spot in the centre of the images that occurred throughout the measurement process. This light was not expected so it was anticipated that the molybdenum foil that was in front of the scintillator could have been damaged. Therefore, after the measurements were taken the molybdenum foil was taken out and viewed under an optical microscope. Small burn holes can be seen of the order of 0.15-0.2mm that arise from the large current density electron beam repeatedly impacting the molybdenum foil without sufficient thermal path to conduct the heat giving rise to extreme temperatures in the foil. While this is a problem and would eventually stop measurement using the scintillator this was not thought to impact the validity of the result gained as these holes are at least half the size of the white light observed. Furthermore the white light does not obscure the observation of the blue wavelength phosphor emission. This is evident in some recorded images where the beam circle enters into the space occupied by the white light.

Figure 7.11. Damaged areas in the molybdenum foil used in the scintillator experiments.

7.5.1 Estimation of beam diameter and velocity ratio

The electron beam profile picture gained through these experiments not only allows one to describe the nature of the electron beam – axis-encircling or solid beam – but allows one to calculate the diameter of the beam and from this the velocity ratio of the electron beam at the scintillator position. Through this knowledge one can compare the results obtained to the MAGIC simulations which assists further experimental work. It is possible the cathode is not in the designed position so knowing the exact magnetic field at the cathode surface is difficult. Therefore, measurement of the alpha value produced by a value of the reverse coil current would allow one to know what reverse coil currents to use in the gyro-BWO experiment in order to achieve a set alpha value. The outer and inner diameter of the beam on the scintillator image was very visible however this may not be so visible in a printed format so to assist this has been overlaid on the image in Figure 7.12. The scaling factor of these images was calculated as the outer ring of light visible in Figure 7.9 corresponds to the outer ring of the scintillator holder which is 6.2mm. Therefore the average radius of this ring can be seen to be 0.36mm.

In order to find the alpha value of the beam one must first calculate the relativistic Lorentz factor, γ. This is dependent on the accelerating voltage, V, and could be calculated from equation (7.2). With the 40kV accelerating voltage the relativistic Lorentz factor is $\gamma = 1.078$ showing a weakly relativistic electron beam.

$$\gamma = 1 + \frac{eV}{m_0 c^2} \tag{7.2}$$

Then the perpendicular electron velocity is derived from the average radius of the electron beam, r.

$$\mathrm{v}_{\perp} = \frac{eB}{\gamma m_0} r \tag{7.3}$$

In the case where the cavity coil was 195A, the reverse coil was 161A, the average radius was calculated to be 0.36mm. The magnetic field at the position of the scintillator disc which was 0.9B where B is the magnetic field of the flat top region as the scintillator was located after the flat top of the magnetic field. The perpendicular velocity in this case was 8.08×10^7 ms^{-1}. The parallel velocity could be

calculated from equations (7.4) and (7.5). In this case the parallel velocity was $7.81 \times 10^7 \text{ms}^{-1}$. The velocity ratio can then be calculated from equation (7.6) to be $\alpha = 1.03$ at the scintillator position. This means that at the flat top region of the magnetic field the electron beam velocity ratio could be calculated to be $\alpha = 1.14$.

$$V = \sqrt{1 - \left(\frac{1}{\gamma}\right)^2} c^2 \qquad (7.4)$$

$$v_{\parallel} = \sqrt{V^2 - v_{\perp}^2} \qquad (7.5)$$

$$\alpha = \frac{v_{\perp}}{v_{\parallel}} \qquad (7.6)$$

The picture of the electron beam has two defined circles, albeit with scattered electrons around the circles, and from this many different properties can be calculated including: average radius, velocity and alpha. The image is shown in Figure 7.12 where the outer radius and inner radius of the beam are highlighted along with the centre of this beam. This picture shows the inside diameter is 0.65mm and the outside diameter 0.79mm corresponding to an average radius of 0.72mm.
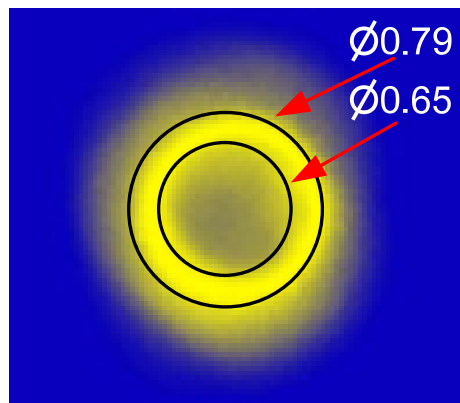
Figure 7.12. Cross sectional size of the axis-encircling electron beam produced by the cusp electron gun.

The electron beam was recorded at different values of reverse coil current and so different alpha values, shown in Figure 7.13. When the alpha value was low the beam had a small thickness, the first image. When the alpha value increases the thickness increases, the second image. Noticeable here is the beam cloud around the

electron beam ring is not uniform and in some areas does not appear to be as prominent as others. This indicates that the beam suffers from some degree of beam scraping.
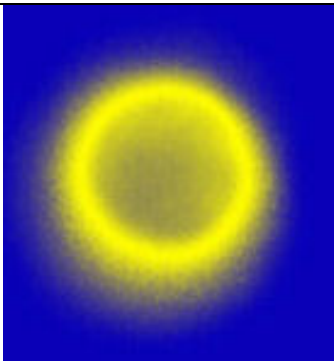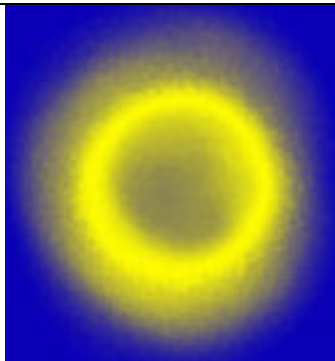
Reverse coil current	156.4A	161A
Cavity solenoid current	195A	195A
Average diameter	0.62mm	0.72mm
Alpha at scintillator	0.80	1.03
Alpha at maximum B-field	0.88	1.14

Figure 7.13. Electron beam profiles at different values of reverse magnetic field.

Through analysis of the electron beam images the alpha value can be measured and is shown in Figure 7.14. This shows the alpha value increasing as the negative magnetic field at the cathode surface is increased as one would expect. The measured, simulated and analytically calculated results are shown on this graph for two locations along the beam tube, Z_1 and Z_2. These positions represent a maximum magnetic field, Z_1, and a point where the magnetic field tailed off to 90% of the value, Z_2. The measured result was taken at point Z_2 and compares very well to the analytically calculated value and reasonably well to the MAGIC simulated values. At the highest alpha values the difference from the prediction to the measurement is increased which could be explained by increased beam scraping of the electron beam.
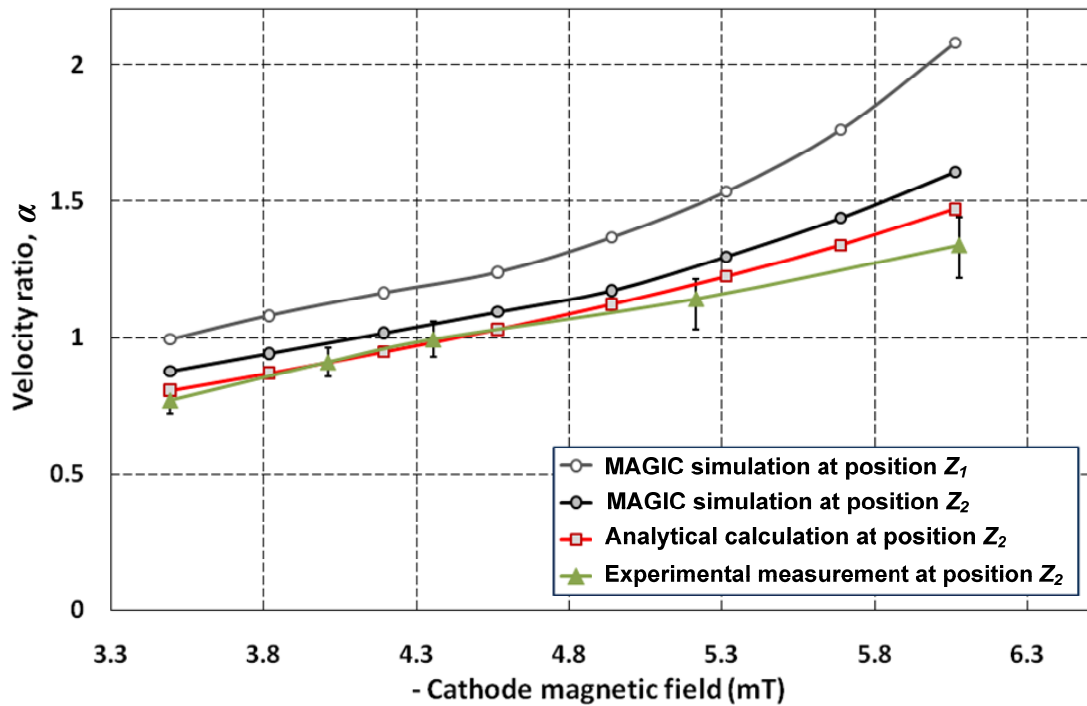
Figure 7.14. Variation of simulated, calculated and measured alpha values at two positions along the beam tube. Positions Z_1 and Z_2 correspond to a maximum and 90% of the magnetic field strength.

7.6 Comparison of experimental results with MAGIC simulations

The experimental results gained in this chapter are very encouraging however a comparison with the MAGIC simulated results is prudent in order to see if what is produced has a good agreement to what was simulated and created the high quality electron beam. Although the electron gun was simulated in two codes the comparison between MAGIC and the experimental results is focused on the MAGIC results as this program was used most extensively for calculating the electron beam parameters and the electron gun was designed with this program.

7.6.1 Accelerating voltage pulse and electron beam current

In the simulated case the voltage pulse, shown in Chapter 5 Figure 5.17, has a very fast rise time, less than 1ns, and stays very stable at 40 kV after this. The timescale of the pulse was chosen for a short simulation time. It is extremely difficult to replicate

that voltage pulse in the experimental situation. The rise time is dependent on many elements that make up the pulsed power system and a 1ns rise time would not be possible. In comparison the experimentally produced voltage pulse, shown in Figure 7.1, has a much longer rise and fall time of 40ns with a voltage that varies around +/- 5%. The variation of this voltage pulse is quite standard for experimental work and the pulse here is as close to the simulations as allowed by the experimental setup. The electron beam created by this voltage pulse should be able to effectively drive the gyro-BWO and produce an electron beam similar to the MAGIC simulations.

The emitted electron beam predicted by MAGIC, discussed in Chapter 5 and shown in Figure 5.18, shows a stable beam of 1.57A (1.5A emitted from the emission surface and 0.7A from the gap between cathode and focus electrode). The transported electron beam current was close to 100% while the reflected electrons are thought to be an effect caused by the simulation setup rather than a design flaw. The emitted current observed through experimental work, shown in Figure 7.6, shows a relatively stable pulse once the noise in the measurement and displacement current are removed from the pulse.

The transported electron beam current is one area where comparison between simulation and experiment should, if the setup is operating correctly, agree to a large degree. Both the MAGIC and experimental case show diodes operating in the temperature limited regime. In the simulated case the transported electron beam current was ~100% in the experimental results this value changed as the reverse coil was changed but peaked at 96%. This gives a very good indication of the successful operation of the cusp gun and a result that matches the simulated case almost exactly. The difference between the 96% transported beam current and the lower values can be explained by parasitic electron beam emission and electron beam scraping.

In both experiment and simulation a 40kV, 1.5A annular shaped axis-encircling electron beam is generated.

When the cathode was operated in the temperature limited regime adjustable diode

current of up to 1.5A was measured. This beam was fully transported to the downstream uniform region.

7.6.2 Electron beam diameter and velocity ratio

The electron beam diameter measurement from the experiment is shown in Figure 7.12 and is estimated to be 0.72mm. This electron beam image was taken at a position just after the maximum magnetic field and under those experimental conditions the magnetic field at the scintillator would be 1.37T. In MAGIC simulations analysing the electron beam under the same conditions the average diameter would be 0.71mm. The agreement between the experiment and MAGIC simulations allows one to be confident with the successful operation of the cusp electron gun.

7.7 Performance of electron gun

While the experimental results have been presented within this chapter a comparison of both the experimental results, simulated results and the targeted performance of the cusp electron gun is important. A summary of the performance targets against simulated and experimentally achieved values is given in Table 7.1. It is clear to see in this table of results that the experimentally achieved values meet the targets set out and the simulated values. The experimental performance of the cusp electron gun was excellent and compares well to the simulations.

Parameter	Target	MAGIC Simulated value	Opera-3D Simulated Value	Experimentally achieved value
Accelerating voltage	40kV	40kV	40kV	40kV +/- 5%
Beam current	1.5A	1.5A	1.5A	1.5A
Alpha	1.65	1.65	1.67	1.48*
Transported current ratio	100%	99.97 %	100 %	96% maximum

* Value limited due to limitation in reverse coil power supply.

Table 7.1. Summary of the performance targets set out, MAGIC and Opera-3D design predictions and experimentally achieved performance.

It is important to compare the performance of this electron gun in terms of other research on cusp electron guns. While this electron gun is not that new in terms of discovery, the 1960's, the application for microwave devices is a modern application, late 1980's. As such the construction and successful operation of a cusp electron gun is not an easy task and three main groups, outside the University of Strathclyde, world-wide have experimentally operated a cusp electron gun. These groups are: the University of California-Davis in collaboration with Northrop Grumman; A collaboration between the universities of Seoul and Tohoku in Japan; The Institute of Applied Physics. These groups have operated with thermionic cathode operating mostly with lower frequency than used here. Although the researchers in Japan[188] have operated a gyrotron with a cusp electron gun at W-band frequencies and above they do so at a high harmonic. The operational range is 89.3 GHz, 112.7 GHz and 138GHz operating in the modes $TE_{3,11}$, $TE_{4,11}$ and $TE_{5,11}$ respectively. This requires that the magnetic field is significantly lower than required for such high frequency operation. Their magnetic field system varies from 0.97T to 1.18T. The microwave power archived in that work was 1.7kW max. In comparison the magnetic field range for this W-band gyro-BWO was 1.65T to 2.1T. This represents a significant magnetic field compression and opens the possibility for a large microwave power up to 10kW out. Furthermore, the beam power in the Japanese experiment was 52kW while this work is higher at 60kW. At the University of California-Davis the cusp electron gun that was designed was proposed for application driving a 94GHz gyrotron operating at the eighth-harmonic. This very high harmonic gyrotron required a magnetic field of 0.25T. The testing of this beam was at a reduced voltage of 10kV and the beam image was observed. The transmission was measured to be 98%. While in these tests the magnetic field is 1.82T, 40kV and transmission was 96% as well. It is obvious therefore that this electron gun sees a significant advancement in both power and magnetic field compared to this gun. Operating at a high magnetic field strength means the electron beam and beam tube reduce in size resulting in more difficult and complexity in experimental testing of the electron gun. Also, when generating an electron beam of a very small width it is much easier to use it in millimetre-wave applications.

7.8 Microwave measurement

The microwave signal measurement was performed using a crystal detector. The setup of the detector is shown in Figure 7.15. The system consists of a microwave horn to collect the microwaves, an attenuator to reduce the strength of the signal, a crystal detector to record the data as a voltage signal and matched load to dispose of the microwave radiation. The detection system was placed a screened metal box connected to an oscilloscope, situated in a screened room outside the experimental bay, through a BNC cable. The detector was 36.5cm away from the microwave horn, with 0dB attenuation on the detector.
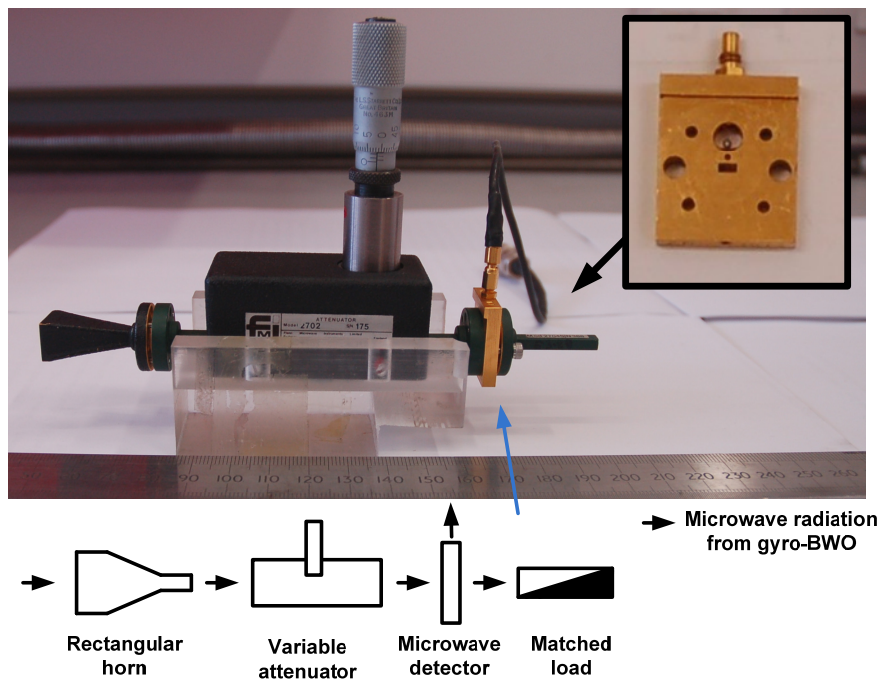
Figure 7.15. Microwave detection system.

The microwave output was observed at a cavity solenoid current of 230A to 245A corresponding to a cavity magnetic field of 1.79T to1.91T. The frequency of the microwaves can be determined, approximately, from the dispersion characteristics of the helically corrugated waveguide. The dispersion shows that the frequency of the observed microwave would be 91-100GHz. The frequency could not be directly measured through the use of a microwave mixer as this equipment was not available. The microwave signal is shown in Figure 7.16 against the voltage pulse used for the

cathode. The profile of the signal shows that the beam resonance is sensitive to beam voltage. While the voltage output from the Blumlein was lower in this experiment that in the previous scintillator and Faraday cup experiments. The strongest microwave output was observed above 35kV voltage. The microwave power level can be estimated from the detector sensitivity and is discussed in Section 7.9. The magnetic field used to produce this microwave signal is 1.93T which corresponds to an interaction at 96GHz. Two cut-off filters were used to verify the frequency of the microwave pulse. The cut-off filters had a diameter of 1.83mm and 1.79mm corresponding to cut-off frequencies of 96GHz and 98GHz respectively. It was shown that this pulse would have a frequency between 96GHz and 98GHz which is consistent with theoretical predictions.
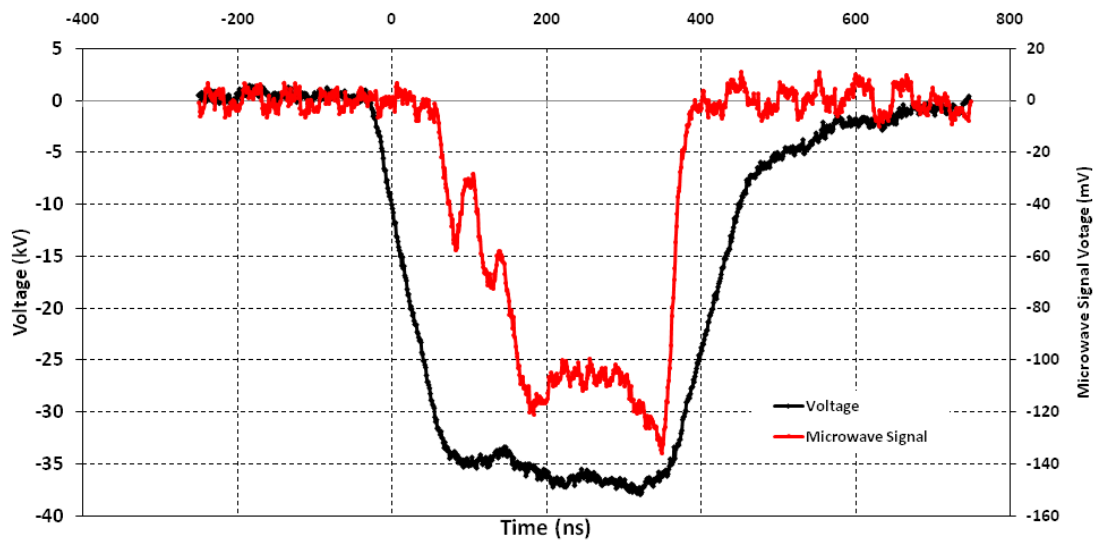
Figure 7.16. Measured microwave signal and voltage pulse.

The variation of the reverse coil current will vary the alpha value of the electron beam. When the reverse coil current reduces the alpha value should reduce until no microwave output is observed. The variation of reverse coil current is shown in Figure 7.17. In this graph it can be seen that the microwave signal output grows in strength as the reverse coil increases and at 181A reverse coil current the signal is still increasing. This shows that either the maximum signal strength is at this value of or above it. However, due to a limitation of the available power supply the reverse coil could not be driven higher than 181A. Furthermore, since the microwave signal

could be observed to increase up to 181A this means that there is no significant loss of the electron beam current over this range. Meaning, that as the alpha value increases, the radius of the electron beam will increase and yet the electron beam does not impact on the beam tube wall. The variation of the reverse coil against microwave signal provides further proof of the generation of an axis-encircling electron beam. When the reverse coil current is changed the alpha value of the beam should also change. This continues to increase the microwave output power as the reverse coil current is increased until a point of saturation occurs (when the electron beam starts to hit the beam tube or the interaction is saturated).
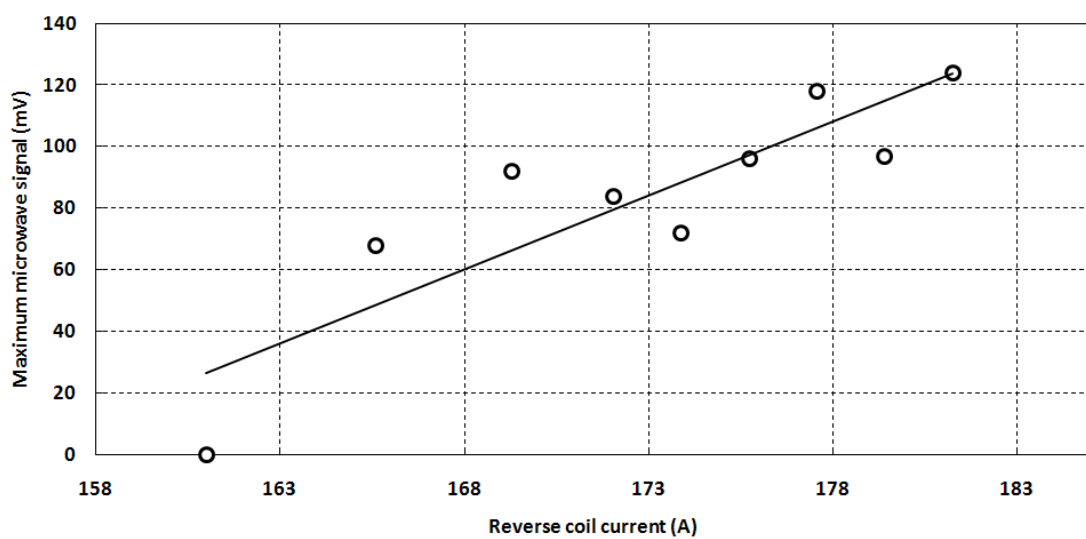
Figure 7.17. Variation in microwave output power from the gyro-BWO as the reverse coil current changes.

7.9 Microwave power

The power produced by the gyro-BWO was radiated from the output system consisting of a horn and a single layer sapphire window into the free space. A small proportion of the radiation was received by the receiving horn and measured by a detector. The calculation of the microwave power therefore needs to take into account the radiation pattern of the microwave horn. The radiation pattern by the circular horn is shown in Figure 7.18, taken from Ref. 189, where there is a "major lobe" and smaller "minor lobes".
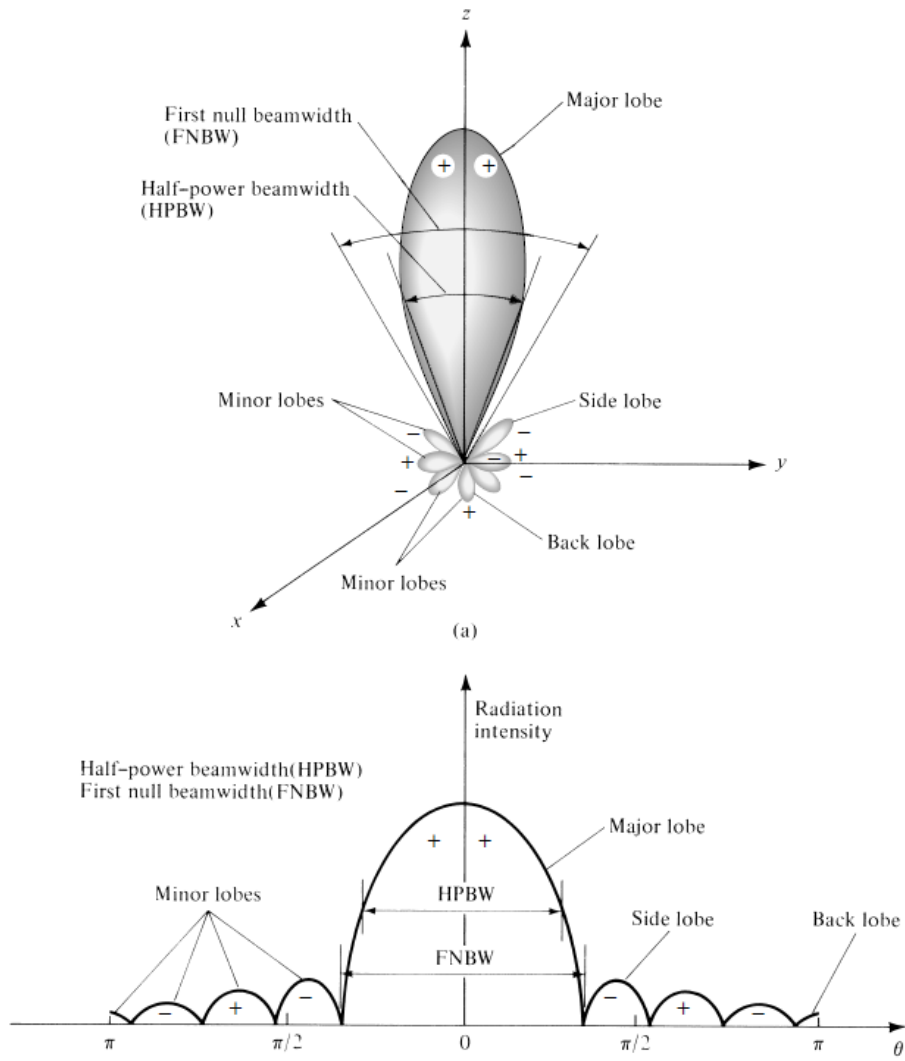
Figure 7.18. Radiation pattern from a microwave horn showing (a) radiation lobes and power bandwidths in an antenna pattern and (b) a linear plot of the power pattern with the associated lobes.

The distance between horn and receiver as this determines if the receiver is in the far-field or near-field region. The distance between the antenna (or horn) and detector allows calculation of the Rayleigh distance R, which is equal to the right hand of equation (7.7) and therefore the detector has to meet the condition given by equation (7.7) in order to be in the far-field region. Distances further than R mean the detector is in the far-field range and closer mean near-field range.

$$R_{ant} > \frac{2D_{ant}^2}{\lambda} \qquad (7.7)$$

Where R_{ant} is the separation distance between transmitter and receiver antenna, D_{ant} is the diameter of the antenna and λ is the wavelength of the microwave.

214

In the far-field region the radiation power varies inversely to the square of the distance from the antenna. In the measurement of the gyro-BWO, the detector was at a distance of 36.5cm from the microwave horn which was in the far-field region. The power density, ρ_P, in the antenna, with gain G, at a distance r away from the horn radiating a power of P_i is described through equation (7.8).

$$\rho_P = P_i G / (4\pi r^2) \qquad \textbf{(7.8)}$$

The gain of the antenna can be calculated analytically, simulated numerically or measured. In order to find the gain of the constructed horn a model was built in CST Microwave Studio that radiates the power into free space. A circularly polarised wave is injected from the right hand side through W-band waveguide at 96GHz. The 3D model can be seen in Figure 7.19(a) and the maximum gain can be calculated directly from this program to be 21.05dB. Over the receiving antenna area this can be approximated to be 20dB. The polar graph can be seen in Figure 7.19(b) shows radiation output in the major lobe with not much in the minor lobes.

The power density can be represented as a function of the received power, P_r, and the effective area of the receiving antenna A_{eff} to be given in equation (7.10). The effective area of the antenna is slightly smaller than the actual area of the aperture and is described through equation (7.11).

$$\rho_P = \frac{P_r}{A_{eff}} \qquad \textbf{(7.9)}$$

$$A_{eff} = 0.81A \qquad \textbf{(7.10)}$$

These equations allow the output power to be expressed in terms of the received power as described in equation (7.12).

$$P_i = \frac{P_r}{A_{eff}} \frac{4\pi r^2}{G} \qquad \textbf{(7.11)}$$

The rectangular receiving horn at W-band has an effective area of 71.28×10^{-6}m. The received power is the only term unknown now and so this needs to be measured through a calibration of the detector. The detector was measured against the output of a VNA which outputs at +5dBm, equal to 3.16mW, to give a voltage of 3mV. The

(a)

(b)
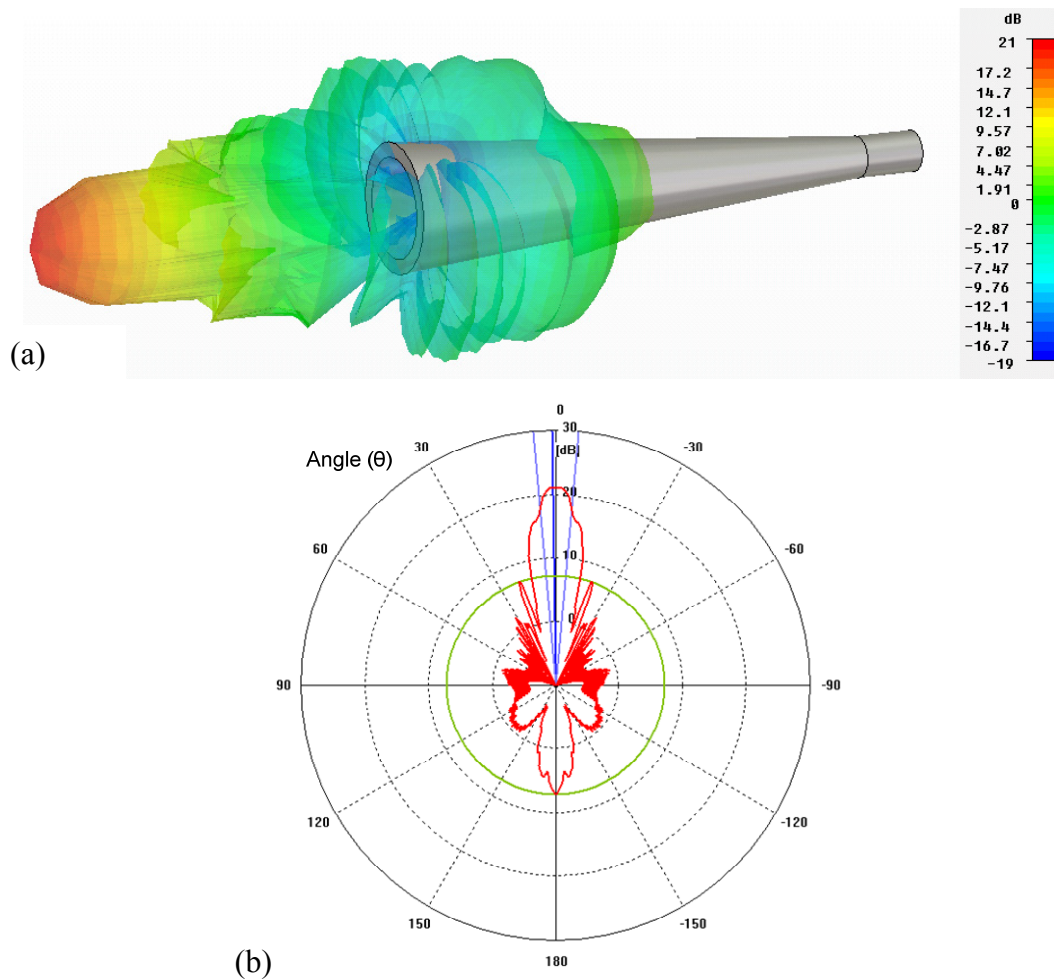
Figure 7.19. CST Microwave Studio simulation of output horn showing (a) a 3D view of the geometry and radiation pattern and (b) a polar graph of the radiation pattern.

detected power had a peak value of ~140mV which can be extrapolated from the detectors sensitivity graph to give a power of 150mW. The microwave power generated in the gyro-BWO can be calculated through equation (7.11) to be ~35.38W. For a circular polarised wave this means a power of ~70.7W. The microwave window measurement shown in Figure 6.24 shows that at 96GHz the reflection S-parameter, S_{11}, is -0.92dB. This means that 80.9% of the power is reflected and only 19.1% is transmitted. Therefore 370W if microwave power was generated within the gyro-BWO. This power is lower than the predicted 10kW and possible reasons for this could be higher than expected spreads in electron beam axial velocity and alpha or a mis-alignment in the solenoids resulting in the electron beam propagation only partially through the helical waveguide and then colliding on the waveguide walls.

7.10 Discussion

To sum up the work achieved in the experiments a 40kV 400ns voltage pulse was produced with a 320ns flat top and a 40ns rise and fall time. This pulse was used to accelerate the electrons from a thermionic cathode at high temperature. It was found that the diode operated in the temperature limited regime as designed. The electron beam current was measured to be 1.5A with a flat profile with minimal beam scraping under certain conditions. A maximum transported beam current of 96% was measured and is a very positive result as many other cusp guns suffer from beam alignment issues. The profile of the electron beam was measured with a scintillator and from this the beam diameter as well as alpha values were measured and calculated respectively. This cusp gun was operated at magnetic fields up to 1.9T which is close to the maximum required field of 2.1T. The high DC field is higher than other cusp electron guns that normal operate with pulsed coils of less than 2T. The gyro-BWO was demonstrated to output millimetre waves over the magnetic field range of 1.79T to 1.91T corresponding to a millimetre wave output in the 91-100GHz frequency range. Microwave generation over a large reverse coil range was also observed with a maximum measured millimetre wave power of 370W. Both the cusp electron gun and gyro-BWO compare well to numerical predictions and simulations. The cusp electron gun has an alpha value trend close to both analytical calculation and as predicted by numerical simulation. The gyro-BWO outputs millimetre waves, under one condition, at a frequency between 96GHz and 98GHz while the dispersion profile predicts a frequency of 96GHz. The results demonstrated throughout this chapter have shown for the first time that a gyro-BWO based on a helically corrugated waveguide and cusp electron gun can generate tuneable, millimetre waves.

7.11 Summary

In this chapter the results of the gyro-BWO experiment were given. Initially the voltage pulsed used to drive the electron gun was optimised and had a 40kV pulse over ~400ns with ~40ns rise time. The investigation of the cusp electron gun showed that the cathode operated in the temperature limited regime with a demonstrated

current variation up to 7A. The electron beam current was measured to be 1.5A with a flat profile and the transported beam current showed a limiting value of ~2A. The electron beam profile was captured and used to calculate the velocity ratio alpha of the beam as being up to 1.56. The electron beam experiment showed a good comparison to simulations with the alpha trend being close to analytical and numerical predictions. The discrepancy is possibly due to scraping of the high alpha beam though the tube. The gyro-BWO experiment recorded microwave pulses of varying strength over the magnetic field range 1.79T to 1.91T which meant the output frequency was tuned from 91 to 100GHz. At one operating condition it was approximated that the power generated was ~370W at a frequency of ~96GHz.

Chapter 8.

Conclusions and Future Work

8.1 Introduction

The work presented in this thesis describes the theoretical, numerical and analytical design, simulation and experiment of a W-band gyro-BWO with helically corrugated waveguide and cusp electron gun. First the analytical and numerical design of the helically corrugated waveguide with the construction and microwave measurements of the waveguide was described. The was followed by the analytical and numerical design and simulation of the cusp electron gun. This was followed by the construction details of the experiment and finally the experimental results of the electron beam generated by a cusp diode and observation of microwave radiation in the W-band generated by the gyro-BWO.

This chapter will combine the results and conclusions from the various chapters and explain the results gained and comparison, where appropriate, between the results achieved via theory/simulation and experiment. This chapter will also introduce the future work of the research which will utilize the successful novel W-band cusp electron gun along with the state-of-the-art helically corrugated waveguide optimized for 84 to 104GHz frequency range.

8.2 Review of results obtained

8.2.1 Numerical modelling and experimental analysis of the helically corrugated waveguide

The helically corrugated waveguide was a critical component of the gyro-BWO. The initial design of the waveguide arose from analytical calculations of the dispersion profile. Working from the theory of perturbation both the dispersions with and without the electron beam present were calculated and the corrugation properties of the waveguide were calculated. The small signal growth rate was calculated for various dimensions of the helical waveguide then an optimised geometry was chosen for the tuning range of 84 – 104GHz.

The analytical calculation of the dispersion of the helical waveguide was verified

with a numerical simulation using CST Microwave Studio. The model was built in Microwave Studio that replicated the experimental setup that would be used later on in the measurement. Namely an elliptical polariser was used to convert the linear polarised waves into circularly polarised waves. The simulation replicated the experiment and had successfully predicted the dispersion of the waveguide. The results from the simulation and experiment agreed with each other nicely. However the dispersion results below ~80GHz and above ~100GHz were expected to have certain errors because the elliptical polarisers have a limited operation band of ~80-~100GHz.

The waveguide was constructed as a 4-period helical waveguide involving the manufacture process of rapid prototyping, gold plating, copper electroplating and acid erosion and was measured using a vector network analyser. The loss over the 4-period length (15mm) was ~ 0.8dB which was rather high for the given length due to a number of flaws on the inner surface of the waveguide. An improved manufacture process was then identified involving the manufacture of an aluminium former that was directly machined using a precision CNC lathe, then copper electroplating and acid erosion was carried out to construct a 34-period helical waveguide. This resulted in ~0.6dB loss but over a much greater length of 12.75cm. This dispersion measurement here was again close to analytical calculation and numerical simulation.

8.2.2 Numerical modelling of the cusp electron gun

The numerical modelling of the cusp electron gun was carried out in two stages, first the design was conceptualised and modelled with the 3D PiC code MAGIC and secondly the results were verified with the 3D finite element simulation suite Opera-3D. Analytical calculations of the velocity ratio alpha of the electron beam were also performed and the three different methods were compared.

The numerical predictions of the gyro-BWO performance showed that it would operate over a magnetic field range of 1.65T − 2.1T and the strongest interaction

occurred with a 1.5A, 40kV electron beam with alpha = 1.65, As the corrugated interaction region lowers the effect of axial velocity and alpha spreads the electron beam was targeted to have an alpha spread close to 10% and axial velocity spread less than 10%.

The initial MAGIC model was designed in order to produce an electron beam of the required current and energy and then optimized through adjustment of diode geometry and the magnetic configuration until the electron beam met targeted values. At 40kV, 1.82T and alpha value of 1.65 the axial velocity spread was $\Delta v_z / v_z = 8.1\%$ and alpha spread was $\Delta \alpha / \alpha = 10.7\%$.

The optimized cusp gun design was simulated in Opera-3D in order analyse comparatively with the previous MAGIC simulations. The meshing in this program is different to MAGIC and produces a very slightly different geometry than the MAGIC design. The first parameter that was compared was the magnetic field profile. The magnetic field profile in MAGIC was produced from a more simplistic method than Opera-3D however the two profiles agreed almost exactly. The quality of the electron beam generated in the two simulations was comparable. In Opera-3D the beam had 11.1% axial velocity spread with 14.4% alpha spread, at central magnetic field strength of 1.82, compared to the 8.1% axial velocity and 10.7% alpha spreads calculated using MAGIC.

The agreement between the codes that the electron gun design generated a high quality electron beam over the full magnetic field range lead to the construction of the cusp electron gun.

8.2.3 Gyro-BWO experimental results

The cusp electron gun was tested in four stages: the accelerating voltage pulse, used to drive the electron beam, was measured and optimised; the emitted current from the cathode was measured without a magnetic field at first and calibrated against emitted current at various specific configurations; the transported electron beam current was

measured; the electron beam cross-sectional shape recorded. The electron beam parameters remained the same throughout these experiments with a 40kV accelerating voltage and 1.5A current.

In the first stage the voltage pulse was measured through a voltage divider and provided a very good quality pulse with a time of 400ns with a rise time of 40ns and a flat top region that deviated +/-5% from the medium value. The profile of the voltage pulse was very important as a low quality pulse could cause a detrimental effect to the generated electron beam.

In the next stage the diode current was measured and then a real value of the current was deduced. This current showed an oscillatory profile with two larger peaks of current corresponding to the displacement current at both rising and falling edges of the voltage pulse. The emitted current from the cathode as a function of the heater power (related to cathode temperature) was measured.

The third stage was to measure the transported electron beam current using a Faraday cup. The transported electron beam current was measured with various powers of heater power and 1.5A transported beam current was measured at full operating temperature.

The fourth stage was to measure the profile of the electron beam recorded by a scintillator witness plate technique. The profile of the beam in some case was a spot beam as the alpha value was not high enough or beam transport became an issue. However, when the reverse coil was at a correct value the beam image was a ring as expected consistent with an axis-encircling electron beam. The alpha value for various values of cathode magnetic field was able to be measured through this technique.

The final stage was to observe the successful operation of the gyro-BWO with the microwave signal measured. The microwave pulse was measured over a range of reverse coil current, therefore alpha, values. The frequency and power of the signal

were not directly measured but inferred from the dispersion and calibration tests respectively. Under one condition the frequency of the microwaves was determined though cut-off filters to be between 96GHz and 98GHz.

8.3 Future work of the gyro-BWO experiment

The future work the gyro-BWO is numerous and provides interesting research opportunities. The work presented in this thesis showed the successful operation of the cusp electron gun and showed the helically corrugated waveguide had the desired dispersion profile while providing a low transmission loss. There are many areas that could be investigated further including: a power calibration test of the interaction region; a broadband microwave window design and fabrication.

Power calibration: The power calibration is required in order to know the output power of the gyro-BWO. A proposed method is to couple a known microwave signal into the gyro-BWO and measure the detected signal in the far field region of the output horn. This test signal will then be compared to the output of gyro-BWO with the appropriate amount of attenuation in the system so that the power output of the gyro-BWO could be measured by calibration of the system and all the factors that could give rise to the errors are eliminated. Therefore an input coupler is required.

Broadband frequency measurement of the gyro-BWO (window design): The microwave window used within this work was a single layer sapphire window which has a resonant transmission at a single frequency within the W-band range. This is useful for proof-of-principle tests where microwave generation of any frequency within the band is a very successful result but time constraints dictated that experiments to ascertain the full operational range of the helically corrugated waveguide could not be completed within the time period available for the submission of the thesis. In order to design a broadband microwave window some initial studies were performed but not completed due to the time constraints of the PhD. It would be highly beneficial to realize the initial microwave window design which shows that if the microwave window has three quartz plates which can be moved using a micrometer scale then broadband frequency output is possible.

Improved solenoid design: The solenoids designed within this thesis operate at a very high magnetic field DC. They have been tested at 1.85T and no problems with cooling have been found so the design is extremely successful in this case. However, as discussed within Chapter 6 the construction of the solenoids was slightly flawed. One shim coil was not right and needs to be corrected.

8.4 Other proposed research using the gyro-BWO architecture

The gyrotron backward wave oscillator designed, constructed and operated is the first of its kind in the world operating in the W-band frequency range. Utilizing the experimental setup designed, simulated and constructed within this thesis, there are three on-going projects that are proposed:-

1. 7th Harmonic gyrotron.
2. W-band gyrotron travelling wave amplifier.
3. W-band gyrotron backward wave oscillator with depressed collector.

The 7th harmonic gyrotron experiment is designed and simulated by F. Li et al.[190] and intends to use the same experimental setup as discussed before in Chapter 6 with modifications to the beam tube to allow a new interaction region to be placed into the setup. This experiment proposes to use the electron beam generated by this cusp electron gun to drive a 7th harmonic gyrotron interaction. The electron beam differs to the one here although the power (60kW) is the same the alpha value will be much higher at alpha = 3. Simulation of the electron gun performed[183] at this alpha show that the cusp electron gun will still have an acceptable quality even with the very high alpha and higher magnetic field compression. In the future this high harmonic gyrotron will be constructed using most of the same architecture as described in this thesis and using the same cusp gun designed and constructed. The predicted output of this gyrotron was calculated to be 600W over 400ns pulsed output at ~390GHz in the TE_{71} waveguide mode.

The W-band gyro-TWA that was proposed by W. He at al[191] uses the same design setup as explained in Chapter 6 however with the addition of an input coupler just after the back stop filter with an elliptical polariser just after this in order to produce

circularly polarised microwaves. The helically corrugated waveguide would then have to be changed in order that sufficient gain would be achieved between the interaction of the input microwaves and the electron beam. Operating as an amplifier the gyro-TWA would require a lower alpha value than the gyro-BWO at ~1.2. The gyro-TWA has been simulated through MAGIC and is predicted to produce high power microwaves with 10% bandwidth of 90-100GHz. The applications for the amplifier would be most useful in high field Electron Spin Resonance where the bandwidth allows for shorter pulsed microwaves and more resolution in their spectroscopic measurements.

The gyro-BWO with a helically corrugated waveguide has an increased electronic efficiency over a conventional gyro-BWO however this can be further increased through use of a depressed collector method, as previously discussed in Chapter 4. L. Zhang et al.[192] have simulated the depressed collector through MAGIC and propose to employ a 4-stage depressed collector for the W-band gyro-BWO. The efficiency of the gyro-BWO is predicted to increase from ~17% to ~42% with a collection efficiency of 77%. This would make the gyro-BWO a truly world class device important for many scientific applications such as high field Electron Spin Resonance, high field Dynamic Nuclear Polarisation, high resolution radar and sensing.

References

[1] R. S. Elliott, "The History of electromagnetic as Hertz would have known it," *IEEE Trans. Microwave Theory Tech.*, **36**, pp. 806-823, (1988).

[2] C. Susskind, "Heinrich Hertz: a short life," *IEEE Trans. Microwave Theory Tech.*, **36**, pp. 802-805, (1988).

[3] H. Friedburg, "Hertz at work in 1988," *MTT-S Int. Microwave Symp.*, New York, May 25-27, (1988).

[4] J. D. Kraus, "Heinrich Hertz-theorist and experimenter," *IEEE Trans. Microwave Theory Tech.*, **36**, pp. 824-829, (1988).

[5] J. E. Brittain, "The legacy of Hertz: Some highlights in microwave history from 1889 to 1945," *MTT-S Int. Microwave Symp.*, New York, May 25-27, (1988).

[6] G. Caryotakis, E. Jongewaard, R. L. Kustom, N. C. Luhmann, Jr., M. I. Petelin, G. Scheitrum, and A. Vlieks, "W-band micro-fabricated modular klystrons," *Proc. SPIE*, **3158**, pp. 129-136, (1997).

[7] C. Kory, L. Ives, M. Read, J. Booske, H. Jiang, D. Van der Weide, and P. Phillips, "Microfabricated W-band travelling wave tubes" *Proc. Joint 30th Int. Conf. Infrared and Millimeter Waves and 13th Int. Conf. Terahertz Electron.*, Williamsburg. VA, pp. 85-86, (2005).

[8] R. L. Ives, "Microfabrication of high-frequency vacuum electron devices," *IEEE Trans. Plasma Sci.*, **32**, pp. 1277-1291, (2004).

[9] Special Technology Area Review on Vacuum Electronics Technology for RF Applications, Department of Defence advisory group on electron devices report, USA, (2005).

[10] J. H. Collins, "A Short History of Microwave Acoustics," *IEEE Trans. Microwave Theory Tech.*, **32**, pp. 1127-1140, (1984).

[11] J. H. Bryant, "The first century of microwaves – 1886 to 1986: Parts I and II," *IEEE Trans. Microwave Theory Tech.*, **36**, pp. 830-858, (1988).

[12] J. C. Wiltse, "History of millimeter and submillimeter waves," *IEEE Trans. Microwave Theory Tech.,* **32**, pp. 1118-1126, (1984).

[13] H. Sobol, "Microwave communications – An historical perspective," *IEEE Trans. Microwave Theory Tech.,* **32**, pp. 1170-1181, (1984).

[14] R. Warnecke, W. Kleen, A. Lerbs, O. Doehler, and H. Huber, "The magnetron type travelling-wave amplifier tube," *Proc. I.R.E..,* **38**, pp. 486-495, (1950).

[15] R. Beringer, "The Absorption of One-Half Centimeter Electromagnetic Waves in Oxygen," *Phys. Rev.*, **70**, pp. 53-57, (1946).

[16] M. J. Bernstein and N. M. Knoll, "Magnetron research at Columbia radiation laboratory," *IRE Trans. Microwave Theory Tech.,* **2**, pp. 33-37, (1954).

[17] B. B. van Iperen, "Reflex Klystrons for Millimeter Waves," *Proc. Symp. Millimeter Waves*, Polytechnic Inst. of Brooklyn, NY, **IX**, pp. 249-259, (1959).

[18] R. M. Philips, "The Ubitron, a high-power travelling-wave tube based on a periodic beam interaction in unloaded waveguide," *IRE Trans. Electron Dev.*, **7**, pp. 231-241, (1960).

[19] M. Friedman, R. Fernsler, S. Slinker, R. Hubbard, and M. Lampe, "Efficient Conversion of the Energy of Intense Relativistic Electron Beams into rf Waves," *Phys. Rev. Lett.*, **75**, pp. 1214-1217, (1995).

[20] R. K. Parker, R. H. Jackson, S. H. Gold, H. P. Freund, V. L. Granatstein, P. C. Efthimion, M. Herndon, and A. K. Kinkead, "Axial Magnetic-Field Effects in a Collective-Interaction Free-Electron Laser at Millimeter Wavelengths," *Phys. Rev. Lett.*, **48**, pp. 238-242, (1982).

[21] V. A. Flyagin, A. V. Gaponov-Grekhov, M. I. Petelin, and B. K. Ylpatov, "The Gyrotron," *IEEE Trans. Microwave Theory Tech.,* **25**, pp. 514-521, (1977).

[22] A. V. Gaponov, M. I. Petelin, and V. K. Yulpatov, "The induced radiation of excited classical oscillators and its use in high-frequency electronics," *Radiopys. Quantum Electron*, **10**, pp. 794-813, (1967).

[23] A. A. Andronov, V. G. Usov, and V. K. Yulpatov, "The gyrotron: High-power source of millimeter and submillimeter waves," *Infrared Phys.*, **18**, pp. 385-395, (1978).

[24] J. Schneider, "Stimulated Emission of Radiation by Relativistic Electrons in a Magnetic Field," *Phys. Rev. Lett.*, **2**, pp. 504-505, (1959).

[25] A. V. Gaponov, "Interaction between electron fluxes and electromagnetic waves in waveguides," *Izv VUZ Radiofizika*, **2**, pp. 450-462, (1959).

[26] J. L. Hirshfield and V. L. Granatstein, "The Electron Cyclotron Maser—An Historical Survey," *IEEE Trans. Microwave Theory Tech.*, **25**, pp. 522-527, (1977).

[27] P. Sprangle, V. L. Granatstein, and A. Drobot, "The electron cyclotron maser instability," *Journal de physique*, **C6**, pp. C6-135 – C6-152, (1977).

[28] P. Sprangle and A. T. Drobot, "The Linear and Self-Consistant Nonlinear Theory of Electron Cyclotron Maser Instability," *IEEE Trans. Microwave Theory Tech.*, **25**, pp. 528-544, (1977).

[29] Special Technology Area Review on Vacuum Electronics Technology for RF Applications, Department of Defence advisory group on electron devices report, USA, (2005).

[30] D. J. Sullivan, "High power microwave generation from a virtual cathode oscillator (VIRCATOR)," *IEEE Trans. Nucl. Sci.*, **30**, pp. 3426-3428, (1983).

[31] T. J. T. Kwan, "High-power coherent microwave generation from oscillating virtual cathodes," *Phys. Fluids,* **27**, pp. 228-232, (1984).

[32] H. A. Davis, R. R. Bartsch, T. J. T. Kwan, E. G. Sherwood, and R. M. Stringfield, "Gigawatt-level microwave burst from a new type of virtual cathode oscillator," *Phys. Rev. Lett.,* **59**, pp. 288-291, (1987).

[33] A. V. Pashchenko and B. N. Rutkevich, "Generator of nanosecond pulses," A.s. USSR, vol. 646787, H 01 J 25/00, August 9, (1974).

[34] J. W. Poukey and N. Rostoker, "One-dimensional model of relativistic electron beam propagation," *Plasma Phys.*, **13**, pp. 593-598, (1981).

[35] R. A. Mahaffey, P. Sprangle, J. Golden, and C. A. Kapetanakos, "High-Power Microwaves from a Nonisochronic Reflecting Electron System," *Phys. Rev. Lett.,* **39**, pp. 843-846, (1997).

[36] B. W. J. McNeil, G. R. M. Robb, and D. A. Jaroszynski, "Self-amplification of coherent spontaneous emission in the free electron laser," *Opt. Commun.*, **165**, pp. 65-70, (1999).

[37] K-J. Kim, "Three-Dimensional Analysis of Coherent Amplification and Self-Amplified Spontaneous Emission in Free-Electron Lasers," *Phys. Rev. Lett.*, **57**, pp. 1871-1874, (1986).

[38] D. Misra, *Radio-Frequency and Microwave Communication Circuits*, Wiley, New Jersey, USA, 2004.

[39] M. Skolnik, *Introduction to Radar Systems*, 3rd Ed, McGraw-Hill, New York, 2002.

[40] R. E. Mudgett, "Microwave food processing," *Food Techology*, **43**, pp. 117-126, (1989).

[41] J. Yongsawatdigul, and S. Gunasekaran, "Mirowave vacuum drying of cranberries: Part I: Energy use and efficiency," *Journal of Food Processing and Preservation*, **20**, pp. 121-143, (1996).

[42] J. Yongsawatdigul, and S. Gunasekaran, "Mirowave vacuum drying of cranberries: Part II: Quality evaluation," *Journal of Food Processing and Preservation*, **20**, pp. 121-143, (1996).

[43] S. Hunsche and M. C. Nuss, "Terahertz 'T-ray' tomography," *Proc. SPIE*, **3465**, pp. 426-433, (1998).

[44] B. B. Hu and M. C. Nuss, "Imaging with terahertz waves," *Opt. Lett.*, **20**, pp. 1716-1718, (1995).

[45] D. Arnone, C. Ciesla, and M. Pepper, "Terahertz imaging comes into view," *Phys. World*, **13**, pp. 35-40, (2000).

[46] D. D. Arnone, C. M. Ciesla, A. Corchia, S. Egusa, M. Pepper, J. M. Chamberlain, C. Bezant, E. H. Linfield, R. Clothier, and N. Khammo, "Applications of terahertz (THz) technology to medical imaging," *Proc. SPIE*, **3828**, pp. 209-219, (1999).

[47] J. Handley, A. Fitzgerald, T. Loeffler, K. Seibert, E. Berry, and R. Boyle, "Potential medical applications of THz imaging," *Proc. Medical Imaging Understanding and Analysis 2001*, pp. 17-20, (2001).

[48] A. J. Fitzgerald, E. Berry, N. N. Zinovev, G. C. Walker, M. A. Smith, and J. M. Chamberlain, "An introduction to medical imaging with coherent terahertz frequency radiation," *Phys. Med. Bio.*, **47**, pp. R67-R84, (2002).

[49] E. Pickwell and V. P. Wallace, "Biomedical applications of terahertz technology," *J. Phys. D*: *Appl. Phys.*, **39**, pp. 301-310, (2006).

[50] P. H. Siegel, "Terahertz technology in biology and medicine," *IEEE Trans. Microwave Theory Tech.*, **52**, pp. 2438-2447, (2004).

[51] M. R. Scarfi, M. Romano, R. Di. Pietro, O. Zeni, A. Doria, G. P. Gallerano, E. Giovenale, G. Messina, A. Lai, G. Campurra, D. Coniglio, and M. D'Arienzo, "THz exposure of whole blood for the study of biological effects on human lymphocytes," *J. Biol. Phys.*, **29**, pp. 171-176, (2003).

[52] J. F. Federici, B. Schulkin, F. Huang, G. Dale, R. Barat, F. Oliveira, and D. Zimdars, "THz imaging and sensing for security applications − Explosives, weapongs and drugs," *Semiconductors Sci. Technol.*, **20**, pp. S266-S280, (2005).

[53] M. C. Kemp, P. F. Taday, B. E. Cole, J. A. Cluff, A. J. Fizgerald, and W. R. Tribe, "Security applications of terahertz technology," *Proc. SPIE*, **5070**, pp. 44-52, (2003).

[54] E. L. Jacobs and S. Moyera, "Concealed weapon identification using terahertz imaging sensors," *Proc. SPIE*, **6212**, pp. 62120J-1, (2006).

[55] S. Mitsudo, Aripin, T. Shirai, T. Matsuda, T. Kanemaki, and T. Idehara, "High power, frequency tunable, submillimeter wave ESR device using a Gyrotron as a radiation source," *Int. J. Infrared Millim. Waves*, **21**, pp. 661-676, (2000).

[56] C. Bonifazi, M. Ruggieri, and A. Paraboni, "The DAVID Mission in the Heritage of SIRO and ITALSAT Satellites," *IEEE Trans. Aerospace Electron Syst.*, **38**, pp. 1371-1376, (2002).

[57] M. Ruggieri, S. De Fina, M. Pratesi, A. Salome, E. Saggesè, and C. Bonifazi, "The W-band data collection experiment of the DAVID mission," *IEEE Trans. Aerospace Electron Syst.*, **38**, pp. 1377-1378, (2002).

[58] A. Jebril, L. Scucchia, M. Lucente, M. Ruggieri, P. Camriani, T. Rossi, A. Bosisio, A. Pisano, A. Salomè, L. Ronzitti, M. Musso, A. Iera, S. Pulitanó, S. Morosi, V. Dainell, and V. Speziale, "The WAVE Mission Payload," *Proc. IEEE Aerospace Conference*, Big. Sky, USA, paper no. 1229, (2005).

[59] A. Jebril, C. Fragale, M. Lucente, M. Ruggieri, and T. Rossi, "WAVE – A new satellite mission in W-band," *Proc. IEEE Aerospace Conference*, Big. Sky, USA, paper no. 1007, (2005).

[60] NASA's CloudSat official mission website. Online at: http://www.nasa.gov/mission_pages/cloudsat/main/index.html.

[61] G. L .Stephends, D. G. Vane, R. J. Boain, G. G. Mace, K. Sassen, Z. Wang, A. J. Illingworth, E. J. O'Connor, W. B. Rossow, S. L. Durden, S. D. Miller, R. T. Austin, A. Benedetti, and C. Mitrescu, "The CloudSat mission and the A-Train," *Bull. Amer. Meteorol. Soc.*, **83**, pp. 1771-1790, (2002).

[62] G. Galati, M. Ferri, P. Mariano, and F. Marti, "Advanced Integrated Architecture for Airport Ground Movements Surveillance," *Record of the IEEE International Radar Conference,* pp. 282-287, (1995).

[63] H. M. Assenheim, *Introduction to Electron Spin Resonance*, Plenum, New York, USA, (1996).

[64] J. E. Wertz and J. R. Bolton, *Electron Spin Resonance: Elementary Theory and Practical Applications*, McGraw-Hill, New York, USA, (1967).

[65] A. Schweiger and G. Jeschke, *Principles of pulse electron paramagnetic resonance*, OUP, Oxford, UK, (2001).

[66] J. W. A. Coremans, O. G. Poluektov, E. J. J. Groenen, G. W. Canters, H. Nar, and A. Messerschmidt, "A W-Band Electron Parametic Resonance Study of a Single Crystal of Azurin," *J. Am. Chem. Sco.*, **116**, pp. 3097-3101, (1994).

[67] T. Tatsukawa, T. Shirai, T. Imaizumi, T. Idehara, I. Ogawa, and T. Kanemaki, "Ruby ESR over a wide frequency range in millimeter wave region," *Int. J. Millim. Wave*, **19**, pp. 859-874, (1998).

[68] W. B. Lynch, K. A. Earle, and J. H. Freed, "1-mm wave ESR spectrometer," *Rev. Sci. Instrum.*, **59**, pp. 1345-1351, (1988).

[69] R. Kompfner, "Travelling-wave tubes," *Rep. Prog. Phys.*, **15**, pp. 275-327, (1952).

[70] R. Kompfner, "The invention of travelling wave tubes," *IEEE Trans. Electron Dev.*, **23**, pp. 730-738, (1976).

[71] R. L. Wathen, "Genesis of a generator – The early history of the magnetron," *Journal of the Franklin Institute*, **255**, pp. 271-281, (1953).

[72] S. Tsimring, *Electron Beams and Microwave Vacuum Electronics*, Wiley, New York, USA, (2007).

[73] H. A. H. Boot and J. T. Randall, "The cavity magnetron," *Proc. IEEE Radiolocation Conf.*, **93**, pp. 928, (1946).

[74] H. Guerlack, "Radar in World War II," *The History of Modern Physics, 1800-1950*, **8**, New York: American Institute of Physics, (1987).

[75] R. H. Varian and S. F. Varian, "A high frequency oscillator and amplifier," *J. Appl. Phys.*, **10**, pp. 321-327, (1939).

[76] S. Tsimring, *Electron Beams and Microwave Vacuum Electronics*, Wiley, New York, USA, (2007).

[77] J. Benford, J. Swegle, and E. Schamiloglu, *High-Power Microwaves* 2nd ed. Artech House, MA, USA, (2006).

[78] D. Rees, M. Lynch, and P. Tallerico, "Accelerator production of tritium 700 MHz and 350 MHz klystron test results," *Proc. 19th Int. LINAC Conf.*, Chicago, IL, USA, pp. 231-233, (1998).

[79] A. V. Haeff, "An ultra-high-frequency power amplifier of novel design," *Electronics*, **12**, pp. 30-32, (1939).

[80] R. Kompfner, "The travelling-wave tube as Amplifier at Microwaves," *Proc. I.R.E.*, **32**, pp. 124-127, (1947).

[81] J. Feng, J. Cai, X. Wu, S. Ma, Y. Hu, and M. Huang, "Design investigation of 10W W-Band folded waveguide TWT," *Proc. IEEE International Vacuum Electronics Conference (IVEC)*, pp. 77-78, (2007).

[82] L. M. Earley, F. L. Krawczyk, E. I. Smirnova, B. E. Carlsten, Z.F. Wang, W.B. Haynes, and S.J. Russell, "Simulation and Measurement of the Los Alamos 94GHz TWT RF Structure," *Proc. IEEE International Vacuum Electronics Conference (IVEC)*, pp. 449-450, (2009).

[83] R. Kompfner and N.T. Williams, "Backward wave tubes." *Proc. I.R.E.*, **41**, pp. 1602-1611, (1953).

[84] R. J. Barker and E. Schamiloglu, *High-Power Microwave Sources and Technologies*, IEEE Press, New Jersey, USA, (2001).

[85] A. V. Gunin, A. I. Klimov, S. D. Korovin, I. K. Kurkan, I. V. Pegel, S. D. Polevin, A. M. Roitman, V. V. Rostov, A. S. Stepchenko, and E. M. Totmeninov, "Relativistic X-Band BWO with 3-GW Output Power," *IEEE Trans, Plasma Sci.*, **26**, pp. 326-331, (1998).

[86] J. F. Gittins, "Some experiments with a TWT buncher klystron," *SER J.*, **42**, (1956.)

[87] S. V. Yadavalli, "On the performance of a class of hybrid tubes," *Proc. I.R.E. (Corresp.),* **42**, p. 263, (1960).

[88] A. J. Lichtenberg, "Prebunched beam travelling-wave tube studies," *IRE Trans. Electron Dev.*, **9**, pp. 345-351, (1962).

[89] A. D. LaRue and R. R. Rubert, "Multi-megawatt hybrid TWTs at S-band and C-band," *presented to the IEEE Electron Dev. Meet.*, Washington, D.C., Oct. (1964).

[90] T. Roumbanis, "Centipede Twystron amplifiers and travelling wave tubes for broadband, high-efficiency, super-power amplification," *Proc. 7th Int. Conf. on Microwave and Optical Generation and Amplification,* Hamburg, Germany, Sept. 16-20, (1968).

[91] P. A. Sturrock, "Kinematics of growing waves," *Phys. Rev.*, **112**, pp. 1488-1503, (1958).

[92] T. Idehara, T. Saito, H. Mori, H. Tsuchiya, La Agusu, S. Mitsudo, "Long Pulse Operation of the THz Gyrotron with a Pulse Magnet," *Int. J. Infrared Milli. Waves*, **29**, pp. 131-141, (2008).

[93] V. A. Flyagin, A. G. Luchinin, G. S. Nusinovich, "Submillimeter-wave gyrotrons: theory and experiment," *Int. J. Infrared Milli. Waves*, **4**, pp. 629-637, (1983).

[94] S. E. Spira-Hakkarainen, K. E. Kreischer, and R. J. Temkin, "Submillimeter-wave harmonic gyrotron experiment," *IEEE Trans.Plasma Sci.*, **18**, pp. 334-342, (1990).

[95] G. G. Denisov, A. G. Litvak, V. E. Myasnikov, E. M. Tai, and V. E. Zapevalov, "Development in Russia of high-power gyrotrons for fusion," *Nucl. Fusion*, **48**, 054007, (2008).

[96] V. K. Yulptov, "Nonlinear theory of interaction between a periodic electron beam and an electromagnetic wave," *Radiophy. Quantum Electron*, **10**, pp. 471-476, (1967).

[97] N. S. Ginzburg, I. G. Zarnitsyna, and G. S. Nusinovich, "Theory of relativistic cyclotron autroresonace maser with opposite wave," *Radio Eng. Electron Phys.*, **24**, pp. 113-118, (1979).

[98] A. K. Ganguly and S. Ahn, "Non-linear analysis of the gyro-BWO in three dimensions," *Int. J. Electron*, **67**, pp. 261-276, (1989).

[99] G. S. Nusinovich and O. Dumbrajs, "Theory of gyro-backward wave oscillator with tapered magnetic field with waveguide cross section," *IEEE Trans. Plasma Sci.*, **24**, pp. 620-629, (1996).

[100] V. L. Granatstein, M. E. Read, and L. R. Barnett "Measured performance of Gyrotron oscillators and amplifers," *Int. J. Infrared Millimeter Waves*, **5**, pp. 267-302, (1982).

[101] K. R. Chu, "Overview of research on the Gyrotron travelling-wave amplifier," *IEEE Trans. Plasma Sci*., **30**, pp. 903-908, (2002).

[102] A. A. Tolkachev, B. A. Levitan, G. K. Solovjev, V. V. Veytsel, and V. E. Farber, "A megawatt power mullimeter-wave phased-array radar," *IEEE Aerosp. Electron. Syst. Mag*., **15**, pp. 25-31, (2000).

[103] W. Lawson, J. Cheng, J. P. Calame, M. Castle, B. Hogan, V. L. Granatstein, M. Reiser, and G. P. Saraph, "High-power operation of a three-cavity X-band coaxial Gyroklystron," *Phys. Rev. Lett*., **81**, pp. 3030-3033, (1998).

[104] R. M. Philips and D. W. Sprehn, "High-power klystrons for the next linear collider," *Proc. IEEE*, **87**, pp. 738-751, (1999).

[105] J. P. Calame, B. G. Danly, M. Garven, and B. Levush, "Studies of electronic noise in gyroklystrons," *Phys. Plasmas*, **7**, pp. 2180-2185, (2000).

[106] H. Guo, J. Rodgers, S. Chen, M. Walter, and V. L. Granatstein, "Experimental investigation of a phase-locked harmonic multiplying inverted gyro-twystron," *Proc. International Conference on Plasma Science (ICOPS)*, 3-5 June (1996).

[107] G. S. Nusinovich and M. Walter, "Theory of the inverted Gyrotwystron," *Phys. Plasmas*, **4**, pp. 3394-3402, (1997).

[108] H. Guo, S. H. Chen, V. L. Granatstein, J. Rodgers, G. S. Nusinovich, M. T. Walter, J. Zhao, and W. Chen, "Operation of a high performance, harmonic-multiplying, inverted Gyrotwystron," *IEEE Trans. Plasma Sci*., **26**, pp. 451-460, (1998).

[109] H. Guo, S. H. Chen, V. L. Granatstein, J. Rodgers, G. S. Nusinovich, M. Walter, B. Levush, and W. J. Chen, "Operation of a highly overmoded, harmonic-multiplying, wideband gyrotron amplifier," *Phys. Rev. Lett.*, **79**, pp. 515-518, (1997).

[110] S. H. Chen, *A two stage phase-coherent, harmonic-multiplying, inverted Gyrotwystron*, PhD dissertation, Inst. Plasma Res., Univ. Maryland, College Park. (1997).

[111] J. Zhao, H. Guo, G. S. Nusinovich, J. C. Rodgers, and V. L. Granatstein, "Studies of a Three-Stage Inverted Gyrotwstron," *IEEE Trans. Plasma Sci.*, **28**, pp. 657-664, (2000).

[112] M. K. Thumm, "State-of-the-art of high power gyro-devices and free electron masers update 2008," Scientific Report FZKA 7289, Forschungszentrum Karlsruhe, Germany, (2008).

[113] K. Flech, M. Blank, P. Borchard, P. Calahan, S. Cauffman, T. S. Chu, and H. Jory, "Demonstration of a 95 GHz, 100 kW CW Gyrotron oscillator," *Proc. IEEE International Vacuum Electronics Conference (IVEC)*, pp. 63-64, (2004).

[114] M. Blank, K. Felch, B. G. James, P. Borchard, P. Cahalan, T. S. Chu, H. Jory, B. G. Danly, B. Levush, J. P. Calame, K. T. Nguyen, and D. E. Pershing, "Development and demonstration of high-average power W-band gyro-amplifiers for radar applications," *IEEE Trans. Plasma Sci.*, **20**, pp 865-875, (2002).

[115] B. G. Danly, M. Blank, J. P. Calame, B. Levush, K. T. Nguyen, D. E. Pershing, R. K. Parker, K. L. Felch, B. G. James, P. Borchard, P. Cahalan, T. S. Chu, H. R. Jory, T. A. Hargreaves, R. B. True, W. G. Lawson, and T. M. Antonsen. Jr. "Development and Testing of a High-Average Power, 94-GHz Gyroklystron," *IEEE Trans. Plasma Sci.*, **28**, pp. 713-726, (2000).

[116] M. Blank, P. Borchard, P. Cahalan, S. Cauffman, T. S. Chu, K. Felch, and H. Jory, "Development and demonstration of Gyrotron oscillators and amplifiers at CPI" *Poc. 5th Int. Workshop on Strong Microwaves in Plasmas*, **1**, pp. 7-15, (2003).

[117] E. V. Zasypkin, L. G. Gachev, I. I. Antakov, and E. V. Sokolov, "W-band pulsed 300 kW Gyroklystron amplifier," *26th International Conf. Infrared and Millimeter Waves*, Toulouse, France, Sept. 10-14, pp. 5-86–5-88, (2001).

[118] M. Blank, B. G. Danly, and B. Levush, "Experimental demonstration of a W-band (94 GHz) gyrotwystron amplifier," *IEEE Trans. Plasma Sci.*, **27**, pp. 405-411, (1999).

[119] C. K. Chong, D. B. McDermott, and N. C. Luhmann. Jr., "Large-signal operation of a third-harmonic slotted gyro-TWT amplifier," *IEEE Trans. Plasma Sci.*, **26**, pp. 500-507, (1998).

[120] M. Thumm, "Novel applications of millimeter and submillimeter wave gyro-devices," *Int. J. Millim. Waves*, **22**, pp. 377-386, (2001).

[121] S. Knorr, A. Grupp, M. Mehring, U. Kirbach, A. Bartl, L. Dunsch, "Pulsed ESR investigation of anisotropic interactions in M@C82 (M=Sc,Y,La)," *Appl. Phys. A: Mater. Sci. Process.*, **66**, pp. 257-264, (1998).

[122] N. C. Chen, C. F. Yu, and T. H. Chang, "A TE21 second-harmonic gyrotron backward-wave oscillator with slotted structure," *Phys. Plasmas*, **14**, 123105, (2007).

[123] R. M. Rozental, N. S. Ginzburg, M. Y. Glyavin, and A. S. Sergeev, "Novel source of the chaotic microwave radiation based on the gyro-Backward-Wave Oscillator," *IEEE Trans. Microwave Theory Tech.*, **54**, pp. 2741-2744, (2006).

[124] M. A. Basten, W. C. Guss, K. E. Kreischer, R. T. Temkin, and M. Caplan, "Experimental investigation of a 140 GHz gyrotron-backward wave oscillator," *Int. J. Millim. Waves*, **16**, pp. 889-905, (1995).

[125] R. Bashirullah and A. Mortazawi, "A slotted-waveguide power amplifier for spatial power combining applications," *IEEE Trans. Microwave Theory Tech.*, **48**, pp. 1142-1147, (2000).

[126] A. W. Cross, W. He, A. D. R. Phelps, K. Ronald, C. G. Whyte, A. R. Young, C. W. Robertson, E. G. Rafferty, and J. Thompson, "Helically corrugated waveguide gyrotron traveling wave amplifier using a thermionic cathode electron gun," *Appl. Phys. Lett.*, **90**, 253501, (2007).

[127] S. J. Cooke and G. G. Denisov, "Linear theory of a wide-band gyro-TWT amplifier using spiral waveguide," *IEEE Trans. Plasma Sci.*, **26**, pp. 519-530, (1998)

[128] I. V. Konoplev, A. W. Cross, A. D. R. Phelps, W. He, C. G. Whyte, C. W. Robertson, and P. MacInnes, "Experimental and theoretical studies of a coaxial free-electron maser based on two-dimensional distributed feedback," *Phys. Rev. E*, **76**, 056406, (2007).

[129] J. C. Maxwell, "A dynamical theory of the electromagnetic field," *Phil. Trans. Roy. Soc. (London)*, **155**, pp. 459-512, (1865).

[130] I. S. Grant and W. R. Philips, *Electromagnetism*, Wiley, New York, USA, (1975).

[131] Lord Rayleigh, "On the passage of electric waves through tubes," *Phil. Mag.*, **43**, pp. 125-132, 1897. Reprinted in *Collected Papers*, Cambridge Univ. Press, (1903).

[132] R. S. Packard, "The origins of waveguides: A case of multiple rediscovery," *IEEE Trans. Microwave Theory Tech.*, **32**, pp. 961-969, (1984).

[133] J. Vanderlinde, *Classical Electromagnetic Theory*, Wiley, New York, USA, (1993).

[134] E. S. Weibel, "Spontaneously growing transverse waves in a plasma due to an anisotropic velocity distribution," *Phys. Rev. Lett.*, **2**, pp. 83-84, (1959).

[135] J. L. Hirshfield, J. M. Bernstein, and J. M. Wachtel, "Cyclotron resonance interaction of microwaves with energetic electrons," *IEEE J. Quantum Electron*, **QE-1**, pp. 237-245, (1965).

[136] C. F. Kennel, and H. E. Petschek, "Collisionless shock waves in high β plasmas, 1," *J. Geophys. Res.*, **72**, pp. 3303-3326, (1967).

[137] E. S. Weibel, "Spontaneously Growing Transverse Waves in a Plasma Due to an Anisotropic Velocity Distribution," *Phys. Rev. Lett.*, **2**, pp. 83-84, (1959).

[138] G. G. Denisov, V. L. Bratman, A. W. Cross, W. He, A. D. R. Phelps, K. Ronald, S. V. Samsonov, and C. G. Whyte, "Gyrotron Traveling Wave Amplifier with a Helical Interaction Waveguide," *Phys. Rev. Lett.*, **81**, pp. 5680-5683, (1998).

[139] V. L. Bratman, A. W. Cross, G. G. Denisov, W. He, A. D. R. Phelps, K. Ronald, S. V. Samsonov, C. G. Whyte, and A. R. Young, "High-Gain Wide-Band Gyrotron Traveling Wave Amplifier with a Helically Corrugated Waveguide," *Phys. Rev. Lett.*, **82**, pp. 2746-2749, (2000).

[140] W. He, K. Ronald, A. R. Young, E. G. Rafferty, A. D. R. Phelps, A. W. Cross, C. G. Whyte, and J. Thompson, "Experiments of a thermionic gyro-TWA based on a helical interaction waveguide," *Proc. ICMMT 4th International Conference on Microwave and Millimeter Wave Technology, 2004,* pp. 292-295, (2004).

[141] W. He, K. Ronald, A. R. Young, A. W. Cross, A. D. R. Phelps, C. G. Whyte, E. G. Rafferty, J, Thomson, C. W. Robertson, D. C. Speirs, S. V. Samsonov, and G. G.

Denisov, "Gyro-BWO Experiments Using a Helical Interaction Waveguide," *IEEE Trans. Electron Dev.*, **52**, pp. 839-844, (2005).

[142] S. V. Samsonov, A. D. R. Phelps, V. L. Bratman, G. Burt, G. G. Denisov, A. W. Cross, K. Ronald, W. He, and H. Yin, "Compression of Frequency-Modulated Pulses using Helically Corrugated Waveguides and Its Potential for Generating Multigigawatt rf Radiation," *Phys. Rev. Lett.,* **92**, 18301, (2004).

[143] G. Burt, S. V. Samsonov, A. D. R. Phelps, V. L. Bratman, K. Ronald. G. G. Denisov, W. He, A. R. Young, A. W. Cross, and I. V. Konoplev, "Microwave Pulse Compression Using a Helically Corrugated Waveguide," *IEEE Trans. Plasma Sci.*, **33**, pp. 661-667, (2005).

[144] G. Burt, *Sweep-Frequency Microwave Pulse Compression Using a Helically Corrugated Waveguide*, University of Strathclyde, Ph D, Thesis.

[145] G. G. Denisov, V. L. Bratman, A. D. R. Phelps, and S. V. Samsonov, "Gyro-TWT TWT with a Helical Operating Waveguide: New Possibilities to Enhance Efficiency and Frequency Bandwidth," *IEEE Trans. Plasma Sci.*, **26**, pp. 508-518, (1998).

[146] W. He, A. W. Cross, A. D. R. Phelps, K. Ronald, C. G. Whyte, S. V. Samsonov, V. L. Bratman, and G. G. Denisov, "Theory and simulations of a Gyrotron backward wave oscillator using a helical interaction region," *Appl. Phys. Lett.*, **89**, 091504, (2006).

[147] G. Burt, S. V. Samsonov, K. Ronald, G. G. Denisov, A. R. Young, V. L. Bratman, A. D. R. Phelps, A. W. Cross, I. V. Konoplev, W. He, J, Thompson, and C. G. Whyte, "Dispersion of helically corrugated waveguides: Analytical, numerical, and experimental study*," Phys. Rev. E*, **70**, 046402, (2004).

[148] CST Microwave Studio, - Computer Simulation Technology, Wellesley Hills, MA, USA.

[149] V. L. Bratman, A. W. Cross, G. G. Denisov, W. He, A. D. R. Phelps, K. Ronald, S. V. Samsonov. C. G. Whyte, and A. R. Young, "High-Gain Wide-Band Gyrotron Traveling Wave Amplifier with a Helically Corrugated Waveguide," *Phys. Rev. Lett.*, **84**, pp. 2746-2749, (2000).

[151] H. Yin, A. W. Cross, W. He, A. D. R. Phelps, and K. Ronald, "Psudospark experiments: Cherenkov interaction and electron beam post-acceleration," *in Pseudospark Physics and Applications, special issue of IEEE Trans. Plasma Sci.,* **32**, pp. 233-239, (2004).

[152] H. Yin, W. He, A. W. Cross, A. D. R. Phelps, and K. Ronald, "Single-gap pseudospark discharge experiments," *J. Appl. Phys.*, **90**, 3212, (2001).

[153] H. Yin, A. W. Cross, W. He, A. D. R. Phelps, K. Ronald, D. Bowes, and C. W. Robertson, "Millimeter wave generation from a psudospark-sourced electron beam," *Phys. Plasmas*, **16**, 063105, (2009).

[154] J. R. Pierce, *Theory and Design of Electron Beams*, Van Nostrand, New York, USA, (1954).

[155] K. R. Chu, "Theory of electron cyclotron maser interaction in a cavity at the harmonic frequencies," *Phys. Fluids*, **21**, pp. 2354-2364, (1978).

[156] G. Schmidt, "Nonadiabatic Particle Motion in Axialsymmetric Fields," *Phys. Fluids,* **5**, pp. 994-1002, (1962).

[157] J. Sinnis and G. Schmidt, "Experimental Trajectory Analysis of Charged Particles in a Cusped Geometry," *Phys. Fluids,* **6**, pp. 841-845, (1963).

[158] M. J. Rhee and W. W. Destler, "Relativistic electron dynamics in a cusped magnetic field," *Phys. Fluids*, **17**, pp. 1574-1581, (1974).

[159] W. W. Destler and M. J. Rhee, "Radial and axial compression of a hollow electron beam using an asymmetric magnetic cusp," *Phys. Fluids*, **20**, pp. 1582-1584, (1977).

[160]. W. W. Destler, R. Kulkarni, C. D. Striffler, and R. L. Weiler, "Microwave generation from rotating electron beams in magnetron-type waveguides," *J. Appl. Phys*, **54**, pp. 4152-4162, (1983).

[161]. D. B. McDermott, A. J. Balkcum, and N. C. Luhmann, Jr., "35-GHz 25-kW CW low-voltage third-harmonic Gyrotron," *IEEE Trans. Plasma. Sci.*, **24**, pp. 613-629, (1996).

[162] L. Zhang, W. H, A. W. Cross, A. D. R. Phelps, K. Ronald, and C. G. Whyte, "Design of an Energy Recovery System for a Gyrotron Backward-Wave Oscillator," *IEEE Trans. Plasma Sci.*, **37**, pp. 390-394, (2009).

[163] S. Humphries, Jr., *Charged Particle Beams*, Wiley, New York, USA, (1990).

[164] K. R. Chu, "Theory of electron cyclotron maser interaction in a cavity at the harmonic frequencies," *Phys. Fluids*, **21**, pp. 2354-2364, (1978).

[165] K. R. Chu, and A. T. Lin, "Gain and bandwidth of the gyro-TWT and CARM amplifier," *IEEE Trans. Plasma Sci.*, **16**, pp. 90-104, (1988).

[166] W. Lawson, "Design of low velocity-spread cusp guns for axis encircling beams," *Appl. Phys. Lett.*, **50**, pp. 1477-149, (1987).

[167] W. Lawson and P.E. Latham, "The design of a small-orbit/large-orbit gyroklystron experiment," *J. Appl. Phys.*, **61**, pp. 519-528, (1987).

[168] S. G. Jeon, C. W. Baik, D. H. Kim, G. S. Park, N. Sato, and K. Yokoo, "Study on velocity spread for axis-encircling electron beams generated by single magnetic cusp," *Appl. Phys. Lett.*, **80**, pp. 3703-3705, (2002).

[169] S. Sabchevski, T. Idehara, M. Glyavin, S. Mitsudo, I. Ogawa, K. Ohashi, and H. Kobayashi, "Design of a large orbit Gyrotron with permanent magnet system," *Vacuum*, **62**, pp. 133-142, (2001).

[170] S. B. Harriet, D. B. McDermott, D. A. Gallagher, and N. C. Luhmann, Jr., "Cusp Gun TE$_{21}$ Second-Harmonic Ka-Band Gyro-TWT Amplifier," *IEEE Trans. Plasma Sci.*, **30**, pp. 909-914, (2002).

[171] T. Idehara, I. Ogawa, S. Mitsudo, Y. Iwata, S. Watanabe, Y. Itakura, K. Ohashi, H. Kobayashi, T. Yokoyama, V. E. Zapevalov, M .Y. Glyavin, A. N. Kuftin, O. V. Malygin, and S.P. Sabchevski, "A High Harmonic Gyrotron With an Axis-Encircling Electron Beam and Permanent Magnet," *IEEE Trans. Plasma Sci.*, **32**, pp. 903-909, (2004).

[172] S. G. Jeon, C. W. Baik, D. H. Kim, G. S. Park, N. Sato, and K. Yokoo, "Experimental verification of low-velocity spread axis-encircling electron beam," *Appl. Phys. Lett.*, **84**, pp. 1994-1996, (2004).

[173] D. A. Gallagher, M. Barsanti, F. Scafuri, and C. Armstrong, "High-Power Cusp Gun for Harmonic Gyro-Device Applications," *IEEE Trans. Plasma Sci.*, **28**, pp. 695-699, (2000).

[174] W. He, A. D. R. Phelps, C. R. Donaldson, A. W. Cross, and K. Ronald, "The Design and Simulation of a W-band Gyro-BWO," *Proc. IEEE International Vacuum Electronics Conference (IVEC)*, pp. 231-232, (2007).

[175] B. Goplen, L. Ludeking, D. Smithe, and G. Warren., "User-configurable MAGIC for electromagnetic PIC calculations," *Computer Physics Communications,* **87,** pp. 54-86. (1995).

[176] L. Ludeking, D. Smithe, and T. Gray, *Introduction to MAGIC*, Mission Research Corporation, Virginia, USA, (2003).

[177] B. Goplen, R. E. Clark, and S. J. Flint, "Geometrical Effects in Magnetically Insulated Power Transmission Lines," Mission Research Corporation Report, MRC/WDC-R-001, (1979).

[178] B. Goplen, R. E. Clark, B. Goldstein, and R. Stettner, "Three-Dimensional SGEMP," *In 1980 Annual Conference on Nuclear and Space Radiation Effects*, 15-18 July (1980).

[179] B. Goplen, R. S. Coats, and J. R. Freeman, "Three-Dimensional Simulation of the PROTO-II Convolution," *In 4th IEEE Pulsed Power Conference*, 6-8 June, New Mexico, USA, (1983).

[180] K. S. Yee, "Numerical Solution of Initial Boundary Value Problems Involving Maxwell's Equations in Isotropic Media," *IEEE Trans. Antennas Propagat.,* **14**, pp. 302-307, (1966).

[181] J. E. Jung, J. H. Choi, Y. J. Park, H. W. Lee, Y. W. Jin, D. S. Chung, S. H. Park, J. E. Jang, S. Y. Hwang, T. Y. Ko, Y. S. Choi, S. H. Cho, C. G. Lee, J. H. You, N. S. Lee, J. B. Yoo, and J. M. Kim, "Development of triode-type carbon nanotube field-emitter arrays with suppression of diode emission by forming electroplated Ni wall structure," *J. Vac. Sci. Technol.,* **B 21,** pp. 375-381, (2003).

[182] D. Rowlands, *A cusp gun and novel microwave components for gyro-devices*, University of Strathclyde, Ph.D. Thesis, (2004).

[183] C. R. Donaldson, W. He, A. W. Cross, A. D. R. Phelps, F. Li, K. Ronald, C. W. Robertson, C. G. Whyte, A. R. Young, and L. Zhang, "Design and numerical optimization of a cusp-gun-based electron beam for millimetre-wave gyro-devices," *IEEE Trans. Plasma Sci.*, **37**, pp. 2153-2157, (2009).

[184] COMSOL, Multiphysics, Comsol, Inc., www.comsol.com.

[185] Program available online at: http://www.geocities.com/richgetze/.

[186] I. C. Somerville, S. J. MacGregor, and O. Farish, "An efficient stacked-Blumlein HV pulse generator," *Meas. Sci. Technol.*, **1**, pp. 865-868, (1990).

[187] A. M. Bork, "Maxwell, Displacement Current, and Symmetry," *American Journal of Physics*, **32**, pp. 854-859, (1963).

[188] T. Idehara, I. Ogawa, S. Mitsudo, Y. Iwata, S. Watanabe. Y. Itakura, K. Ohashi, H. Kobayashi, T. Yokoyama, V. E. Zapevalov, M. Y. Glyavin, A. N. Kuftin, O. V. Malygin, and S. P. Sabchevski, "A high harmonic gyrotron with axis-encircling electron beam and permanent magnet," *IEEE Trans. Plasma Sci.*, **32**, pp. 903-909, (2004).

[189] C. A. Balanis, *Antenna Theory: Analysis and Design*, 3rd Ed, Wiley, New York, USA, (2005).

[190] F. Li, W. He, A. W. Cross, C. R. Donaldson, L. Zhang, A. D. R. Phelps, and K. Ronald, "Design and simulation of a ~390 GHz seventh harmonic gyrotron using a large orbit electron beam," *J. Phys. D: Appl. Phys.*, **43**, 155204, (2010).

[191] W. He, A. D. R. Phelps, A. W. Cross, C. R. Donaldson, and K. Ronald, "A W-Band Gyrotron Travelling Wave Amplifier Using a Helically Corrugated Waveguide," *The 17th High-Power Particle Beams Conference (Beams' 08).* Xi'an, China, p. 646. (2008).

[192] L. Zhang, W. He, A. W. Cross, A. D. R. Phelps, K. Ronald, and C. G. Whyte, "Simulation of a F-our stage Depressed Collector for a W-band Gyro-BWO," *2nd UK/Europe-China Workshop on Millimetre Waves and Terahertz Technologies*, p. 96, (2009).

Appendix

Appendix – Authors Publications

Journals

1. C. R. Donaldson, W. He, A. W. Cross, A. W. Cross, A. D. R. Phelps, F. Li, K. Ronald, C. W. Robertson, C. G. Whyte, A. R. Young, and L. Zhang, "Design and numerical optimization of a cusp-gun-based electron beam for millimeter wave gyro-devices," *IEEE Trans. Plasma Sci*., **11**, pp. 2153-2157, (2009).

2. C. R. Donaldson, W. He, A. W. Cross, F. Li, A. D. R. Phelps, L. Zhang, K. Ronald, C. W. Robertson, C. G. Whyte, and A. R. Young, "A cusp electron gun for millimetre wave gyrodevices," *Appl. Phys. Lett*., **96**, 141501, (2010).

3. F. Li, W. He, A. W. Cross, C. R. Donaldson, L. Zhang, A. D. R. Phelps, and K. Ronald, "Design and Simulation of a ~390 GHz 7th Harmonic Gyrotron using a large orbit electron beam," *J. Phys. D: Appl. Phys*., **43**, 155204, (2010).

Conference

1. W. He, C. R. Donaldson, F. Li, A. W. Cross, A. D. R. Phelps, K. Ronald, C. W. Robertson, C. G. Whyte, and L. Zhang, "Design, simulation and experiment of a cusp electron beam for millimeter wave gyro-devices," *IEEE Vacuum Electronics Conference (IVEC)*, pp. 517-518, (2009).

2. W. He, C. R. Donaldson, A. W. Cross, F. Li, A. D. R. Phelps, L. Zhang, K. Ronald, C. W. Robertson, C. G. Whyte, and A. R. Young, "Experiment of a high power W-Band Gyro-BWO using a Helically Corrugated Waveguide," *International Conference on Infrared, Millimeter and Terahertz Waves (IFMMW-THz),* (2009).

3. W. He, C. R. Donaldson, A. D. R. Phelps, A. W. Cross, F. Li, K. Ronald, C. W. Robertson, C. G. Whyte, A. R. Young, and L. Zhang, "W-band Gyro-devices using helical interaction waveguides and cusp guns," *2nd UK/Europe-China Workshop on Millimetre Waves and Terahertz Technologies*, p. 68, (2009).

4. F. Li, W. He, A. D. R. Phelps, A. W. Cross, C. R. Donaldson and K. Ronald, "The design of a 390 GHz gyrotron based on a Cusp electron gun," *2nd UK/Europe-China Workshop on Millimetre Waves and Terahertz Technologies*, p. 85, (2009).

5. C. R. Donaldson, W. He, A. D. R. Phelps, F. Li, A. W. Cross, K. Ronald, A. R. Young, and C. G. Whyte, "A ~10kW W-Band Gyro-BWO using a Helically Corrugated Waveguide," *International Conference on Infrared, Millimeter and Terahertz Waves (IFMMW-THz)*, pp. 201-202, (2008).

6. F. Li, W. He, A. D. R. Phelps, A. W. Cross, C. R. Donaldson, and K. Ronald, "The design of a 390 GHz gyrotron based on a cusp electron gun," *International Conference on Infrared, Millimeter and Terahertz Waves (IFMMW-THz)*, pp. 167-168, (2008).

7. C. R. Donaldson, W. He, A. D. R. Phelps, A. W. Cross, K. Ronald, A. R. Young, C. G. Whyte, and F. Li, "A W-Band Gyro-BWO using a Helically Corrugated Waveguide," *IEEE Vacuum Electronics Conference (IVEC)*, pp. 93-94, (2008).

8. F. Li, W. He, A. D. R. Phelps, A. W. Cross, C. R. Donaldson, K. Ronald, and C. G. Whyte, "The simulation of an High Power 390GHz Large-orbit Harmonic Gyrotron," *IEEE Vacuum Electronics Conference (IVEC)*, pp. 235-236, (2008).

9. W. He, A. D. R. Phelps, A. W. Cross, C. R. Donaldson, and K. Ronald, "A W-band Gyrotron Traveling Wave Amplifier using a Helically Corrugated Waveguide," *The 17th High-Power Particle Beams Conference (Beams '08)*, pp. 646-648, (2008).

10. C. R. Donaldson, W. He, A. D. R. Phelps, F. Li, A. W. Cross, K. Ronald, A. R. Young, and C. G. Whyte, "A W-band Gyro-BWO using a Helically Corrugated Waveguide," *The 17th High-Power Particle Beams Conference (Beams '08)*, pp. 527-528, (2008).

11. F. Li, W. He, A. D. R. Phelps, A. W. Cross, C. R. Donaldson, and K. Ronald, "A high power 390 GHz harmonic Gyrotron based on cusp electron gun," *The 17th High-Power Particle Beams Conference (Beams '08)*, pp. 269-271, (2008).

12. W. He, A. D. R. Phelps, C. R. Donaldson, A. W. Cross, and K. Ronald, "A W-band Gyro-BWO based on a helically corrugated waveguide," *International Conference on Infrared, Millimeter and Terahertz Waves (IFMMW-THz),* pp. 573-574, (2007).

13. W. He, A. D. R. Phelps, C. R. Donaldson, A. W. Cross, and K. Ronald, "The Design and Simulation of a W-band Gyro-BWO," *IEEE International Vacuum Electronics Conference (IVEC)*, pp. 231-232, (2007).

14. C. R. Donaldson, W. He, A. D. R. Phelps, A. W. Cross, and K. Ronald, "Design and Simulation of W-Band Gyro-BWO based on a Helically Corrugated Waveguide," *International Conference on Plasma Science (ICOPS)*, p. 812, (2007).

15. C. R. Donaldson, W. He, A. D. R. Phelps, A. W. Cross, and K. Ronald, "The Design and Simulation of a Cusp Electron Beam Source for a W-Band Gyro-BWO Experiment," *IEEE International Vacuum Electronics Conference (IVEC)*, pp. 273-274, (2007).

16. C. R. Donaldson, W. He, A. D. R. Phelps, A. W. Cross and K. Ronald, "Design and Simulation of a W-Band Gyro-BWO based on a Helically Corrugated Waveguide," *Proc. National Vacuum Electronics Conference (NVEC)*, (2007).

17. W. He, C. R. Donaldson, A. D. R. Phelps, A. W. Cross, and K. Ronald, "A W-band Gyro-BWO based on a Helically Corrugated Waveguide," *International Conference on Infrared, Millimeter and Terahertz Waves (IFMMW-THz)*, p. 88, (2006).

Design and Numerical Optimization of a Cusp-Gun-Based Electron Beam for Millimeter-Wave Gyro-Devices

Craig R. Donaldson, Wenlong He, Adrian W. Cross, Alan D. R. Phelps, Fengping Li, Kevin Ronald, Craig W. Robertson, Colin G. Whyte, Alan R. Young, and Liang Zhang

Abstract—**A novel thermionic cusp electron gun operating in the temperature-limited regime that produces a large-orbit electron beam through a nonadiabatic magnetic-field reversal was designed, analyzed, and optimized to give an electron-beam ideal for driving gyro-devices, particularly in the millimeter-to-submillimeter-wavelength range due to its small cross-sectional size. The annular-shaped axis-encircling electron beam had a beam current of 1.5 A at an acceleration potential of 40 kV, a tunable velocity ratio α ($= v_\perp/v_z$) between one and three, an optimized axial velocity spread $\Delta v_z/v_z$ of $\sim8\%$, and a relative alpha spread $\Delta\alpha/\alpha$ of $\sim10\%$ at an alpha value of 1.65.**

Index Terms—**Axis-encircling electron beam, cusp electron gun, gyro-BWO, gyro-TWT, high-harmonic gyrotron, THz electron-beam source, W-band.**

I. INTRODUCTION

HIGH-POWER high-frequency coherent radiation sources, particularly in the range of millimeter and submillimeter wavelengths, have attracted significant research interest recently due to their desirable applications in many areas such as remote sensing [1], medical imaging [2], plasma heating [3], and spectroscopy [4]. Gyro-devices [5] are promising candidates to fulfil such a demand due to their inherent characteristic fast-wave interaction. Many high-frequency gyro-devices operate at harmonics [6]–[9] to allow for the use of a larger cavity size and to decrease magnetic fields by a factor of s, the harmonic number. However, operating at harmonics could introduce undesired-mode competition, as well as parasitic oscillations. Therefore, it is advantageous for an electron gun to be able to generate a mode-selective beam. This paper presents the innovative design and performance of such a beam from a novel electron gun that is capable of driving high-power millimeter-wave vacuum electron devices through generation of an annular-shaped axis-encircling electron beam. An axis-

encircling electron beam is ideal for harmonic operation of gyro-devices as the mode-selectivity nature of such a beam requires that the harmonic number is equal to the azimuthal index of a waveguide mode for effective beam-wave coupling [10], which leads to a reduced possibility of parasitic oscillations. Furthermore, due to the high power of the spent electron beam, an annular-shaped electron beam is desirable for beam-energy recovery using a depressed collector.

Initially, transport of an electron beam through opposing magnetic fields (the so-called "magnetic cusp") was investigated in the 1960s [11], [12] for plasma-heating applications. Schmidt [11] described a threshold for magnetic mirroring and the effects on the electrons after they have passed the cusp region, namely, azimuthal rotation around the central axis of symmetry due to conservation of the electron canonical momentum. Building on the work of Schmidt *et al.*, continuous efforts and progress have been made through both theoretical analysis and experimental study in the generation of cusp-based electron-beam sources [13], [14]. Special concentration was paid on the methods to produce an ideal sharp cusp shape by using complex arrays of magnetic coils, magnetic poles, and, possibly, magnetic material inside the cathode [15]–[18]. This culminated in a "state-of-the-art" cusp gun in 2000 by Northrop Grumman [19], which generated an electron beam of 70-kV energy, 3.5-A current, and 1.5 velocity ratio with a small axial velocity spread of 5% at a magnetic field of ~0.25 T. These studies have been based on the configuration where a magnetic cusp was located at or after the anode where a large cusp amplitude was required due to a fully accelerated electron momentum. However, in this paper, an electron gun based on a "smooth" cusp [20], formed by two simple coils without any magnetic shaping poles, located immediately after the cathode, is presented.

Despite these theoretical and experimental studies over the last few decades, it was not until 1983 that a cusp electron gun was first used in microwave sources, specifically in a magnetron [21]. Recently, gyro-devices have begun to adopt cusp guns as their electron beam sources, notably in lower frequency harmonic gyro-devices [22].

A cold cusp gun was developed for an X-band gyrotron traveling-wave amplifier (gyro-TWA) at the University of Strathclyde in 2007 [18]. The methodology of the design was validated through results from numerical simulations, from the 3-D particle-in-cell code MAGIC [23], agreeing well with the

experimental results. In this paper, we present a thermionic cusp gun that was designed and numerically optimized based on the valid methodology for millimeter-wave gyro-devices. It was designed for three high-frequency devices, including a W-band gyro-BWO [24], a W-band gyro-TWA [25], and a THz harmonic gyrotron [26]. The second-harmonic W-band gyro-BWO uses a helically corrugated waveguide [27], [28] and is calculated to produce 10-kW CW at 18% efficiency, with a 3-dB frequency tuning bandwidth between 85 and 105 GHz. A W-band gyro-TWA has been designed to operate at an alpha of 1.2 and give an output of 5-kW CW. The THz harmonic gyrotron that operates at the seventh harmonic has been simulated to produce 600-W CW at 390 GHz with a TE_{71} output at an $\alpha = 3$. These devices operate over a wide range of frequencies from 75 GHz to 390 GHz with an α value of one to three.

II. DIODE DESIGN

It is possible to show [18] that the velocity ratio in the downstream uniform magnetic-field (B_0) region can be described approximately by the equation $\alpha = \sqrt{(-r_c^2 \omega_c \omega_0 / v_0^2 + r_c^2 \omega_c \omega_0)}$. Here, r_c is the average radius of the cathode; v_0 is the total electron velocity; $\omega = eB/\gamma m_e$ is the electron cyclotron frequency, where γ is the Lorentz factor of the electrons at the downstream region and e and m_e are the charge and the rest mass of the electron, respectively; and subscripts "c" and "0" denote the cathode and the downstream uniform magnetic-field region, respectively.

The parameters of the electron beam were chosen to be as follows: beam energy $E = 40$ keV and current of $\sim$1.5 A, with $\alpha = 1-3$ and $B_0 = 1.7-2.1$ T for high-frequency gyro-device experiments. Assuming the cathode operation with a current density of 6 A/cm^2 in the temperature-limited regime [29], a cathode with $r_c = 6.0$ mm and $\Delta r_c = 0.5$ mm was chosen. Therefore, a magnetic-field amplitude of $\sim$50 G at the cathode is required to achieve an alpha value of 1.65, at $B_0 = 1.82$ T, which corresponds to a magnetic compression ratio of $\sim$360 and a radial compression of $\sim$19 for the electron beam. It is important that a small value of $\Delta r_c / r_c$ was chosen because the smaller it is, the smaller the alpha spread in the electron beam. The thermal loading of the gun was estimated to be $\sim$100 W at an operating temperature of $\sim$1000 °C. To reduce the stray magnetic field, the heating coil should be wired in a bifilar format. A stray magnetic field of $\sim 10^{-4}$ T was simulated by using CST Microwave Studio at a driving current of the heating coil of 10 A. It is of primary importance that the stray magnetic field from the heating coil is significantly lower than the magnetic field at the cathode to achieve a stable alpha and axial velocity of the electron beam.

The geometry of the cusp gun is shown in Fig. 1. The emitting surface is annular shaped and porous tungsten impregnated with barium oxide to reduce the work function to achieve the designed beam current at an operating temperature of $\sim$1000 °C. Two fine gaps of 0.1-mm width were used to separate the cathode ring from the outer and inner focusing electrodes for the following purposes: 1) reducing the thermal loading and 2) stopping the migration of the barium of the cathode. The length of the cathode–anode gap is chosen so
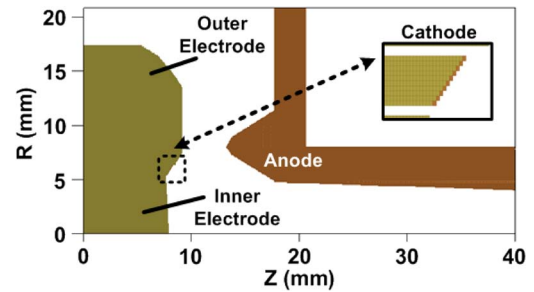
Fig. 1. Geometry of the cathode and anode of the cusp electron gun.

that the electric fields at the cathode are below 10 MV/m at an applied voltage of 40 kV to avoid problems such as field emission and vacuum breakdown. An anode tip is further used in the design to focus and transport the electron beam to the downstream region. The outer radius of the outer electrode was chosen to be large enough so that its effects on the electric field distribution between the cathode and anode are negligible while keeping its distance to the anode large enough to avoid problems such as field emission and vacuum breakdown. To avoid microwaves entering the gun region, a cylindrical low-frequency cutoff waveguide of 0.84-mm radius is used.

Two coils, namely, one "reverse" coil behind the cathode producing negative magnetic field, and the other a solenoid producing a uniform positive magnetic field B_0 at the downstream region, were used to form a magnetic cusp at the front of the cathode. Because of the relative low energy (approximately a few kiloelectron volts) of the electrons at the cusp, the amplitude of the cusp was greatly reduced (a few tens of gauss), and the Larmor step is on the order of meters due to the small amplitude of the cusp and the small transverse velocity component. This allows a field reversal over a longer distance. Therefore, in this design, it is not necessary to use any magnetic poles to sharpen the shape of the magnetic cusp. This makes this cusp gun a simple and effective alternative because of its simplified manufacture and optimization process, as well as flexibility in its operation. For example, the driving currents, averaged radius, and start and end positions of the coils can be changed to allow the adjustment of cusp position.

Various configurations of the cusp gun were optimized to give the highest quality electron beam, which include the following: the length of the cathode–anode gap, the shape of the anode tip, the cathode slope, the inner and outer focusing electrode geometries, and the size and position of the coils relative to the cathode surface. After the average radius and width are decided, the sizes of the dimensions of a, b, c, d, e, f, g, h, i, and j, as shown in Fig. 1, are varied for optimized beam quality in the simulation. Dimensions c, d, e, and f are used to adjust the slope angle relative to the z-axis of the inner and outer electrodes, as well as the relative position of the emitting surface to the electrodes. Adjustment of the relative position in the z-axis between the emitting surface and the electrodes is important to compensate the defocusing effect of the gaps on the electrons emitted from the corners of the cathode. Optimization of the slope of the electrodes and dimensions a and b is important because this decides the beam trajectory in the gun region. Dimension g should be chosen large enough to avoid

TABLE I
LIST OF OPTIMIZATION PARAMETERS, OPTIMIZED VALUES, AND OPTIMIZATION RANGES

Dimension Denotation	Optimised Value (mm)	Range of optimisation (mm)
a	0.30	0.00-0.60
b	5.44	5.30-6.00
c	0.27	0.10-0.45
d	0.25	0.10-0.45
e	0.60	0.40-0.80
f	1.01	0.70-1.30
g	4.48	2.50-5.00
h	3.23	2.00-4.00
i	4.13	3.50-5.10
j	4.80	4.00-5.20

Fig. 2. Snapshot of the simulated electron-beam trajectory with magnetic-field profile and a cross-sectional shape of the beam at the downstream region.

vacuum breakdown and field emission. Dimensions h, i, and j are used to optimize the focusing effect at the anode region. Simulations of the electron beam aim to reduce beam envelope oscillation, axial velocity spread, and alpha spread over a wide range of magnetic fields. Table I summarizes the optimized dimensions and the optimization ranges of these variables used in the simulation.

III. SIMULATION RESULT

Electron-beam emission was modeled using the Richardson–Dushman equation for thermionic emission. The accelerating voltage was applied using a smooth rising function with a rise time of 1 ns to avoid high-frequency loading of the gun. The simulated electron-beam trajectory from the cusp gun with its magnetic-field profile ($B_0 = 1.82$ T) is shown in Fig. 2. The cross-sectional shape of the beam at the downstream region is also shown in Fig. 2, and it clearly shows an annular-shaped axis-encircling beam. The magnetic-field profile is a smooth transition from the cathode to the downstream uniform magnetic-field region, with the cusp being located at ∼4.6 mm in front of the emission surface. It should be noted that some low-energy electrons of a few milliamperes over a period of a few nanoseconds (emitted when the accelerating voltage was rising) were reflected back at a high alpha value due to the magnetic-mirror effect, as
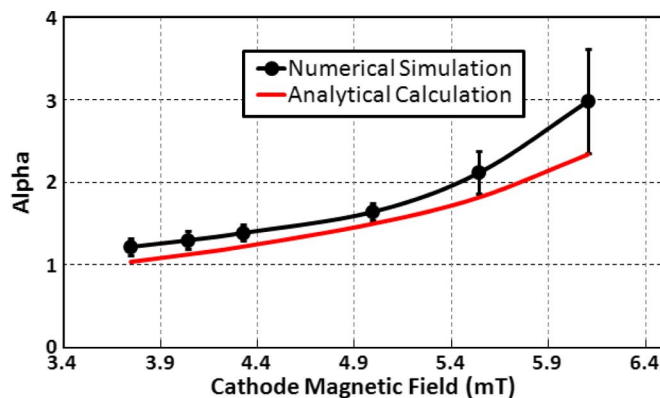
Fig. 3. Numerically simulated and analytically calculated alpha values for different values of cathode magnetic field at $B_0 = 1.82$ T.

shown in Fig. 1. However, after a few nanoseconds, 100% of the emitted current was transported to the downstream region. From simulation, to obtain an alpha value of one to three, the required magnetic field at the cathode was ∼3.0–6.7 mT. At a constant value of B_0, a larger α value could be achieved by increasing the magnetic-field amplitude at the cathode (B_c). The simulated average alpha of the electron beam as a function of the magnetic-field amplitude at the cathode is shown in Fig. 3 at $B_0 = 1.82$ T. The spread in alpha is also shown in this figure as bars, deviating from the average values. The alpha values calculated from the previous equation are also shown in Fig. 3 for comparison. Minimum axial velocity spreads of ∼8% and relative alpha spreads of ∼10% were achieved at an alpha value of 1.65 at this constant magnetic field. At B_0 values of 2.1 and 1.7 T, the optimum alpha spreads were ∼23% and ∼15% for alpha values of 3 and 1.2, respectively, and the corresponding axial velocity spreads for these cases were ∼20% and ∼10%. At the central magnetic field B_0 of 1.82 T, the beam had an inner and an outer radius of 0.23 and 0.42 mm, with an envelope ripple ∼13%. Beam transport through the tube was measured to be 100% after the initial low potential electrons were reflected. The feasibility of
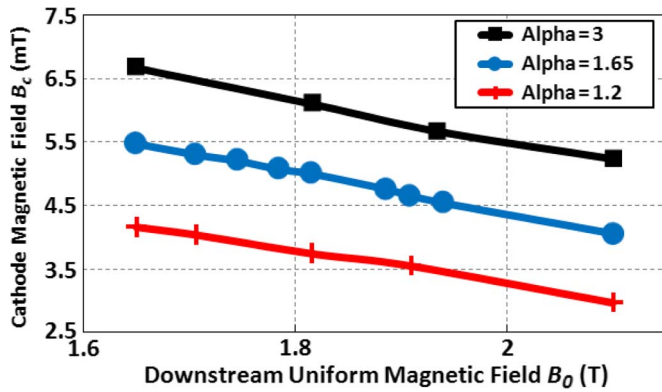
Fig. 4. Magnetic-field operation ranges for different values of velocity ratio (α).

operating this cathode at different alpha values for the three aforementioned microwave sources was also investigated with different magnetic-field operation ranges and is shown in Fig. 4. The gun is able to operate at an alpha from one to three over the magnetic-field tuning range of 1.65–2.1 T.

IV. CONCLUSION, DISCUSSION, AND FUTURE WORK

In conclusion, a cusp electron gun was simulated and optimized to generate an axis-encircling annular-shaped electron beam to drive millimeter-wave gyro-devices. At a velocity alpha of 1.65, the beam was optimized to achieve an axial velocity spread of 8% and a velocity spread of 10%. The viability of using the designed gun over a large alpha and magnetic-field range was demonstrated. It should be noted that the optimization for the generation of electron beams with alpha values of 1.2 and 3 has been performed by adjusting the position of the cusp, i.e., by adjusting the positions of the reversed and cavity coil only while the shape and size of the inner and outer electrodes are kept unchanged. Therefore, future work includes the optimization of the focusing electrodes to achieve optimized beam quality for harmonic-gyrotron and gyro-TWA applications. The structure of the cusp gun was designed in a way that allows the focusing electrodes to be changed.

REFERENCES

[1] W. M. Manheimer, G. Mesyats, and M. I. Petelin, *Applications of High-Power Microwaves*, A. V. Gaponov-Grekhov and V. L. Granatstein, Eds. Norwood, MA: Artech House, 1994, pp. 169–207.

[2] D. D. Amone, C. M. Cielsla, A. Corchia, S. Egusa, M. Pepper, J. Chamberlain, C. Bezant, E. H. Linfield, R. Clothier, and N. Khammo, "Application of terahertz (THz) technology to medical imaging," in *Proc. SPIE—Terahertz Spectrosopy Applications II*, Munich, Germany, 1999, vol. 3823, pp. 209–219.

[3] T. Imai, N. Kobayashi, R. Temkin, M. Thumm, M. Q. Tran, and V. Alikaev, "ITER R&D: Auxiliary systems: Electron cyclotron heating and current drive system," *Fusion Eng. Des.*, vol. 55, no. 2/3, pp. 281–289, Jul. 2001.

[4] T. I. Smirnova, A. I. Smirnov, and R. B. Clarkson, "W-band (95 GHz) EPR spectroscopy of nitroxide radicals with complex proton hyperfine structure: Fast motion," *J. Phys. Chem.*, vol. 99, no. 22, pp. 9008–9016, Jun. 1995.

[5] G. S. Nusinovich and O. Dumbrajs, "Theory of gyro-backward wave oscillators with tapered magnetic field and waveguide cross section," *IEEE Trans. Plasma Sci.*, vol. 24, no. 3, pp. 620–629, Jun. 1996.

[6] M. Garven, J. P. Calame, B. G. Danly, K. T. Nguyen, B. Levush, F. N. Wood, and D. E. Pershing, "A gyrotron-traveling-wave tube amplifier experiment with a ceramic loaded interaction region," *IEEE Trans. Plasma Sci.*, vol. 30, no. 3, pp. 885–893, Jun. 2002.

[7] T. Idehara, I. Ogawa, S. Mitsudo, Y. Iwata, S. Watanabe, Y. Itakura, K. Ohashi, H. Kobayashi, T. Yokoyama, V. E. Zapevalov, M. Y. Glyavin, A. N. Kuftin, O. V. Malygin, and S. P. Sabchevski, "A high harmonic gyrotron with an axis-encircling electron beam and a permanent magnet," *IEEE Trans. Plasma Sci.*, vol. 32, no. 3, pp. 903–909, Jun. 2004.

[8] T. H. Chang, C. F. Yu, C. L. Hung, Y. S. Yeh, M. C. Hsiao, and Y. Y. Shin, "W-band TE_{01} gyrotron backward-wave oscillator with distributed loss," *Phys. Plasmas*, vol. 15, no. 7, p. 073 105, Jul. 2008.

[9] Q. S. Wang, H. E. Huey, D. B. McDermott, Y. Hirata, and N. C. Luhmann, Jr., "Design of a W-band second-harmonic TE_{02} gyro-TWT amplifier," *IEEE Trans. Plasma Sci.*, vol. 28, no. 6, pp. 2232–2237, Dec. 2000.

[10] K. R. Chu, "Theory of electron cyclotron maser interaction in a cavity at the harmonic frequencies," *Phys. Fluids*, vol. 21, no. 12, pp. 2354–2364, Dec. 1978.

[11] G. Schmidt, "Nonadiabatic particle motion in axialsymmetric fields," *Phys. Fluids*, vol. 5, no. 8, pp. 994–1002, Aug. 1962.

[12] J. Sinnis and G. Schmidt, "Experimental trajectory analysis of charged particles in a cusped geometry," *Phys. Fluids*, vol. 6, no. 6, pp. 841–845, Jun. 1963.

[13] M. J. Rhee and W. W. Destler, "Relativistic electron dynamics in a cusped magnetic field," *Phys. Fluids*, vol. 17, no. 8, pp. 1574–1581, Aug. 1974.

[14] W. W. Destler and M. J. Rhee, "Radial and axial compression of a hollow electron beam using an asymmetric magnetic cusp," *Phys. Fluids*, vol. 20, no. 9, pp. 1582–1584, Sep. 1977.

[15] G. P. Scheitrum and R. True, "A triple pole piece magnetic field reversal element for generation of high rotational energy beams," in *IEDM Tech. Dig.*, Washington, DC, 1981, vol. 27, pp. 332–335.

[16] K. T. Nguyen, D. N. Smithe, and L. D. Ludeking, "The double-cusp gyro-gun," in *IEDM Tech. Dig.*, 1992, pp. 219–222.

[17] G. P. Scheitrum, R. S. Symons, and R. B. True, "Low velocity spread axis encircling electron beam forming system," in *IEDM Tech. Dig.*, 1989, pp. 743–746.

[18] S. G. Jeon, C. W. Baik, D. H. Kim, G. S. Park, N. Sato, and K. Yokoo, "Study on velocity spread for axis-encircling electron beams generated by single magnetic cusp," *Appl. Phys. Lett.*, vol. 80, no. 20, pp. 3703–3705, May 2002.

[19] D. A. Gallagher, M. Barsanti, F. Scafuri, and C. Armstrong, "High-power cusp gun for harmonic gyro-device applications," *IEEE Trans. Plasma Sci.*, vol. 28, no. 3, pp. 695–699, Jun. 2000.

[20] W. He, C. G. Whyte, E. G. Rafferty, A. W. Cross, A. D. R. Phelps, K. Ronald, A. R. Young, C. W. Robertson, D. C. Speirs, and D. H. Rowlands, "Axis-encircling electron beam generation using a smooth magnetic cusp for gyrodevices," *Appl. Phys. Lett.*, vol. 93, no. 12, p. 121 501, Sep. 2008.

[21] W. W. Destler, R. Kulkarni, C. D. Striffler, and R. L. Weiler, "Microwave generation from rotating electron beams in magnetron-type waveguides," *J. Appl. Phys.*, vol. 54, no. 7, pp. 4152–4162, Jul. 1983.

[22] D. B. McDermott, A. J. Balkcum, and N. C. Luhmann, Jr., "35-GHz 25-kW CW low-voltage third-harmonic gyrotron," *IEEE Trans. Plasma Sci.*, vol. 24, no. 3, pp. 613–619, Jun. 1996.

[23] T. Gray, D. N. Smithe, and L. D. Ludeking, *Introduction to MAGIC*. Washington, DC: Mission Research Corp., 2003.

[24] C. R. Donaldson, W. He, A. D. R. Phelps, F. Li, A. W. Cross, K. Ronald, A. R. Young, and C. G. Whyte, "A ~10 kW W-band gyro-BWO using a helically corrugated waveguide," presented at the Joint 33rd Int. Conf. Infrared Millimeter, 16th Int. Conf. Terahertz Electronics, Pasadena, CA, 2008, Paper ICIMW.2008.4665519.

[25] W. He, A. D. R. Phelps, A. W. Cross, C. R. Donaldson, and K. Ronald, "A W-band gyrotron travelling wave amplifier using a helically corrugated waveguide," in *Proc. 17th High-Power Particle Beams Conf. (Beams)*, Xi'an, China, 2008, p. 646.

[26] F. Li, W. He, A. D. R. Phelps, A. W. Cross, C. R. Donaldson, and K. Ronald, "The design of a 390 GHz gyrotron based on a cusp electron gun," presented at the Joint 33rd Int. Conf. Infrared Millimeter, 16th Int. Conf. Terahertz Electronics, Pasadena, CA, 2008, Paper ICIMW.2008.4665500.

[27] G. G. Denisov, V. L. Bratman, A. D. R. Phelps, and S. V. Samsonov, "Gyro-TWT with a helical operating waveguide: New possibilities to enhance efficiency and frequency bandwidth," *IEEE Trans. Plasma Sci.*, vol. 26, no. 3, pp. 508–518, Jun. 1998.

[28] W. He, A. W. Cross, A. D. R. Phelps, K. Ronald, C. G. Whyte, S. V. Samsonov, V. L. Bratman, and G. G. Denisov, "Theory and simulations of a gyrotron backward wave oscillator using a helical interaction waveguide," *Appl. Phys. Lett.*, vol. 89, no. 9, p. 091 504, Sep. 2006.

[29] S. Humphries, *Charged Particle Beams*. New York: Wiley, 1990.

Craig R. Donaldson received the B.Sc.(Hons.) degree in physics and the M.Sc. degree in high power RF from the University of Strathclyde, Glasgow, U.K., in 2005 and 2006, respectively, where he is currently working toward the Ph.D. degree in physics in the Department of Physics.

He is also currently with SUPA, University of Strathclyde. His main research interests include electron-beam generation, gyro-TWT/BWOs, and helically corrugated waveguides.

Wenlong He received the B.Sc. degree in physics from Suzhou University, Jiangsu, China, in 1983, the M.Sc. degree in accelerator physics from the China Academy of Engineering Physics, Chengdu, China, in 1988, and the Ph.D. degree in relativistic electron beams and masers from the Department of Physics, University of Strathclyde, Glasgow, U.K., in 1995.

He is currently a Senior Research Fellow with the Department of Physics, University of Strathclyde, where he is also with SUPA. His main research interests include relativistic electron beams, CARMs, FELs, gyro-TWT/BWOs, and other high-power microwave devices.

Adrian W. Cross received the B.Sc.(Hons.) degree in physics and the Ph.D. degree from the University of Strathclyde, Glasgow, U.K., in 1989 and 1993, respectively.

He joined the ABP Group, University of Strathclyde, initially as a Research Fellow in 1993 and then as a Lecturer in 2000, where he is currently a Reader with the Department of Physics and also with SUPA. He has been involved in various aspects of research on gyrotrons, cyclotron autoresonance masers, free-electron lasers, superradiant sources, and plasma applications. More recently, he has primarily been concerned with research on radiation sources for use in accelerators and pseudospark physics.

Alan D. R. Phelps was born in 1944 in the U.K. He received the B.A.(Hons.) degree in physics and the M.A. degree from Cambridge University, Cambridge, U.K., in 1966 and 1970, respectively, and the Dr.Phil. degree in plasma research from Oxford University, Oxford, U.K., in 1970.

He founded a research group at the University of Strathclyde, Glasgow, U.K., in 1978, where he became a Full Professor in 1993. He is currently with the Department of Physics, University of Strathclyde, where he was the Head from 1998 to 2001, and also with SUPA. His research interests include high-power free-electron radiation sources and plasmas.

Prof. Phelps is a fellow of the Institute of Physics and The Royal Society of Edinburgh.

Fengping Li received the B.Sc. degree in applied physics from the University of Science and Technology of China, Hefei, China, in 2001 and the M.Sc. degree in accelerator physics from the China Academy of Engineering Physics, Chengdu, China, in 2004. He is currently working toward the Ph.D. degree in relativistic electron beams in the Department of Physics, University of Strathclyde, Glasgow, U.K.

He was awarded a SUPA prize studentship in 2006 and is with SUPA, Department of Physics. His main research interests include pulsed-power technology, X-ray diagnostics, lasers, plasma science, electron-beam generation and gyro-TWT/BWOs.

Kevin Ronald was born in Glasgow, U.K. He received the B.Sc.(Hons.) and Ph.D. degrees in physics from the University of Strathclyde, Glasgow, in 1992 and 1997, respectively.

He is currently a Lecturer with the Department of Physics, University of Strathclyde, where he is also with SUPA.

Craig W. Robertson was born in Ayrshire, U.K., in 1977. He received the B.Sc.(Hons.) degree in physics and the Ph.D. degree from the University of Strathclyde, Glasgow, U.K., in 1999 and 2004, respectively.

He is currently with SUPA, Department of Physics, University of Strathclyde. His interests include low-temperature plasma production and diagnostics, as well as high-power microwave sources.

Colin G. Whyte was born in Selkirk, U.K., in 1969. He received the B.Sc. degree in physics from the University of Glasgow, Glasgow, U.K., in 1991 and the M.Sc. degree in laser physics and pulsed-power technology and the Ph.D. degree in physics from the University of St Andrews, St Andrews, U.K., in 1992 and 1996, respectively.

He has been with the University of Strathclyde, Glasgow, since 1996 in the ABP Group, Department of Physics, where he is also currently with SUPA. His research interests include the design and experimental investigation of high-power broadband microwave amplifiers and oscillators, including novel helical gyro-TWT devices and reverse-guide-field free-electron lasers. He also designs and builds high-voltage pulsed-power supplies.

Alan R. Young received the B.Sc. degree in physics, the M.Sc. degree in information technologies systems, and the Ph.D. degree, with a dissertation on high-quality electron beams for CARMs, from the University of Strathclyde, Glasgow, U.K., in 1993, 1994, and 1998, respectively.

He has since continued to work as a Research Fellow with the Department of Physics, University of Strathclyde, on a variety of gyro-devices, including CARM and gyro-TWT, where he is also currently with SUPA.

Liang Zhang received the B.Sc. degree in applied physics from the University of Science and Technology of China, Hefei, China, in 2004 and the M.Sc. degree in application of nuclear techniques from the China Academy of Engineering Physics, Chengdu, China, in 2007. He is currently working toward the Ph.D. degree in relativistic electron beams in the Department of Physics, University of Strathclyde, Glasgow, U.K.

He was awarded a SUPA prize studentship in 2007 and is with SUPA, Department of Physics, University of Strathclyde. His main research interests include pulsed-power technology, electron-beam generation, and gyro-TWT/BWOs.

A cusp electron gun for millimeter wave gyrodevices

C. R. Donaldson,[a)] W. He, A. W. Cross, F. Li, A. D. R. Phelps, L. Zhang, K. Ronald, C. W. Robertson, C. G. Whyte, and A. R. Young
Department of Physics, SUPA, University of Strathclyde, Glasgow G4 0NG, United Kingdom

The experimental results of a thermionic cusp electron gun, to drive millimeter and submillimeter wave harmonic gyrodevices, are reported in this paper. Using a "smooth" magnetic field reversal formed by two coils this gun generated an annular-shaped, axis-encircling electron beam with 1.5 A current, and an adjustable velocity ratio α of up to 1.56 at a beam voltage of 40 kV. The beam cross-sectional shape and transported beam current were measured by a witness plate technique and Faraday cup, respectively. These measured results were found to be in excellent agreement with the simulated results using the three-dimensional code MAGIC. © *2010 American Institute of Physics.* [doi:10.1063/1.3374888]

Further to the design and numerical optimization of a cusp electron beam source,[1] in this paper we present the experiment of the cusp gun and the measured results of the generated axis-encircling electron beam. Due to its small cross-sectional size (less than 1 mm in diameter) in a large magnetic field (a few tesla) such a beam is capable of driving millimeter and submillimeter wave gyrodevices which have many modern applications notably in remote sensing,[2] medical imaging,[3] plasma heating,[4] and electron spin resonance spectroscopy.[5] In order to reach higher frequencies, gyrodevices are more commonly operating at a higher indexed waveguide mode and a harmonic of the electron cyclotron frequency;[6–10] the advantage being that it lowers the required magnetic field strength by a factor of s, the harmonic number. However, operating at harmonics could introduce undesired mode competition, as well as parasitic oscillations. An axis-encircling electron beam is ideal for harmonic gyrodevices due to its good mode selectivity as the beam-wave coupling requires that the azimuthal index of the waveguide mode, m be equal to s.[11] Compared to previous cusp guns,[12–15] this cusp gun has the advantage of (1) simple design and structure with reduced manufacturing complexity due to the "smooth cusp" configuration[16] using two coils without any need for extra magnetic poles and/or material and (2) smaller cusp amplitude because the cusp is located immediately after the cathode where the electron is not fully accelerated.

The electron gun was designed and optimized using the three-dimensional particle-in-cell code MAGIC. The applications were for three microwave sources being developed including a W-band gyrotron backward-wave oscillator (gyro-BWO)[17] and a W-band gyrotron traveling-wave tube[18] both using a helically corrugated waveguide and a terahertz seventh harmonic gyrotron.[19] These devices are based on the previous radiation sources operating at X-band (8.4 to 12 GHz) frequencies.[20–22] The cusp gun was designed to generate an electron beam of 1.5 A, 40 kV with velocity ratio α =1–3 in order to generate millimeter and submillimeter waves of 75 GHz to 390 GHz over a magnetic field range of 1.50–2.1 T. Based on the simulation results for one particular set of parameters which yields an optimized beam for an

alpha range of 1–2, the cusp electron gun of Fig. 1 was manufactured.

The cathode assembly and the anode were arranged in a coaxial configuration (Fig. 1). The cathode head included three following interchangeable parts: outer, inner focusing electrodes, and the thermionic cathode emitter which was located between the electrodes and constructed from porous tungsten impregnated with barium oxide. Facing the cathode head was an interchangeable anode tip. The beam trajectories are determined by the dimensions of these interchangeable parts. The cathode heating coil was bifilar wound in order to minimize any contribution to the field at the cathode.[1] Two fine gaps of 0.1 mm in width between the emitter and the focusing electrodes were used to reduce the thermal loading of the cathode and to stop the migration of barium from the emitter. Layers of thin tubes and disks made from molybdenum, located between the outer electrodes and the emitter and behind the emitter, respectively, were used as radiation shields to further reduce the thermal loading of the cathode. The beam tunnel tapered down from the anode aperture (radius 4 mm) to the cut-off filter (radius 0.84 mm), followed by an experimental region, a cylindrical tunnel of radius 3.0 mm and length 292 mm, and then to the up-taper and finally the window region. This experimental region allowed the beam diagnostic apparatus such as the Faraday cup and the scintillator witness plate to be inserted. A single layer sapphire window was used in this beam experiment for observation of the visible light generated by the scintillator. The whole system was evacuated to 10^{-9} mBar.

The magnetic field coils were wound from annealed, varnish-coated, square copper wire of cross section 2.2 $\times$ 2.2 mm^2, enclosed in watertight, stainless steel chambers, and cooled by high pressure recirculating water when in operation. The cavity solenoid which generates a uniform B-field in the beam-wave interaction region has 14 layers each of 103 turns. Two extra layers of coils were added to both ends of the main solenoid to reduce the rise and fall distance of its B-field profile for a certain length of the flat-top so that the overall turns, length of the solenoid, and hence the driving electric power were reduced. At maximum achievable magnetic field strength of 2.1 T the required driving power was $\sim$65 kW at a current of $\sim$270 A. The layers were separated by 0.4 mm gaps to allow cooling water to

a)Electronic mail: craig.donaldson@strath.ac.uk.
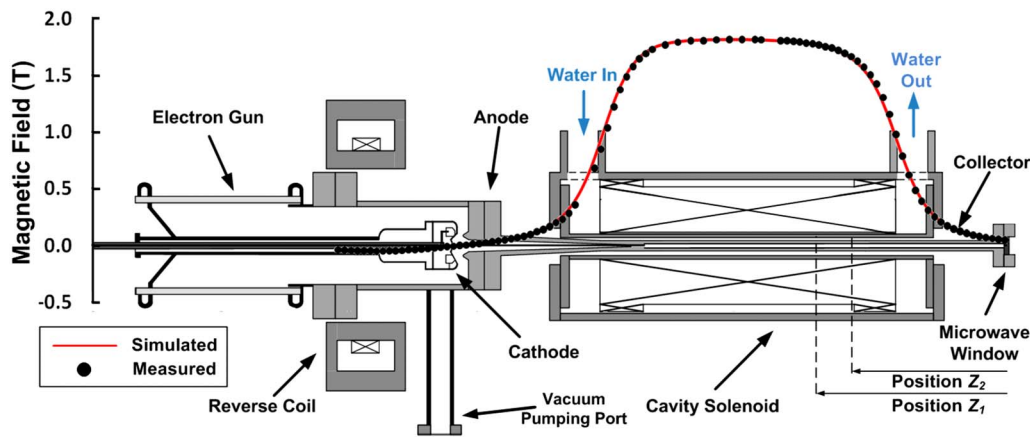
FIG. 1. (Color online) Schematic diagram of the cusp electron gun with simulated and measured magnetic field profile overlaid.

pass from one end to the other end of the solenoid. Simulations of the fluid dynamics and heat exchange including heat conduction, convection, and diffusion were performed by using the MultiPhysics code COMSOL.[23] The reverse coil, having four layers each of ten turns, produced the reverse B-field for the cusp gun. The magnetic field profiles measured using an axial Hall probe and calculated from MAGIC are shown in Fig. 1.

A double cable Blumlein[24] which could output a ~380 ns, 40 kV pulse was used to drive the cusp gun. The beam voltage was measured using a two-stage voltage divider made from metal film resisters. The emitted current was measured with a Rogowski coil located in the earth line between the anode and the cable Blumlein and the beam current by a Faraday cup at Z_1 location (see Fig. 1).

The beam cross-sectional shape and dimensions were recorded by a phosphor scintillator plate and digital camera system[25] after the Faraday cup was removed. The scintillator, a round transparent disk coated with a thin layer of phosphor, produces visible light when electrons impact on the surface. A thin titanium disk of thickness ~8 μm was placed before the scintillator to reduce the impact energy of the beam. The scintillator disk was located at position Z_2 (see Fig. 1), 10.5 cm from the window so as to match with the focal length of the camera, at this position the magnetic field tailed off to 90% of the cavity B-field. By using the equation in Ref. 16, the α value in the cavity (in particular, at Z_1) could be calculated from the B-field and α values at Z_2.

Typical traces of beam voltage and beam current are shown in Fig. 2. The emitted current from the cathode could be varied from 0 to ~1.6 A by increasing the operating

temperature of the cathode, at the applied beam voltage of 40 kV. Further increase in the temperature did not result in an increase in the beam current. This indicated that the operation of the cathode had become space-charge limited. In Fig. 2, we can see the beam current reached a steady value of 1.5 A. When the cavity B-field was 1.82 T ~96% of this current reached the Faraday cup.

A typical scintillator image, after the optical noise was removed, is shown in Fig. 3. The image shows clearly that an axis-encircling electron beam was generated. The simulated beam cross-sectional shape is shown for comparison together with beam trajectories in the $R-Z$ plane. For this particular measurement, at a cavity B-field of 1.64 T, the annular beam was measured to have an average radius of ~0.37 mm. It was calculated from the equation in Ref. 16 that the corresponding α was 1.34 ± 0.11. This corresponded to an α value of 1.56 ± 0.16 at the Z_1 position.

By adjusting the reverse coil current the magnetic field at the cathode and hence the value of the velocity ratio of the beam in the cavity could be controlled. At $B_0 = 1.64$ T the velocity ratio at position Z_2 as a function of cathode B-field was measured and is shown in Fig. 4. For comparison of the simulated α at Z_1 and Z_2 as well as analytically calculated value at Z_2 are also shown in Fig. 4. From the diagram, the measured α value had the same trend and good agreement with both the numerical simulated and analytically calculated values. However investigation at higher alphas was limited by the capability of the existing power supply.

In summary, when the thermionic cusp gun for millimeter/submillimeter wave gyrodevices was tested, the
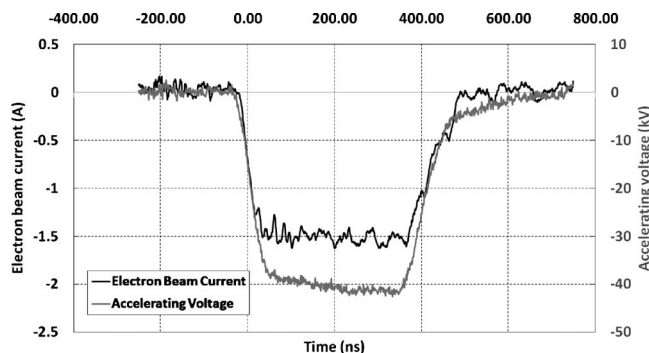
FIG. 2. The typical traces of the measured beam voltage and beam current.
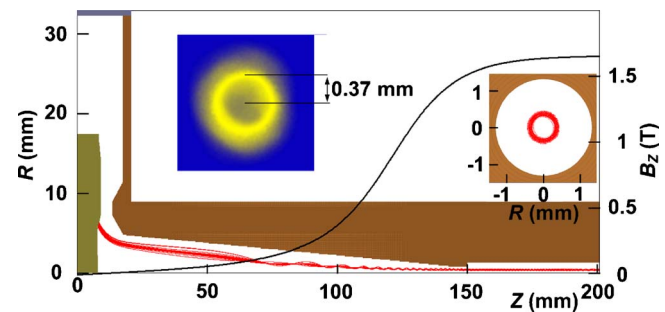
FIG. 3. (Color online) Snapshot of the simulated electron beam trajectory with magnetic field profile overlaid, also simulated and scintillator recorded beam cross-sectional shape at the downstream region.
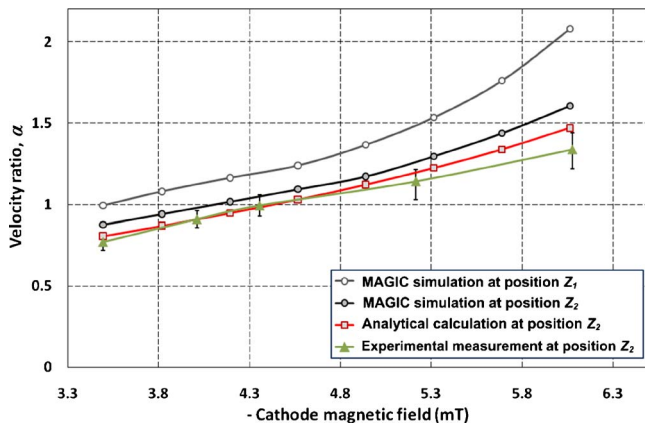
FIG. 4. (Color online) The measured, simulated, and analytically calculated beam velocity ratio as a function of cathode magnetic field at $B_0 = 1.64$ T.

measured beam parameters were in excellent agreement with the MAGIC simulation. In addition, in a recent experiment, the beam from this cusp gun has been used in a helical waveguide gyro-BWO which generated microwave radiation in the frequency range 92–100 GHz.[26]

[1] C. R. Donaldson, W. He, A. W. Cross, A. D. R. Phelps, F. Li, K. Ronald, C. W. Robertson, C. G. Whyte, A. R. Young, and L. Zhang, IEEE Trans. Plasma Sci. **37**, 2153 (2009).

[2] W. M. Manheimer, G. Mesyats, and M. I. Petelin, in *Applications of High-Power Microwaves*, edited by A. V. Gaponov-Grekhov and V. L. Granatstein (Artech House, Norwood, 1994), pp. 169–207.

[3] R. M. Woodward, B. E. Cole, R. J. Pye, D. D. Amone, E. H. Linfield, and M. Pepper, Phys. Med. Biol. **47**, 3853 (2002).

[4] T. Imai, N. Kobayashi, R. Temkin, M. Thumm, M. Q. Tran, and V. Alikaev, Fusion Eng. Des. **55**, 281 (2001).

[5] H. M. Assenheim, *Introduction to Electron Spin Resonance* (Plenum, New York, 1966).

[6] M. Garven, J. P. Calame, B. G. Danly, K. T. Nguyen, B. Levush, F. N. Wood, and D. E. Pershing, IEEE Trans. Plasma Sci. **30**, 885 (2002).

[7] G. F. Brand, P. W. Fekete, K. Hong, K. J. Moore, and T. Idehara, Int. J.

[Electron. **68**, 1099 (1990).

[8] T. Idehara, I. Ogawa, S. Mitsudo, Y. Iwata, S. Watanabe, Y. Itakura, K. Ohashi, H. Kobayashi, T. Yokoyama, V. E. Zapevalov, M. Y. Glyavin, A. N. Kuftin, O. V. Malygin, and S. P. Sabchevski, IEEE Trans. Plasma Sci. **32**, 903 (2004).

[9] T. H. Chang, C. F. Yu, C. L. Hung, Y. S. Yeh, M. C. Hsiao, and Y. Y. Shin, Phys. Plasmas **15**, 073105 (2008).

[10] Q. S. Wang, H. E. Huey, D. B. McDermott, Y. Hirata, and N. C. Luhmann, Jr., IEEE Trans. Plasma Sci. **28**, 2232 (2000).

[11] K. R. Chu, Rev. Mod. Phys. **76**, 489 (2004).

[12] J. Sinnis and G. Schmidt, Phys. Fluids **6**, 841 (1963).

[13] M. Friedman, Phys. Rev. Lett. **24**, 1098 (1970).

[14] W. Lawson, Appl. Phys. Lett. **50**, 1477 (1987).

[15] S. G. Jeon, C. W. Baik, D. H. Kim, G. S. Park, N. Sato, and K. Yokoo, Appl. Phys. Lett. **80**, 3703 (2002).

[16] W. He, C. G. Whyte, E. G. Rafferty, A. W. Cross, A. D. R. Phelps, K. Ronald, A. R. Young, C. W. Robertson, D. C. Speirs, and D. H. Rowlands, Appl. Phys. Lett. **93**, 121501 (2008).

[17] C. R. Donaldson, W. He, A. D. R. Phelps, F. Li, A. W. Cross, K. Ronald, A. R. Young, and C. G. Whyte, *Joint 33rd International Conference on Infrared and Millimeter and 16th International Conference on Terahertz Electronics*, Pasadena, CA, 2008 (IEEE, New York, 2008).

[18] W. He, A. D. R. Phelps, A. W. Cross, C. R. Donaldson, and K. Ronald, The 17th High-Power Particle Beams Conference (Beams' 08), Xi'an, China (Chinese Pulsed Power Society, Chinese Particle Accelerator Society, 2008), p. 646.

[19] F. Li, W. He, A. D. R. Phelps, A. W. Cross, C. R. Donaldson, and K. Ronald, *Joint 33rd International Conference on Infrared and Millimeter and 16th International Conference on Terahertz Electronics*, Pasadena, CA, 2008 (IEEE, New York, 2008).

[20] A. W. Cross, W. He, A. D. R. Phelps, K. Ronald, C. G. Whyte, A. R. Young, C. W. Robertson, E. G. Rafferty, and J. Thomson, Appl. Phys. Lett. **90**, 253501 (2007).

[21] W. He, K. Ronald, A. R. Young, A. W. Cross, A. D. R. Phelps, C. G. Whyte, E. G. Rafferty, J. Thomson, C. W. Robertson, E. C. Speirs, S. V. Samsonov, V. L. Bratman, and G. G. Denisov, IEEE Trans. Electron Devices **52**, 839 (2005).

[22] W. He, A. W. Cross, A. D. R. Phelps, K. Ronald, C. G. Whyte, S. V. Samsonov, V. L. Bratman, and G. G. Denisov, Appl. Phys. Lett. **89**, 091504 (2006).

[23] COMSOL, Multiphysics, Comsol, Inc., www.comsol.com

[24] I. C. Somerville, S. J. MacGregor, and O. Farish, Meas. Sci. Technol. **1**, 865 (1990).

[25] W. He, H. Yin, A. D. R. Phelps, A. W. Cross, and S. N. Spark, Rev. Sci. Instrum. **72**, 4266 (2001).

[26] W. He, C. R. Donaldson, A. W. Cross, F. Li, A. D. R. Phelps, L. Zhang, K. Ronald, C. W. Robertson, C. G. Whyte, and A. R. Young, The 34th International Conference on Infrared, Millimeter, and Terahertz Waves, Busan, Korea (IEEE, New York, 2009).

Design and simulation of a $\sim$390 GHz seventh harmonic gyrotron using a large orbit electron beam

Fengping Li, Wenlong He, Adrian W Cross, Craig R Donaldson, Liang Zhang, Alan D R Phelps and Kevin Ronald

SUPA, Department of Physics, University of Strathclyde, Glasgow, G4 0NG, UK

E-mail: Fengping.li@strath.ac.uk

Abstract

A $\sim$390 GHz harmonic gyrotron based on a cusp electron gun has been designed and numerically modelled. The gyrotron operates at the seventh harmonic of the electron cyclotron frequency with the beam interacting with a TE_{71} waveguide mode. Theoretical as well as numerical simulation results using the 3D particle-in-cell code MAGIC are presented. The cusp gun generated an axis-encircling, annular shaped electron beam of energy 40 keV, current 1.5 A with a velocity ratio α of 3. Smooth cylindrical waveguides have been studied as the interaction cavities and their cavity Q optimized for 390 GHz operation. In the simulations $\sim$600 W of output power at the design frequency has been demonstrated.

(Some figures in this article are in colour only in the electronic version)

1. Introduction

Microwave radiation sources are one of the crucial technologies for modern society. High power sub-millimetre wave sources have attracted significant interest recently due to their potential applications in electron cyclotron resonance heating [1], plasma diagnostics [2], space radar systems [3], communication systems [4], materials science and medical imaging and spectroscopy [5, 6].

The gyrotron is well known as a coherent millimetre wave source capable of high power and high frequency output which is extendable to the terahertz (THz) frequency region. Recently a gyrotron achieved kilowatts of output power operated at the fundamental electron cyclotron frequency of 1 THz [7] by using a pulsed solenoid. However, continuous wave (CW) operation at such a frequency is a formidable task because of the large magnetic field ($\sim$40 T) that is required. As the output frequency increases, both larger magnetic fields and reduced interaction region size are needed when operating at the fundamental cyclotron frequency. An alternative approach to generate CW high frequency radiation is to work at higher cyclotron harmonics [8–11] which allow the use of larger cavity sizes and smaller magnetic fields by a factor of s, where s is the harmonic number.

A CW high harmonic gyrotron operating at a frequency of $\sim$390 GHz at relatively lower B-field was designed and is presented in this paper. In this gyrotron cyclotron resonance takes place between the seventh harmonic of the electron cyclotron frequency ($s = 7$) and the TE_{71} waveguide mode. A large orbit electron beam from a cusp gun is used to reduce the possibility of parasitic interactions. The small-signal theory of the beam–wave interaction was used to calculate the growth rate and the starting current. A smooth-bore cavity was designed with a suitable Q value by optimizing the angle of the output taper and the length of the cavity so that the starting current requirement is met. Finally, the beam–wave interaction of the gyrotron was simulated using the 3D particle-in-cell (PIC) code MAGIC and the results are presented.

2. Cusp electron gun

While operating at harmonics, undesired mode competition as well as parasitic oscillations will be more problematic as the harmonic number increases; therefore, it is advantageous for an electron gun to be able to generate a mode-selective beam. A large orbit electron beam from a cusp gun was selected because, for such a beam, its harmonic of the cyclotron mode (s) only interacts with a TE_{mn} waveguide mode (m and n are
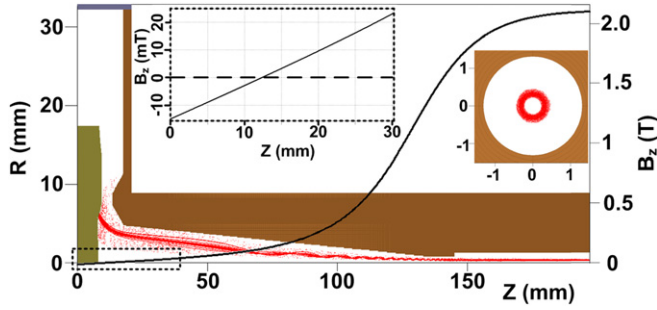
Figure 1. Simulated cusp gun and resultant beam trajectories with the detailed magnetic field configuration at the cusp point.

the azimuthal and the radial mode index, respectively) when $s = m$ [12]. A cusp electron gun operates by an electron beam passing through a non-adiabatic magnetic field reversal from negative to positive sign. Invariance of the magnetic moment results in a large orbit, annular electron beam [13–15].

Several successful terahertz range large orbit harmonic gyrotron experiments have been carried out at resonant magnetic fields 10.5–14 T [16, 17].

The 3D PIC code MAGIC was used to simulate and optimize the design of the cusp electron beam source. The optimized geometry of the cusp gun including the magnetic field profile and the resultant beam trajectories are shown in figure 1. An insertion shows in detail the B-field reversal in the cusp region.

The B-field profile of the cusp was produced by two coils, a main coil and a reverse coil. The main coil produces a uniform magnetic field at the downstream region which should have a certain length of the flat-top region required by the beam–wave interaction in the cavity. Two extra layers of coils were added to both ends of the main solenoid to sharpen its B-field profile so that the overall turns and length of the solenoid were reduced. These extra coils were carefully designed to avoid any bumps in the magnetic field profile while minimizing the rise and fall distance of the magnetic field. The design parameters were optimized resulting in the production of a 40 kV, 1.5 A large orbit electron beam in the simulations. This electron beam has been optimized through adjustment of the magnetic coil arrangement to operate at a velocity ratio α from 1.2 to 3 [18, 19] with an inner radius of 0.27 mm and an outer radius of 0.36 mm. This is consistent with the analytical calculated Larmor radius of 0.31 mm. The reflected electrons in figure 1 are low energy electrons emitted during the rise-time of the applied voltage pulse. A velocity pitch α spread of ∼25% was simulated when α reaches 3. Further increase in the beam α would result in a significant increase in beam spread in α, hence the reflection of some beam electrons.

3. Gyrotron design

Gyrotrons are based on the cyclotron resonance maser (CRM) [20] instability and operate through a fast cyclotron wave interaction, which takes place near the frequency cut-off region of the waveguide mode. In a high harmonic gyrotron, the beam (harmonic number $s > 1$) interacts with a high order TE$_{mn}$ waveguide mode where $m = s$.
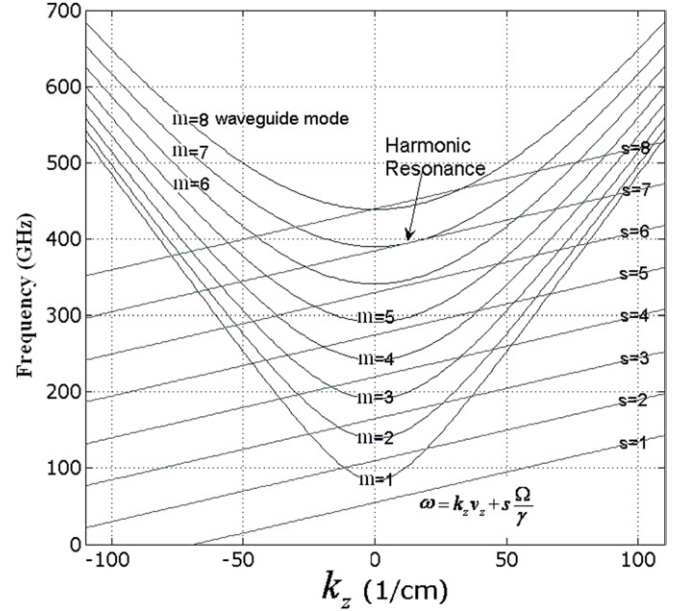
Figure 2. Dispersion of the TE$_{m1}$ waveguide modes ($m = 1$–8) and beam–wave resonances at different harmonics.

All the possible interactions are shown in figure 2. When the seventh harmonic of the electron cyclotron frequency is in resonance with the TE$_{71}$ mode, interactions below this mode are eliminated because the corresponding harmonic beam lines are far below their corresponding TE$_{m1}$ waveguide mode curves except for the case of the TE$_{61}$ mode and $s = 6$. The other possible parasitic interactions might be from higher modes, i.e. TE$_{81}$ with $s = 8$ and TE$_{91}$ with $s = 9$, etc. However, the most dangerous one is with the neighbouring TE$_{81}$ interaction as the starting current increases as the mode index increases. But the TE$_{81}$ interaction has a starting current higher than the beam current. In this way any other parasitic interactions of higher modes are automatically eliminated.

As the gyrotron works near the cut-off frequency region, and a large orbit gyrotron requires $s = m$, the operating frequency (390 GHz) and harmonic number ($s = 7$) as well as the azimuthal index of the waveguide mode ($m = 7$) were chosen prior to the cavity size.

The interaction of the waveguide mode and axis-encircling electron beam cyclotron mode can be described by the equation below [21, 22]:

$$\omega^2 - k_z^2 c^2 = -\frac{4\beta_\perp^2}{\left(x_{mn}^2 - m^2\right)\left(\omega - k_z v_z - s\Omega\right)^2}$$
$$\times \left(\frac{I}{I_A}\right)\left(\frac{x_{mn}c}{r_w}\right)^4 \left(\frac{J'_m\left(x_{mn}r_L/r_w\right)}{J_m\left(x_{mn}\right)}\right)^2, \quad (1)$$

where k_z is the propagation constant; x_{mn} is the nth root of $J'_m(x) = 0$. r_w is the radius of the cylindrical cavity; N_e is the axial linear density of electrons. $\gamma_0 = 1 + eV/m_0c^2$ is the relativistic Lorentz factor; m_0 is the rest mass of an electron, V is the electron beam voltage. $\beta_\perp = v_\perp/c$; $r_L = v_\perp/\Omega$ is the electron Larmor radius. $\Omega = eB/\gamma_0 m_0$ is the electron gyrating frequency, where B is the magnetic field. I is the beam current and $I_A = 4\pi\varepsilon_0 m_0 c^3/e \approx 17$ kA is the Alfven current.
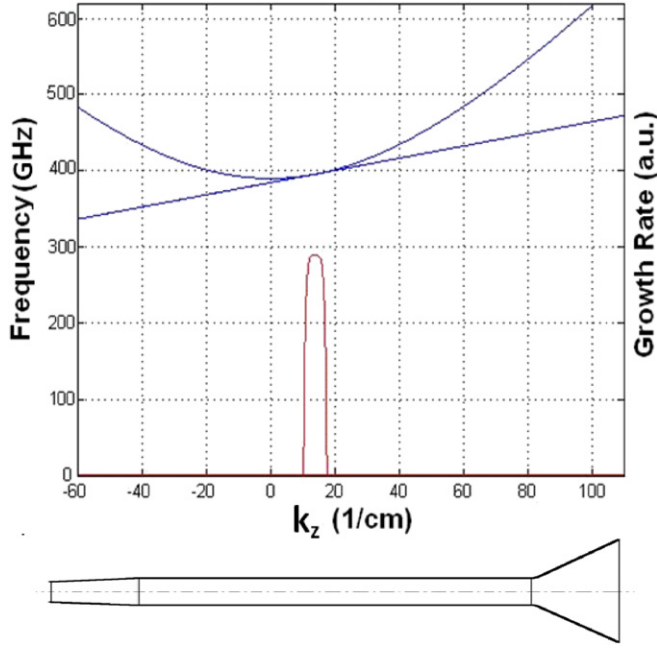
Figure 3. The growth rate at the seventh harmonic interaction (upper diagram) and the schematic gyrotron geometry (lower diagram).

The growth rate of this interaction can be obtained by solving the imaginary part of ω in equation (1) as a function of axial wavenumber k_z and is shown in figure 3. In the diagram the TE$_{71}$ cylindrical waveguide mode is interacting with the seventh harmonic of the electron cyclotron frequency of a beam with a velocity ratio α of 3 at a magnetic field of 2.09 T. The radius of the cylindrical cavity is 1.055 mm and the cavity length is 50 mm at a reasonable cavity Q of 2000.

The cavity length L and the output taper angle are optimized for a reasonably high Q which is a very important parameter in any gyrotron design. The total Q of the resonant cavity is given by

$$\frac{1}{Q} = \frac{1}{Q_d} + \frac{1}{Q_\Omega}. \tag{2}$$

The diffraction quality factor Q_d and the ohmic quality factor Q_Ω which are caused by diffraction and ohmic losses, respectively, can be calculated using the equations below:

$$Q_d = 4\pi \frac{(L/\lambda)^2}{1 - |R_1 R_2|}, \tag{3}$$

$$\frac{1}{Q_\Omega} = \left(\frac{\delta}{r_w}\right) \left[\frac{c^2}{\omega^2} \frac{x_{mn}^2}{r_w^2} + \left(\frac{x_{mn}^2}{x_{mn}^2 - m^2}\right) \right], \tag{4}$$

where $\delta = \sqrt{2/\omega\mu\sigma}$ is the skin depth of the cavity wall, σ is the conductivity of the cavity material, μ is the absolute permeability. R_1 and R_2 are the reflection coefficients at both ends of the cavity interaction region.

The cavity Q was calculated using the code Cascade [23]. In figure 4(*a*) the curve shows the simulated cavity Q as a function of the output taper angle at 390 GHz. In this diagram, the cavity was a 40 mm long smooth cylindrical cavity with a radius of $r_w = 1.055$ mm. The output taper was 10 mm in
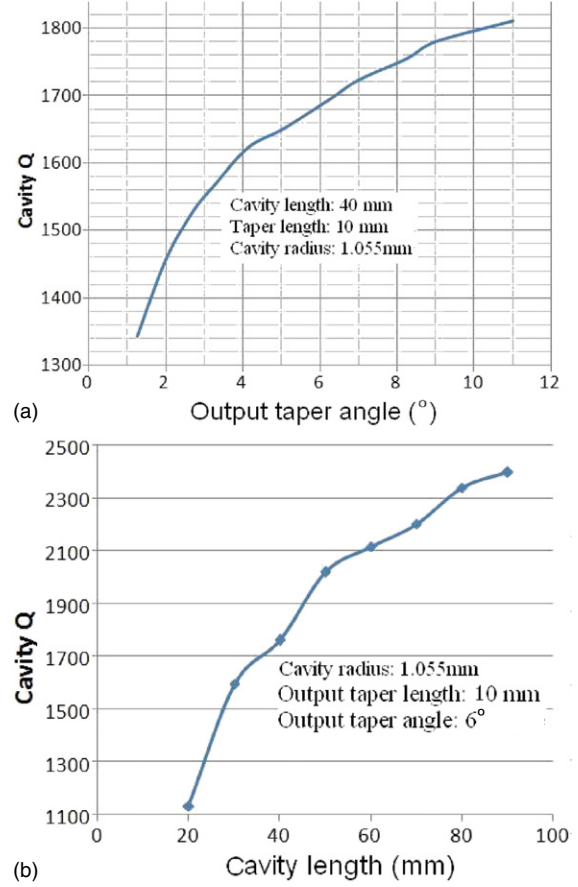
Figure 4. (*a*) Cavity Q as a function of output taper angle and (*b*) cavity Q as a function of cavity length.

length and the input section of the cut-off taper had a fixed radius of 0.8 mm and a length of 20 mm. Though in a real situation the tolerance of the cavity dimensions, roughness of the cavity surface [24] and the purity of the materials will affect the value of the ohmic losses at high frequencies, the ideal surfaces and oxygen free high conductivity copper were applied to these calculations. From the diagram we can see the cavity Q increases as the angle increases, but in order to sustain enough output power and to decrease the heat load of the cavity [25], the taper angle needs to be properly selected. Considering all of these factors a 6° output taper was chosen in the cavity design. The cut-off taper angle was also studied by changing the length of the taper with a fixed cut-off input radius 0.8 mm. Cascade simulations show that these changes do not affect the cavity Q value very much (less than 20 when the cut-off taper length was varied from 5 to 20 mm).

Figure 4(*b*) shows the simulated cavity Q as a function of cavity length using the code Cascade. In the simulation the input end had a 20 mm taper with an input radius of 0.8 mm. The cavity radius remains the same as before, which was 1.055 mm, and at the end it had a 6° output taper. Simulations using CST Microwave Studio showed that there is no significant mode conversion (<10% of power) for this output taper at the operating mode. However, further increase in the output taper length or output taper angle will cause significant mode conversion. For example, when the
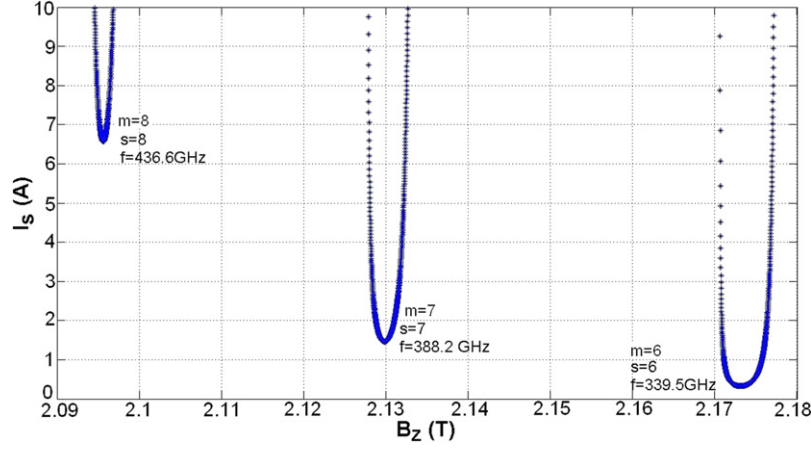
Figure 5. Starting currents for the seventh harmonic TE_{71} mode and its neighbouring TE_{m1} modes.

taper length was increased to 20 mm, 70% of the power was converted to the TM_{52} mode.

The starting oscillation currents for this cavity at the design mode and competing modes can be calculated using the equation shown below [12]:

$$I_s = \left(\frac{I_A}{Q}\right)\left(\frac{\omega}{s\Omega}\right)\left(\frac{\gamma L r_w^2 \omega k_z^2 \beta_z^2}{16c}\right)\left(1 - \frac{m^2}{x_{mn}^2}\right)$$
$$\times \left(\frac{J_m(x_{mn})}{J_m'(x_{mn}\beta_\perp c/r_w\Omega)}\right)^2 R(X)^{-1}, \tag{5}$$

where

$$R(X) = \left\{2 - 2x\left(\frac{\beta_\perp^2}{\beta_z}\right)\left(\frac{k_z c}{s\Omega}\right) + \left[\left(\frac{r_w s\Omega}{\beta_\perp c x_{mn}}\right)^2 - 1\right]\right.$$
$$\times \left(\frac{J_n(x_{mn}\beta_\perp c/r_w\Omega)}{J_n'(x_{mn}\beta_\perp c/r_w\Omega)}\right)^2 + \left(\frac{2x_{mn}\beta_\perp c}{r_w\Omega}\right)$$
$$\times \left.\left(\frac{J_n''(x_{mn}\beta_\perp c/r_w\Omega)}{J_n'(x_{mn}\beta_\perp c/r_w\Omega)}\right)\right\} G(X)$$
$$+ \left(\frac{\beta_\perp^2}{\beta_z}\right)\left(\frac{\omega}{s\Omega}\right)\left[\frac{\omega}{ck_z} - \left(\frac{ck_z}{\omega}\right)X^2\right] G'(X) \tag{6}$$

and $X = (\omega - s\Omega)/k_z\beta_z c$,

$$G(X) = \begin{cases} \left[\cos\left(\pi q X/2\right)/\left(1 - X^2\right)\right]^2 & (\text{odd } q), \\ \left[\sin\left(\pi q X/2\right)/\left(1 - X^2\right)\right]^2 & (\text{even } q). \end{cases} \tag{7}$$

Here $q = k_z L/\pi$, and the calculation result is shown in figure 5. In this calculation the cavity $Q = 2000$ and the electron beam velocity ratio α was 3.

The minimum starting current for the seventh harmonic mode is 1.4 A, at a magnetic field of 2.13 T which are both within the capability of our cusp gun design current of 1.5–1.7 A and the solenoid magnetic field of 2.16 T. This diagram clearly shows that the neighbouring modes $s = 8$ and $s = 6$ will be eliminated as the starting current for the eighth harmonic requires a starting current of more than 6 A and the magnetic field requirement for the sixth harmonic is above 2.17 T.
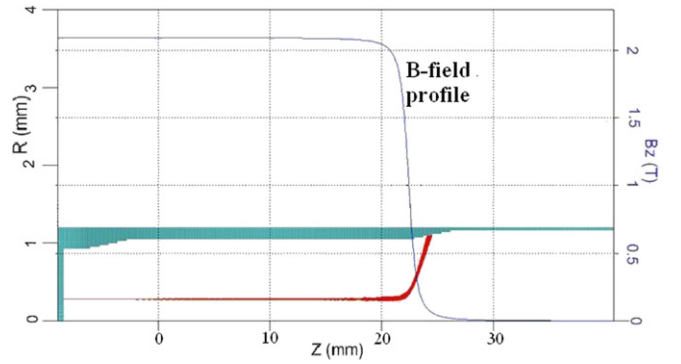
Figure 6. A schematic diagram of the gyrotron in the R–Z plane with simulated electron beam trajectories.

4. Simulation results

In order to demonstrate the beam–wave interaction can take place in the designed gyrotron cavity, the code MAGIC was used to simulate the harmonic gyrotron interaction. The R–Z plane geometries of the smooth cylindrical structures and electron trajectories are shown in figure 6. An ideal beam with the parameters from the cusp electron simulation but without velocity and radius spreads was emitted from the left end of the cavity and propagated in a uniform B-field produced by a solenoid in the MAGIC simulation. The right end of the solenoid sits in the middle of the output taper in the Z-axis. During the simulation, the cavity length was reduced from 50 to 30 mm as the cavity ohmic loss was neglected in the simulation. A schematic diagram of the simulation is shown in figure 6 with the magnetic field profile produced by the solenoid.

The simulation result is shown in figure 7. In the simulation the large orbit annular electron beam had a voltage of 40 kV, a current of 1.5 A and a beam velocity ratio α of 3. The magnetic B-field applied in the cavity was 2.09 T. The magnetic field difference between the MAGIC and the analytical calculation is due to the grid density in the gyrotron simulation; when a higher grid density is used, the B-field required in the simulation will be larger and closer to the analytically calculated value.
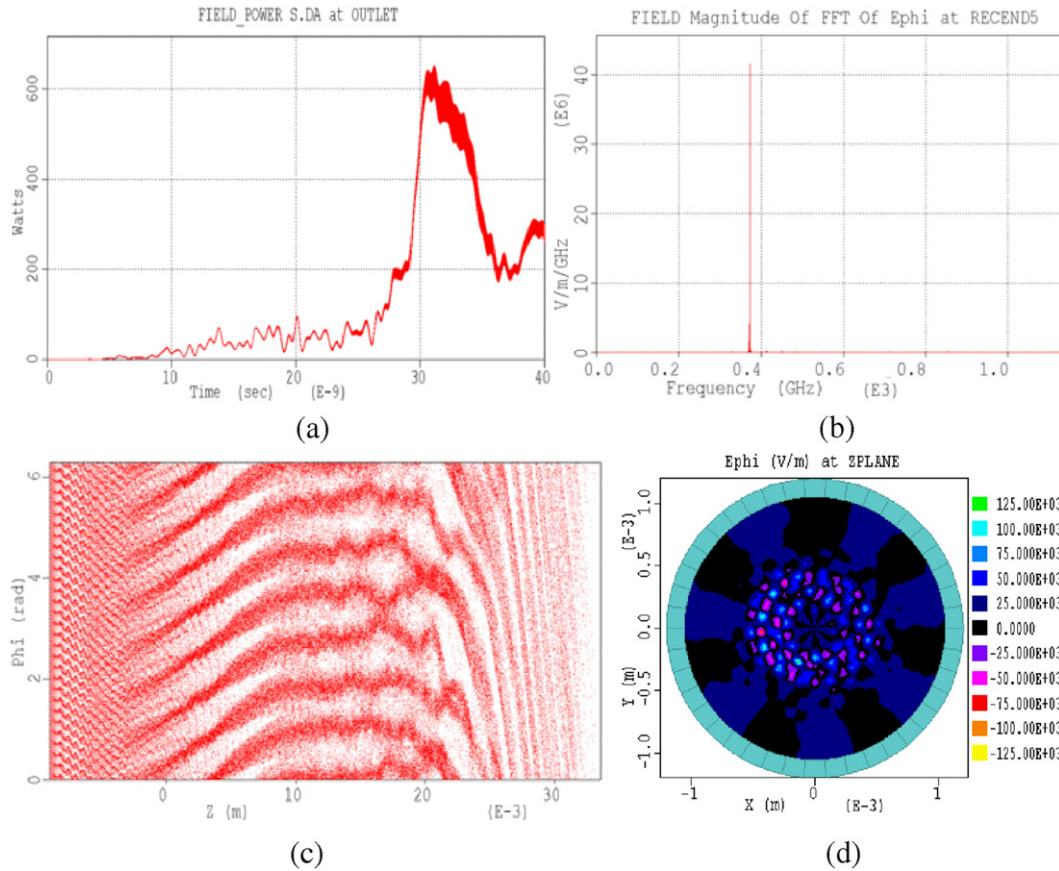
Figure 7. Simulation results of the seventh harmonic gyrotron with a smooth cavity: (*a*) output power, (*b*) output spectrum and (*c*) electron phase angle as a function of axial position (*d*) microwave E_Φ field pattern at resonance.

The electron phase angle as a function of axial position Z (figure 7(*c*)) indicates the interaction occurred at the seventh harmonic of the electron cyclotron frequency. Very pure radiation output at a frequency of 384 GHz was observed in the simulation as shown in figure 7(*b*), and ∼600 W of output power was achieved in this simulation. The reduction in power observed after ∼30 ns arises due to the cavity of 30 mm in length being sufficiently long in the absence of wall loss, for the interaction to enter phase trapped saturation resulting in re-absorption of the wave energy—this can be seen in figure 7(*c*) where the electron distribution in phase angle illustrates the trapping occurring. When 0.1 mm beam thickness and 25% beam spread were introduced in the simulation, it was found that the total output power dropped to ∼500 W while a competing TE$_{61}$ became slightly dominant at the output. The output power at the designed frequency and mode dropped to ∼200 W.

5. Conclusion

In conclusion a ∼390 GHz harmonic gyrotron based on a large orbit electron beam was designed and simulated. The cavity has been analysed and optimized. Theoretical and numerical simulation results demonstrate that the beam interacts with the single TE$_{71}$ mode and a simulated output power of ∼600 W was achieved while using a 40 kV, 1.5 A, large orbit electron beam with velocity ratio α of 3. It was found from simulation that

a spread in α will cause the reduction in the output power and start-up of mode competition. The effect that beam parameters, such as velocity spread and envelop ripple, might have on the starting current and mode excitation [26] will be studied both numerically and experimentally in the future.

Acknowledgments

References

[1] Wagner D *et al* 2007 The new multi-frequency electron cyclotron resonance heating system for ASDEX Upgrade *Fusion Sci. Technol.* **52** 313–20
[2] Saito T *et al* 2008 Development of a sub terahertz high power pulse gyrotron for collective Thomson scattering *Presented at the Joint 33rd Int. Conf. Infrared Millimeter, 16th Int. Conf. Terahertz Electronics (Pasadena, CA, 2008)* Paper ICIMW.2008.4665739
[3] Bhartia P and Bahl I J 1984 *Millimeter Wave Engineering and Applications* (New York: Wiley)
[4] Siegel P H 2002 Terahertz Technology *IEEE Trans. Microw. Theory Tech.* **50** 910–28

[5] Clery D 2002 Brainstorming their way to an imaging revolution *Science* **297** 761–3

[6] Torrezen A C *et al* 2008 CW Operation of a tunable 330/460 GHz gyrotron for enhanced nuclear magnetic resonance *Presented at the Joint 33rd Int. Conf. Infrared Millimeter, 16th Int. Conf. Terahertz Electronics (Pasadena, CA, 2008)* Paper ICIMW.2008.4665733

[7] Glyavin M Yu, Luchinin A G and Golubiantnikov G Yu 2008 Generation of 1.5 kW 1 Thz coherent radiation from a gyrotron with a pulsed magnetic field *Phys. Rev. Lett.* **100** 015101

[8] Idehara T *et al* 2004 A high harmonic gyrotron with an axis-encircling electron beam and a permanent magnet *IEEE Trans. Plasma. Sci.* **32** 903–9

[9] Wang Q S *et al* 1994 Stable 1 MW, third-harmonic gyro-TWT amplifier *IEEE Trans. Plasma. Sci.* **22** 608–15

[10] Wang Q S *et al* 2000 Design of a W-band second-harmonic TE$_{02}$ gyro-TWT amplifier *IEEE Trans. Plasma Sci.* **28** 2232–7

[11] La Agusu *et al* 2006 Design of a 400 GHz gyrotron for DNP-NMR spectroscopy *Presented at the Joint 31rd Int. Conf. Infrared Millimeter, 14th Int. Conf. Terahertz Electronics (Shanghai, China, 2006)* Paper ICIMW.2006.368290

[12] McDermott D B, Luhmann N C Jr, Kupisedwski A and Jory H R 1983 Small-signal theory of a large-orbit electron-cyclotron harmonic maser *Phys. Fluids* **26** 1936–41

[13] Schmidt G 1962 Nonadiabatic particle motion in axialsymmetric fields *Phys. Fluids* **5** 994–1002

[14] He W *et al* 2006 A W-band gyro-BWO based on a helically corrugated waveguide *Infrared Millimeter Waves and 14th Int. Conf. on Terahertz Electronics, Joint 31st Int. Conf. on IRMMW-THz (Shanghai, Sept. 2006)* pp 88–8

[15] He W 2008 Axis-encircling electron beam generation using a smooth magnetic cusp for gyro-devices *Appl. Phys. Lett.* **93** 121501

[16] Bratman V L *et al* 2005 Submillimeter-wave large-orbit gyrotron *Radiophys. Quantum Electron.* **48** 731–6

[17] Bratman V L, Kalynov Yu K and Manuilov V N 2009 Large-orbit gyrotron operation in the terahertz frequency range *Phys. Rev. Lett.* **102** 245101

[18] He W *et al* 2009 Design, simulation and experiment of a cusp electron beam for millimeter wave gyro-devices *IVEC (Rome, Italy, 2009)*

[19] Donaldson C R *et al* 2009 Design and numerical optimization of a cusp-gun-based electron beam for millimeter-wave gyro-devices *IEEE Trans. Plasma Sci.* **37** 2153–7

[20] Chu K R 2004 The electron cyclotron maser *Rev. Mod. Phys.* **76** 489–540

[21] Chu K R and Anthony T Lin 1988 Gain and bandwidth of the gyro-TWT and CARM amplifiers *IEEE Trans. Plasma Sci.* **16** 90–104

[22] Furuno D S *et al* 1990 Operation of a large-orbit high-harmonic gyro-traveling-wave tube amplifier *IEEE Trans. Plasma Sci.* **18** 313–20

[23] Ives L, Nelson J and Vogler W 2003 Cascade—an advanced computational tool for waveguide components and window design *Proc. 2003 Particle Accelerator Conf. (Portland, OR, 2003)*

[24] Thorpe T S 1954 RF conductivity in copper at 8 mm wavelengths *Proc. Instn. Electr. Eng.* (Part III) **101** 357–9

[25] Zapevalov V E *et al* 1994 Low-Q cavities for high-power gyrotrons *Radiophys. Quantum Electron.* **37** 233–6

[26] Bratman V L, Kalynov Yu K and Fedotov A E 1998 Theory of gyro devices with thin electron beams (large-orbit gyrotron) *Tech. Phys.* **43** 1219–25